IntechOpen

Stability Control and Reliable Performance of Wind Turbines

Edited by Kenneth Eloghene Okedu

STABILITY CONTROL AND RELIABLE PERFORMANCE OF WIND TURBINES

Edited by **Kenneth Eloghene Okedu**

Stability Control and Reliable Performance of Wind Turbines
http://dx.doi.org/10.5772/intechopen.72160
Edited by Kenneth Eloghene Okedu

Contributors

Saad Saad, Naser El Naily, Faisal Mohamed, Abdelsalam Elhaffar, Jamal Wafi, Jaeha Ryi, Satya Kiran Raju Alluri, Devender Gujjula, B Krishnaveni, G Dhinesh, Svs Phanikumar, Mv Ramanamurthy, Yao Li, Caichao Zhu, Kerrouche Kamel Djamel Eddine, Emad Elhaji, Chikako Fujiyama, Yasuhiro Koda, Noriaki Sentoh, Tahere Pourseif, Hassan Zeynali, Arash Shams, Majid Taheri Andani, Hamed Pourgharibshahi, Kenneth Eloghene Okedu

© The Editor(s) and the Author(s) 2018
The rights of the editor(s) and the author(s) have been asserted in accordance with the Copyright, Designs and Patents Act 1988. All rights to the book as a whole are reserved by INTECHOPEN LIMITED. The book as a whole (compilation) cannot be reproduced, distributed or used for commercial or non-commercial purposes without INTECHOPEN LIMITED's written permission. Enquiries concerning the use of the book should be directed to INTECHOPEN LIMITED rights and permissions department (permissions@intechopen.com).
Violations are liable to prosecution under the governing Copyright Law.

Individual chapters of this publication are distributed under the terms of the Creative Commons Attribution 3.0 Unported License which permits commercial use, distribution and reproduction of the individual chapters, provided the original author(s) and source publication are appropriately acknowledged. If so indicated, certain images may not be included under the Creative Commons license. In such cases users will need to obtain permission from the license holder to reproduce the material. More details and guidelines concerning content reuse and adaptation can be foundat http://www.intechopen.com/copyright-policy.html.

Notice

Statements and opinions expressed in the chapters are these of the individual contributors and not necessarily those of the editors or publisher. No responsibility is accepted for the accuracy of information contained in the published chapters. The publisher assumes no responsibility for any damage or injury to persons or property arising out of the use of any materials, instructions, methods or ideas contained in the book.

First published in London, United Kingdom, 2018 by IntechOpen
eBook (PDF) Published by IntechOpen, 2019
IntechOpen is the global imprint of INTECHOPEN LIMITED, registered in England and Wales, registration number: 11086078, The Shard, 25th floor, 32 London Bridge Street
London, SE19SG – United Kingdom
Printed in Croatia

British Library Cataloguing-in-Publication Data
A catalogue record for this book is available from the British Library

Additional hard and PDF copies can be obtained from orders@intechopen.com

Stability Control and Reliable Performance of Wind Turbines
Edited by Kenneth Eloghene Okedu

p. cm.

Print ISBN 978-1-78984-147-3

Online ISBN 978-1-78984-148-0

eBook (PDF) ISBN 978-1-83881-662-9

Meet the editor

Kenneth Eloghene Okedu was a Massachusetts Institute of Technology (MIT) Fellow in the Department of Electrical and Computer Engineering at Cambridge, Boston, USA, in 2013. He obtained his Ph.D. in the Department of Electrical and Electronic Engineering, Kitami Institute of Technology, Hokkaido, Japan, in 2012. He received his B.Sc. and M.Eng. degrees in Electrical and Electronic Engineering from the University of Port Harcourt, Nigeria, in 2003 and 2007, respectively, where he has been a Faculty since 2005. He was also a visiting Faculty to the Petroleum Institute, Abu Dhabi National Oil Company, Abu Dhabi. He is presently a visiting Faculty to Caledonian College of Engineering, Muscat, Oman (a university college connected with Glasgow Caledonian University, UK). His research interests include renewable energy systems, stabilization of wind farms using doubly fed induction generator variable speed wind turbines, augmentation and integration of renewable energy into power systems, power system stability, grid frequency dynamics, wind energy penetration, FACTS devices and power electronics, renewable energy storage, and hydrogen and fuel cells.

Contents

Preface

This book contains three sections. Section 1 Stability Control and Reliable Performance of Wind Turbines – Modelling, Stability, and Control of Wind Turbines and Section 2 Stability Control and Reliable Performance of Wind Turbines – Assessment, Reliability and Prospects of Wind Turbines. Many authors with sound academic and industrial experience in the field of wind turbine technology have contributed to this book, which it is hoped will foster the knowledge and information for engineering applications, academia, and industries.

Section 1 contains five chapters. Chapter 1 gives an introduction to the book by exploring the current state of the art of wind turbine technology. This chapter covers the following: renewable energy, overview of wind energy and wind turbine technology, types of wind turbine, wind turbines and the operational grid requirements (grid codes) for stability control, structure of wind turbines, onshore and offshore wind farms, global wind turbine installation capacity, and wind turbine manufacturers and market trends. Chapter 2 describes power oscillation inter-area damping considering a permanent magnet synchronous generator (PMSG) wind turbine. Different buses of the IEEE-30 model were connected to the PMSG, with a scenario that an H-infinity design controller is proposed to regulate the power variations of the grid network. The chapter presents the effectiveness of a wind generator in enhancing the damping of the system. In Chapter 3, the impact of power quality and system stability in the penetration of renewable energy sources in a distribution network is investigated. Shortcomings relating to the quality and reliability of the electric power fed into a grid-connected network will be analyzed based on grid requirements. The chapter further states that the presence of renewable energy sources modifies the short-circuit fault level in a grid-connected system, and thus the ability of protective apparatus in the distribution network will be affected. The integration of a wind farm system on the Libyan distribution network, considering various penetration conditions, is analyzed technically to understand the impact on the power quality and voltage profile of the system. The exact model of the wind turbines is uncertain, and because of this wind turbines are classed as nonlinear complex systems. Consequently, there are challenges in controlling this system, since many wind turbines work in extreme weather conditions. Chapter 4 presents a Mu robust controller in wind turbines in severe cold weather conditions. In this chapter, the wind turbine blades are assumed to be iced, thereby making the model unreliable. A robust controller is proposed to control the pitch angle of the wind turbine. Chapter 5 presents a dual robust control strategy for doubly fed induction generator (DFIG) grid-connected wind turbines attending to unbalanced grid conditions. In this chapter, the low-voltage ride-through (LVRT) capability of the DFIG wind generator is investigated using hardware and software solutions. A low-cost effective LVRT scheme based on the dual sequence decomposition technique and Lyapunov-based robust control theory is proposed. The salient benefit of this proposed scheme is that it effectively removes oscillations of active and reactive power exchanged between the generator and the grid, in addition to symmetrical and sinusoidal grid current injection. Thus, the proposed scheme will reduce torque, stator power, and current pulsations compared to the traditional vector control strategy of the single control scheme.

Section 2 has four chapters. Evaluation and stability analysis of onshore wind turbine supporting structures is presented in Chapter 6. The findings of the effect of stability of a supporting structure on onshore wind turbine foundations considering field measurements, finite element analysis, and laboratory validations are presented in this chapter. The models considered employ three-dimensional nonlinear finite element analyses for examining the damage processes of reaching failure and the limited state of foundations that are individually based on the fatigue limit state of the concrete. As a result, assessment of the existing structure will consider the stress number of cycle diagram obtained from experiment and analysis, respectively. In Chapter 7, an estimation method is proposed to obtain a noise reduction effect from an airfoil with a serrated trailing edge for a wind turbine rotor. A wind tunnel experiment is used to investigate the changes in the aerodynamic performance of a wind turbine caused by a two-dimensional airfoil with a serrated trailing edge designed to mitigate noise from the rotor blade of the turbine. The study in this chapter was carried out based on Howe's theory, which is a key theory of the study of noise reduction effects emanating from a serrated trailing edge. An empirical noise prediction formula that changes the boundary layer thickness of a two-dimensional airfoil is proposed. The use of offshore wind energy is on the rise, because more energy can be extracted from offshore winds than onshore winds. Chapter 8 presents an offshore wind feasibility study in India. Offshore wind provides a scalable alternative to conventional resources. This chapter provides an insight into the Ministry of Earth Science's various activities for offshore wind power realization in India. The assessment results in this chapter show high offshore potential areas, levelized cost of electricity, and internal rate of return on investment. The port facilities along the Gujarat and Tamil Nadul coastline are assessed and the methodology of the installation is developed based on marine spread along the Indian coast. With the rapid development of the wind power industry, it is imperative to research the reliability of wind turbines. In Chapter 9, the failure models and research progress of wind turbine reliability is analyzed. The chapter emphasizes a number of failure modes, failure causes, and detection methods of some key components in wind turbines. Furthermore, some frequently used approaches to reliability analysis and wind turbine reliability research status are analyzed. The chapter also covers methods and measures to improve wind turbine reliability, condition monitoring and assessment process, supervisory control, and data acquisition, respectively. The chapter recommends that it is paramount to mitigate the cost of operation and maintenance and improve the safety of wind turbines.

Dr. Kenneth Eloghene Okedu
National University of Science and Technology (Glasgow Caledonian University)
Muscat, Oman

Section 1

Modelling, Stability, and Control of Wind Turbines

Introductory Chapter: Stability Control and Reliable Performance of Wind Turbines

Kenneth Eloghene Okedu

Additional information is available at the end of the chapter

http://dx.doi.org/10.5772/intechopen.80237

1. Renewable energy sources

Energy is essential for the growth and socio-economic development of any economy. Recently, the use of renewable energy sources for energy generation is on the raise. Wind energy is one of the renewable energy sources that is indigenous in nature and could help in mitigating fossil fuels dependency [1]. Presently, about 87% of total energy in the world is obtained from traditional fossil fuels (coal, oil and natural gas), while 6% is obtained from nuclear plants and the remaining 7% is generated from renewable sources (especially hydropower, wind and solar) [2]. Unfortunately, the amounts of fossil fuel and nuclear power resources are limited. Based on the current estimates given in the literature, natural uranium used for nuclear power technology will last only about 50 years; oil, no more than 100 years; natural gas, 150 years; and coal, 200 years.

Due to the fact that fossil and nuclear fuels are highly depended upon for energy generation, there are environmental pollution and safety challenges, which are now becoming dominant issues in the society and international world. Recently, there was a Paris climate agreement in France. “The agreement is within the United Nations Framework Convention on Climate Change (UNFCCC), dealing with greenhouse gas emissions mitigation, adaptation and finance, commencing in the year 2020” [3, 4]. The terms of the agreement was deliberated by 196 representatives during the 21st Conference of the UNFCCC in Paris and on December 12, 2015, it was adopted by consensus. The world is drastically focusing on clean and safe renewable energy sources due to the effects of environmental pollution on global warming. In the long run, the resulting change of climate has disastrous consequences on the planet.

There are enormous resources of wind energy, and it has been estimated in the literature that if 10% of the wind energy could be barely tapped, the electricity needs of the world could be supplied [2, 5]. With the recent advancement of variable speed wind turbines, power electronics, drives and control system technologies, wind energy is now competitive with traditional coal and natural gas power. However, one of the shortcomings of wind energy is that it is stochastic in nature, thus making its availability sporadic, consequently, needs back up by other conventional power sources.

The solar photovoltaic systems have the merit of being static and require less repair and maintenance. However, it is five times more expensive than wind power, although recently, there is huge research and development to produce low cost photovoltaic solar panels for widespread applications. Solar power conversion performance efficiency is basically 16%, and its availability is also sporadic like the wind power.

Hydrogen gas is the primary fuel for fuel cell energy or a fossil fuel type like gasoline or methanol, with a reformer. Fuel cells are static and have high conversion efficiency of about 60% compared to wind and solar power. However, fuel cells are heavy, expensive and possess poor transient response in their current state. Although, fuel cells show tremendous promise for the future, especially for electric cars, however, a tremendous amount of research and development is needed to achieve this aim.

2. Overview of wind energy technology

Wind energy is the indirect form of solar energy which is always being replenished by the sun. The differential heating of the earth's surface by the sun causes wind. It has been estimated that about 10 million MW of energy are continuously available in the earth's wind [6–8]. Wind energy could act as an environmental friendly alternative and national energy security especially during times of limited global reserves of fossil fuels, which threatens the long-term sustainability of global economy.

The technology of wind turbine has a technical identity and demand that is unique in terms of the design methods. Recently, remarkable advances and improved reliability in wind power design have been achieved owing to developments in modern technology. The structural dynamics advances and aerodynamics along with micrometeorology since 1980, have led to about 5% increase annually in wind turbines energy yield [9–13]. Present science and engineering research methods are producing better, stronger, lighter and more efficient blades for wind turbines. Wind turbines annual energy output has increased enormously and the weights, emitted noise of the wind turbine during operation have been halved over the last few years. A considerable amount of power can be obtained from wind energy technology by establishing more wind monitoring stations, effective selection of wind farm site with proper wind generator, enhanced maintenance procedures and practices of wind turbines, increase the wind generator availability, the use of large capacity wind generator, low wind regime turbine, higher heights of tower, wider rotor blade swept area, improved structural design and aerodynamics, proficient and enhanced technique for computer-based machining, improved power factor and better policies of the government.

Wind power generation has an edge over the other renewable energy technologies application, because of its technological maturity, good infrastructure and relative cost competitiveness. In the near future, wind energy is expected to play a vital role in both national and international levels regarding energy scenarios [1, 5, 14]. Basically the kinetic energy of the wind is converted to electrical energy via the wind turbine blades rotation. According to Greenpeace report in the literature, by the year 2020, about 10% electricity in the world can be obtained by the wind energy. However, wind power is already competitive with conventional fossil fuel power stations at good windy sites. With this enhanced and mature wind technology, together with superior economics, experts predict wind power would capture 5% of the world energy market by 2020. Advanced wind turbines must be more reliable, efficient, robust and less expensive than current wind turbines.

3. Wind turbine technology

There are three main types of wind turbines used nowadays [15]: the Fixed Speed Wind Turbines with Squirrel-Cage Induction Generator (FSWT SCIG), the Variable Speed Wind Turbines with Doubly Fed Induction Generator (VSWT DFIG) and the Variable Speed Wind Turbines with Permanent Magnet Synchronous Generator (VSWT PMSG). Wind energy technology has experienced important improvement in several last decades [16] due to the technological improvement of wind turbines from fixed speed to variable speed. A brief distinction of the three types of wind turbine driven generators is given below.

The SCIG are used in general as fixed speed wind turbine generators due to their superior characteristics such as brushless and rugged construction, low cost, maintenance free and operational simplicity. However, this type of wind turbine technology requires large reactive power to recover the air gap flux when a short circuit fault occurs or grid disturbances in the power system. SCIG wind turbine technology has limited ability to provide voltage and frequency control, except it is supported with some expensive external power electronic control strategy, hence not commonly used in modern wind turbines.

The variable speed turbines are becoming the norm for new wind farm installations, because of high energy capture efficiency couple with reduced drive train stresses [17]. The PMSG VSWT, also known as the direct-drive synchronous generator with permanent magnet excitation and the DFIG VSWT with doubly fed back-to-back power converter type technologies, have become the two generator alternatives. The former has the disadvantage of cost mainly due to a power converter rated for the full power. Although in the latter, a gear box is needed, the DFIG requires a converter of only 20–30% of the generator rating for an operating speed range of 0.7–1.3 per unit (p.u) resulting in a lower cost.

Although the DFIG is not as rugged and robust as the squirrel-cage wind turbine type, however, the brushes have little wear and sparking when compared to DC machines and is the only acceptable option for alternative energy conversion in the megawatts power range. With the help of modern power electronic devices, it is possible to recover the slip power dissipated in resistances [2]. The DFIG wind turbine use a back-to-back power inverter system connected between the rotor side and the grid side of the machine, while the stator is directly connected to the grid. The DFIG can effectively operate at a wide range of speed based on the available wind speed and other specific operation requirements. Consequently, better capture of wind energy [2, 18, 19], with dynamic slip and pitch control could lead to effective rebuilding of the wind turbine terminal voltage, at the same time maintaining the power system stability after clearance of an external short circuit fault [20]. Besides, DFIG wind turbine has shown better behavior regarding system stability during short circuit fault in comparison to SCIG, because of its ability to decouple the active and reactive power output control. The DFIG superior dynamic performance is achieved from the frequency or power converters which typically operates with sampling and switching frequencies of above 2 kHz [21]. The Insulated Gate Bipolar Transistors (IGBTs) of the DFIG converter system are normally off, during lower voltages down to 0% and the system remains in standby mode [22–26]. During grid disturbances, if the voltages are high above a set cutoff or threshold value, the DFIG wind turbine system is very quickly synchronized and is back in operation again.

The VSWT PMSG is connected through a back-to-back converter to the grid. This provides maximum flexibility, enabling full real and reactive power control and fault ride through capability during voltage dips, as compared to the VSWT DFIG technology. However, the use of this wind turbine technology is limited when compared to the DFIG technology due to high cost. The schematic diagrams of the three wind turbine technologies are shown in **Figures 1–3**, while a comparison between the fixed and variable speed wind turbine technology is given in **Table 1**.

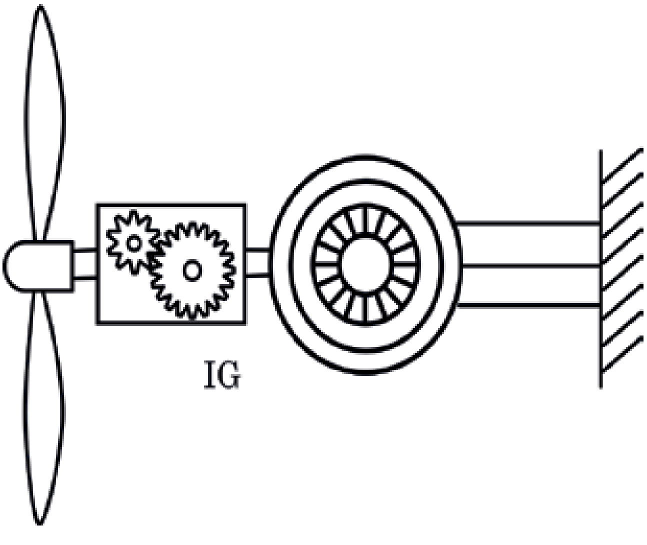

Figure 1. Fixed speed induction generator wind turbine.

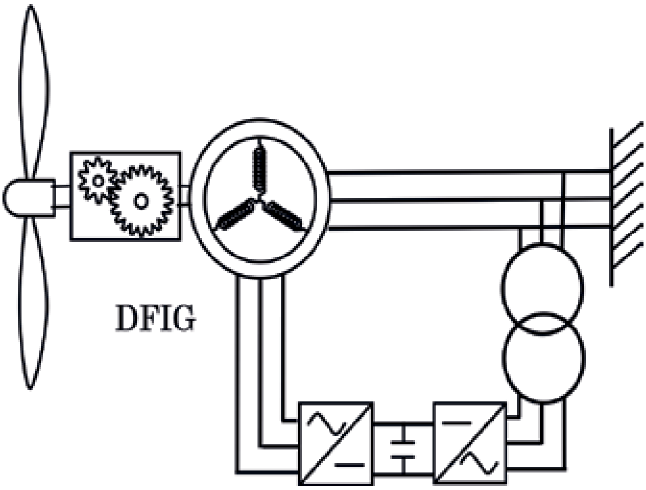

Figure 2. Doubly fed induction generator variable speed wind turbine.

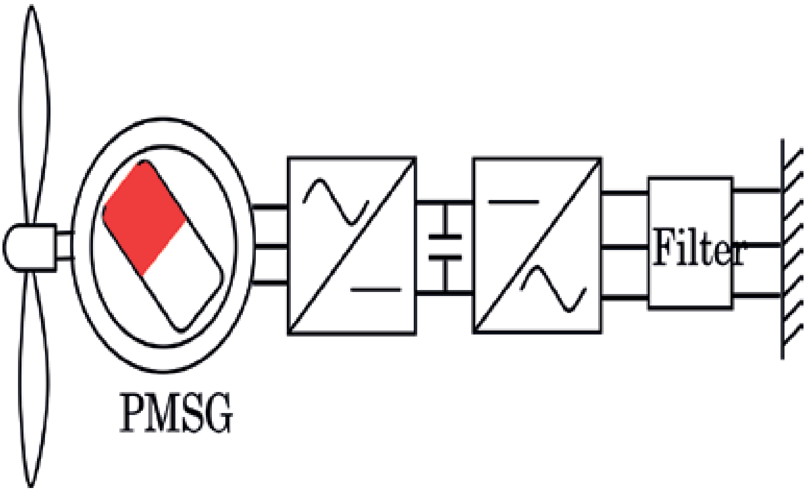

Figure 3. Permanent magnet synchronous generator variable speed wind turbine.

Fixed speed wind generator	**Variable speed wind generator**
1. This type of wind turbine has fixed speed operation, thus the power captured is in limited range.	1. This type of wind turbine has variable speed operation, making it possible to achieve a high efficiency of energy conversion compared to constant speed operation especially in low wind speed areas.
2. The technology of this turbine has limited ability to provide voltage and frequency control.	2. The technology of this turbine has ability to decouple control of active and reactive powers rapidly and independently by secondary excitation control. Thus, the grid connected turbine system tends to be more stable during network disturbances.

Fixed speed wind generator	Variable speed wind generator
3. This wind turbine has superior characteristics such as brushless and rugged construction, low cost, maintenance free and operational simplicity.	3. This wind turbine technology has reduction of mechanical stresses and acoustic noise.
4. The technology of this wind turbine requires large reactive power to recover the air gap flux when a short circuit fault or grid disturbance occurs in the power system.	4. The technology of this wind turbine improves the power quality of the grid connected system without expensive external reactive power compensation devices.
5. This wind turbine requires the installation of expensive external reactive power compensation devices to provide and support reactive power, thus, increasing the overall cost of the system.	5. This wind turbine has the required capacity of the power converters for secondary excitation, and this can be less than half for the case of a DFIG system, thus the total cost decreases.

Table 1. Comparative study of fixed and variable speed wind generators.

4. Wind turbines and operational grid requirements

The fast growth and penetration of wind generation through the installation of large number of wind turbines has led to primary concern about the effect of wind power on the transient and frequency stability of the electric utility grid. In several countries, institutional support on renewable energy sources has led to implementation of a large number of wind farms [27]. As the amount of wind power is drastically increasing in years to come, maintaining power system, voltage and frequency stability during a short circuit fault or grid disturbance will be more paramount in order to ensure power supply safety and other important tasks. It would

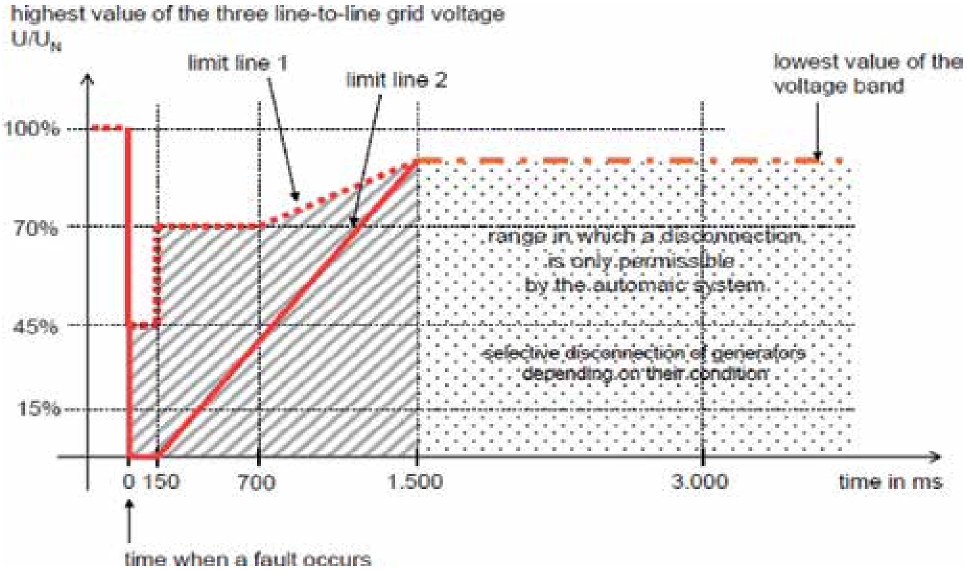

Figure 4. Fault ride through (low voltage ride through) requirement for wind farms as set by E.ON NETZ GmbH.

be imperative to perform new studies to evaluate the behavior of the wind farms during and after severe faults, in order to improve the design of the wind farms in an efficient and economy way. Hence, the most demanding requisite for wind farm is the Fault Ride Through

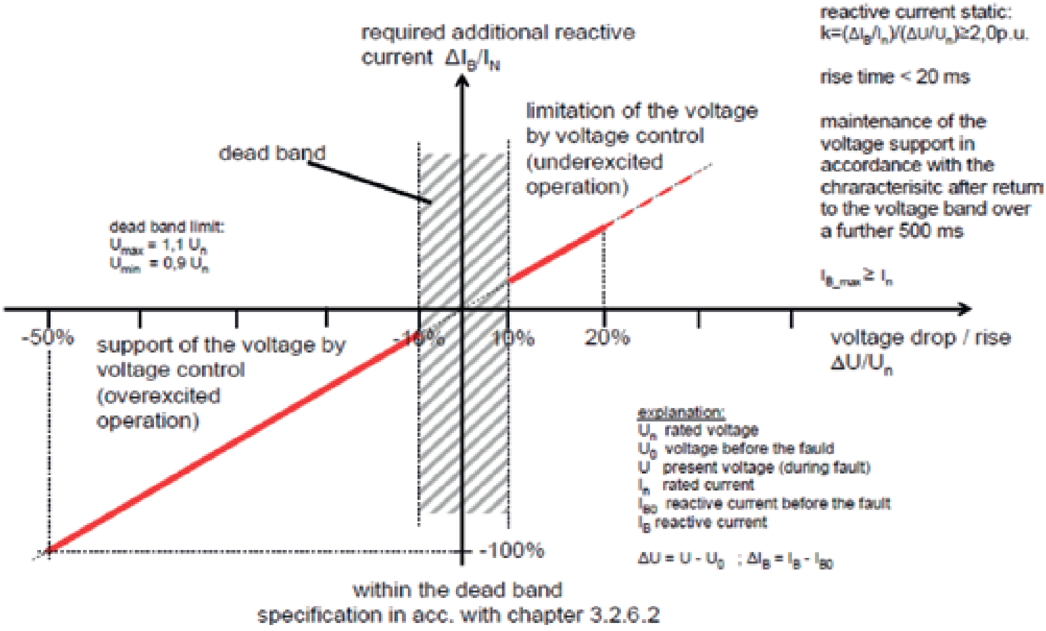

Figure 5. The rule of voltage support during grid fault as set by E.ON NETZ GmbH.

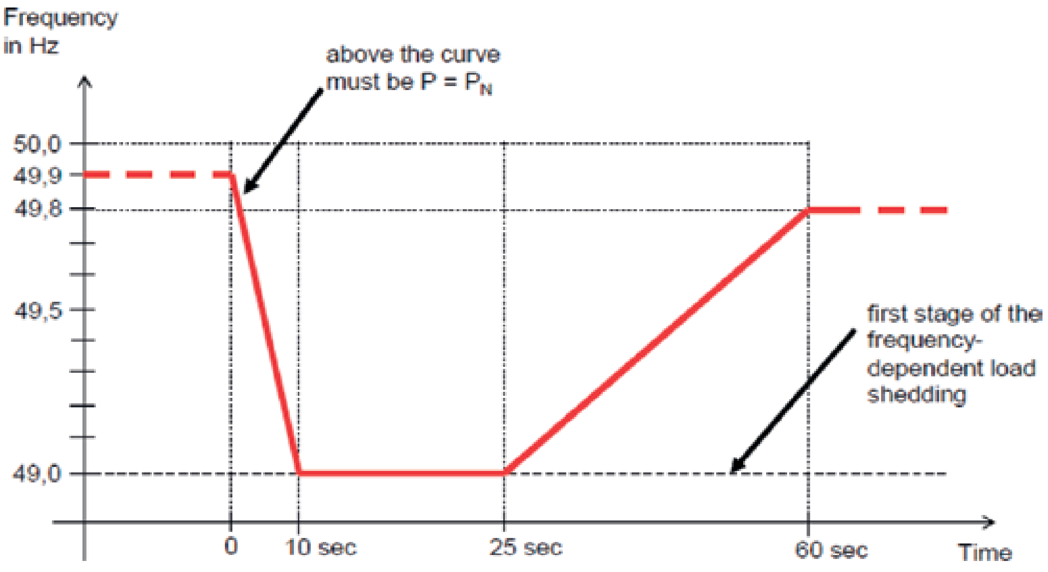

Figure 6. Grid frequency requirement of wind farms as set by E.ON NETZ GmbH.

(FRT) or Low Voltage Ride Through (LVRT) capability. Wind farms connected to high voltage transmission system must stay connected when a voltage dip or frequency disturbance occurs in the grid, otherwise, the sudden disconnection of great amount of wind power may contribute to the voltage dip and drop of frequency, with terrible consequences in the utility grid. Therefore, the transient and dynamic analysis of wind generators in wind farms are necessary. Several solutions could be used in the stability analysis and improvement of wind turbines during grid disturbances, so that they can contribute to voltage and frequency control. Some of these solutions are the use of power electronic devices and reactive power compensation units like static synchronous compensator (STATCOM), superconducting magnetic energy storage (SMES), energy capacitor system (ECS), crowbar, static series compensator (SSC), a dynamic voltage restorer (DVR), series dynamic braking resistor (SDBR), superconducting fault current limiter (SFCL), passive resistance network, series antiparellel thyristors and among others discussed in the literature.

4.1. Operational grid requirements

The big challenges that wind farms must face is voltage and frequency dip in the grid during grid disturbances [28]. The magnitude of the voltage is controlled by the reactive power exchange, while the frequency is controlled by the active power. **Figure 4** displays the typical requirement for fault ride through grid code regarding terminal voltage of the wind farm. The wind farm must remain connected to the grid if the voltage drop is within the defined r.m.s. value and its duration is also within the defined period as shown in the curve. **Figure 5** shows the required reactive current support from the generating plants during voltage dip, while **Figure 6** shows the permissible grid frequency requirement [29].

5. Structure of wind turbines

Some of the structures and installation configurations of wind turbines are presented in **Figure 7**. In **Figure 7a**, the complete layout of a typical wind turbine connection is shown. The major components of the wind turbine are the rotor blade, gearbox, nacelle, generator, power cables and tower. The output power of the wind turbine is distributed to the network grid via transformer and switchyard. The wind turbine generator is housed in the nacelle and **Figure 7b** and **c** shows the detailed structure of the nacelle containing the low speed shaft, gearbox, controller, anemometer, wind vane, high speed shaft, yaw motor tower and others. In **Figure 7d**, the details of the wind turbine blades and other ancillary components are described. The wind turbine rotor blade is basically made of glass reinforced plastic, while the Yaw shaft with the slip ring ensures 360° rotation. The tail pole and wind connects the body of the wind turbine through a sensitive bearing, while the tower of the wind turbine is of high quality spray painting and galvanized to be salt and acid proof. The wind turbine generator in the nacelle is extremely light and small, low in sound, swift in startup, quick in heat dissipation and of high efficiency. The nose cone of the wind turbine is made up of reinforced aluminum alloy and antisepsis casting.

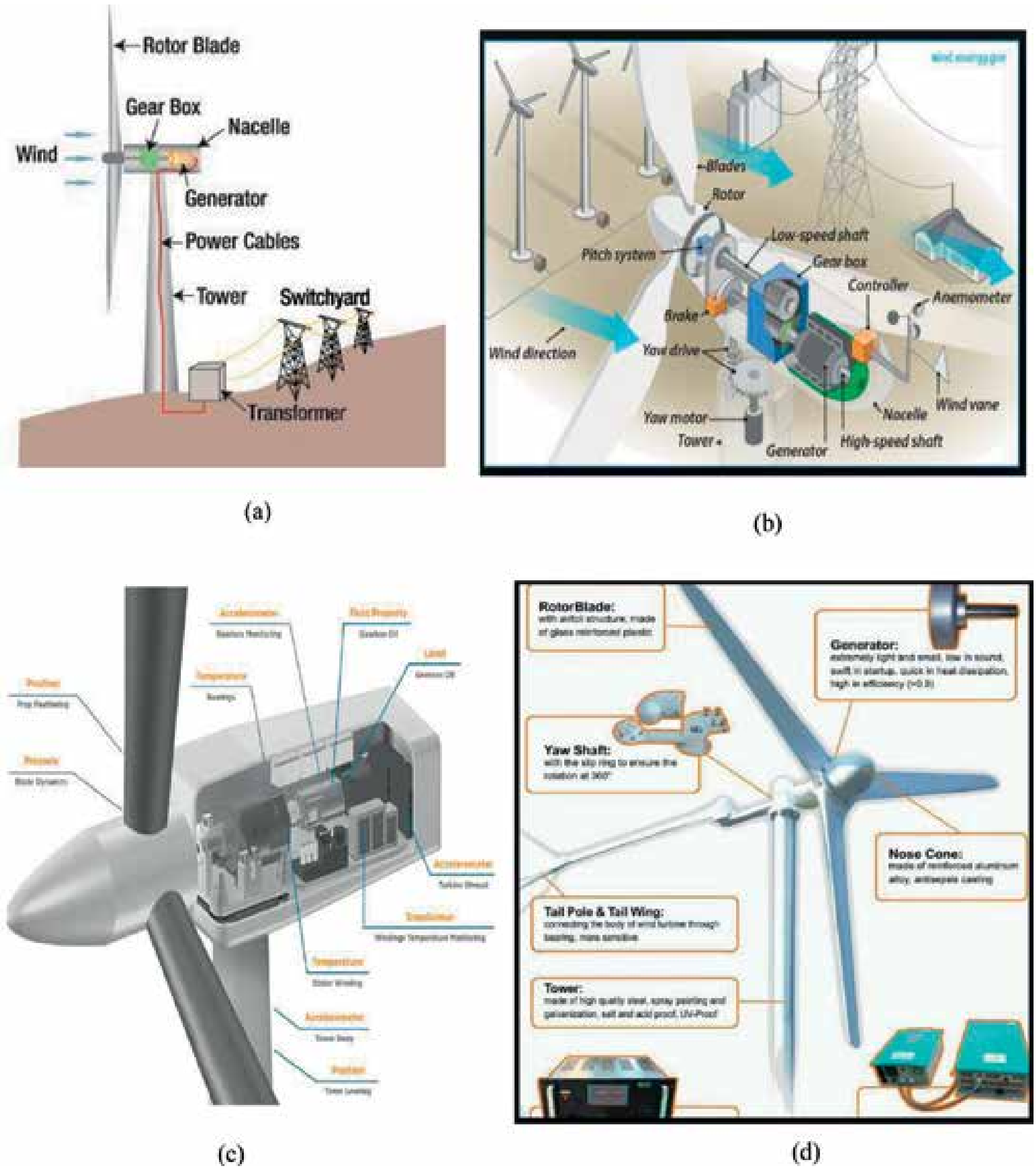

(a) (b)

(c) (d)

Figure 7. Structures and configuration of a typical wind turbine [30].

6. Onshore and offshore wind farms

A wind farm is a collection of wind turbines of the same type of technology or different type of technology. Although, in most wind farms, the technology of the wind turbines are same, however, it has been proposed in the literature to developed modern wind farms to compose of both fixed speed and variable speed wind turbine technology. This is because the variable speed wind turbine technology can be used to stabilize the fixed speed type, while at the same time generating power to the grid system. **Figure 8** shows typical onshore and offshore wind farms. More winds are achieved in offshore or coastal wind farms than onshore wind farms, however, the cost of installation and maintenance is high for this type of wind farm.

(a) (b)

Figure 8. Onshore and offshore wind farms.

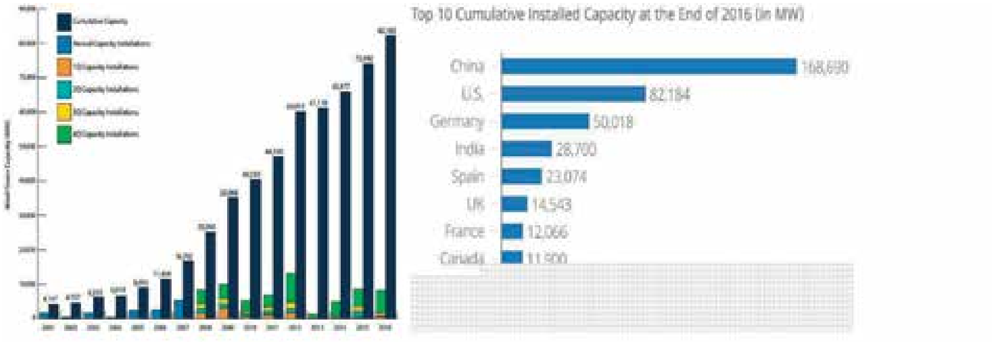

(a) Cummulative (b) Top countries

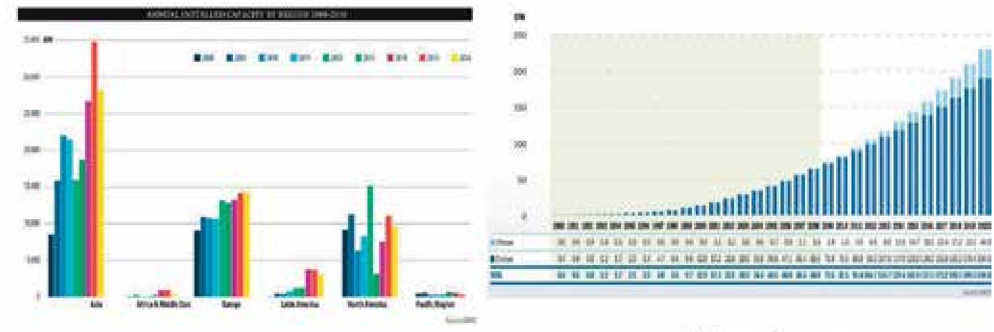

(c) By regions (d) Future Forecast

Figure 9. Global wind turbine installations [30]. (a) Cummulative; (b) Top countries; (c) By regions; (d) Future Forecast.

6.1. Global wind turbine installation capacity

Figure 9a shows the cumulative capacity, annual capacity installations, first, second, third and fourth quarter capacity installations of wind turbines globally from the year 2001 to 2016. This is tremendous increase in the number of wind turbine installations over the years from the figure. As at 2016, the wind power capacity is already 82,183 MW as against 4147 MW in the year 2001. The cumulative installed capacity over these years by countries is shown in **Figure 9b**, with China taking the lead, then the United States and Germany behind China. The wind turbine installation by regions of the world is shown in **Figure 9c**, from 2008 to 2016. Asia is leading with about 35,000 MW annual installed capacity in 2015. This value, however, dropped in 2016 to about 28,000 MW. There was considerably decrease in the annual installed capacity of wind turbines in Asia during 2012 from the figure, however, between 2013 and 2016, the annual installed capacity increased. In Europe, the annual installed capacities in 2015 and 2016 are same with a rough estimate of 14,000 MW. In North America, the highest annual installed capacity of 15,000 MW wind turbine was achieved in the year 2012, and in 2013, the value dropped drastically to 2500 MW. In 2015, the annual installed capacity rose to about 12,000 MW, thereafter, in 2016, the value dropped below 10,000 MW. The distribution of wind turbine installation in North America is irregular over the years due to less interest in renewable energy. The Pacific region, Africa and the Middle East are the least in annual installed capacity of wind turbine, respectively. The future forecast of the installed onshore and offshore wind turbines from 1990 to 2020 is shown in **Figure 9d**, with a value of 230 GW wind capacity excepted by 2020.

7. Wind turbine manufacturers and market trend

Some of the manufacturers of wind turbines are shown **Figure 10a**. The top major wind turbine manufacturers are Vestas, GE energy, Goldwind, Gamesa, Enercon, Siemens, Nordex, Envision, Ming Yang and United Power, respectively. The designs and control strategy employed in the wind turbine system is slightly different for each manufacturer. The wind turbine market trend is shown in **Figure 10b** from 2012 to 2017. There is cumulative increase

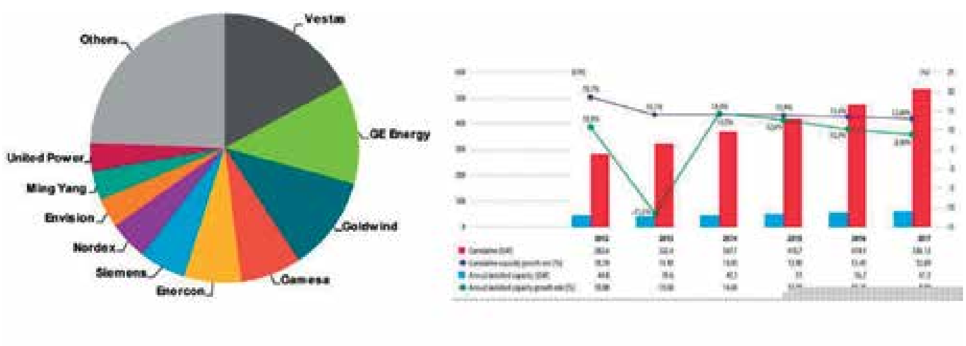

(a) (b)

Figure 10. Wind turbine manufacturers and market trend [30] (a) Wind turbine manufacturers; (b) Wind turbine market trend.

in power (GW) from 2012 to 2017, the cumulative capacity growth rate and annual installed capacity growth rate decreased over the considered years. There is little or no difference in the annual installed capacity (GW) over the considered years.

Author details

Kenneth Eloghene Okedu

Address all correspondence to: kenokedu@yahoo.com

Department of Electrical and Computer Engineering, National University of Science and Technology, Muscat, Sultanate of Oman

References

[1] Joselin Herbert GM, Iniyan S, Sreevalsa E, Rajapandian S. A review of wind energy technologies. Renewable and Sustainable Energy Reviews. 2007;**11**:1117-1145

[2] Godoy Simoes M, Farret FA. Renewable Energy Systems: Design and Analysis with Induction Generators. LLC, Florida: CRC Press; 2004

[3] Sutter JD, Berlinger J. Final Draft of Climate Deal Formally Accepted in Paris, Cable News Network (CNN), Turner Broadcasting System, Inc. [Retrieved: 12-12-2015]

[4] Jump up, "Paris Climate Talks: France Releases 'Ambitious, Balanced' Draft Agreement at COP21", ABC Australia. 12 December 2015

[5] Ezio S, Claudio C. Exploitation of wind as an energy source to meet the world's electricity demand. Wind Engineering Journal. 1998;**74-76**:375-387

[6] MNES, Ministry of Non-Conventional Energy Sources, Annual Report, Ministry of New and Renewable Energy, Government of India; 2005

[7] Kocak KA. Method for determination of wind speed persistence and its applications. Energy. 2002;**27**(10):967-973

[8] Okedu KE, Uhunmwangho R. Optimization of renewable energy efficiency using HOMER. International Journal of Renewable Energy Research. 2014;**4**(2):421-427

[9] Weisser DA. Wind energy analysis for Grenda: An estimation using the Weibull density function. Renewable Energy. 2003;**28**:1803-1812

[10] Panda RK, Sarkar TK, Bhattacharya AK. Stochastic study of wind energy potential of India. Energy. 1990;**15**:921-930

[11] Lambert MJ, Ogle MH, Smith BW. Investigation of wind induced fatigue in tall guyed steel masts. Journal of Wind Engineering and Industrial Aerodynamics. 1988;**30**:55-65

[12] Jamil M, Parsa S, Majidi M. Wind power statistics and an evaluation of wind energy density. Renewable Energy. 1995;**6**:623-638

[13] Sen Z, Sahin AD. Regional assessment of wind power in Western Turkey by the cumulative semivarigram method. Renewable Energy. 1997;**12**:169-177

[14] Fung KT, Scheffler RL, Stolpe J. Wind energy-a utility perspective. IEEE Transactions on Power Apparatus and Systems. 1981;**100**:1176-1182

[15] Okedu KE. Wind turbine driven by permanent magnetic synchronous generator. Pacific Journal of Science and Technology. 2011;**12**(2):168-175

[16] Okedu KE, Muyeen SM, Takahashi R, Tamura J. Protection schemes for DFIG considering rotor current and DC-link voltage. In: Proceedings of the 24th IEEE-ICEMS (International Conference on Electrical Machines and System). Beijing, China; 2011. pp. 1-6

[17] Bozhko S, Asher G, Li R, Clare J, Yao L. Large offshore DFIG-based wind farm with line-commutated HVDC connection to the main grid: Engineering studies. IEEE Transactions on Energy Conversion. 2008;**23**(1):1119-1127

[18] Santos S, Le HT. Fundamental time-domain wind turbine models for wind power studies. Renewable Energy. 2007;**32**:2436-2452

[19] Haberberger M, Fuchs FW. Novel Protection Strategy for Current Interruptions in IGBT Current Source Inverters. Oslo, Norway: Proceedings EPE-PEMC; 2004

[20] Okedu KE, Muyeen SM, Takahashi R, Tamura J. Wind farms fault ride through using DFIG with new protection scheme. IEEE Transactions on Sustainable Energy. 2012;**3**(2): 242-254

[21] El-Sattar AA, Saad NH, Shams El-Dein MZ. Dynamic response of doubly fed induction generator variable speed wind turbine under fault. Electric Power Systems Research. 2008;**78**:1240-1246

[22] Takahashi T. IGBT Protection in AC or BLDC Motor Drives. El Segundo, CA: Technical Paper, International Rectifier; 2004

[23] Xie H. Voltage source converters with energy storage capability [Ph.D thesis]. Stockholm, Sweden: Royal Institute of Technology, School of Electrical Engineering, Division of Electrical Machines and Power Electronic; 2006

[24] Chowdhury BH, Chellapilia S. Doubly-fed induction generator control for variable speed wind power generation. Electric Power Systems Research. 2006;**76**:786-800

[25] Karim-Davijani H, Sheikjoleslami A, Livani H, Karimi-Davijani M. Fuzzy logic control of doubly fed induction generator wind turbine. World Applied Science Journal. 2009; **6**(4):499-508

[26] Okedu KE, Muyeen SM, Takahashi R, Tamura J. Wind farm stabilization by using DFIG with current controlled voltage source converters taking grid codes into consideration. IEEJ Transactions on Power and Energy. 2012;**132**(3):251-259

[27] Ledesma P, Usaola J, Rodriguez JL. Transient stability of a fixed speed wind farm. Renewable Energy. 2003;**28**:1341-1355

[28] Heir S. Grid Integration of Wind Energy Conversion Systems ISBN 10: 047197143. New York, USA: John Wiley & Sons Ltd; 1998

[29] E. ON NETZ GmbH. Grid Connection Regulations, Grid Codes High and Extra High Voltage; April 2006

[30] Annual Report by The Global Wind Energy Industry. The Global Wind Energy Council (GWEC); 2017. https://gwec.net

Chapter 2

Modeling and Control of Wind Turbine to Damp the Power Oscillation

Emad M. Elhaji

Additional information is available at the end of the chapter

http://dx.doi.org/10.5772/intechopen.74835

Abstract

Damping inter-area oscillation by using a permanent magnet synchronous generator (PMSG) wind turbine is considered. The PMSG wind turbine is connected to the IEEE-30 bus power system at different buses. H-infinity design controller is proposed to modulate the power where the input of the H-infinity control is the variation of the local grid generator speed and the output is feedback to activate the PMSG speed control, blade pitch angle control and dc voltage control. MATLAB/SIMULINK is used in this study. The IEEE-30 bus system is reduced to 7 buses based on the number of generators to simplify the stability study. The method is applied to a seven-area power system that exhibits undamped oscillations. Results presented in this study demonstrate the effectiveness of the wind generator in increasing system damping considerably.

Keywords: permanent magnet synchronous generator, IEEE 30 bus system, reduced system, wind generator, H-infinity, inter-area oscillation, dynamic stability, small signal stability

1. Introduction

The reason to use the renewable energy is to reduce the pollution emissions such as carbon dioxide CO_2 in the air. Renewable energy such as wind energy is one of the cost-effective forms of energy available today to generate electricity [1, 2]. The development of modern wind energy started almost 30 years ago but were not installed significantly for long period. Over the past decade, the power from wind turbines increased from 23,900 to 486,790 MW from 2001 to 2016, respectively [3, 4]. The blade size of modern wind turbines has increased to increase the amount of power from the wind [4, 5]. In general, two types of wind turbine can be installed to the power grid such as fixed-speed wind turbine and variable-speed wind turbine. The fixed speed wind turbines were installed in early 1990 to generate electricity regards of wind speed. This kind of wind turbines connected directly to the grid and its speed fixed at speed determined by the frequency of the grid [6–8]. After that in 1996, the variable speed wind turbine started connecting to the grid [9]. The classification of these turbines, fixed speed and variable speed wind turbines, is based on the principle of the generator and its operation [10]. The induction generator specifically squirrel cage induction generator is used with fixed speed wind turbine [11, 12]. In variable speed wind turbine two kind of generators can be used such as permanent magnet synchronous generator (PMSG) and doubly-fed induction generator (DFIG) [13–15]. Various of controls scheme can be applied in fixed and variable speed wind turbines such as stall control, blade pitch angle control, active stall control, dc voltage control, torque control and point of common coupling control (PCC) [16]. Nowadays, most of the wind turbines installed in power system are permanent magnet synchronous generator (PMSG) and doubly-fed induction generator (DFIG). PMSG connected directly to the power grid via back to back converter; therefore, the power from wind directly transferred to the grid. On the other hand, DFIG has two windings; stator winding connected directly to the power grid and rotor winding connected to the power grid via back to back converter [17, 18]. Therefore, the power from the wind transferees to the grid via stator and rotor. From the stator, the wind power directly transferees to the grid while from the rotor the power transferees to the grid or grid to the rotor depends on the operating conditions: over-synchronous condition if the power flows from rotor to grid and sub-synchronous condition if the power flows from grid to the rotor. DFIG required a slip rings to operate properly, but it has a high maintenance cost in long run for normal operation [13, 18].

The PMSG will be focused in this study. It is called also a brushless DC machine and just the rotor of the DC machine is replaced by a permanent magnet. Therefore, the PMSG will be a small in size compared to the DC machine, and the inertia of a PMSG will be higher. The result, PMSG has a good reliability and more higher power compared to the size [12, 14, 19]. In wind turbines application, the small generator in size with a higher power is preferred because the generator of wind turbine is placed hundreds of above the ground and then reduce the maintenance cost. The PMSG also has a back-to-back converter to control the flowing power from the wind, but it increases the cost of the PMSG in addition to the expensive permanent magnets [12, 14]. The maintenance of the PMSG is nearly free; therefore, it is highly desirable for wind turbine applications. Now, PMSG wind turbine is focused in area of research [12, 14].

When the wind turbines penetration to the power grid, the system stability become more significant. The PMSG is investigated for its capability to enhance the damping of dynamic oscillations in a multi-area system. The basic control applied to the PMSG is a field orientation control (FOC) [20, 21]. FOC is widely used in a research area especially in wind turbines. The FOC implemented in generator and grid sides of PMSG wind turbine to control the wind power that transferred to the grid [20, 21]. The synchronous frame of reference, a d-q frame of reference, is applied to the modeling of the generator side and grid side and a decoupled strategy is used to simplify the control design of the FOC. The proportional integral controls are used in the FOC in both sides of wind turbine as a result of a good steady state error. In generator side, the FOC is designed to control the torque of PMSG wind turbine by controlling the q-axis current of PM generator while in grid side, it is designed to control the dc voltage to guarantee the power transfers from the wind to the grid. The FOC cannot damp any oscillation if there is any disturbance happen on the system such as wind speed change, power load change or symmetrical and unsymmetrical fault. These disturbances will cause a low-frequency oscillation due to many synchronous generators and wind turbines located in many areas with long tie-line as in **Figure 1** [22]. This oscillation with a range of frequency between 0.1 and 0.8 HZ is known as an inter-area oscillation [23, 24]. The system will be unstable if this oscillation increase in amplitude. Therefore, to make the system more stable, an auxiliary feedback control has to be added to damp the oscillation.

In [25–27], numerous of controls are applied to the PMSG wind turbine concern with the stability under the presence of grid dynamics. In [28, 29], implemented some devices to improve the system stability such as power system stabilizer (PSS) and flexible alternative current transmission system (FACTS), but these devices may not be sufficient to damp inter-are oscillations at high penetrations levels. In some literature use the frequency feedback in DFIG to damp the oscillation [30, 31]. In this study, the dynamic of the PMSG wind turbine is discussed through a suitable small-signal model. The PMSG connected to the IEEE 30 bus system at different buses such as generator and load buses. The PMSG wind turbine model is linearized and reduced in order to simplify the analysis of the system. This model is applied to case of damping the inter-area oscillation. To damp the inter-area oscillation, three modulation feedback loops were applied: dc-ink voltage, PMSG speed and blade pitch angle modulation. The feedback design method used in the study is based on the H-infinity control concept [32–35].

Section 2 describes a suitable dynamic model of the PM wind generator that can be used in dynamic studies. Section 3 demonstrates the small signal stability. Section 4 describes the H-infinity control method. Section 5 describes the simulation results and Section 5 provides the conclusion.

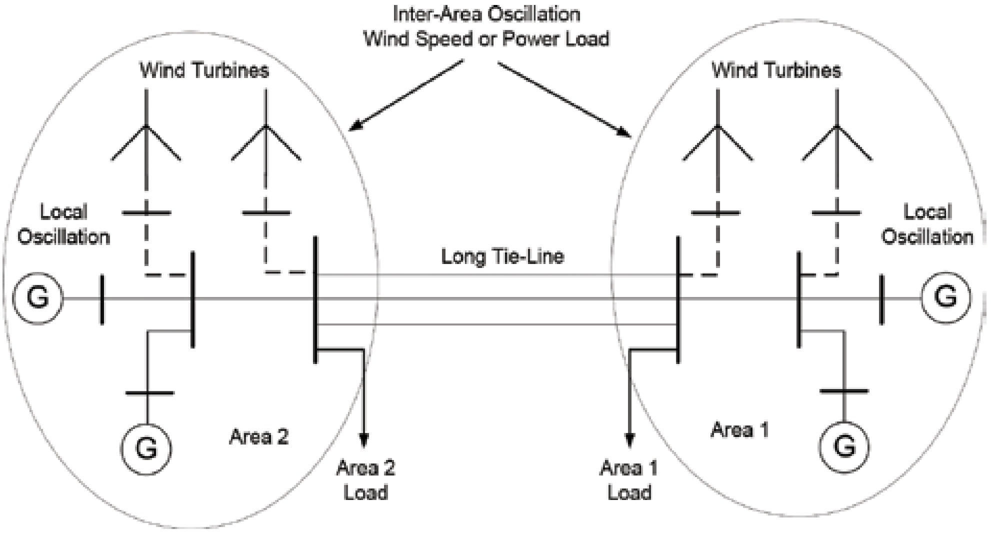

Figure 1. Two area power system connected with many of synchronous generators and wind turbines.

2. System modeling

The rotational of the wind turbine rotor blade converts the kinetic energy of the wind to the mechanical power. The mechanical power converts by the generator to the electrical power that is fed to the grid through a back-to-back converter. The wind turbine scheme as shown in **Figure 2** combines the mechanical subsystem and electrical subsystem. The mechanical subsystem includes the two mass system and rotor shaft, and the electrical subsystem includes a PMSG, back-to-back converter, and grid. The interconnection system modeling of the generator and grid sides are described in an appropriate frame for developing a suitable control scheme which will be discussed in detail in the following section [35–41]. The modeling of the both sides of wind turbine as well as back to back converter will be in details in the following section.

2.1. Wind turbine model

The extracted power from the wind turbine can be expressed as in (Eq. (1)) [13, 14, 19]; where σ is the air density, R is the blade radius, v_w is the wind speed, $C_p(\lambda,\beta)$ is the turbine power coefficient and it is a nonlinear function as in (Eq. (2)). The value coefficients in (Eq. (2)) c_1 to c_6 c6 are: $c_1 = 0.5167$, $c_2 = 116$, $c_3 = 0.4$, $c_4 = 5$, $c_5 = 21$, and $c_6 = 0.0068$ [17]. Also, the torque of wind turbine can be presented in terms of the wind power and rotational speed of the shaft as in (Eq. (3)) [27, 37, 42–44].

$$P_w = \frac{1}{2}\,\sigma\,\pi R^2\,C_p(\lambda,\beta)v_w^3 \tag{1}$$

$$C_p(\lambda,\beta) = c_1\left(c_2\left(\frac{1}{\lambda - 0.008\,\beta} - \frac{0.035}{\beta^3+1}\right) - c_3\,\beta - c_4\right)e^{-c_5\left(\frac{1}{\lambda-0.008\,\beta} - \frac{0.035}{\beta^3+1}\right)} + c_6\,\lambda, \qquad \lambda = \frac{R\,\omega_T}{v_w} \tag{2}$$

$$T_w = \frac{P_w}{\omega_T} = \frac{1}{2}\,\frac{\sigma\pi R^3}{\lambda}\,C_p(\lambda,\beta)v_w^2 \tag{3}$$

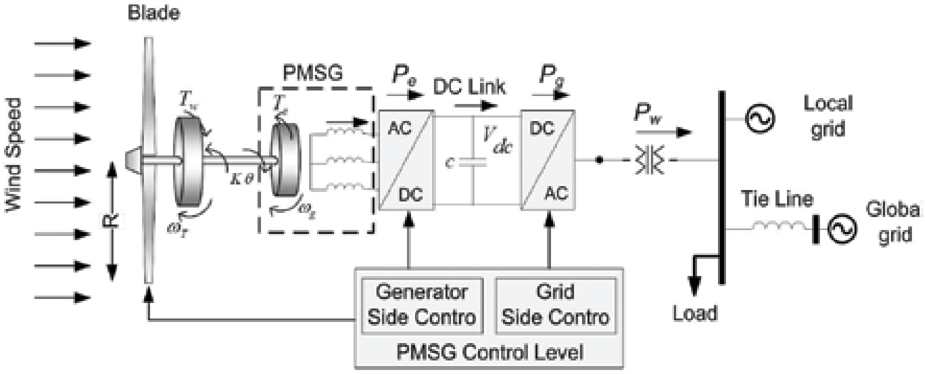

Figure 2. Configuration of the permanent magnet synchronous generator wind turbine.

Figure 3 shows the turbine power coefficient at different tip ratio and blade pitch angle. As seen from the same figure, the maximum value of power coefficient is 0.48 when the tip ratio is 8.1 and blade pitch angle is zero. The blade pitch angle control is zero that mean the wind speed is equal or less than the rated speed. The rated wind speed which extracted the maximum power is 12 m/s. The blade pitch angle control activates when the wind speed is more the rated value to decrease the turbine power coefficient so as to $\mathrm{C_p}(\lambda, \beta)$ achieve the maximum power extracted from the wind.

2.2. Permanent magnet synchronous generator (PMSG) model

The dynamic model of the PMSG is derived based on the two-phase d-q synchronous frame of reference and **Figure 4** shows its equivalent circuit [27, 43, 44]. The electrical model of the PMSG in the synchronous frame of reference is by

$$\begin{aligned} v_{sd} &= -R_s i_{sd} - L_{sd}\frac{d\, i_{sd}}{dt} - \omega_e L_{sq} i_{sq} \\ v_{sq} &= -R_s i_{sq} - L_{sq}\frac{d\, i_{sq}}{dt} + \omega_e L_{sd} i_{sd} + \omega_e \psi_f \end{aligned} \tag{4}$$

where R_s is the armature resistance, $\mathrm{L_{ls}}L_{sd}$, L_{sq} are the inductance in d-q axes and they are equal in the round rotor, ψ_f is the permanent magnetic flux, $\omega_e = p\ \omega_g$ is the electrical rotating speed, ω_g is related to the mechanical rotating speed of the generator, and p is the number of pole pairs.

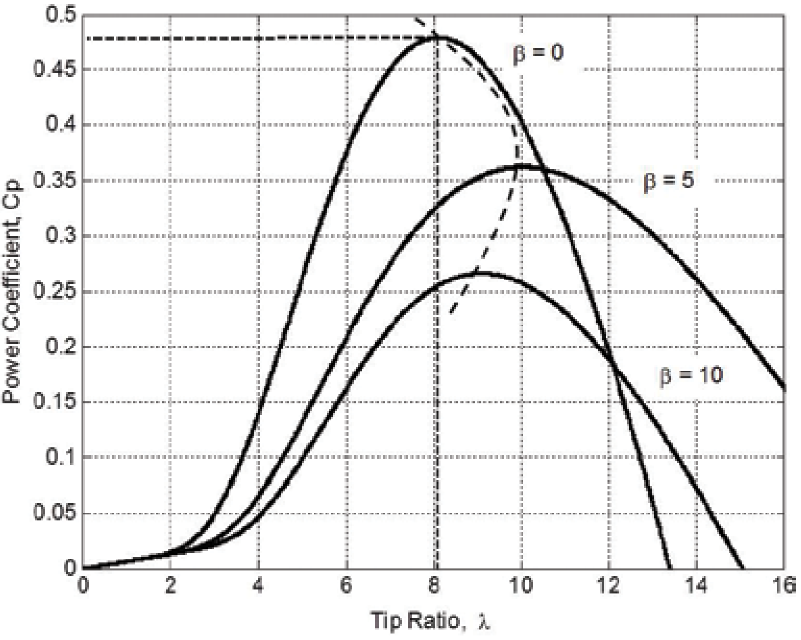

Figure 3. Power coefficient and tip ratio.

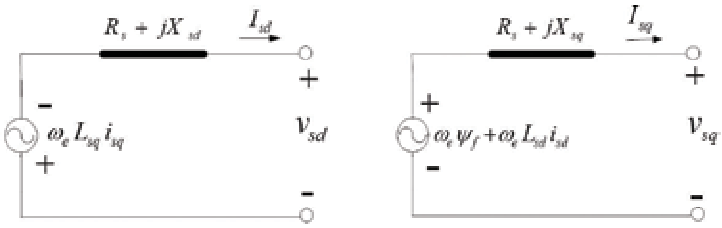

Figure 4. Equivalent circuit of PMSG.

The expressions of the electromagnetic torque T_e and active power of the PMSG P_e are given by [27, 44].

$$\begin{aligned} T_e &= \frac{3}{2}\, p\ \psi_f i_{sq} \\ P_e &= \frac{3}{2}\left(v_{sd} i_{sd} + v_{sq} i_{sq}\right) \end{aligned} \tag{5}$$

2.3. Rotor shaft model

The rotor shaft of PMSG wind turbine is presented as a two-mass system and the motion equations are given in (Eq. (6)) where K is the stiffness of the shaft, θ is the shaft angle, J_g is the inertia of PMSG and J_T is the inertia of the wind turbine [44].

$$\begin{bmatrix} \dot{\omega}_T \\ \dot{\omega}_g \\ \dot{\theta} \end{bmatrix} = \begin{bmatrix} 0 & 0 & -\dfrac{K}{J_T} \\ 0 & 0 & \dfrac{K}{J_g} \\ 1 & -1 & 0 \end{bmatrix} \begin{bmatrix} \omega_T \\ \omega_g \\ \theta \end{bmatrix} + \begin{bmatrix} \dfrac{1}{J_T} \\ -\dfrac{1}{J_g} \\ 0 \end{bmatrix} \begin{bmatrix} T_w \\ T_e \end{bmatrix} \tag{6}$$

2.4. Grid model

The modeling of the grid side as shown in **Figure 5a** has two parts. The first part of modeling includes elements between the grid side convertor and the point of common coupling bus, which is known as a PCC bus. The first part dynamic model is based on the d-q frame of reference as shown in (Eq. (7)) [43, 44]; Where ω_s is the angular frequency of the grid, L_g and R_g are the inductance and resistance of the connecting transformer and power lines between the inverter and the PCC bus, respectively, v_{dpcc}, v_{qpcc}, $\mathrm{u_{di}}v_{di}$, and v_{qi} $\mathrm{u_{qi}}$ represent the d- and q-axis components of the PCC voltage and grid side convertor, respectively, and i_{gd}, i_{gq} represent the d-q-axis components of the current flowing between the grid side convertor and the AC system. The expression of the active power is represented in (Eq. (8)) [43, 44].

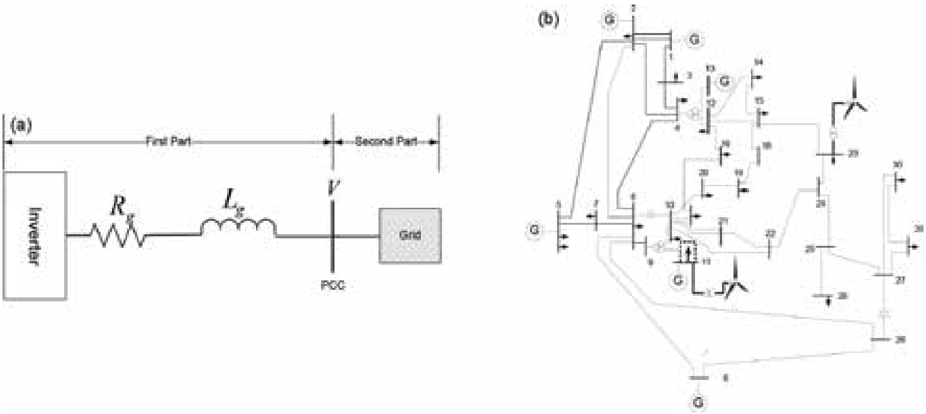

Figure 5. Grid side; (a) two parts of grid sides, (b) 30-bus system.

$$\begin{aligned} v_{di} &= R_g i_{gd} + L_g \frac{d\, i_{gd}}{dt} - \omega_s L_g i_{gq} + v_{dpcc} \\ v_{qi} &= R_g i_{gq} + L_g \frac{d\, i_{gq}}{dt} + \omega_s L_g i_{gd} + v_{qpcc} \end{aligned} \tag{7}$$

$$P_g = \frac{3}{2}\left(v_{di}\ i_{gd} + v_{qi}\, i_{gq}\right) \tag{8}$$

The second part of the modeling is the grid model as shown in **Figure 5b** which is presented the IEEE 30 bus system using here as a sample of a 7-area system, where Area 5 and 7 are equipped with the PMSG wind turbine [45]. To simplify study the system stability, the power system loads have to be converted to the impedance as in (Eq. (9)), Therefore, the generators and loads impedances of the power system have to be include in the Y-bus. Also, the number of the buses in the original IEEE 30-bus have to be reduced to the number of generators [46]. The IEEE-30 bus system has 6 generators and two PMSG wind turbines. One of the PMSG wind turbines connected to the load bus and the another wind turbine connected to the PV bus. Therefore, The IEEE 30-bus reduced to the 7 bus or 7 areas system. In the area 5, the load was added to provide the disturbance of the system.

$$Y_L = \frac{P_L - J\, Q_L}{V_L^2} \tag{9}$$

The rotor variational dynamics of the synchronous generators, generator 1,2 to 7, in the reduced system are described in (Eq. (10)) [22], where D_j is the machine damping coefficient, $K_{sij} = V_i\, V_j\, Y_{ij}\, \sin\left(\theta_{ij} - \delta_i + \delta_j\right)$ are the synchronizing coefficient, P_w is the wind power, P_{mi} is the power that is from grid generators, ω_i is the speed of mass of the generators, and δ_i is the angular position of the mass. Area 7 connected to the load bus where $\omega_7 = K\, V_{dc}$ and K is a constant value. The unit of t is in s, ω in per-unit and $\omega_o = 314\frac{r}{s}$.

$$
\begin{aligned}
\dot{\omega}_1 &= \frac{\omega_0}{2\,H_1}\left(-D_1\,\omega_1 - \sum_{j=1}^{7} K_{s1}\,\delta_j + P_{m1} - P_{L1}\right), & \dot{\delta}_1 &= \omega_0\,\omega_1 \\
\dot{\omega}_2 &= \frac{\omega_0}{2\,H_2}\left(-D_2\,\omega_2 - \sum_{j=1}^{7} K_{s2}\,\delta_j + P_{m2} - P_{L2}\right), & \dot{\delta}_2 &= \omega_0\,\omega_2 \\
\dot{\omega}_3 &= \frac{\omega_0}{2\,H_3}\left(-D_3\,\omega_3 - \sum_{j=1}^{7} K_{s3}\,\delta_j + P_{m3} - P_{L3}\right), & \dot{\delta}_3 &= \omega_0\,\omega_3 \\
\dot{\omega}_4 &= \frac{\omega_0}{2\,H_4}\left(-D_4\,\omega_4 - \sum_{j=1}^{7} K_{s4}\,\delta_j + P_{m4} - P_{L4}\right), & \dot{\delta}_4 &= \omega_0\,\omega_4 \\
\dot{\omega}_5 &= \frac{\omega_0}{2\,H_5}\left(-D_5\,\omega_5 - \sum_{j=1}^{7} K_{s5}\,\delta_j + P_{m5} - P_{L5} + P_w\right), & \dot{\delta}_5 &= \omega_0\,\omega_5 \\
\dot{\omega}_6 &= \frac{\omega_0}{2\,H_6}\left(-D_6\,\omega_6 - \sum_{j=1}^{7} K_{s6}\,\delta_j + P_{m6} - P_{L6}\right), & \dot{\delta}_6 &= \omega_0\,\omega_6 \\
\dot{\omega}_7 &= \frac{\omega_0}{2\,H_7}\left(-D_7\,\omega_7 - \sum_{j=1}^{7} K_{s7}\,\delta_j - P_{L7} + P_w\right), & \dot{\delta}_7 &= \omega_0\,\omega_7
\end{aligned}
\tag{10}
$$

2.5. DC-link model

The dc-link capacitor as shown in the **Figure 2** is connected between the generator and grid converter sides. The energy stored in the capacitor C is given by $E_{dc} = \frac{1}{2} C\, V_{dc}^2$, where V_{dc} is a dc-link voltage, and it depends on the difference between the generator power P_e and grid power P_g if the losses of both converters are considered very small as [8, 44].

$$
C\,V_{dc}\,\frac{dV_{dc}}{dt} = P_e - P_g \tag{11}
$$

To sending power from the wind turbine to the grid, the variation of the dc voltage has to be small or equal to zero which means the sending power P_e and receiving power P_g are equal.

3. Small signal stability

In this study, the small signal stability of the PMSG wind turbine connected to the power grid is going to be discuss at a particular operating point. The small signal stability is ability of the system to maintain stable during any small disturbance occurrence. In the power system, disturbances with small magnitude are very common and can occur due to change in the generation power, power load. To study the small signal stability, the nonlinear system modeling such as wind turbine and dc-link modes has to be linearized to derive the state space matrix for the entire system by using the component connection techniques [22].

3.1. Linearization of the wind torque model

As in (Eq. (3)), the torque of the wind turbine is a function of the $C_p(\lambda,\beta)$; therefore, it has to be linearized respect to the wind speed, rotational speed, and blade pitch angle at operating point as [44].

$$\Delta T_w = K_w\,\Delta \mathrm{V_w} + K_T\,\Delta\omega_\mathrm{T} + K_\beta\,\Delta\beta \tag{12}$$

where

$$K_w = \frac{\partial T_w}{\partial V_w} = \frac{\sigma\,\pi R^2 V_{wo}^2}{2\,\omega_{\mathrm{To}}}\left[3\,C_p(\lambda_o,\beta_o) - \lambda_o\,\frac{\partial C_p(\lambda,\beta_o)}{\partial\lambda}\right]_{op}$$

$$K_T = \frac{\partial T_w}{\partial\omega_\mathrm{T}} = \frac{\sigma\,\pi R^2 V_{wo}^3}{2\,\omega_{\mathrm{To}}^2}\left[-C_p(\lambda_o,\beta_o) + \lambda_o\,\frac{\partial C_p(\lambda,\beta_o)}{\partial\lambda}\right]_{op}$$

$$K_\beta = \frac{\partial T_w}{\partial\beta} = \frac{\sigma\,\pi R^2 V_{wo}^3}{2\,\omega_{\mathrm{To}}}\,\frac{\partial C_p(\lambda_o,\beta)}{\partial\beta}$$

3.2. Linearization of a DC-link model

After substituting the sending and receiving power in to (Eq. (11)), the linearization of the d-link can be presented as

$$\begin{aligned}\Delta\dot{V}_{dc} &= \frac{3V_{sd}}{2CV_{dc}}\,\Delta i_{sd} + \frac{3I_{sd}}{2CV_{dc}}\,\Delta v_{sd} + \frac{3I_{sd}V_{sd}}{2CV_{dc}^2}\,\Delta v_{dc} + \frac{3V_{sq}}{2CV_{dc}}\,\Delta i_{sq} + \frac{3I_{sq}}{2CV_{dc}}\,\Delta v_{sq} + \frac{3I_{sq}V_{sq}}{2CV_{dc}^2}\,\Delta v_{dc} - \\ &= \frac{3V_{di}}{2CV_{dc}}\,\Delta i_{gd} - \frac{3I_{gd}}{2CV_{dc}}\,\Delta v_{di} + \frac{3I_{gd}V_{di}}{2CV_{dc}^2}\,\Delta v_{dc} - \frac{3V_{qi}}{2CV_{dc}}\,\Delta i_{gq} + \frac{3I_{gq}}{2CV_{dc}}\,\Delta v_{qi} + \frac{3I_{gq}V_{qi}}{2CV_{dc}^2}\,\Delta v_{dc}\end{aligned} \tag{13}$$

where Δv_{dc} is a variation of a DC voltage.

After describing the system modeling and its linearization, the interconnection method between the system modeling with its control has to be apply to create the state space equation for the entire system to study the system stability. **Figure 6(a–e)** shows the generator and grid sides with their controls. The way how to connect all the system models and controls together will be presented by getting the state variable of the entire system modeling with their controls as follows [47].

$$\begin{aligned}\dot{X} &= A\,X + B\,U \\ Y &= C\,X + D\,U\end{aligned} \tag{14}$$

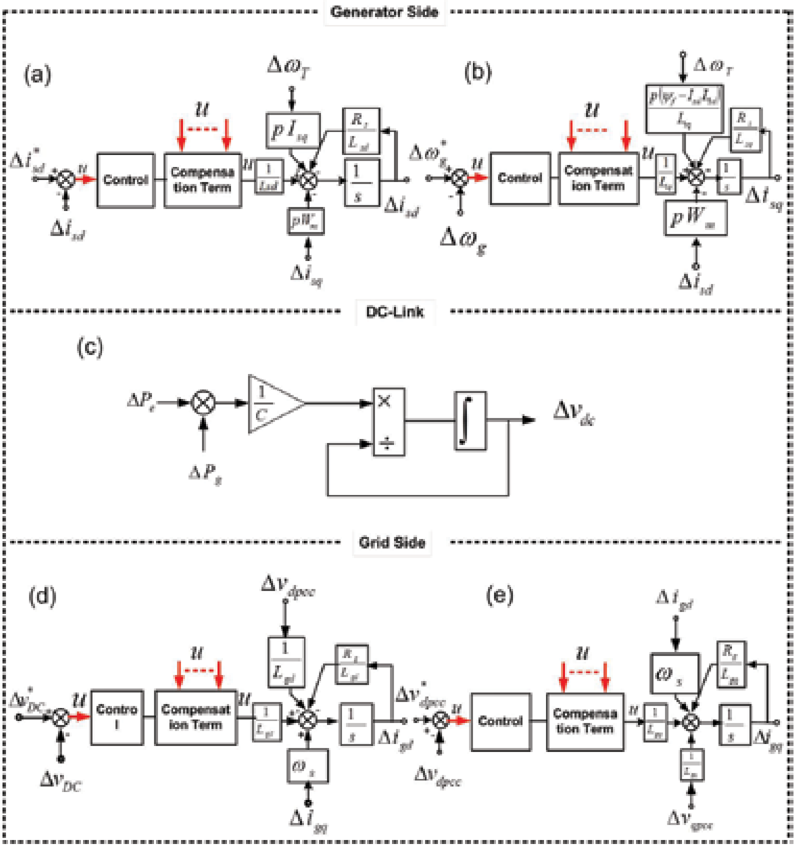

Figure 6. Connection of the PMSG models with its controls.

The system modeling of the PMSG with its controls as in **Figure 6** has to be connected together to get the state space equation. The interconnection matrix which connect the PMSG wind turbine models together with their controls is as [47].

$$U = E\,Y + F\,U^{*} \tag{15}$$

Matrix E is the states input and control inputs, u, as described in **Figure 6** while matrix F represents the reference input of the controllers. By substituting the output of (Eq. (14)) to (Eq. (15)), the input of the system will be as

$$U = (1 - ED)^{-1}\,E\,C\,X + (1 - ED)^{-1}\;F\,U^{*} \tag{16}$$

By substituting the input U in (Eq. (16)) into the (Eq. (14)), the (Eq. (14)) can be represented as [47].

$$\begin{aligned} \dot{X} &= \widehat{A}\;X + \widehat{B}\;U^{*} \\ Y &= \widehat{C}\;X + \widehat{D}\;U^{*} \end{aligned} \tag{17}$$

where X is a state variables of the whole system and its controls, U is an input control, Y is an output of the system, $\widehat{A} = A + B\,(1 - ED)^{-1}\,EC$ is a state matrix for the whole system and its control, $\widehat{B} = B\,(1 - ED)^{-1}\,F$ is the input system matrix after connecting with its control, $\widehat{C} = C + D\,(1 - ED)^{-1}\,EC$ is the output matrix of whole system, and $\widehat{D} = D\,(1 - ED)^{-1}\,F$ is the direct transition matrix of the entire system. By getting the state matrixes of the entire system the eigenvalue sensitivity method can be study. The original system of PMSG wind turbine with its control in **Figure 2** is of 15th order which is presented as $[\Delta i_{sd}, \Delta i_{sq}, \Delta\omega_T, \Delta\omega_g, \Delta\theta, \Delta v_{dc}, \Delta i_{gd}, \Delta i_{gq}, \Delta x_1, \Delta x_2, \Delta x_3, \Delta x_4, \Delta x_5, \Delta x_6, \Delta\theta_{pll}]$ corresponding to the d-current of PMSG, q-current of PMSG, mechanical speed of the wind turbine PM generator speed, rotor shaft angle, dc voltage, d-current of grid, q-current of grid, PMSG speed control, PMSG speed control, dc-voltage control, q-current of grid control, PCC voltage control, PLL control and PLL angle, respectively; where; this original system can be reduced by ignoring the fast dynamic mode into 5th order as in **Figure 7**. As a result, the slow dynamic modes of the system are the Δi_{sq}, $\Delta\omega_T$, $\Delta\omega_g$, $\Delta\theta$ and Δx. With reference to **Figure 2**, the PI speed controller determines the q-axis stator voltage. The state equation of this controller is given by (Eq. (18)) and its output by (Eq. (19)). According to the same figure, the v_{sd} determined such that i_{sd} is zero for unity power

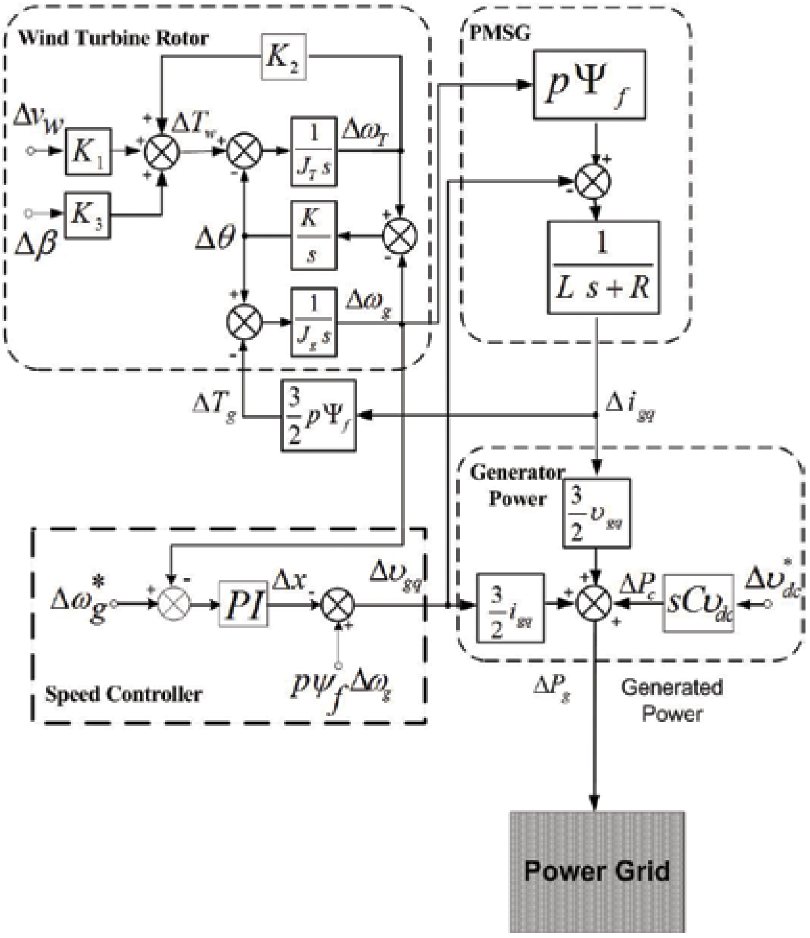

Figure 7. Reduced system.

factor operation. Because of the response of this loop is considerably faster than the inter-area dynamics of interest, the d-axis of (Eq.(4)) can be eliminated from the motor state equation by assuming that $\Delta \mathrm{i}_{\mathrm{sd}} = \Delta \mathrm{i}^{\cdot \mathrm{sd}} = 0$. Therefore, using (Eq. (19)) into q-axis of (Eq. (4)) and the previous condition, one obtains (Eq. (20)) that describes the simplified q-axis dynamics [44].

$$\Delta \dot{x} = \Delta \omega_{\mathrm{g}}^{*} - \Delta \omega_{g} \tag{18}$$

$$\Delta v_{gq} = K_p \left(\Delta \omega_{\mathrm{g}}^{*} - \Delta \omega_{g} \right) + \mathrm{K_i}\, \mathit{\Delta} x + \mathrm{p}\, \psi_{\mathrm{f}}\, \Delta \omega_{g} \tag{19}$$

$$\Delta i_{gq} = -\frac{\mathrm{R}}{\mathrm{L_{sq}}}\, \Delta v_{gq} + \frac{K_p}{\mathrm{L_{sq}}}\, \Delta \omega_{g} - \frac{K_i}{\mathrm{L_{sq}}}\, \mathit{\Delta} x - \frac{K_p}{\mathrm{L_{sq}}}\, \Delta \omega_{\mathrm{g}}^{*} \tag{20}$$

The reduced system equation is described in (Eq. (6)), (Eq. (18)), and (Eq. (20)), which can be written as [44].

$$\begin{bmatrix} \Delta \dot{\omega}_T \\ \Delta \dot{\omega}_g \\ \Delta \dot{\theta} \\ \Delta \dot{x} \\ \Delta \dot{i}_{\mathrm{sq}} \end{bmatrix} = \begin{bmatrix} \frac{K_T}{J_T} & 0 & -\frac{K}{J_T} & 0 & 0 \\ 0 & 0 & \frac{K}{J_g} & 0 & -\frac{\frac{3}{2} p\, \psi_f}{J_g} \\ 1 & -1 & 0 & 0 & 0 \\ 0 & -1 & 0 & 0 & 0 \\ 0 & \frac{K_p}{L_{sq}} & 0 & -\frac{K_i}{L_{sq}} & -\frac{R_s}{L_{sq}} \end{bmatrix} \begin{bmatrix} \Delta \omega_{\mathrm{T}} \\ \Delta \omega_{\mathrm{g}} \\ \mathit{\Delta} \theta \\ \mathit{\Delta} x \\ \Delta \mathrm{i}_{\mathrm{sq}} \end{bmatrix} + \begin{bmatrix} \frac{K_w}{J_T} & \frac{K_\beta}{J_T} & 0 \\ 0 & 0 & 0 \\ 0 & 0 & 0 \\ 0 & 0 & 1 \\ 0 & 0 & -\frac{K_p}{L_{sq}} \end{bmatrix} \begin{bmatrix} \Delta \mathrm{v_w} \\ \mathit{\Delta} \beta \\ \Delta \omega_{\mathrm{g}} \end{bmatrix} \tag{21}$$

4. H_∞ control method with wind generation

Figure 8 shows the H-infinity feedback control from grid to the PMSG speed, dc-voltage, and blade pitch angle controls. The wind generators in Area 5 and Area 7 act as a power source in the dynamic equation to increase the system damping by using the local frequency of machine 5 and wind turbine in Area 7, in order to achieve power modulation proportional to the frequency deviation of the area, e.g. $\Delta P_w = D\, \Delta \omega_5$ and $\Delta P_w = D\, \Delta \omega_7$. From **Figure 8**, the input power to the grid ΔP_w can be presented as

$$\Delta P_w = \frac{3}{2}\, \rho\, \psi_f \left(i_{sq}\, \Delta \omega_g + \omega_g\, \Delta i_{sq} \right) - C\, V_{dc}'\, \Delta \dot{V}_{dc} \tag{22}$$

The feedback signal is the locally derived system frequency deviation, $\Delta \omega_5$ and $\Delta \omega_7$, and the control outputs are the variations of the blade pitch angle, $\mathit{\Delta} \beta$, the rotor speed reference, $\Delta \omega_{\mathrm{g}}^{*}$, and the rate of change of the dc link voltage reference, $\Delta \dot{\mathrm{V}}_{\mathrm{dc}}$. To design the H-infinity control, the plant consisting of the wind generation and the power system is considered controllable and observable. The state representation of the plant including the disturbance is given by (Eq. (23)) [48].

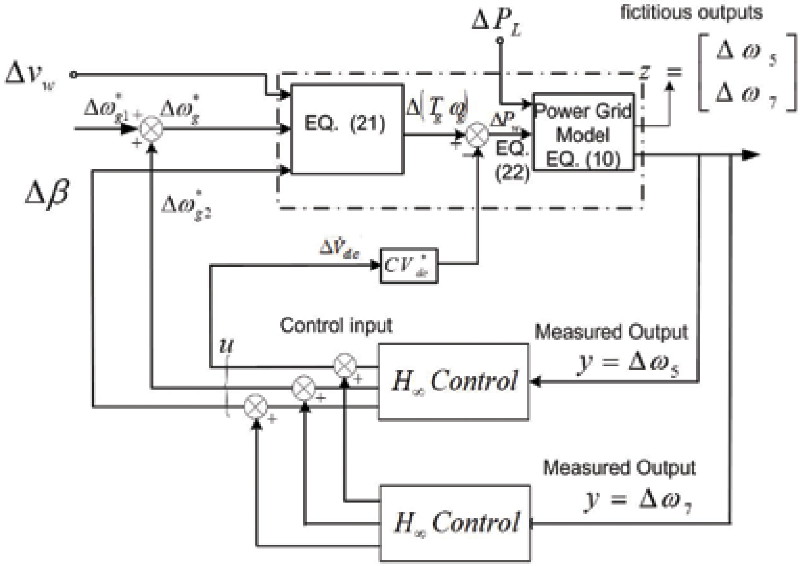

Figure 8. Power modulation control of the PMSG wind generator based on the H∞ controller.

$$\begin{bmatrix} x \\ z \\ y \end{bmatrix} = \begin{bmatrix} A & B_d & B_u \\ C_1 & D_{11} & D_{12} \\ C & D_{21} & D_{22} \end{bmatrix} \begin{bmatrix} x \\ d \\ u \end{bmatrix} \tag{23}$$

where is the state vector, $z = [\Delta\omega_5, \Delta\omega_7\,]^T$ is the fictitious output, $y = [\Delta\omega_5, \Delta\omega_7]$ is the measurement vector, $u = \left[\Delta\beta, \Delta\omega_2^*, \Delta\dot{V}_{dc}\right]$ is the control input vector, and $d = [\Delta v_w, \Delta P_L]$ is the disturbance vector of the plant. A, B_d, B_u, C_1, D_{11}, D_{12}, C, D_{21} and D_{22} are constant matrices of appropriate size depending on the power system order. For simplicity it is assumed that there is no direct feedback through term, i.e. $D_{22} = 0$. The state representation of the H∞ controller is given by (Eq. (24)) [48].

$$\begin{bmatrix} \dot{x} \\ u \end{bmatrix} = K \begin{bmatrix} x \\ y \end{bmatrix} \tag{24}$$

where $K = \begin{bmatrix} \widehat{A} & \widehat{B} \\ \widehat{C} & \widehat{D} \end{bmatrix}$ is the controller matrix and $\widehat{x}$ is the controller state. The state representation of the closed-loop system is obtained by combining (23, 24); therefore:

$$\begin{bmatrix} \dot{x} \\ \dot{\widehat{x}} \\ - \\ z \end{bmatrix} = \begin{bmatrix} A + B_uKC & 0 & - & B_d + B_uKD_{21} \\ 0 & K & - & 0 \\ - & - & - & - \\ C_1 + D_{12}KC & 0 & - & D_{11} + D_{12}KD_{21} \end{bmatrix} \begin{bmatrix} x \\ \widehat{x} \\ - \\ d \end{bmatrix} = \begin{bmatrix} A_K & B_K \\ C_K & D_K \end{bmatrix} \begin{bmatrix} x_K \\ d \end{bmatrix} \tag{25}$$

The closed-loop transfer function, $\mathcal{F}(\mathrm{s})$, from d to z will be denoted as

$$f(s) = [D_{11} + D_{12}KD_{21}] + [\,C_1 + D_{12}KC \quad 0\,]\left(s\begin{bmatrix}1 & 0\\0 & 1\end{bmatrix} - \begin{bmatrix}A + B_uKC & 0\\0 & K\end{bmatrix}\right)^{-1}\begin{bmatrix}B_d + B_uKD_{21}\\0\end{bmatrix} \tag{26}$$

Matrices $\widehat{A},\ \widehat{B},\ \widehat{C},\ \widehat{D}$ are selected that the $f(s)$ is stable and the infinite norm, $\|f(s)\| < \gamma$ where, γ is a specified positive number.

5. Simulation studies

The IEEE 30-bus system as in **Figure 5(b)** was studied. The data for the lines, generators and loads are shown in [45]. Generator at bus 1 is the slack bus, in the simulations, and it is equipped with a governor for regulating frequency. The data of the wind generator on area 5 and area 7 are given in **Table 1**. Initially 50 wind generators were installed in each area, area 5 and area 7.

At the steady state generators 1–7 generate respectively 38, 43, 59, 5, 38, 13, and 77 MW. The initial wind velocity at the wind generator site is 11 m/s, and the wind generator generates an additional 77 MW of power. The power system dynamics are of the 14th order according to (Eq. (10)). The combined system including the dynamics of the wind generator from (Eq. (21)) is of the 19th order. The system and controller above was simulated in the time domain in MATLAB/SIMULINK. Two case studies were considered and the results are presented below.

Parameters	**Value**
Pole pairs	40
Rated power per generator	2 MVA
Generator rated voltage	575 V
Frequency	50 Hz
Stator resistance	0.0025 pu
Inductance in d-axis	0.43 pu
Inductance in q-axis	0.43 pu
Permanent magnet flux	1pu
PMSG inertia	2.5×10^5 kgm^2
Wind turbine inertia	3.7×10^6 kg m^2
DC link voltage	1500 V
DC-link capacitor per generator	60,000 μF

Table 1. Wind generator parameters [27].

Case 1: Load change.

The load on Bus 5 changes from 50 to 60 MW at t = 1 s and the was operated at steady state. **Figure 9** shows the responses of the system with and without the feedback control from the wind generator. The result shows a power unbalance in the area 5 initiating and the net power exported by each area causes a large oscillations. As the system is adjusting to the new steady state, the exported power from the slack Bus 1 is increasing and that of Area 5 is decreasing by the same amount equal to the load change of 10 MW. From the figure the changing of the load power is absorbed by the infinite bus. Another Areas start oscillation when the load change and goes to the same operating point.

Figure 10(a) shows the response of the wind power resulting from the disturbance. The wind generator response is immediate providing approximately a peak variation of 5 MW power. The modulation power is created by the deviation of the dc link voltage, blade pitch angle, and generator speed shown in **Figure 10 (b–d)** respectively. The deviation of the dc link voltage of only 100 V or 6.6% is sufficient, and variation of the blade pitch angle is less than 0.1 degree and PMSG speed is very small.

Case 2: Wind speed change.

The system operates at the same steady state described above. At t = 1 s, the wind generator power increases from 77 to 100 MW when the wind velocity changes from 11 to 12 m/s.

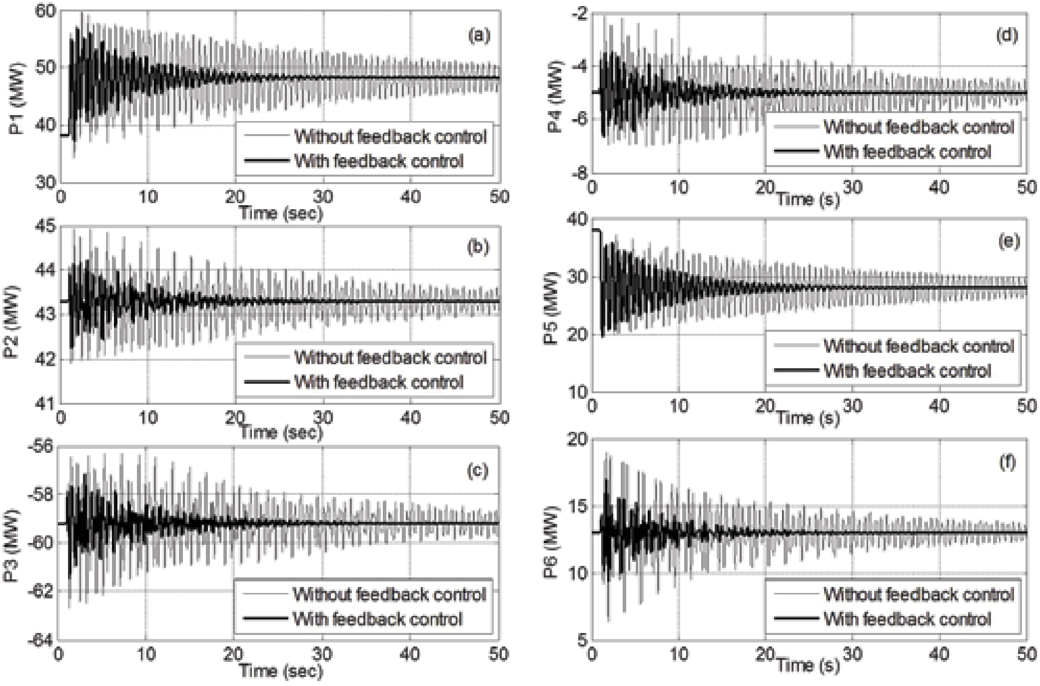

Figure 9. Case 1, load change: (a) net power of area 1; (b) net power of area 2; (c) net power of area 3, (d) net power of area 4; (e) net power of area 5; (f) net power of area 6.

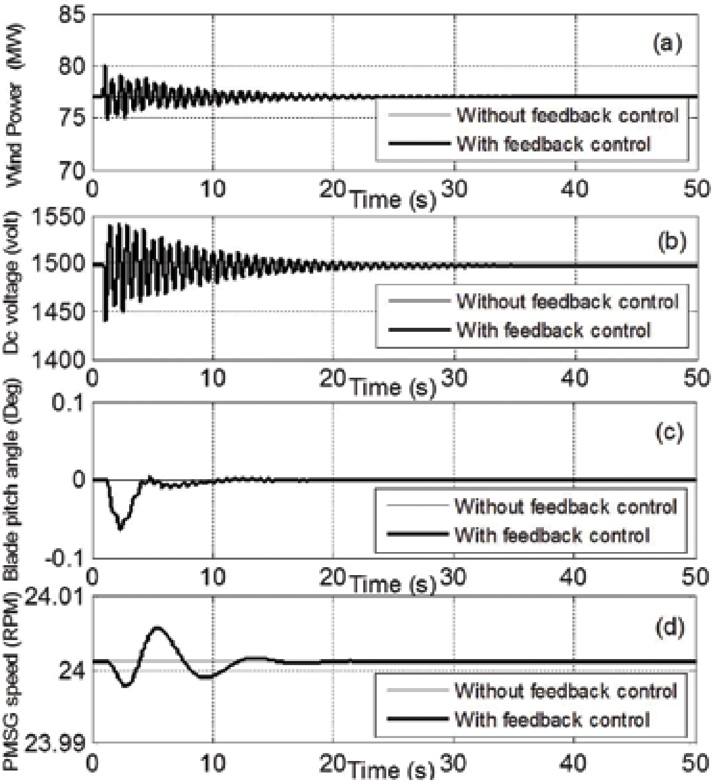

Figure 10. Load change: (a) wind power; (b) DC voltage response; (c) pitch angle response; (d) PMSG speed response.

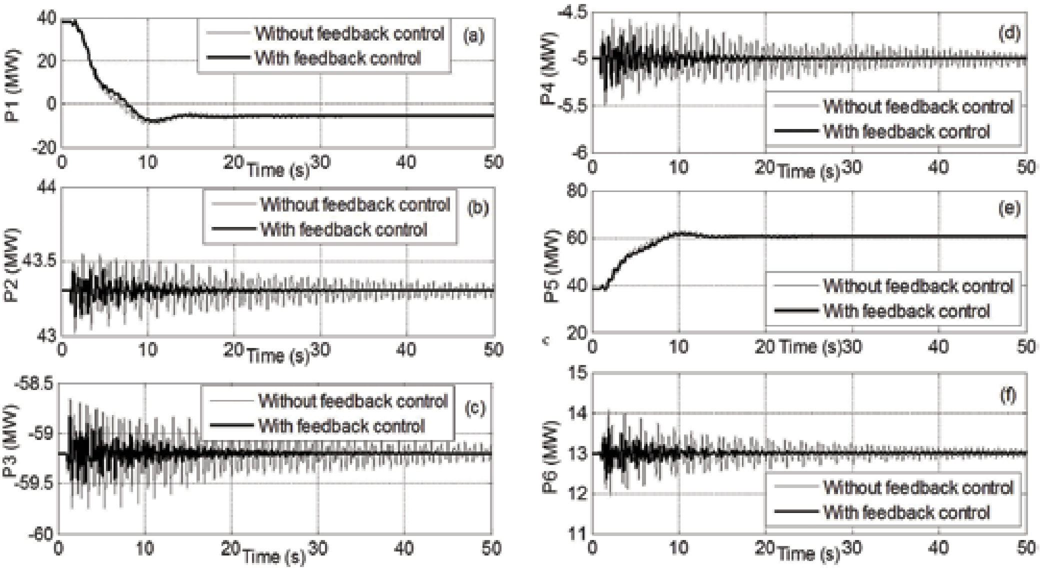

Figure 11. Case 1, load change: (a) net power of area 1; (b) net power of area 2; (c) net power of area 3. (d) Net power of area 4; (e) net power of area 5; (f) net power of area 6.

Therefore, the additional power injected into areas 5 and 7 initiate acceleration of the machines at areas 5 and 7 and, subsequently, similar response at the other machines. **Figure 11(a–f)** shows the net power with and without power modulation feedback when the wind speed changed from 11 to 12 m/s at t = 1 s. The event causes a power unbalance in the area served by area 5 and 7 initiating exhibiting large oscillations. As the system is adjusting to the new steady state, the exported power from the slack Bus 1 is decreasing and that of area 5 and area 7 are decreasing by the same amount equal to the wind power change by of 46 MW. The effectiveness of the wind power modulation by using H-infinity feedback control can be seen in **Figure 11(a–f)** comparing to the responses without power modulation. The oscillation damping has increased significantly and the system arrives at the steady state approximately 20s.

Figure 12 shows the responses of the system with and without the feedback control from the wind generator at t = 1 with changing of the wind speed from 11 to 12 m/s. The output of the wind generator power as in **Figure 12(a)** is smooth increasing to accelerate the PM-generator.

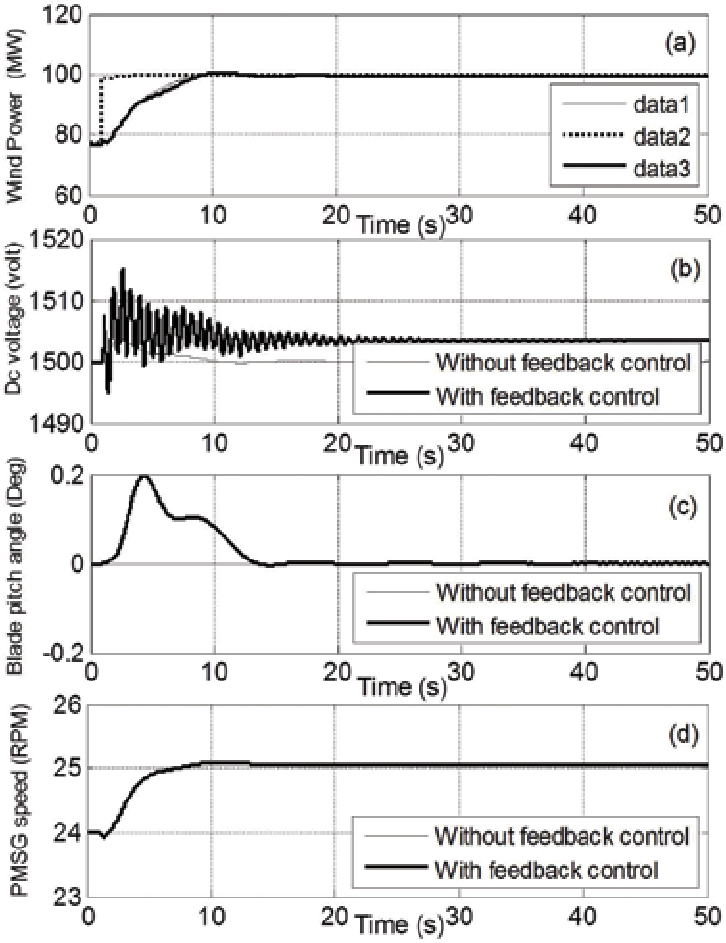

Figure 12. Wind speed change: (a) wind power; (b) DC voltage response; (c) pitch angle response; (d) PMSG speed response.

The oscillations in the dc link voltage are greater in the case where modulation feedback is used resulting partly in the stabilizing power modulation. The deviation of the dc link voltage of only 20 V or 1.3% is sufficient. The blade pitch angle, in **Figure 12(c)**, is activated only by the power modulation feedback and the variation of the blade pitch angle is less than 0.2°. The generator speed, in **Figure 12(d)**, immediately accelerates as a result of the increasing wind power input and its variation is very small.

6. Conclusion

The power modulation by using a PMSG wind turbine to damp the power oscillation in a multi-area power system is studied. H-infinity control is applied as a feedback control; where, the input is the variation of the local grid generator speed and the output feedback to the dc-voltage, blade pitch angle and PMSG speed controls. The high-order dynamic model of the wind generator system is reduced to simplify the analysis. The PMSG wind turbine connected to the IEEE 30 bus in different areas such as area 5 and 7. The results showed the effectiveness of the wind generator in significantly increasing damping. The dc link voltage modulation provides more damping to the grid power oscillations as it compares to the PMSG speed and rotor blade pitch angle modulations. The MATLAB/Simulink is used to design the controller and validate the results.

Author details

Emad M. Elhaji[1,2]

Address all correspondence to: emadelhaji@siu.edu

1 Misurata University, Misurata, Libya

2 Sothern Illinois University, Carbondale, USA

References

[1] Forsberg CW. Sustainability by combining nuclear, fossil and renewable energy sources. Progress in Nuclear Energy. 2009;**51**:192-200

[2] Matas J, Castilla M, Guerrero JM, Garcia De Vicuna L, Miret J. Feedback linearization of direct-drive synchronous wind-turbines via a sliding mode approach. Power Electronics, IEEE Transactions on, May 2008;**23**(3):1093-1103

[3] Wind Power Today and Tomorrow - NREL - U.S. Department of Energy — Energy Efficiency and Renewable Energy By the National Renewable Energy Laboratory, a DOE National laboratory DOE/GO-102004-1894 March 2004

[4] Global Wind Report Annual Market Update. Gwec.net. Retrieved 2017–05-5

[5] Technology Roadmap Wind energy – International Energy Agency, 2013

[6] González-Longatt FM, Wall P, Terzija V. A simplified model for dynamic behavior of permanent magnet synchronous generator for direct drive wind turbines. In: 2011 IEEE Trondheim PowerTech. Trondheim; 2011. pp. 1-7

[7] Muljadi M, Singh M, Gevorgian V. Fixed-Speed and Variable-Slip Wind Turbines Providing Spinning Reserves to the Grid. National Renewable Energy Laboratory (NREL), Tech. Rep; July 2013

[8] Devaraj D, Jeevajyothi R. Impact of fixed and variable speed wind turbine systems on power system voltage stability enhancement. Renewable Power Generation (RPG 2011), IET Conference on. 2011:1-9

[9] Carlin P, Laxson A and Muljadi E. The history and state of the art of variables speed wind turbine technology. National Renewable Energy Lab., Golden, CO, Tech. Rep. NREL/TP-500-28 607; 2001

[10] Cao W, Xie Y, Zheng T. Wind Turbine Generator Technologies. InTechOpen; 2012

[11] Ali HR. "The dynamic performance of grid-connected fixed-speed wind turbine generator," 2014 6th International Conference on Information Technology and Electrical Engineering (ICITEE), Yogyakarta, 2014, pp. 1-5

[12] Camm EH et al., "Characteristics of wind turbine generators for wind power plants," 2009 IEEE Power & Energy Society General Meeting, Calgary, AB, 2009, pp. 1-5

[13] Fletcher J, Yang J. Introduction to doubly-fed induction generator for wind power applications. In: Nathwani J, Ng AW, editors. Paths to Sustainable Energy. New York, NY, USA: InTech; 2010. pp. 259-278

[14] Morimoto S, Nakayama H, Sanada M, Takeda Y. Sensorless output maximization control for variable-speed wind generation system using IPMSG. IEEE Transactions on Industry Applications. Jan.-Feb. 2005;**41**(1):60-67

[15] Teodorescu R, Liserre M, Rodríguez P. Grid converter structures for wind turbine systems. In: Grid Converters for Photovoltaic and Wind Power Systems. Chichester, UK: John Wiley & Sons, Ltd; 2011. DOI: 10.1002/9780470667057.ch6

[16] Hoffmann R. A comparison of control concepts for wind turbines in terms of energy capture. In: D17 Darmstädter Dissertation. Germany: Department of Power Electronics and Control of Drives, Darmstadt; 2002. p. 134

[17] Tiwari Ramji, Sanjeevikumar P, Ramesh Babu N. "Co-ordinated control strategies for permanent magnet synchronous generator based wind energy conversion system", Energies Journal, MDPI AG Publications, Switzerland, 28 Sept. 2017;**10**(1493):1-17

[18] Courseware Sample: Principles of Doubly-Fed Induction Generators (DFIG), Festo Didactic Ltee/Ltd, 2011

[19] Hanselman DC. Brushless Permanent Magnet Motor Design. USA: McGraw-Hill; 1994

[20] Akin B, Bhardwaj M. "Sensored Field Oriented Control of 3-Phase Induction Motors", Copyright © 2013, Texas Instruments Incorporated, SPRABP8–July; 2013

[21] Liang J and Whitby B. "Field oriented control of a permanent magnet synchronous generator for use in a variable speed tidal stream turbine," Universities' Power Engineering Conference (UPEC), Proceedings of 2011 46th International, Soest, Germany, 2011, pp. 1-6

[22] Kundur P. Power System Stability and Control. USA: McGraw Hill; 1994

[23] Klein M, Rogers GJ, Kundur P. A fundamental study of inter-area oscillations in power systems. In IEEE Transactions on Power Systems. Aug 1991;**6**(3):914-921

[24] Hsu YY, Shyue SW, Su CC. Low frequency oscillations in longitudinal power systems: Experience with dynamic stability of Taiwan power system. In IEEE Transactions on Power Systems. Feb. 1987;**2**(1):92-98

[25] Kim M-K. Optimal control and operation strategy for wind turbines contributing to grid primary frequency regulation. Applied Sciences. 2017;**7**:927

[26] Fatu M, Tutelea L, Boldea I and Teodorescu R. Novel motion sensorless control of stand alone permanent magnet synchronous generator (PMSG): Harmonics and negative sequence voltage compensation under nonlinear load. 2007 European Conference on Power Electronics and Applications, Aalborg, 2007, pp. 1-10

[27] Li S, Haskew TA, Swatloski RP, Gathings W. Optimal and Direct-Current vector control of direct-driven PMSG wind turbines. Power Electronics, IEEE Transactions on. May 2012; **27**(5):2325-2337

[28] Ganesh A, Dahiya R, Singh GK. A novel STATCOM wide area feedback controller for improving stability in multimachine system. In: Power Systems, Energy, Environment. 2014

[29] Tsourakis G, Nomikos BM, Vournas CD. Contribution of doubly fed wind generators to oscillation damping. IEEE Transactions on Energy Conversion. Sep. 2009;**24**(3):783-791

[30] Margaris ID, Papathanassiou SA, Hatziargyriou ND, Hansen AD, Sorensen P. Frequency control in autonomous power systems with high wind power penetration. In IEEE Transactions on Sustainable Energy. April 2012;**3**(2):189-199

[31] Sun YZ, Zhang ZS, Li GJ and Lin J. "Review on frequency control of power systems with wind power penetration," 2010 International Conference on Power System Technology, Hangzhou, 2010, pp. 1-8

[32] Dengying, Zhoujie. LPV H-infinity controller Design for a Wind Power Generator. 2008 IEEE Conference on Robotics, Automation and Mechatronics, Chengdu, 2008, pp. 873-878

[33] Howlader A, Urasaki N, Yona A, Senjyu T, Saber A. Design and Implement a Digital H∞ Robust Controller for a MW-Class PMSG-Based Grid-Interactive Wind Energy Conversion System. Energies. June 2013:pp. 2084-2109

[34] Muhando BE, Wies RW. Nonlinear H_∞ constrained feedback control for grid-interactive WECS under high stochasticity. In IEEE Transactoons Energy Conversion. Dec. 2011;**26**(4): 1000-1009

[35] Muhando EB, Senjyu T, Uehara A, Funabashi T. Gain-scheduled H_∞ control for WECS via LMI techniques and parametrically dependent feedback part I: Model development fundamentals. In IEEE Transactions on Industrial Electronics. Jan. 2011;**58**(1):48-56

[36] Geng H, Dewei X. Stability analysis and improvements for variable-speed multipole permanent magnet synchronous generator-based wind energy conversion system. Sustainable Energy, IEEE Transactions on. Oct. 2011;**2**(4):459-467

[37] Alaboudy A, Daoud A, Desouky S, Salem A. Converter controls and flickers study of PMSG-based grid connected wind turbines. Ain Shams Engineering Journal. March 2013; **4**(1):75-91

[38] Haque Md E, Negnevitsky M, Muttaqi KM. A novel control strategy for a variable-speed wind turbine with a permanent-magnet synchronous generator. Industry Applications, IEEE Transactions on. Jan.-feb. 2010;**46**(1):331-339

[39] Belhadj J, Roboam X. Investigation of different methods to control a small variable-speed wind turbine with PMSM drives. Journal of Energy Resources Technology. 2007;**129**(3): 200-213

[40] Geng H et al. Active damping for PMSG-based WECS with DC-link current estimation. Industrial Electronics, IEEE Transactions on. 2011;**58**(4):1110-1119

[41] Zhang Z, Hackl C, Kennel R. Two direct torque and power control methods for back-to-back power converter PMSG wind turbine systems. presented at the Int. Power Electronics Motion Control Conf. Hefei, China. May 2016

[42] Rosyadi M, Muyeen SM, Takahashi R, Tamura J. Transient stability enhancement of variable speed permanent magnet wind generator using adaptive PI-fuzzy controller. PowerTech, 2011 IEEE Trondheim, 1,6, 19-23 June 2011

[43] Elhaji EM, Hatziadoniu CJ. Damping tie-line power oscillations by modulation feedback of wind generators. Electric Power Systems Research. 2016

[44] Elhaji EM, Hatziadoniu CJ. Interarea oscillation damping using H-infinity control for the permanent magnet wind generator. Electric Power Systems Research. 2017

[45] Power system test cases archive, available on www.ee.wasinton.edu/research/pstca

[46] Anderson, Paul M, and Aziz A. Fouad. Power system control and stability. John Wiley & Sons, 2008.ower system book for 9-bus system

[47] Ortega R, Garcia-Canseco E. Interconnection and damping assignment passivity-based control: A survey. European Journal of Control. 2004;**10**:432-450

[48] Burke JV et al. HIFOO-a MATLAB package for fixed-order controller design and H∞ optimization. In: Fifth IFAC Symposium on Robust Control Design, Toulouse. 2006

Power Quality and System Stability Impact of Large-Scale Distributed Generation on the Distribution Network: Case Study of 60 MW Derna Wind Farm

Saad M. Saad, Naser El Naily, Jamal Wafi,
Faisal A. Mohamed and Abdelsalam Elhaffar

Additional information is available at the end of the chapter

http://dx.doi.org/10.5772/intechopen.74796

Abstract

Wind energy (WE) has become one of the most promising and developed forms of renewable energy source due to its efficiency and the availability of different capacities according to the loading requirements. The integration of wind turbines in the Libyan network has become an indispensable choice due to Libya's distinguished location and for the Libyan National Initiative. Despite the numerous benefits of WE, the penetration of WE sources in the distribution network has some negative impacts related to the quality and reliability of the electric power supplied to the network. Owing to, the intermittent nature of these sources and electronic circuits needed to regulate the extracted power to comply with the grid requirements. In this chapter, implementation of the eastern Libyan network in NEPLAN and MATLAB/SIMULINK packages are carried out to investigate and analyze the significance of wind farm penetration in the medium voltage level of Libyan Distribution Network. A 60 MVA wind farm system has been connected to the Libyan distribution network according to the Libyan National Initiative. Different penetration scenarios are simulated to testify the technical aspects of integrating WE on the distribution level.

Keywords: renewable energy, wind energy, stability studies, power quality, distribution network, harmonics

1. Introduction

Libya is one of the leading and largest exporters and producers of oil and gas in North Africa and the world with a total area of 1,750,000 km^2. It has gifted with a 1900 km Mediterranean coastline, which has given it enormous potential to generate electricity from wind and solar energies. Most of Libya's population lives on the coastline. The total population is approximately 6,273,000 [1]. Despite the potential to generate electric energy from wind and solar as a result of the excellent location, Libya's contribution to alternative energy remains negligible. The production of electricity in Libya depends mainly on fossil fuel sources. After the devastation in Libya since 2011, oil production in Libya has fallen, which has led to a sharp drop in state exports and a frequent shortage of electricity production [2, 3]. As a result of the economic development and reconstruction, the demand for energy will substantially increase in the near future. Therefore, the generation of energy from sustainable energy sources in the country must be taken into account, since it mainly depends on fossil fuels. To avoid the negative results in the near future such as the shortage of oil and gas supplies, and the reduction of emissions from conventional generation sources, the establishment of an urgent plan needs to be considered. However, renewable energy sources have been utilized in Libya since the 1970s, but in small-scale applications. In 1976, solar energy has been applied in the electricity cathodic protection stations for gas pipelines protection. Also, in 1979, four pilot stations in the field of communications were installed. In 1983, the installation of solar energy systems began to pump water for irrigation in El-Agailat city. In 2010, a 60 MW project was launched in Derna due to the high potential for wind power generation with wind speed of between 6 and 7.5 ms^{-1} at a height of 40 m [1, 4].

According to [5], 10% of the world's energy will be available through wind power in the next decade. Also, as a result of planning to make electric power from wind energy sources, one of the main sources of electricity in Libya, investigating and verifying the consequence of penetrating wind energy sources on the electrical grid is one of the most critical studies to provide optimum stability when integrating wind farms to the grid. The dynamic response of squirrel cage induction generator (SCIG) with direct grid connection is carried out. In [6, 7], a study proposed a 36 MW fix speed wind farm connected to the grid. It is found that the study was done through calculating its power curve and investigating the effects of wind speed at the beginning.

Libya has enormous potential for solar and wind power generation. **Figure 1** shows wind speed in several cities and regions in Libya. It shows the potential for high wind power production, as in Benina, Sirte, and Derna. From the research side, the possibility of [8].

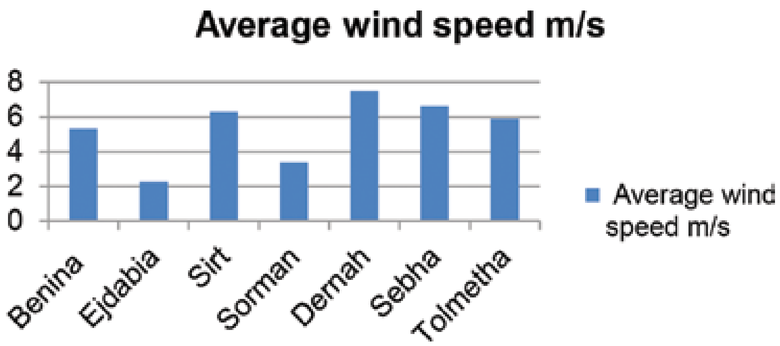

Figure 1. Average wind speed for different cities in Libya.

2. Adverse effects of wind energy conversion units on distribution networks

The electrical power obtained from wind farm system adversely affects the voltage stability in the grid. To improve and maintain the voltage stability, prior understanding of the influences of such sources in terms of power quality and harmonics is significant for better operation and control of the grid.

2.1. Protection problems

The main function of protection system is to ensure the speed of operation and reliability to clear and isolate faulty equipment in case of a fault. The role of protection schemes is to minimize disturbing effects of fault currents and reduce the number of feeder outage. The penetration level of distributed generation (DG) influences the performance of protective relays and deteriorates the distribution network reliability.

The philosophy of protection systems in conventional distribution networks relies on the single direction of power flow from power plants toward the distribution network. The presence of DG turns out the distribution system operation comparable to the transmission system operation [9]. The arrangement of protection schemes becomes more difficult when further DG units connected to the distribution network since DG integration shifts the flow of the power and raises the short-circuit level. Therefore, the protective relays may not carry on its functions accurately, since the operation of the protective relays in the distribution level based upon the short-circuit sensitivity [10]. Introducing DGs to the distribution network associate further protection issues such as blinding of protective devices, false tripping, and reclosure-fuse miscoordination [11, 12]. Moreover, DG units can contribute a large current enough to trip the protective device on the feeder connecting the DG before the protective device on the faulted line, especially in synchronous machines based [13].

2.2. Power quality problems

Voltage regulation may become a challenge in the presence of DGs. Additionally, some DG technologies lack the ability to produce reactive power and compensate for voltage reduction on loaded busbars. The interruption of large DG units in case of faults could influence the reliability of the entire network. The disconnection of synchronous generators with huge capacities and the intermittent nature of DG based on renewable sources may cause voltage fluctuation, especially near these DGs [14, 15]. Some DG technology connected to the grid through power electronic converters such as wind turbine operates with doubly fed induction machine and photovoltaic may become a source of power quality problems too. Capacitors used for induction generators are also a source of harmonics in case of resonances in the network. The growth in integrating single-phase DGs in distribution network could influence the voltage profile and create an eminent unbalancing issue. When wind energy is penetrated into the grid, the power quality of the grid will be affected among other characteristics [16, 17]. The power quality of the grid containing wind systems must comply with the limits and requirements of the facilities. Therefore, the characteristics of the grid must be evaluated properly after the wind energy systems are connected to the grid. Prior knowledge of wind system characteristics must be adequately defined to avoid the drawbacks of connecting such sources. The electrical characteristics of wind turbines are usually specified by the manufacturer, not by specific site location. For this reason, when the electrical characteristics of a particular wind turbine are known, their impact on the power quality when connected to a particular location in the network can be predicted and calculated as a set of units. The necessity for quality requirements, detailed and applicable documentation on the power quality of wind sources is required. The International Electrotechnical Commission (IEC) started work to facilitate this in 1996. As a result, IEC 61400-21 was developed and, today, most large wind turbine manufacturers provide power quality characteristic data accordingly [18, 19].

3. Modeling of Derna wind farm

Darnah wind farm turbines are located in Derna city, which is located on the coastline of Mediterranean around (320 29′ 16.728″ N—latitude 200 49′ 54.264″—longitude), in the eastern part of Libya as shown in **Figure 2** with population of 80,000 [1].

3.1. Modeling of wind turbine

The wind energy system transfers the kinetic energy extracted from wind into mechanical energy through rotor blades of the wind turbine, and the permanent magnet synchronous generator (PMSG) transforms the mechanical energy in the rotor blades into electrical energy.

Figure 2. The geographic situation of Derna-Libya.

The power extracting from wind depends on the covered area A of the rotor and the wind velocity V_w and the air density p. The generated mechanical power P_{mech} is generally computed form wind energy using the coefficient of power C_p as follows [4]:

$$P_{mech} = \left(\frac{1}{2}\right) C_P(\lambda, \theta) A \rho V_w^3 \tag{1}$$

The performance coefficient *Cp* is a function of the A and θ that depends on the wind velocity *Vw*, the rotational speed of the shaft *wr* and the rotor radius *Rr*.

$$\lambda = \left[\frac{\omega_r R_r}{V_\omega}\right] \tag{2}$$

(r.p.m) tends for speed of the rotor, *Rr* stands for e rotor (m) and *Vw* stands for velocity of wind (m/s). The power of the wind turbine versus wind speed and aerodynamic coefficients are shown in **Figure 3**.

3.2. Modeling of drive train

The behavior of the drive train dynamics is considered by taking three different model approaches such as single mass, double mass, and three mass model design in order to know which of the methods are more noticeable in detaining the performance of the network [17]. The study of drive train models depends upon the complexity of the network. If a study takes interest about the torsion fatigue, it just has to consider the dynamics of all parts of the networks [20, 21]. For these aim, double lumped mass or more accurate models are required. For that, when application targets on the interaction between wind farms and connected loads, the considered drive train model considered being a single mass model for the sake of simplicity. Due to the direct connection of generator shafts of the turbine, the model of drive train can be defined as:

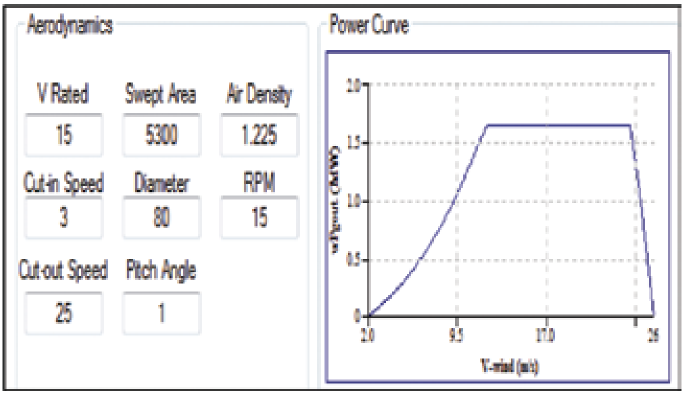

V Rated: 15
Swept Area: 5300
Air Density: 1.225
Cut-in Speed: 3
Diameter: 80
RPM: 15
Cut-out Speed: 25
Pitch Angle: 1

Figure 3. Power coefficient Cp (λ, θ) curves.

$$\frac{d\omega_{mech}}{dt} = \left(\frac{1}{j}\right)(T_{mech} - T_{elec} - f\omega_{mech}) \tag{3}$$

$$\int \omega_{mech} = \theta_{mech} \tag{4}$$

where T_{mech} stands for the mechanical torque generated by the wind turbine, Telec stands for the generated electromagnetic torque by the permanent magnet synchronous generator which can also be represented as a T_{gen}, j stands for the inertia moment and f stands for the viscous friction coefficient that cannot be considered in a medium-scale wind turbine. In order to have the voltage in a-b-c frame from the d-q frame, one can need the angle θ that obtained after integrating the mechanical speed of the rotor h.

3.3. Modeling of permanent magnet synchronous generator

The model used for modeling the synchronous generator, which is based on permanent magnet (PMSG) is developed on the d-q axes 'park' model as shown in **Figure 4**. The mathematical model of PMSG is implemented using two-phase synchronous rotating reference frame theory in which the q-axis is in 90 degrees with the d-axis with reference to the direction of rotation. All the quantities in the rotor are referred to the stator, and it is given as follows [22, 23]:

$$V_{ds} = R_s I_{ds} + \frac{d\phi_{sd}}{dt} - \omega_{elec}\phi_{sq} \tag{5}$$

$$V_{qs} = R_s I_{qs} + \frac{d\phi_{sq}}{dt} - \omega_{elec}\phi_{sd} \tag{6}$$

where the stator fluxes are computed by following equation:

$$\phi_{sd} = L_d I_{ds} + \phi_m \tag{7}$$

$$\phi_{sq} = L_q I_{qs} \tag{8}$$

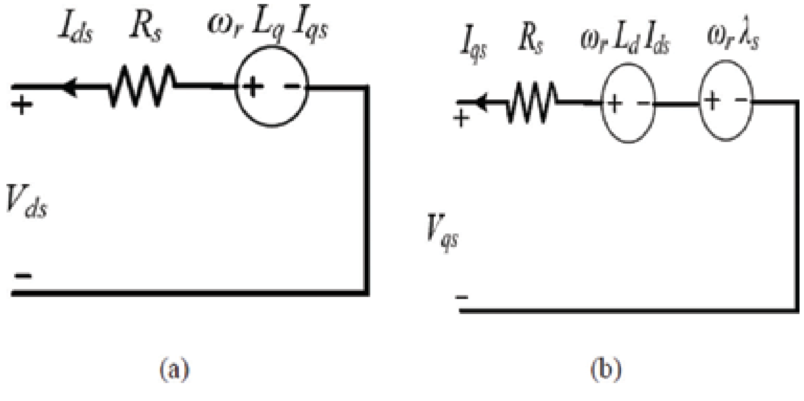

Figure 4. PMSG model in steady state condition with respect to the rotor flux reference frame: (a) direct axis and (b) quadrature axis.

Now putting the value of ϕ_{sd} and ϕ_{sq} in Eqs. (5) and (6), so one can land up with the expression as below:

$$V_{ds} = R_s I_{ds} + \frac{d}{dt}\left(L_d I_{ds} + \phi_m\right) - \omega_{elec}\left(L_q I_{qs}\right) \tag{9}$$

$$V_{qs} = R_s I_{qs} + \frac{d}{dt}\left(L_q I_{qs}\right) + \omega_{elec}\left(L_d I_{ds} + \phi_m\right) \tag{10}$$

So, again resolving the above mentioned equation we can land up with following equation:

$$V_{ds} = R_s I_{ds} + L_d \frac{d}{dt} I_{ds} - \omega_{elec}\left(L_q I_{qs}\right) \tag{11}$$

$$V_{qs} = R_s I_{qs} + L_q \frac{d}{dt} I_{qs} + \omega_{elec}\left(L_d I_{ds} + \phi_m\right) \tag{12}$$

Therefore, in order to solve for the d and q axis stator currents, the above mentioned equation can be formed in the following fashions:

$$\frac{d}{dt} I_{ds} = \left(\frac{1}{L_d}\right)\left[V_{ds} - R_s I_{ds} + \omega_{elec}\left(L_q I_{qs}\right)\right] \tag{13}$$

$$\frac{d}{dt} I_{qs} = \left(\frac{1}{L_q}\right)\left[V_{qs} - R_s I_{qs} - \omega_{elec}(L_d I_{ds}) - \omega_{elec}\phi_m\right] \tag{14}$$

where *Rs* stands for the stator winding resistance, *Ld* stands for the stator inductance in direct axis, *Lq* stands for the stator inductance in quadrature axis, *Vds* stands for the direct axis stator voltage, *Vqs* stands for the quadrature axis stator voltage, Ids stands for the direct axis stator current, *Iqs* stands for the quadrature axis stator current, $W_{elec} = P_{wmech}$ stands for the speed [19, 24].

Since the permanent magnet synchronous generator (PMSG) is a machine similar to wound rotor machine which is better for surface-seated applications, the generated electric torque by the PMSG can be defined as follows:

$$T_{elec} = \left(\frac{3}{2}\right) P\left(\phi_m I_{qs} + \left(L_d - L_q\right) I_{ds} I_{qs}\right) \tag{15}$$

However, if permanent magnet synchronous generator is surface seated, then it is conceivable to favor the assumption of Ld = Lq. Then torque can be expressed as follows:

$$T_{elec} = \left(\frac{3}{2}\right) P\left(\phi_m I_{qs} + (L_d - L_d) I_{ds} I_{qs}\right) \tag{16}$$

So, one can land up with the equation as follows:

$$T_{elec} = \left(\frac{3}{2}\right) P\left(\phi_m I_{qs}\right) \tag{17}$$

In steady-state positions, the active power generated e from permanent magnet synchronous generator is given by:

$$P_s = V_{ds}I_{ds} + V_{qs}I_{qs} \tag{18}$$

The wind farm is connected to the grid via step-up transformer to the 30 kV busbar [25, 26].

4. Simulation results

Figure 5 shows a single-line diagram of a low-voltage network of Derna City simulated in NEPLAN [27]. The electric grid as shown in **Figure 6** consists of different voltage level busbars. The network feeds from the 220 KV busbar which connects it to the rest of the Libyan network through different capacity power transformers. Also, wind turbines with a total capacity of 60 MW, consisting number of turbines with a rated power of 1.65 MW, is connected to the simplified network in our study. **Table 1** shows data for different components in the network and details of the wind turbines system.

4.1. Load profile

One of the most significant purposes for the integration of renewable energy sources into distribution networks is to reduce the costs of electricity to the consumers derived from charging line losses in this cost. The amount of line losses depends on the distance required to transfer the electric power as well as the value of the drawn current by consumers and thus affect the optimal economic dispatch based on the network configuration. Distribution network operators need to apply simple methods to predict the power flow in the network to ensure the balance of energy demand. Proper integration of the renewable energy sources in the distribution network will reduce the power losses in the transmission lines to a certain

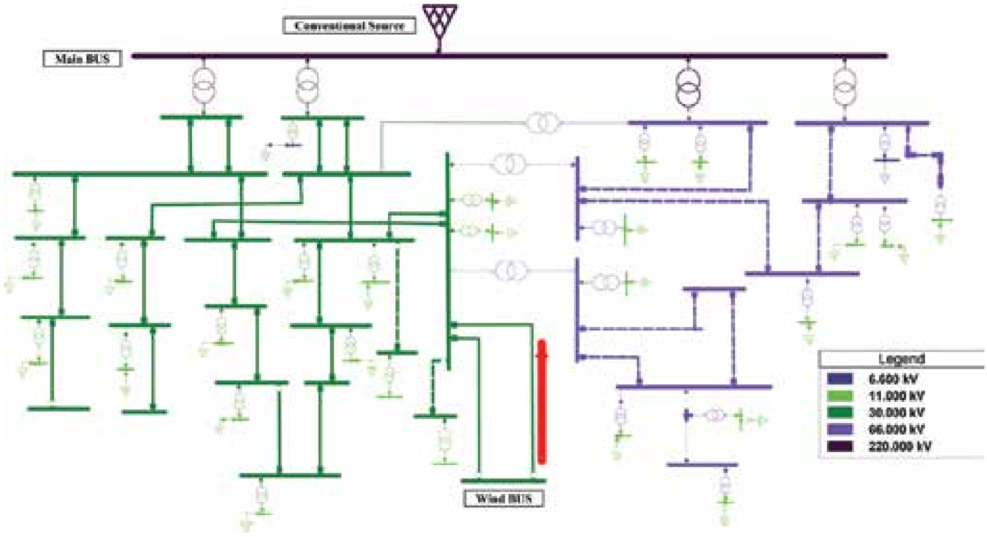

Figure 5. Single-line diagram of a low-voltage network of Derna city simulated in NIPLAN.

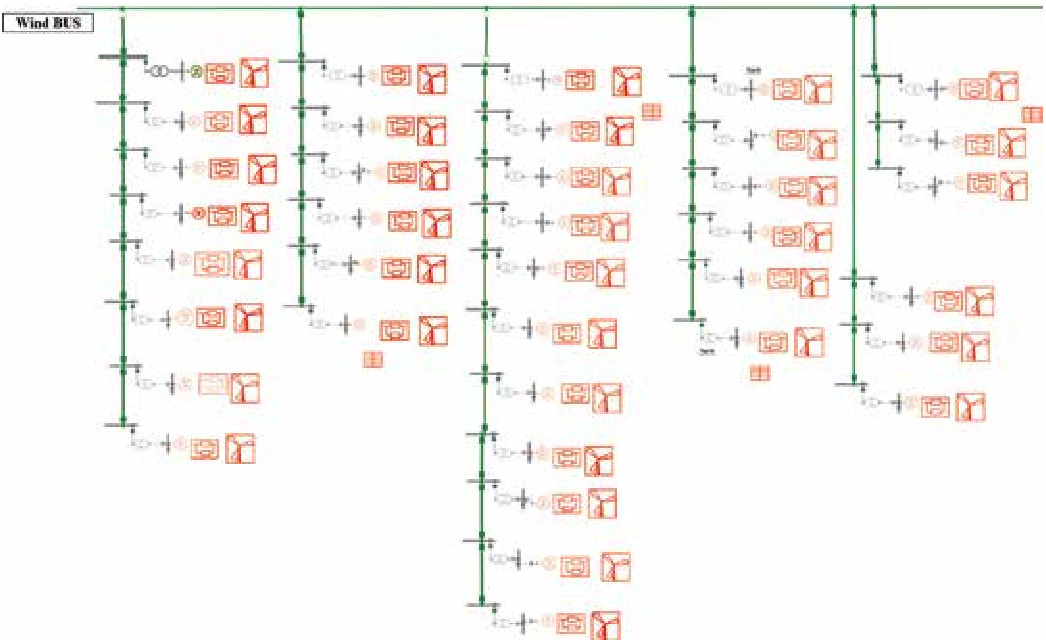

Figure 6. 60 MW wind farm connected to Derna medium voltage network.

Wind bus	Isc-3Ø = 10.02a83.5 Isc-1Ø = 7.99a − 78.9 X0/X1 = 1.73
220/30 KV 63 MVA main transformer	Positive sequence data: impedance voltage = 12.76% X+/R + = 34.1 Zero sequence data: impedance voltage = 12% X0/R0 = 34.1
Wind turbine source	Rating: 1.65 MW, 0.69 KV, PF = 0.9 Turbine rated wind speed = 15 m/s Minimum wind speed = 4 m/s Maximum wind speed = 25 m/s Swept area = 2828 Rotor diameter = 80 m Pitch angle = 1 Air density = 1.225 kg/m^3 RPM = 15
575/30 KV 2 MVA transformer	Positive sequence data: impedance voltage = 6.25% X+/R + = 6 Zero sequence data: impedance voltage = 6.25% X0/R0 = 6
Bear 325 mm^2 30 kV transmission line	Z+ = 0.1162 + 0.385 j Ω/km Z0 = 0.3486 + 1.155 j Ω/km

Table 1. Parameters of electric network and wind energy system.

level. This will contribute to the postponement of network infrastructure promotion. Various methods to determine the optimal capacity and location of each renewable DG at the minimum line losses, among which is Branch power loss formula as given in Eq. (19) [28]. **Figure 7** shows the loading profile of distribution transformers with different capacities through the day. **Figure 8** shows the power supplied by the main feeder of the network in different wind farm penetration level.

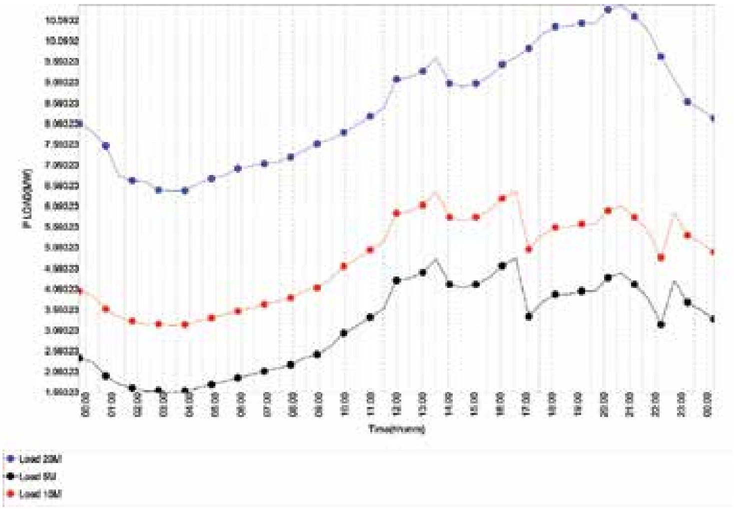

Figure 7. The loading Profile of 20, 10 and 5 MW Distribution Transformers During 24 Hours.

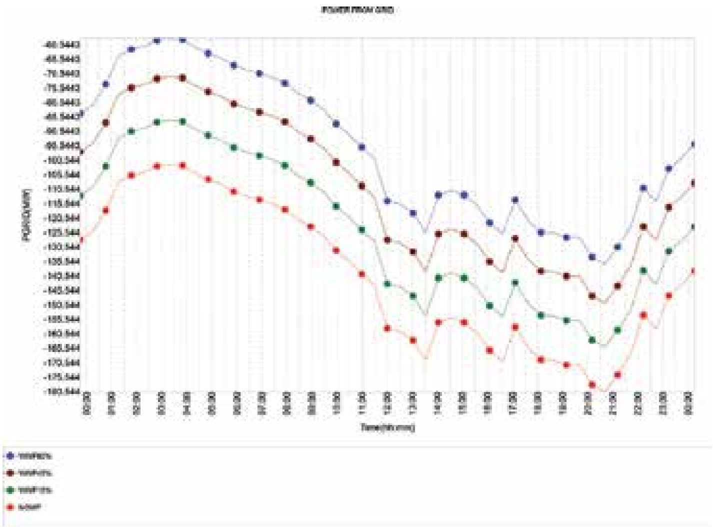

Figure 8. MW power from main feeder with different wind farm penetration.

$$P_{Loss} = \sum_{i=1}^{n} \frac{P_{bi}^2 + Q_{bi}^2}{|V_i|^2} R_i \tag{19}$$

where P_{bi} = Active power at branch i, Q_{bi} = Reactive power at branch i, $|V_i|$ = Magnitude of voltage at bus i.

The investigation of the load curve during the day shows a difference in loading ratios. The maximum rate of loading occurs at 20:30 due to switching lights in most homes. The investigation of energy feeding from the transmission system during the day showed the highest contribution from the grid 180 MW occur during the period of the sunset due to lighting loads, and since most loads in the network is a household loads. The electric supply from the grid decreases at the highest rate of integration of wind farm. This reduces the stress on the cables and improves the voltage profile on all busbars.

4.2. Voltage profile

Injection of renewable energy sources into the distribution network alters the direction of power flow in the grid. As a result, it enhances the voltage profile. The integration of such sources thus improves the voltage at feeder endings and thus improves the quality of the power fed to consumers as a whole [28]. The benefits of DG penetration on the voltage profile improvement can be evaluated as follows:

$$V_{11} = \frac{V_{11/wDG}}{V_{11/w0DG}} \tag{20}$$

$$V_{11/wDG} = \sum_{i=1}^{n} V_i LP_i W_i \tag{21}$$

$$V_{11/woDG} = \sum_{i=1}^{n} V_{i0} LP_i W_i \tag{22}$$

$$\sum_{i=1}^{n} W_i = 1 \tag{23}$$

If all the loads at bus i are equally weighted, Wi expressed as

$$W_1 = W_2 = W_3 = W_n = \frac{1}{n} \tag{24}$$

where

V_{11} = Voltage profile improvement benefits.

$V_{11/wDG}$ = General expression for voltage profile at bus I with the application of renewable DG units.

$V_{11/woDG}$ = General expression for voltage profile at bus I without the application of renewable DG units.

V_{i0} = Voltage at bus I per unit without renewable DG.

V_i = Voltage at bus I per unit with renewable DG.

LP_i = Load at bus I (per unit).

N = Number of busses in the power system.

W_i = weighting factor for bus i.

To investigate the fluctuation effects of wind energy source penetration, the voltage profile of different busbars is considered to display and show the excessive loading on the distribution busbars. The voltage profile for different busbars is illustrated in **Figure 9**. The influence of wind energy penetration on the voltage profile is slightly low, and this effect could be increased on radially connected busbars. The impact of wind generation will be noticeable at the busbar of point of common coupling (PCC) connecting the wind turbine to the electric grid. It is shown in **Figure 10**.

It is clear from the figures above, the voltages of all nodes have improved after interconnection of wind farm. The enhancement in voltage for busbars near from busbar of point of common coupling is better than the rest of other busbars in the network.

4.3. Harmonic distortion

The harmonics are created when non-sinusoidal currents and non-sinusoidal voltages increase in the network, and these distortions are generally called harmonic distortion [29, 30]. The

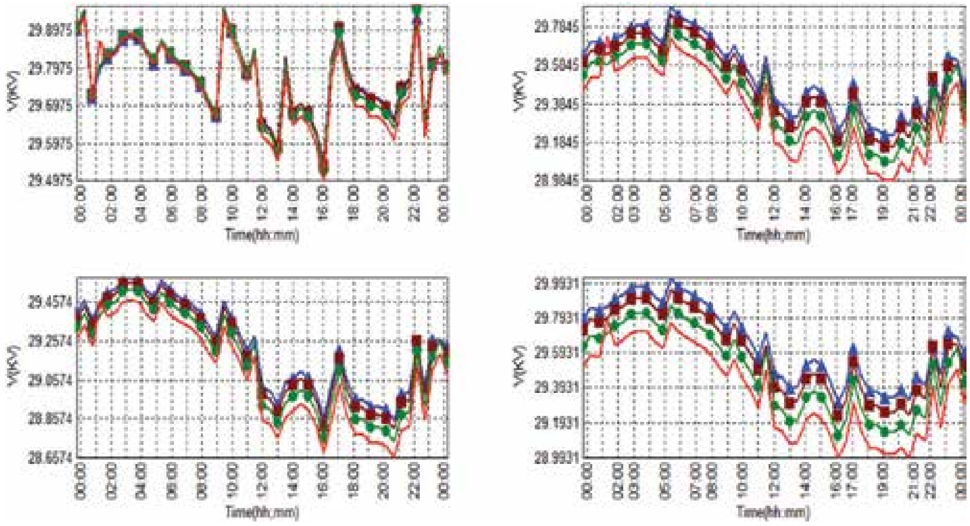

Figure 9. Voltage profile for different busbars for 1 day.

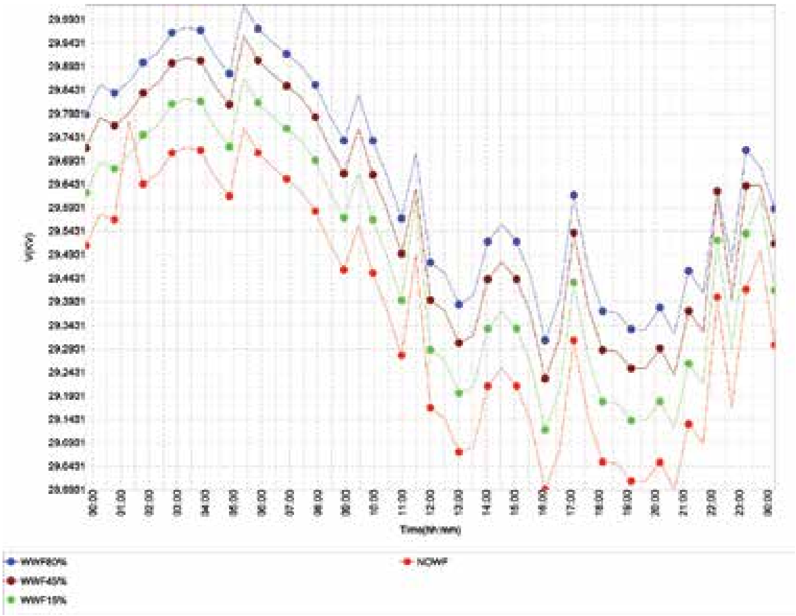

Figure 10. Voltage profile of point of common coupling (PCC).

basic conditions that lead to network consonances usually result from nonlinear loads, voltage imbalances. Power quality studies are carried out due to summation law [31]. The total harmonic current distortion is given as:

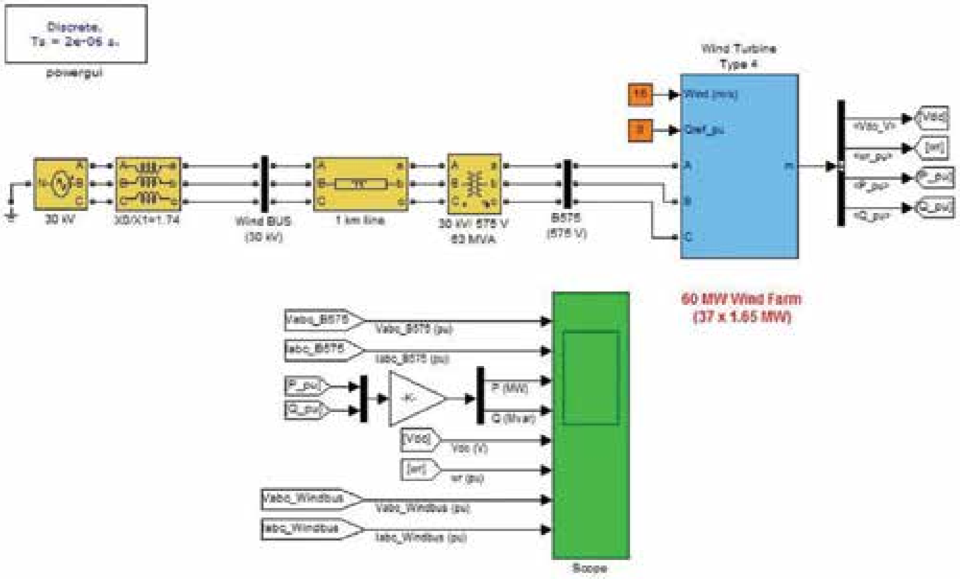

Figure 11. Simulated network with wind energy system.

$$I_{THD} = \sqrt{\sum\nolimits_{h=2}^{40} \frac{I_h^2}{I_1} 100} \tag{25}$$

Harmonics contributed by wind turbines in the network may cause a problem due to the existing harmonics in the network. The current waveform of wind turbines is non-sinusoidal and distorted due to low integer harmonics of second and fifth harmonics. The variable speed of wind turbine equipped with power electronic converters causes an increase in the harmonic distortion at the point of common coupling. **Figure 11** shows the simulated model in MATLAB/SIMULINK.

Measurement of harmonics taken from node 575. Measurement of a number of harmonics in currents has been carried out for different penetration level to study the effect of the penetration on the amount of harmonics in the network. **Figures 12–14** represent the harmonics values

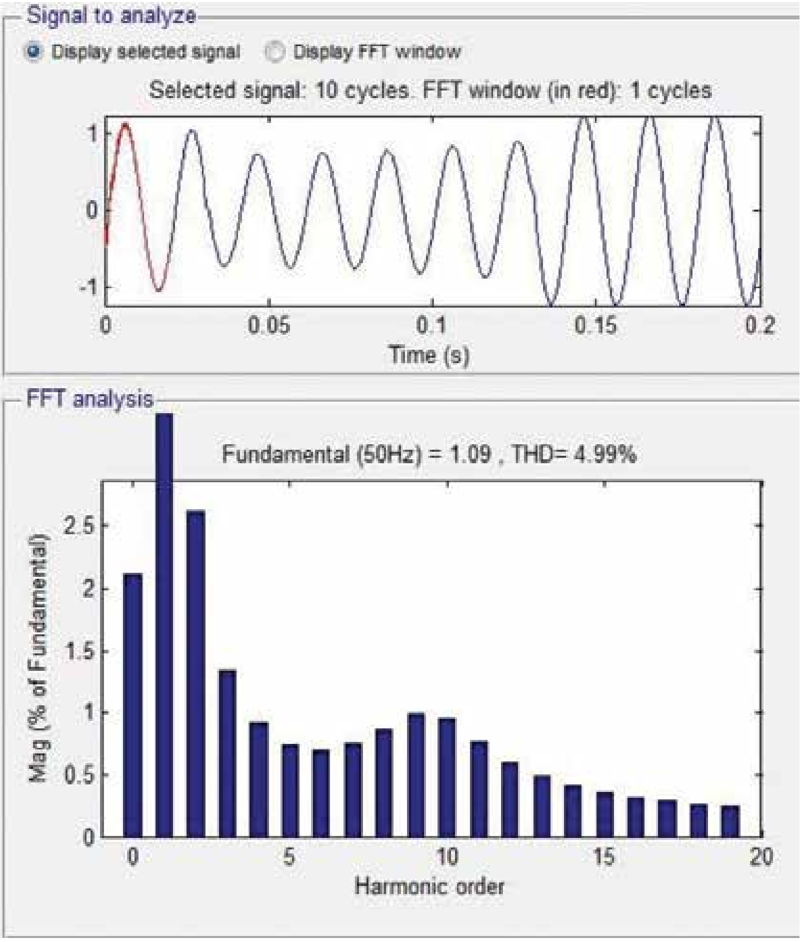
● Display selected signal ○ Display FFT window

Selected signal: 10 cycles. FFT window (in red): 1 cycles

Fundamental (50Hz) = 1.09 , THD= 4.99%

Figure 12. FFT output of total harmonic current distortion for 20 MW penetration.

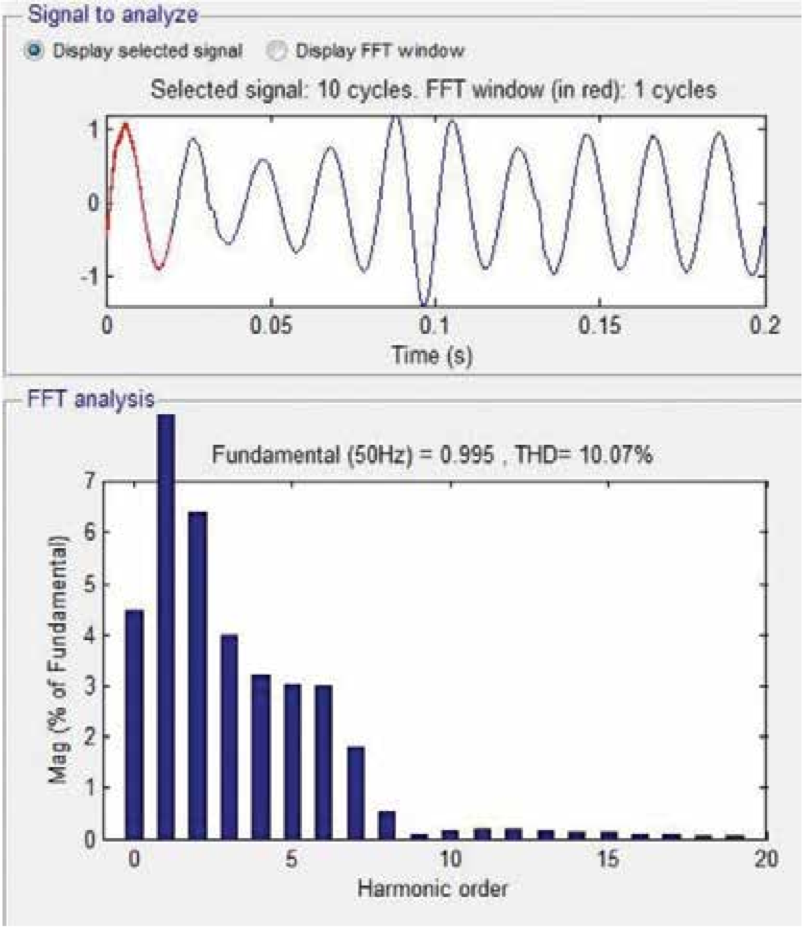

Figure 13. FFT output of total harmonic current distortion for 40 MW penetration.

in currents of the main busbar connecting wind farm for 20, 40, and 60 MW of penetration from wind farm. These results were extracted and implemented using MATLAB/SIMULINK after simplifying several wind turbines as one unit.

Figure 12 represents the harmonic current distortion for 20 MW penetration from wind energy system to the network. However, the total harmonic distortion shows slightly significant increase in the percentage of harmonic currents at PCC specially second and third harmonic currents to reach a value of 4.99% at PCC.

Figure 13 represents the harmonic current distortion for 20 MW penetration from wind energy system to the network. Moreover, the total harmonic distortion shows further slightly increase in the percentage of harmonic currents at PCC especially second and third harmonic currents to reach a value of 10.07% at PCC.

Figure 14 represents the harmonic current distortion for 60 MW penetration from wind energy system to the network. Moreover, the total harmonic distortion shows further highly increase

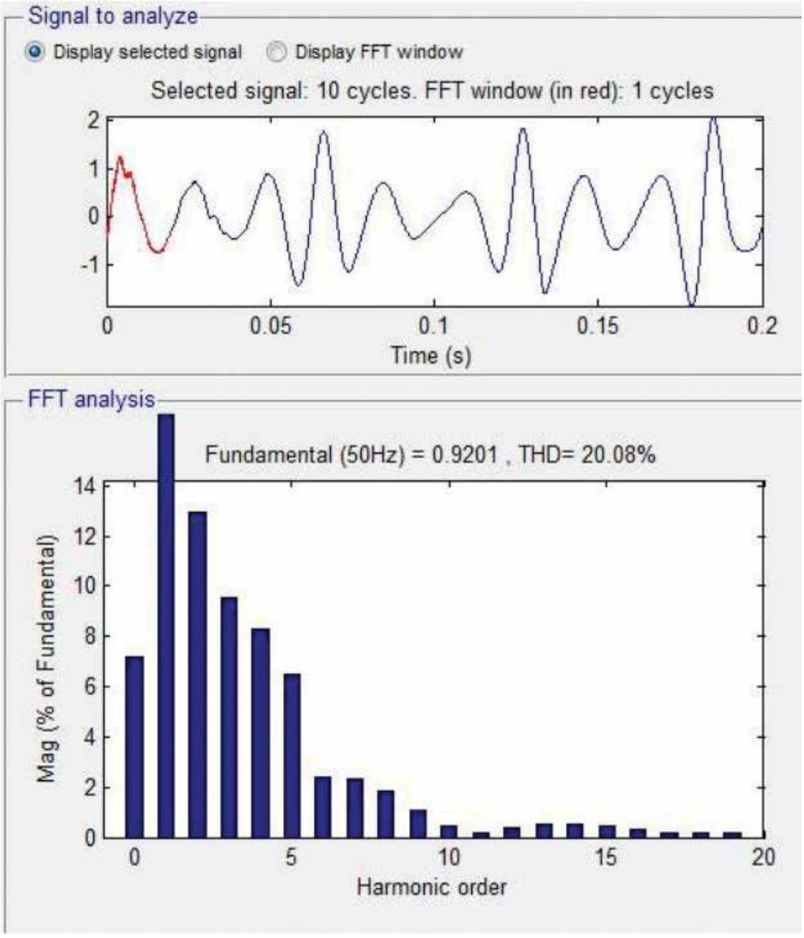

Signal to analyze

● Display selected signal ○ Display FFT window

Selected signal: 10 cycles. FFT window (in red): 1 cycles

FFT analysis

Fundamental (50Hz) = 0.9201 , THD= 20.08%

Figure 14. FFT output of total harmonic current distortion for 60 MW penetration.

in the percentage of harmonic currents at PCC especially second and third harmonic currents to reach a value of 20.08% at PCC.

The simulation is done at the selected PCC of 33 KV busbar system. The simulation result of current THDs is having low values. Three phases waveform of output currents at 33 KV busbar system is shown. From the three graphs, the result summary of harmonic currents is within permissible limits as compared to IEEE standard values and comply with the grid requirements. Therefore, it can be said that the wind farm power quality is sufficient and did not affect the grid system power quality, except for the case of 60 MW.

5. Conclusion

This chapter has interpreted the technical challenges of penetrating wind DG into the distribution system. Renewable DG can perform many significant functions in the economic, technical and environmental operation of an electric network. A wind energy system interconnected to a real network was investigated. Loads were programmed by NEPLAN. Actual wind measurements were used in this study to measure the extent to which wind power can be provided while ensuring a reasonable power quality and commensurate with international standards. It can be noticed from the results that the influence of the wind energy system can be significant on point of common coupling, which is close to the wind farm. Investigation of the cables connected in a mesh is less affected by the fluctuation more than the cables connected in radial can be further performed. It is also noticeable that energy losses decrease with increased penetration of the wind farm. From the analysis of the harmonic currents in MATLAB/SIMULINK, their impact on the power quality of the energy is insignificant, the effect of the harmonic currents on the grid increase with increasing penetration of wind farm. Finally, it can be said that the performance of the wind farm falls within the limits of international standards but may increase its impact on the voltage profile and energy losses, and power quality with increased penetration of wind energy.

Author details

Saad M. Saad[1]*, Naser El Naily[2], Jamal Wafi[2], Faisal A. Mohamed[3] and Abdelsalam Elhaffar[4]

*Address all correspondence to: smuftahndi@gmail.com

1 College of Electrical and Electronics Technology-Benghazi, Benghazi, Libya

2 Electrical and Electronics Engineering Dept., University of Benghazi, Libya

3 Authority of Natural Science Research and Technology, Tripoli, Libya

4 Electrical and Computer Engineering Dept., Sultan Qaboos University, Muscat, Oman

References

[1] Asheibi A, Khalil A, Rajab Z. The economic feasibility of photovoltaic systems for electricity production in Libya. In: The 7th International Renewable Energy Congress (IREC'2016); Hammamet, Tunisia; 2016. pp. 1-6

[2] Khalil A, Asheibe A. The chances and challenges for renewable energy in Libya. In: The Proceedings of the Renewable Energy Conference; 2015

[3] Libya Infrastructure Report 2013, Business Monitor International Ltd; 2013

[4] Khalil A, Rajab Z, Asheib A. Modeling, Simulation, Analysis and Control of Stand-alone PV System at the Seventh International Renewable Energy Congress“IREC 2016”

[5] Asheibe A, Khalil A. The renewable energy in Libya: Present difficulties and remedies. In: The Proceedings of the World Congress; 2013

[6] Mehimmedtsi, chenni rachid “dynamic response of SCIG with direct gideconnection” 4th International Conference on Power Engineering, Energy and Electrical Drives Istanbul, Turkey; 13-17 May 2013

[7] Mohammed MF, Ghosh S. Study of performance and issues of integration of fixed speed scig wind turbines to power system grid. Master of Engineering. In: Power Systems & Electric Drives July 2012

[8] Rajaba Z, Almaktarb M, Al-Nailyc N, Saad Saadd M, Faisal Mohamede A. Modeling approach to evaluate wind turbine performance: Case study for a single wind turbine of 1.65 MW in Dernah, Libya. In: The 8th International Renewable Energy Congress (IREC'2017); Amman, Jorden; 2017

[9] Javadian SAM, Massaeli M. Impact of distributed generation on distribution systems reliability considering recloser-fuse miscoordination – A practical case study. Indian Journal of Science and Technology. 2011;**4**(10):1279-1284

[10] Elhaffar A, El-Naily N, El-Arroudi K. Management of Distribution System Protection with High Penetration of Distributed Generations, Energy System and Management. Cham: Springer; 2015. pp. 279-291

[11] Singh M, Vishnuvardhan T, Srivani SG. Adaptive protection coordination scheme for power networks under penetration of distributed energy resources. IET Generation Transmission & Distribution. Nov. 2016;**10**(16427494):3919-3929

[12] El Naily N, Saad SM, Hussein T, Mohamed FA. Minimizing the impact of distributed generation of a weak distribution network with an artificial intelligence technique”. Springer. Applied Solar Energy. April 2017;**53**(2):109-122

[13] Saad Saad M, Naser El Naily, Abdelsalam Elhaffar, El-Arroudi K, Faisal Mohamed A, Applying adaptive protection scheme to mitigate the impact of distributed generator on existing distribution network. In: The 8th International Renewable Energy Congress (IREC'2017); Amman, Jorden. 2017

[14] Blaabjerg F, Yang Y, Yang D, Wang X. Distributed power-generation systems and protection. Proceedings of the IEEE. 2017;**105**:1-21

[15] Lei Y, Mullane A, Lightbody G, Yacamini R. Modeling of the wind turbine with a doubly fed induction generator for grid integration. IEEE Transactions on Energy Conversion. March 2006;**21**:257-264

[16] Dhlamini N, Chowdhury SP. The impact of wind farm aggregation techniques for analyzing power system dynamics. In: 2015 National Universities Power Engineering Conference (UPEC); Sept 2015; pp.1-6

[17] Geng Z, Conejo AJ, Kang C, Qixin C. Stochastic scheduling ensuring air quality through wind power and storage coordination. IET Generation Transmission & Distribution. June 2017;**11**(8):2031-2040

[18] Bubshait AS, Mortezaei A, Simões MG, Busarello TDC. Power quality enhancement for a grid connected wind turbine energy system. IEEE Transactions on Industry Applications. 2017;**53**:2495-2505

[19] Farhoodnea M, Mohamed A, Shareef H. A comparative study on the performance of custom power devices for power quality improvement. In: Rid Technologies; 2014; pp. 153-157

[20] Sultana B, Mustafa MW, Sultana U, Bhatti AR. Review on reliability improvement and power loss reduction in distribution system via network reconfiguration. Renewable and Energy Reviews. December 2016;**66**:297-310

[21] Miller ML. General Concepts Related to Turbine Generator Insulation Materials Used in Rotor Winding Cal Insulation Conference; 2009. pp. 328-332

[22] Longji L, Geng H, Yang G, Zhang C, Zheng C, Lai C. Comparisons of four rotor speed identification schemes for PMSG based WECS. In: Proc. of International conference on Electrical Machines and Systems (ICEMS); 2011; pp. 1-6

[23] Pavan Kumar AV, Parimi AM, Rao KU. Investigation of small PMSG based wind turbine for variable wind speed. In: Proc. International Conference on Recent Developments in Con Automation and Power Engineering (RDCAPE); 2015; pp. 107-112

[24] Barote L, Marinescu C. PMSG wind turbine system for residential applications. In: Proc. of International Symposium on Power Electronics Electrical Drives Automation and Motion; 2010; pp.772-777

[25] Chiradeja P, Ramakumar R. An approach to qualify the technical benefits of distributed generation. IEEE Transactions on Energy Conversion. 2004;**19**(4):764-773

[26] Patel A, Arya SR. Distributed power generation system using PMSG with power quality features. In: 2016 International Conference on Next Generation Intelligent Systems (ICNGIS); 1-3 September 2016

[27] NEPLA Analysis Software. Available online: http://wloads/2015/01/Electricity.pdf

[28] Adefarati T, Bansal RC. Integration of renewable distributed generators into the distribution system: A review. IET Renewable Power Generation. 2016;**10**(7):873-884

[29] Yang K, Bollen MHJ, Amaris H, Alvarez C. Decompositions of harmonic propagation in wind power plant. Electric Power Systems Research. 2016;**141**:84-90

[30] Liu Z, Rong J, Zhao G, Luo Y. Harmonic assessment for wind parks based on sensitivity analysis. IEEE Transactions on Sustainable Energy. 2017. DOI: 10.1109/TSTE.2017.2680461 in press

[31] Mazhari SM, Kouhsari SM, Ramirez A. A novel frequency-domain approach for distributed harmonic analysis of multi-area interconnected power systems. Electric Power Systems Research. 2017;**143**:669-681

Designing Mu Robust Controller in Wind Turbine in Cold Weather Conditions

Tahere Pourseif, Majid Taheri Andani,
Hamed Pourgharibshahi, Hassan Zeynali and
Arash Shams

Additional information is available at the end of the chapter

http://dx.doi.org/10.5772/intechopen.74626

Abstract

Due to wind turbine is in class of complex nonlinear system so the precise model of this plant is not accessible, therefore it can be categorized as an uncertain model. So, controlling of this system is a demanding topic. Many of schemes which presented for controlling of wind turbines investigate these systems in a good weather condition. However, many turbines work in severe weather condition. In this study, wind turbine is suggested in cold weather, and in ice on turbine blades which they are considered as uncertainties in the model. A robust controller is designed for the wind turbine, to control the pitch angle.

Keywords: ice formation on wind turbine blades, robust mu control, uncertainty, wind turbine

1. Introduction

The growth of the population in world causes to increase of electrical power consumption. Overpopulation also leads to depletion of fossil fuel energy, degradation of environment. These consequences motivate scholars to seeking better ways to produce electrical power [1, 2]. Therefore, alternative energies where their sources are Renewable can be an effective alternative way to produce electricity that generate from natural processes that can be refilled continually and are unpredictable. Therefore, the control of this kind of energy is challengeable. The renewable energy is practical because of its being low-priced, easily accessible, and purity of the energy. Wind turbine is a tool which is operates on a noncomplex principle that transforms the kinetic energy of wind into electrical energy. Various control methods are presented to regulate the wind turbine speed for effective power generation and to maintain the turbine elements within designed speed and torque bounds [1, 3]. In [4] performance of the turbine for working in various operation is investigated and for operating in the third are a controller is designed. In [5], a well-known robust controller which is named as sliding mode controller is utilized to control power as well as to adjust wind's rotor speed and turbine generator. Due to exist the nonlinear in the characteristics of the controller, just two uncertainties such as spring constant and damping coefficient have been considered and employed to the wind turbine system. The main problem of this scheme is the chattering that produce by Sliding mode controller on control actions in [6], another robust controller is proposed to view all of the uncertainties. These uncertainties comprise the uncertainty is produced from the linearization procedure and minor deviations, and from damping coefficient and spring constant. These approaches are applied to control the pitch angle and enlarge electrical power generation [7]. In many cases, the perfuming of the wind turbine is examined in appropriate weather conditions. But, a robust controller is designed in this paper to keep the performing of the wind turbine in a severe weather conditions, like snow or in a situation that rain droplets freeze on the turbine blades [8]. In these scenarios, when the turbine blades freeze, the mass of the rotor would be changed and the electric power decreases. Then, the controller is given to regulate the speed of the generator after employing the uncertainties in the inertia and other factors [9, 10]. In light of the pitch angle and the speed of the rotor the kind of wind turbine applied in this research has different rotor speed and different pitch angle. The regulation of the changeable pitch angle and the changing rotor speed, respectively, lead to increasing of the electrical power and decreasing of the dynamic load of the turbine. It should be mentioned that that the modification of the variable rotor speed not only minimizes the turbine's dynamic load, but also increases the system's lifespan [11, 12]. The aim of designing the controller is to maximize the electrical power production at low wind speed and to keep it at high wind speed. In comparison with other publications that have done on wind turbine, it is the first time which the uncertainty that arises from icing of wind blade is considered, and for this condition then robust controller is proposed.

2. Wind turbine model

2.1. Wind turbine

Effective wind speed is a nonlinear stochastic process that is approximated by a linear model in order to simplify and satisfy the control objectives [9]. There are two terms in the wind model:

$$V = V_t + V_m \tag{1}$$

In this model the wind has two elements, mean value term (V_m) and turbulent term (V_t).

In which:

$$V_m = \frac{1}{T}\int_{t-\frac{T}{2}}^{t+\frac{T}{2}} v(\tau)\,d\tau \tag{2}$$

$$V_t = \frac{k}{(p_1 s + 1)(p_2 s + 1)} e; e \in N(1, 0) \tag{3}$$

The turbulent term V_t can be modeled by:

$$\begin{pmatrix} \dot{V}_t \\ \ddot{V}_t \end{pmatrix} = \begin{bmatrix} 0 & 1 \\ -\frac{1}{p_1 p_2} & -\frac{p_1 + p_2}{p_1 p_2} \end{bmatrix} \begin{pmatrix} V_t \\ \dot{V}_t \end{pmatrix} + \begin{bmatrix} 0 \\ \frac{k}{p_1 p_2} \end{bmatrix} v \tag{4}$$

where, $v \in N(1, 0)$ and the parameters p_1, p_2 and k depend on the mean value of the wind speed (V_m).

2.2. Nonlinear model of wind turbine system

In this section, for deriving the model, the entire wind turbine is separated into four subsystems: aerodynamics subsystem, mechanical subsystem, generator subsystem and pitch actuator subsystem. The aerodynamic subsystem transforms wind forces into mechanical torque and thrust on the rotor. The mechanical subsystem contains of the drivetrain, tower and blades. The drivetrain converts torque of the rotor to the electrical generator. The tower keeps the nacelle and resists the thrust force and the blades transform wind forces into the aerodynamics torque and thrust. The generator subsystem transforms mechanical energy to electrical energy and finally the blade-pitch and generator-torque actuator subsystems are portion of the control model. To model the overall wind turbine, models of these subsystems are attained and at the end they are linked together. A wind model is attained and increased with the wind turbine model to be considered for wind speed estimation. **Figure 1** shows the basic subsystems and their interactions.

Numerous degrees of freedom can be used to model the plant, but for control design mostly just a less important degrees of freedom are used. In this study we just use two degrees of freedom, namely the rotational degree of freedom (DOF) and drivetrain torsion. The subsystems nonlinear model of wind turbine is used in the following:

2.2.1. Aerodynamics subsystem

The following nonlinear equation is the model of the aerodynamics subsystem [13]:

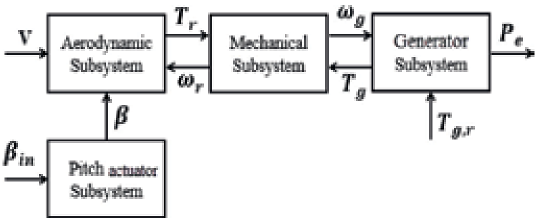

Figure 1. Schematic of the wind turbine.

$$P_r = \frac{1}{2}\rho\pi R^2 V^2 C_p(\lambda, \beta) \tag{5}$$

Where, P_r is the electrical power of rotor, ρ is the density of wind ($\frac{Kg}{m^3}$), R is the radius of the blades (m), V is the wind speed (m/s), λ is the tip speed ratio, β is the pitch angle, C_p the power coefficient, λ is the ratio between the blade tip speed and the wind speed:

$$\lambda = \frac{V}{R\omega_r} \tag{6}$$

where the ω_r is the angular speed of rotor. The derivative of C_p with respect to both λ and β are therefore used extensively in the control designs. In previous work, numerical derivatives of C_p with respect to λ and θ have been successfully obtained and utilize in linear control designs. However, the nonlinear controllers have proven sensitive towards the noise introduced by the numerical derivations, making it difficult to validate the responses obtained by e.g. a feedback linearizing controller. Consequently, it has been Chosen to base the aerodynamic model on an analytic expression of C_p. The relation between C_p, β and λ can be written as [13]:

$$C_p(\lambda, \beta) = 0.22\left(\frac{116}{\lambda_t} - 0.6\beta - 5\right)\exp\left(\frac{12.5}{\lambda_t}\right) \tag{7}$$

where,

$$\frac{1}{\lambda_t} = \frac{1}{\lambda^{-1} + 0.12\beta} - \frac{0.035}{(1.5\beta)^2 + 1} \tag{8}$$

2.2.2. Generator subsystem

The synchronous generator is supposed to be idea, so the power of generator is calculated in [14]:

$$P_e = T_g \omega_g \tag{9}$$

The P_e denoted electrical power of generator, the generator's angular speed is shown by ω_g and the T_g represents generator torque which is controllable, although, it is not practical to change immediately. The response of generator's dynamic is modeled with a first order linear model [6]:

$$\dot{T}_g = -\frac{1}{\tau_T} T_g + \frac{1}{\tau_T} T_{g,r} \tag{10}$$

where $T_{g,r}$ represents the generator torque reference value and the time constant is denoted by τ_T

2.2.3. Pitch actuator subsystem

The blade's pitch begins to change by a hydraulic/mechanical actuator to push the angle of blade β to tracks the reference of blade angle β_{in}, The pitch of the blades is changed by a hydraulic/mechanical actuator Eq. (11) is a first order linear model which is a simplified of the dynamic model [6]:

$$\dot{\beta} = -\frac{1}{\tau_\beta}\beta + \frac{1}{\tau_\beta}\beta_{in} \tag{11}$$

where τ_β is the time constant.

2.2.4. Mechanical Subsystem

Figure 2 shows a schematic of the wind turbine mechanics. The turbine is split into two parts, separated by the transmission: The rotor side and the generator side [15].

J_r denotes the inertia which is on the rotor side and generator side is represented by J_g which is on the leftmost and the rightmost disc respectively. The shaft link the rotor to the transmission is subject to huge torques that leads it to twist, so the shaft is suitably modeled as a damped spring. T_r, which denotes rotor torque, excites the model on the left T_g that represents the generator torque excites the model on the right. The torques and T_{sg} are the torques at each side of the transmission part and has relation by N_g represents the gear ratio which is a relation between T_{sr} and T_{sg} that are named the torque of each side of the transmission part.

$$T_{sg} = \frac{T_{sr}}{N_g} \tag{12}$$

The equations describing the dynamics are obtained using Newton's second law for rotating bodies. This results in two equations: one for the rotor side and one for the generator side.

$$\dot{\omega}_r = T_r - T_{sr} \tag{13}$$

$$\dot{\omega}_g = T_g - T_{sg} \tag{14}$$

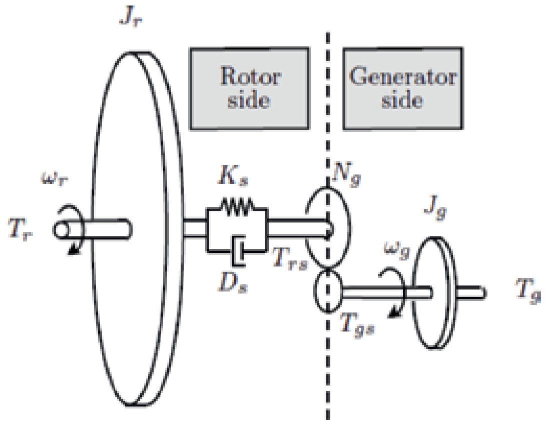

Figure 2. Schematic of the wind turbine mechanics.

Introducing a variable δ [rad] describing the twist of the shaft, leads to the following equation describing the twist of the flexible shaft [16]:

$$T_{sr} = D_r\dot{\delta} + K_r\delta \tag{15}$$

where:

$$\delta = \Omega_r - \frac{\Omega_g}{N_g}, \ \dot{\delta} = \omega_r - \frac{\omega_g}{N_g} \tag{16}$$

In the above equations, D_r represents the damping and K_r denotes spring coefficient, angular speed of rotor is defined by ω_r, the angular speed of generator represent by ω_g, Ω_r and Ω_g are used to define the default shaft angle at the rotor and the default shaft angle at the generator, respectively.

2.3. Linearized models of wind turbine system

As it was discussed in previous section, for design a controller a linear model of the system is needed. The input of this model is wind [17]:

$$input = \begin{bmatrix} V & \beta_{in} & T_{g,r} \end{bmatrix}^T \tag{17}$$

And outputs of the system include:

$$output = \begin{bmatrix} \omega_r & \omega_g & P_e \end{bmatrix} \tag{18}$$

Having all the equations, system equations become: [8]:

$$\dot{\omega}_r = \frac{a - D_r}{J_r}\omega_r - \frac{a - D_r}{J_r N_g}\omega_g - \frac{K_r}{J_r}\delta + a_{14}\beta \tag{19}$$

$$\dot{\omega}_g = \frac{D_r}{N_g J_g}\omega_r - \frac{D_r}{{N_g}^2 J_g}\omega_g + \frac{K_r}{J_g N_g}\delta - \frac{1}{J_g}T_g \tag{20}$$

$$\dot{\delta} = \omega_r - \frac{\omega_g}{N_g} \tag{21}$$

$$\dot{\beta} = -\frac{1}{\tau_\beta}\beta + \frac{1}{\tau_\beta}\beta_{in} \tag{22}$$

$$\dot{T}_g = -\frac{1}{\tau_T}T_g + \frac{1}{\tau_T}T_{g,r} \tag{23}$$

$$\dot{V}_t = V_t \tag{24}$$

$$\ddot{V}_t = -\frac{1}{p_1 p_2}V_t - \frac{p_1 + p_2}{p_1 p_2}\dot{V}_t + \frac{k}{p_1 p_2}v \tag{25}$$

In which J_r and J_g are rotor and generator moments of inertia, τ_β and τ_T are time constants of the first order actuator models

3. Uncertainties model

Various uncertainties have been examined in the current literature. These uncertainties derive from approximated and process parameters in a nonlinear system which changes as the operating point changes, a matter causing the electrical power production to reduce. There are always discrepancies between real system and mathematical models, which lead to uncertain models. In this work, sources of uncertainties are taken to be:

- Uncertainty in the drivetrain stiffness and damping parameters.
- Uncertainty in the linearized model.

Although, all control design presented design for moderate temperature. Decreasing the temperature in winter has devastating properties on the wind turbine. Ice on the elements of wind turbine leads some serious problems. Even a few amount of ice on the blades worsens the aerodynamic performance of the wind turbine. It not only decreases the output power energy, but also raises the abrasion between the elements [11, 16]. In other word, the ice in cold places and the high density of air at cold climate have damaging properties on aerodynamics. Fluctuation of produced power and load are reason for such dysfunctionality. Masses of the ice on the turbine cause fluctuation on the frequency of the turbine's elements and also the behavior of the system's dynamic [10–12]. In addition, this condition has effect on control plant. In other word, the performance of the turbine system worsens through wrong data sending [11]. Previous article dealing with this issue have presented approaches like observation, the use of sensors and monitors, considering aerodynamic sound, etc., to recognize ice. The control schemes are then designed to eliminate the ice [9, 10, 17].

3.1. The impact of cold weather on the operation of wind turbine

In this research, for the first time a new approach is advanced to enhance the wind turbine performance in cold climate conditions and to stop the damage which cause about the shutdown of the turbine. Because of the structure of the wind turbine, when frozen blades' masses changes, the rotor mass will be changed and lead to the inertia of rotor. These variations will effect on equations of the wind turbine and optimal power creation. Therefore, control of turbine and optimal power output could be possible by considering the inertia of the rotor as a new component of uncertainty in the plant. The value of this uncertainty differs with decreasing the temperature and the turbine's production capacity. In [18], imbalance of the blade was simulated by scaling the density of mass of one blade, which generates an imbalance distribution of mass with respect to the rotor. Furthermore, the aerodynamic asymmetry was simulated by adjusting the pitch of one blade, which produces an imbalance torque across the rotor. In our work, the blade imbalance in blade is due to icing on the blade. Thus, the uneven of the blade is considered about 20% as uncertainty. A robust control is designed to control the turbine in the existence of uncertainty because of the blade imbalance icing [19]. The uncertainties in the wind turbine comprise the linearized model parameters which is extracted from the nonlinear plant, spring constant, and damping coefficient that alteration as the working point diverges; another uncertainty which is added to the system because of the presence of noise and disturbance in the input signal. All of these uncertainties are considered in appropriate weather conditions. In this work, cold climate condition and inertia of rotor are considered as other sources of uncertainty in the wind turbine system [20, 21].

3.2. Frequency response of wind turbine

These icy turbine blades change the rotor mass. Under the frequency response analysis of the system is shown in **Figure 3**, the rotor inertia uncertainty can be considered between the range of 0 and 20% and The Wind turbine system is stability:

According to, the red color is nominal frequency response and blue color is system uncertainties that uncertainty is considered between the range of 0–20%. The system has positive phase margin and positive gain margin, so it is stable.

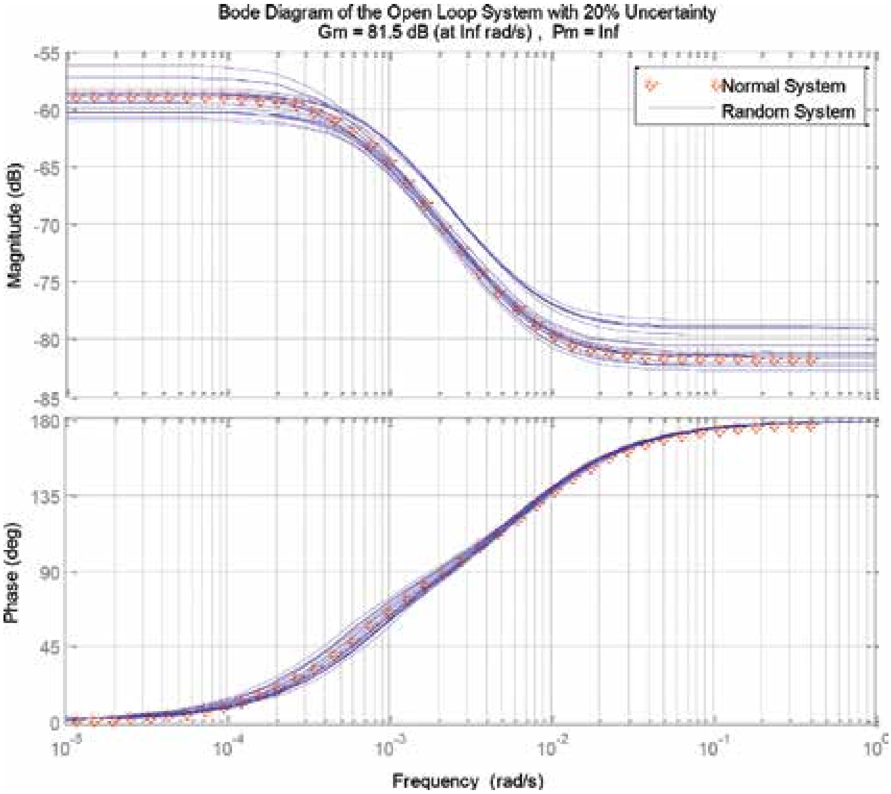

Figure 3. Bode diagram open loop system with 20% uncertainty of inertia rotor.

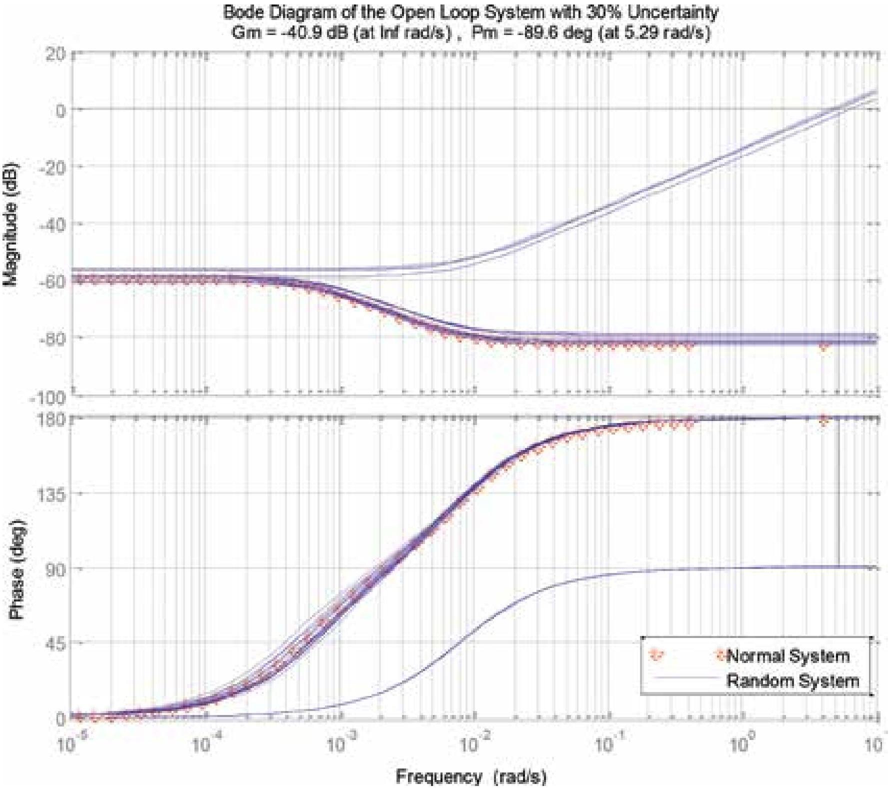

Figure 4. Bode diagram open loop system with 30% uncertainty of inertia rotor.

Figure 4 shows that the system is unstable by considering range of uncertainty between 20 and 30%. So system uncertainties are defined between 0 and 20%.

The uncertainties in parameters can be shown as follows:

$$K_r = \overline{K}_r\left(1 + p_{K_r}\delta_{K_r}\right) \tag{26}$$

$$D_r = \overline{D}_r\left(1 + p_{D_r}\delta_{D_r}\right) \tag{27}$$

$$a = \overline{a}\left(1 + p_a\delta_a\right) \tag{28}$$

$$a_{14} = \overline{a}_{14}\left(1 + p_{a_{14}}\delta_{a_{14}}\right) \tag{29}$$

$$J_r = \overline{J}_r\left(1 + p_{J_r}\delta_{J_r}\right) \tag{30}$$

Two reasons exist which explain that spring coefficient and the damping can be considered as uncertainties. One reason is, there exist divergence in the spring variables from fabrication to fabrication, and manufacturer to manufacturer and other reason, it should be consider that the

Parameter	Description	Unit	Tolerance
K_r	spring coefficient	Nm/rad	±10%
D_r	Damping	$\left(\frac{kg.m^2}{rad.s}\right)$	±10%
A	Linearization parameter	—	±20%
a_{14}	Linearization parameter	—	±20%
J_r	rotor inertia	$kg.m^2$	+20%

Table 1. Parameter uncertainties of the wind turbine.

spring parameter and damping can be changed during a long time because of continuous working, and aging. In previous equations, $\overline{K}_r$, $\overline{D}_r$, $\overline{a}$, $\overline{a}_{14}$ are nominal parameter values, resulting from the spring constant, damping coefficient, linearization process and rotor inertia, respectively. p_{K_r}, p_{D_r}, p_{a}, $p_{a_{14}}$ indicate maximum relative uncertainties that are for uncertainty parameters shown in **Table 1**.

δ_{K_r}, δ_{D_r}, δ_{a}, $\delta_{a_{14}}$ and δ_{J_r} are relative changes in these parameters. Therefore:

$$|\delta_{K_r}| \leq 1, |\delta_{D_r}| \leq 1, |\delta_a| \leq 1, |\delta_{a_{14}}| \leq 1, \left|\delta_{J_r}\right| \leq 1 \tag{31}$$

4. Robust design controller

4.1. Closed loop system design specifications

Figure 5 shows the block diagram of Wind turbine closed loop system, including the feedback structure, the controller, as well as the model uncertainties and performance objectives weights.

In **Figure 5**, (r) shows the reference input, (V) represents the wind speed which has disturbance, (n) denotes noise and e_u and e_y are considered as two output costs. The system (R)

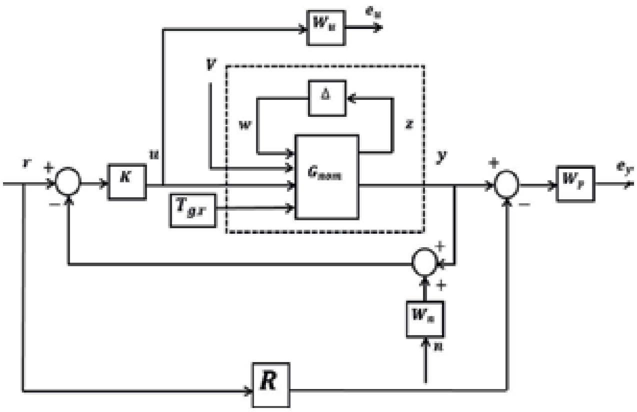

Figure 5. Block diagram of the closed-loop system with performance specifications [22].

represents the performance when model is ideal, to which the designed closed-loop system wants to reach [23]. The transfer function of model is chosen in a way that the time response of the reference signal has an overshoot less than around 5%. Inside the dots rectangle is the ideal model, which shows with, G_{nom} of the wind turbine model and the block $\mathit{\Delta}$ that parameterizes uncertainties in the model. To find the wanted performance, inputs r can be obtained from the transfer function matrix, and we need to find disturbance in V and also n to outputs e_u and e_y. Thus the infinity norm of that transfers function can be minor for the entire existing uncertainty variable. The position noise signal is attained by moving the unit-bounded signal which is shows by n through the weighting transfer matrix which denotes W_n. The transfer matrices W_p and W_u represent the relative significance of the diverse frequency spans for which the performance is needed. So, the performance aim can be reorganize, with probable slight conservativeness, like that transfer function matrix infinity norm be less than 1. So Δ matrix is given in following form:

$$\Delta = \mathrm{diag}\left(p_{K_r}, p_{D_r}, p_a, p_{a_{14}}, p_{J_r}\right) \tag{32}$$

This transfer function can be written as [21]:

$$\begin{bmatrix} e_u \\ e_y \end{bmatrix} = \begin{bmatrix} W_p(\mathrm{S}_o\mathrm{G}_u\mathrm{K} - \mathrm{R}) & W_p\mathrm{S}_o\mathrm{G}_v & -W_p\mathrm{S}_o\mathrm{G}_u K W_n \\ W_u\mathrm{S}_i K & -W_u K\mathrm{S}_o\mathrm{G}_v & -W_u K\mathrm{S}_o W_n \end{bmatrix} \begin{bmatrix} r \\ V \\ n \end{bmatrix} \tag{33}$$

where $S_i = (I + KG)^{-1}$ and $S_o = (I + GK)^{-1}$ are the input and output sensitivities, repectively. Note that S_oG is the transfer function between V and y.

4.1.1. Robust stability

By definition, the closed loop system achieves robust stability if the closed loop system is internally stable for each possible plant dynamics $G = F_u(G_{nom}, \mathit{\Delta})$.

4.1.2. Robust performance

The closed loop system must remain internally stable for each $G = F_u(G_{nom}, \mathit{\Delta})$ and in addition the performance criterion should be satisfied for each $G = F_u(G_{nom}, \mathit{\Delta})$ [21].

4.2. Matching transfer function and weighting transfer functions

In the case of mu controller optimization design, we have to define the model transfer function which is denote with R and the weighting transfer functions that are nominated with W_n, W_p and W_u.

The model transfer function is selected therefore the time response to the reference signal has an overshoot fewer than 50% and a settling time not more than 1 ms. A probable plant which please the requirements is:

$$R(s) = \frac{1}{0.48s^2 + 0.95s + 1} \tag{34}$$

In **Figure 6**, the response of matching model to power electrical input is shown.

The noise shaping function W_n is determined on the basis of the spectral density of the position noise signal. In the given case it is taken as the high-pass filter. In this case output has a noteworthy spectral content more than 500 Hz. For this type of filter, the position noise signal is just 0.95 V in the low-frequency values but it is 1 V in the high-frequency values that matches to a position error of around 5% without width.

$$W_n(s) = 95 \times 10^{-5} \frac{0.1s + 1}{0.001s + 1} \tag{35}$$

So the frequency response is shown in **Figure 7**.

The closed-loop system performance specifications are reflected by the weighting performance function W_p.

$$W_p(s) = 0.95 \frac{2s + 50}{2s + 0.005} \tag{36}$$

Figure 8 shows the frequency response of the inverses of this weighting function.

It is shown that in a selection, the objective is to obtain a minor variance between the system and outputs of the model, and a minor effect of the disturbance on outputs of the system. This will ensure nice tracking of the reference input and minor error because of the low-frequency

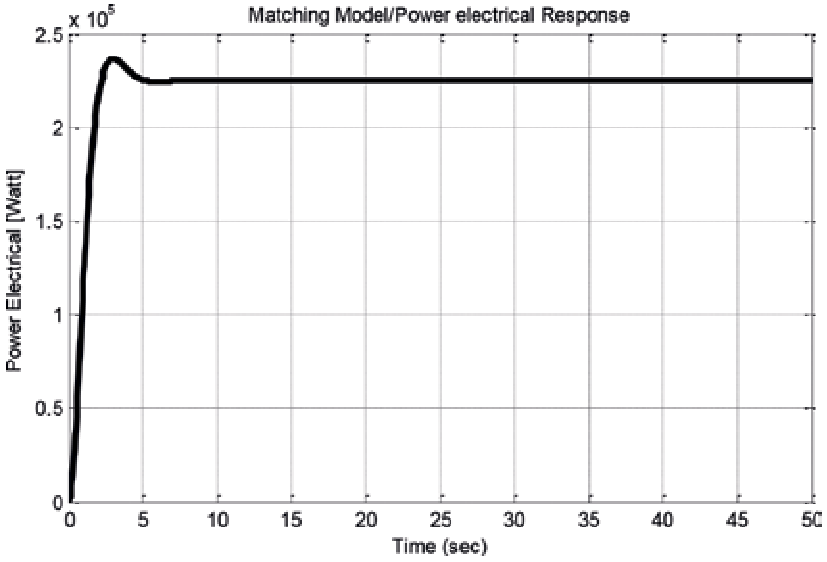

Figure 6. Response of matching model to electrical power input.

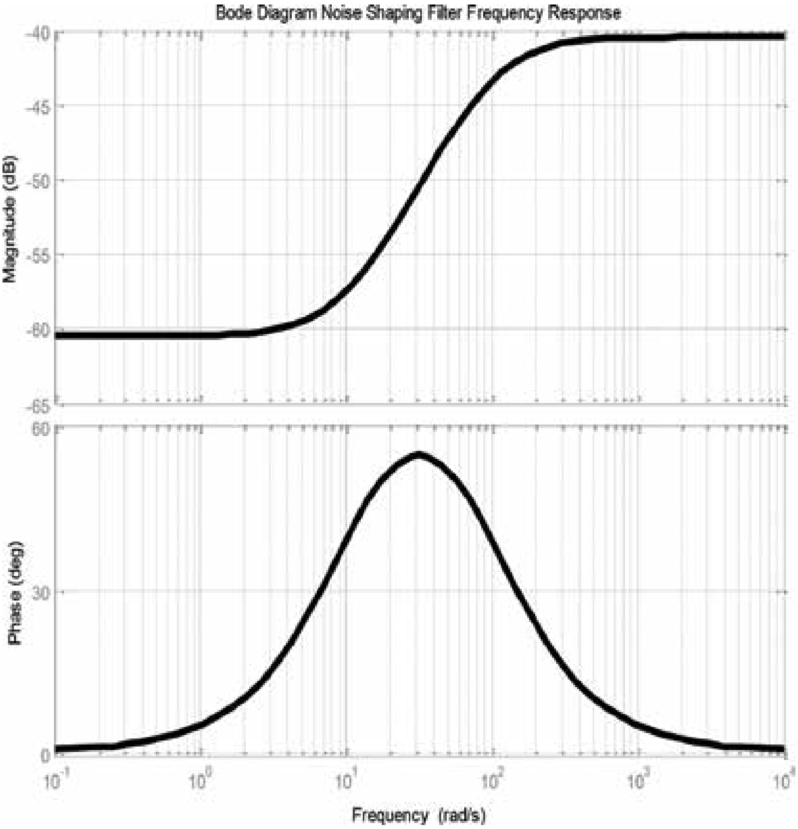

Figure 7. Frequency response of noise filter W_n.

disturbances. The weight of control function is usually selected as high-pass filters to make sure that the control action will not surpass 25°.

$$W_u(s) = 0.022\frac{0.8s^2 + 10s + 2}{3.5 \times 10^{-4}s^2 + 20 \times 10^{-2}s + 2} \tag{37}$$

Figure 9 shows the frequency response of this weighting function W_u.

According to the above figure, effort control is very low in low- frequencies that cause reduced the control cost.

4.3. Robust μ controller design

The objective of controller with applying the μ synthesis scheme is the stabilizing of the closed loop of the plant and pleasing all of the control demands. In the existence of measurement noise, disturbance in the wind, and uncertainties, the closed-loop plant should have the robust efficiency. Therefore, the purpose of μ controller scheme is design a controller where the wind

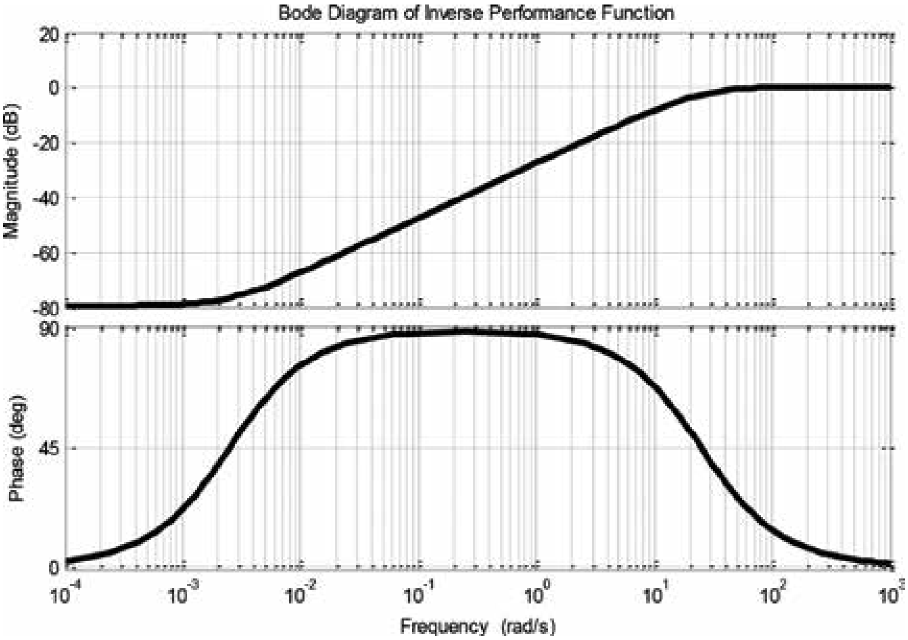

Figure 8. Frequency response of weighting function $\frac{1}{W_P}$.

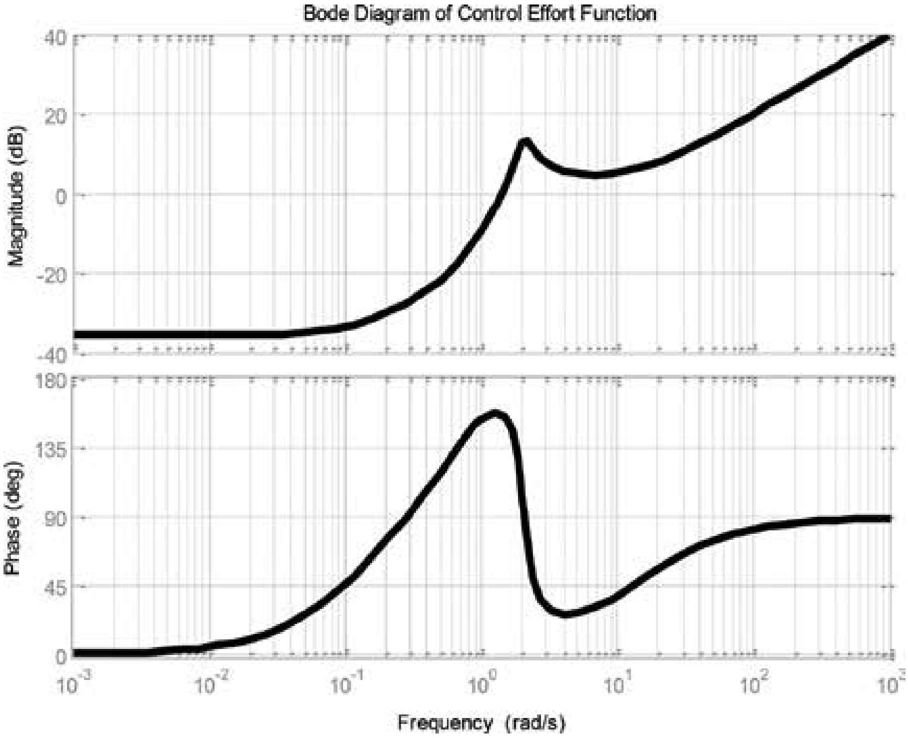

Figure 9. Frequency response of weighting function W_u.

turbine can track the reference input of generated electrical energy when noise and disturbance are exist. In **Figure 10**, the schematic of the closed loop model which is utilized with the defined uncertainties is depicted for μ controller model design.

From the figure, it can be seen that y_c is defined as the difference between noisy output and the reference and the transfer function P(s) shows the open-loop transfer function matrix with 10 inputs and eight outputs. The upper linear fractional transformation (LFT) of the closed loop system is:

$$P = F_u(P_{nom}, \Delta_r) \tag{38}$$

where P_{nom} is the nominal transfer function matrix, Δ_r includes five uncertainties in the wind turbine model. We assume Δ_P is defined the structure of uncertainties block as follows:

$$\Delta_p = \left\{ \begin{bmatrix} \Delta_r & 0 \\ 0 & \Delta_f \end{bmatrix}; \Delta_r \in \mathfrak{R}^{5\times5}, \Delta_f \in C^{4\times2} \right\} \tag{39}$$

Controller, which is attained with this scheme, is typically of high order controller that cause to challenges in a real-world implementation. So for this purpose, it is recommended to decrease the order of the control plant until it is feasible to simplify the closed loop scheme theory and operation. The results of the singular parameter of planned after repeating five iterations of D-K procedure are demonstrated in **Table 2**.

It can be seen that the maximum value of μ is 11.648 that is achieved in the first iteration. Similar to this method, next steps are done to finally value of γ is less than 1. The designed μ controller synthesis is of order 17, and it is achieved after five iterations. In the final iteration, the value of γ is reached to 0.732 and, μ reaches to 0.730 that is less than 1. In other word, the closed-loop scheme has robust performance due to the structured singular parameter is less

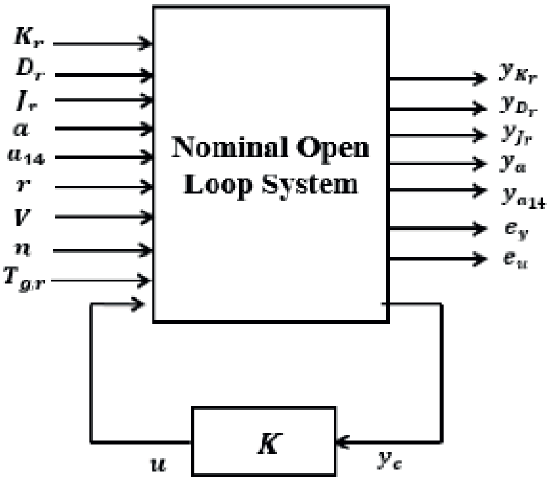

Figure 10. Closed loop system model for design μ robust controller.

Iteration number	γ value achieved	Maximum μ value	Controller order
1	1201.403	11.648	5
2	5.35	3.837	11
3	1.763	0.748	16
4	0.734	0.733	17
5	0.732	0.730	17

Table 2. Obtained results of the robust controller (μ).

than 1 in any frequency. Also, the gamma parameter denotes the value that the function $F_l(P,K)$ infinity norm is fewer than that value.

5. Simulation results of the designed robust controller

The considered wind model in this paper is as follows.

Figure 11 depicts the speed of the wind in the third operating area that is a value between 15 and 25 m/s. In this study, the model of the wind has randomly varies from 15 to 24 m/s In our research, the speed of the wind is considered be highly changeable during the times [8, 9]. As in early times the speed of wind turbine is growing, then its parameter is constant in time and its value fell in the end of the period of the time. The reason for selecting this kind of plant of the random wind is, presentation the robust controller has a good performance in various

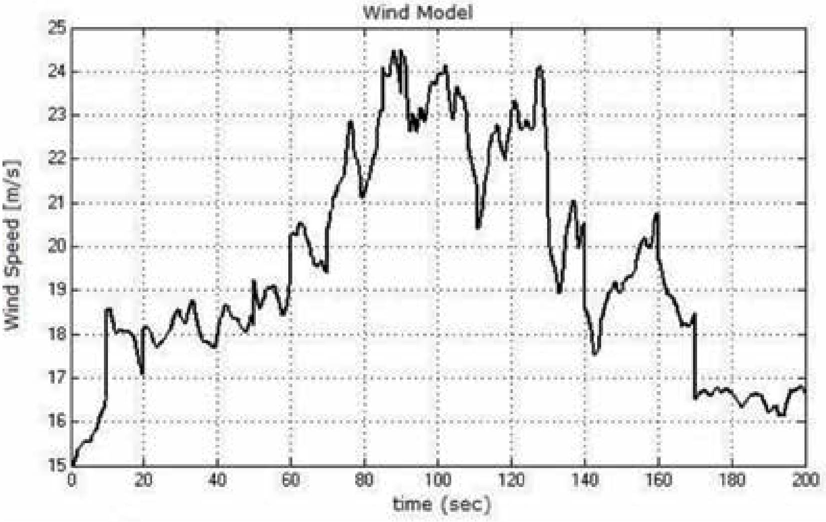

Figure 11. Wind model in different speeds.

speeds. This express that a sudden variation in the wind speed, the robust controller attempts to control the pitch angle for setting the electrical power at it's at most efficiency in the third performance area.

Due to the linear dependency among the speed of the rotor and the speed of generator over the gear ratio, the results of applying the control scheme which seeks to maintain the electrical power fixed and regulate speed of the generator- can be examined after modeling of speed of the wind turbine and modeling the robust μ controller.

Considering **Figure 12(a)**, the deflection of output about the nominal value which is changed by noise and disturbance in wind is not high that is acceptable. Maximum variation around the reference value is 2.1% and it is equal to 0.027 kW that expresses nice disturbance cancelation in areas in the matching scheme. In **Figure 12(b)**, at most variations around nominal values are equivalent to 3.068 rad/s and it is equal to 9.2%. It is sates a disturbance cancelation and nice following of generator reference parameter in the existence of disturbance with wind speed in the good way and with the least variations.

In **Figure 13**, it can be found that the control effort or the adjustment of pitch angle is between of 14 and 22.5°. Due to changed areas of wind turbine efficiency, aim in this work is, regulating the power and speed of the generator at the nominal parameter in the third performance part. So, in this scenario by growing the value of wind to cut-out, the pitch angle has been improved, and this scenario leads to the decrease of power coefficient and the power is at its nominal value [4]. Furthermore, by reducing the speed of the wind, the blade pitch angle is decreased and at this step, to regulate the power and generator speed at nominal value, robust controller is designed. This controller attempts to control the pitch angle for accessing the high electric power and adjust the speed of generator about its nominal value. So, by applying this kind of controller, the control effort remains fewer than 25°, that is the utmost pitch angle of the wind turbine, stays bounded in the third area.

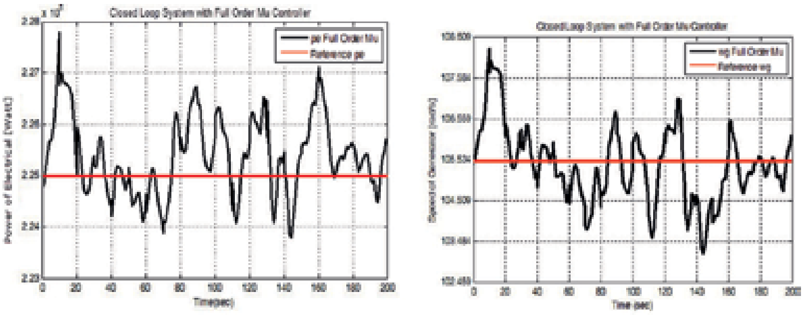

(a)

(b)

Figure 12. (a) The response of electric power produced by wind turbines to track input reference electrical power using μ controller. (b) The response of speed of the wind turbine generator to track input reference speed of generator using μ controller.

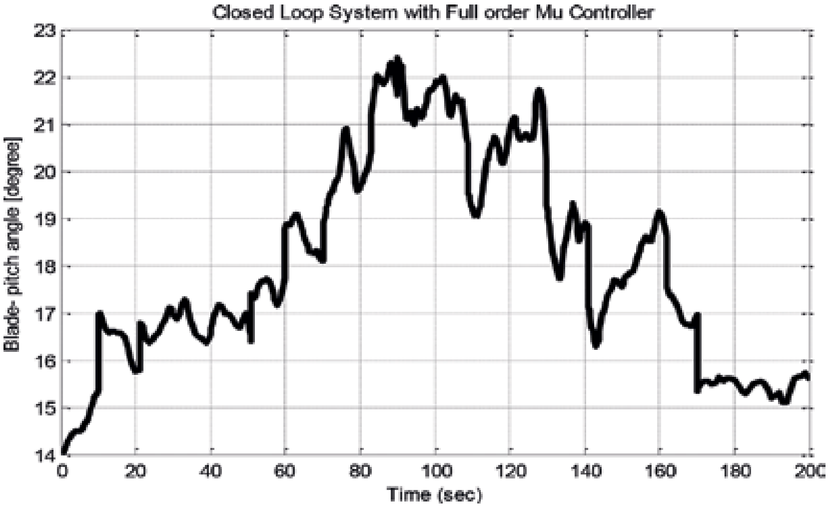

Figure 13. Pitch angle adjustment using the μ controller.

5. Conclusion

This work wanted to control the pitch angle of the wind turbine to regulate the speed of the wind turbine generator in the third area of procedure. In the third area, the generator speed, and electrical power are fix in their nominal parameter, and do constant. The existence of noise and disturbance in the model of wind are the main reason for high error rate in the generation of electrical power and generators' speed. Therefore, this paper suggested that the generation of electrical power and adjustment of the generator speed are practical if robust controller is employed and current errors (uncertainties) in the wind turbine system are taken into account. In most previous works have done, spring constant, damping coefficient and insignificant deviations of the linearization process are listed as uncertainties. These uncertainties are deemed to be true in appropriate weather conditions. Although, cold climate leads the turbine blades to freeze that is followed by mass growth. This mass development results in the decrease of electrical power generation, incorrect model operation and wrong data sending. So, new uncertainties were employed to the system in order to work out the mentioned challenges. After employing these uncertainties, μ controller is presented. Minimal variation about the reference parameter and fewer control action for variation the blades' angle (to obtain optimal power and adjust the speed of the generator) needs the use of μ controller. To be more accurate, the μ controller is more justifiable system in terms of disturbance cancelation.

A. Appendix

The wind turbine that is considered in this paper has the following specifications:

Characteristic of Vestas V29 Wind turbine

Vestas V29 wind turbine characteristic	**Value**
Electrical power of generator	225 KW
Rotor diameter	29 m
Rotor RPM	41/30.8 RPM
Angular speed of rotor	4.29 rad/s
Angular speed of generator	105.6 rad/s
Frequency	50–60 Hz

Author details

Tahere Pourseif[1]*, Majid Taheri Andani[2], Hamed Pourgharibshahi[3], Hassan Zeynali[1] and Arash Shams[1]

*Address all correspondence to: t.pourseif@gmail.com

1 Department of Electrical Engineering, Shahid Beheshti University, Tehran, Iran

2 Department of Electrical Engineering, Tehran University, Tehran, Iran

3 Advanced Technology University, Kerman, Iran

References

[1] Hau E. Wind Turbines: Fundamental, Technologies, Application, Economics Handbook. 3rd ed; 2013

[2] Blaabjerg F, Ma Ke. Future on power electronics for wind turbine systems. IEEE Journal of Emerging and Selected Topics in Power Electronics. 2013;**1**:139-152

[3] Kaldellis J, Zafirakis D. The wind energy revolution: A short review of a long history. Renewable Energy. 2011;**36**:1887-1901

[4] Bazilevs Y, Korobenko A, Deng X, Yan J. Novel structural modeling and mesh moving techniques for advanced fluid–structure interaction simulation of wind turbines. International Journal of Numerical Methods in Engineering. 2015;**102**:766-783

[5] Evangelista C, Valenciaga F, Puleston P. Active and reactive power control for wind turbine based on a MIMI 2-sliding mode algorithm with variable gains. IEEE Transactions on Energy Conversion. 2013;**28**:682-689

[6] Mirzaei M, Henrik H, Niemannand Kjolstad N. A μ ıt-synthesis approach to robust control of a wind turbine. In: Proceedings of 50th IEEE Conference on Decision and Control and European Control Conference, Orlando; 2011. pp. 645-650

[7] Mirzaei M, Henrik H, Niemannand Kjolstad N. DK-iteration robust control design of a wind turbine. In: IEEE International Conference on Control Applications Part of 2011 IEEE Multi-Conference on Systems and Control, Denver; 2011. pp. 1493-1498

[8] Etemaddar M, Hansen MOL, Moan T. Wind turbine aerodynamic response under atmospheric icing conditions. Journal of Wind Energy. 2014;**17**:241-265

[9] Shajiee S, Pao LY, Wagner PN, Moore ED, Mcleod RR. Direct ice sensing and localized closed-loop heating for active de-icing of wind turbine bladed. In: Proceedings of American Control Conference Washington; 2013. pp. 634-639

[10] Sunden B, Wu Z. On icing and icing mitigation of wind turbine blades in cold climate. Journal of Energy Resources Technology. 2015;**137**:1-10

[11] Jafarnejadsani H, Pieper J. Gain- Scheduled l_1-optimal control of variable-speed-variable-pitch wind turbines. IEEE Transactions on Control Systems Technology. 2015;**23**:372-379

[12] Iyasere E, Salah M, Dawson D, Wagner J, Tatlicioglu E. Optimum seeking-based nonlinear controller to maximise energy capture in a variable speed wind turbine. IET Control Theory and Applications. 2012;**6**:526-532

[13] Thomsen SC. Nonlinear control of wind turbine [Master thesis]; 2007

[14] Tang X, Deng W, Qi Z. Investigation of the dynamic stability of microgrid. IEEE Transactions on Power Systems. 2014;**29**:698-706

[15] Girsang IP, Dhupia JS, Muljadi E, Singh M, Pao LY. Gearbox and drivetrain models to study dynamic effects of modern wind turbines. IEEE Transactions on Industry Applications. 2014;**50**:3777-3786

[16] Shahriar MR, Borghesani P, Tan ACC. Speed-based diagnostics of aerodynamic and mass imbalance in large wind turbines. In: Proceedings of IEEE International Conference on Advanced Intelligent Mechtronics; 2015. pp. 796-801

[17] Habibi H, Cheng L, Zhang H, Kappatos V, Selcuk C, Gan T-H. A dual de-icing system for wind turbine blades combining high-power ultrasonic guided waves and low-frequency forced vibrations. Renewable Energy. 2015;**83**:859-870

[18] Gong X, Qiao W. Simulation ınvestigation of wind turbine ımbalance fault. In: Internation Conference on Power System Technology; 2010

[19] pourseif T, Afzalian A. Pitch angle control of wind turbine systems in cold weather conditions using mu robust controller. International Journal of Energy and Environmental Engineering, USA. March 2017;**8**(3):197-207

[20] Xiu-Xing Y, Yong-gang L, Wei L, Ya-jing G, Xiao-Jun W, Peng-fei L. Design, modeling and implementation of a novel pitch angle control system for wind turbine. Renewable Energy. 2015;**81**:599-608

[21] Lamraoui F, Fortin G, Benoit R, Perron J, Masson CH. Atmospheric icing impact on wind turbine production. International Journal of Cold Regions Science and Technology. 2014; **100**:36-49

[22] Pourseif T, Afzalian A. Design mu controller on wind turbine in cold weather conditions. In: The 4th International Conference on Control, Instrumentation and Automation (ICCIA), Qazvin, Iran; January 2016

[23] Skogestad S, Postlethwaite I. Multivariable Feedback Control Analysis and Design. John Wiley; 2013

Chapter 5

Dual Robust Control of Grid-Connected DFIGs-Based Wind-Turbine-Systems under Unbalanced Grid Voltage Conditions

Kamel Djamel Eddine Kerrouche, Lina Wang,
Alex Van Den Bossche, Azzedine Draou,
Abdelkader Mezouar and Larbi Boumediene

Additional information is available at the end of the chapter

http://dx.doi.org/10.5772/intechopen.75518

Abstract

In this chapter, a comparative analysis is made for doubly-fed induction-generator (DFIG) low-voltage ride-through (LVRT) solutions. It is supposed to improve the LVRT capability of DFIG under unbalanced grid voltage conditions by hardware or software solutions. Therefore, this chapter proposes a low-cost software LVRT solution based on an efficient control scheme of DFIG driven by a wind turbine. The proposed control scheme is based on dual-sequence decomposition technique and Lyapunov-based robust control (RC) theory. Under an unbalanced grid voltage conditions, the proposed control strategy not only eliminates effectively the oscillations of the active and reactive powers exchanged between the generator and the grid but also achieves the symmetrical and sinusoidal grid currents injection. Simulation analysis under MATLAB®/ Simulink® has been carried out on a 1.5 MW DFIG-based wind-turbine-systems, and the results are presented and discussed to demonstrate the feasibility and the efficiency of the control strategy for a grid-connected application under unbalanced voltage supply. The proposed dual control scheme is shown to be able to successfully mitigate torque, stator power and currents pulsations as compared with the conventional vector control based on the single control scheme.

Keywords: DFIG, LVRT, unbalanced grid voltage, robust control

IntechOpen

1. Introduction

Variable wind turbines are known to be able to efficiently capture energy from a wide range of wind speed. Most of the variable speed wind turbines employ doubly-fed induction-generator (DFIG) due to their various advantages such as the decoupled control of the active and reactive powers, lower converter size and cost, and the feasibility of both stand-alone and grid connected operation [1, 2]. It consists of a wind turbine, gearbox, DFIG, Rotor Side Converter (RSC), Grid Side Converter (GSC) and electrical grid. In grid integration systems of DFIGs, several research studies assumed a balanced grid voltage with conventional control strategies [3]. However, in recent years, the control and operation of DFIG under disturbances and grid unbalanced have been widely studied [4]. The transient and steady-state responses of these generators during unbalanced grid voltage conditions have been presented in [5]. It has been specified from [6] that if the unbalanced grid voltage is not included in the synthesis of DFIG's controllers, high oscillations will occur in the generator torque and the injected powers might be very harmful to wind turbine components and grid connection stability. Moreover, unbalanced stator and rotor currents and DC-link voltage oscillations may lead to the increase in generator losses, temperature increase and reduction of the lifetime of DC-link capacitor [7]. Under unbalanced grid voltage, direct power control (DPC) has been adopted to control the grid-connected wind turbine-driven DFIGs in [5] by using proportional-resonant (PR) controller [7] and sliding mode control (SMC) approach [8, 9]. Moreover, in [10, 11], conventional vector control (VC). Moreover, conventional vector control (VC) with an auxiliary PI current controller has also been adopted to help regulating the negative sequence current components. Otherwise, if no negative grid voltage sequence is considered in the control loop, the occurrence of unbalanced faults can deteriorate the performance of DFIGs. Nevertheless, the control loops considered in [7, 8] keep both active and reactive power constant with reduced power ripples and at the same time significant odd order current harmonics are generated, which is not allowed by the IEEE 519-1992 [12, 13]. Therefore, an additional cost is required by active filtering [3] may not be a practicable solution for grid-connected WECS. In [14], it has been shown that during balanced or symmetrical three-phase fault, an additional STATCOM system is reported as a promising device for applications of WECS based grid-connected.

In this chapter, a review of the recently published LVRT schemes is discussed. Then, a VC approach-based dual-sequence decomposition approach associated to the Lyapunov based robust control (RC) is proposed; in order to reduce the torque ripples, minimize the active and reactive powers pulsations by obtaining sinusoidal and symmetrical injected grid currents, when the voltage at the stator is unbalanced. The details of DFIG modeling, positive and negative components separation methods and RC technique are theoretically explained in this chapter. Moreover, comprehensive simulation tests and results of the WECS are carried out and included in this chapter.

2. Wind energy generator system

In recent years, several configurations are used for the dynamic model of DFIG systems, which can be shown in various reference frames such as stationary reference frame [9] or rotating reference frame [6, 11]. In this chapter, DFIG is modeled in a rotating reference frame under balanced and unbalanced operation conditions.

2.1. Balanced DFIG model

Using the assumption of linear magnetic circuits, the stator and rotor voltages expressions of the DFIG under balanced operating condition are written as follows [2, 15]:

$$V_s = \begin{pmatrix} v_{ds} \\ v_{qs} \end{pmatrix} = \begin{pmatrix} R_s\, i_{ds} + \dfrac{d\phi_{ds}}{dt} - \omega_s\, \phi_{qs} \\ R_s\, i_{qs} + \dfrac{d\phi_{qs}}{dt} + \omega_s\, \phi_{ds} \end{pmatrix}, V_r = \begin{pmatrix} v_{dr} \\ v_{qr} \end{pmatrix} = \begin{pmatrix} R_r\, i_{dr} + \dfrac{d\phi_{dr}}{dt} - (\omega_s - \omega)\, \phi_{qr} \\ R_r\, i_{qr} + \dfrac{d\phi_{qr}}{dt} + (\omega_s - \omega)\, \phi_{dr} \end{pmatrix} \tag{1}$$

where i_{ds}, i_{qs}, i_{dr} and i_{qr} are, respectively, the direct and quadrature stator and rotor currents. R_s and R_r are stator and rotor resistances. ω_s, ω are stator and rotor electrical angular speed, with $\omega = p \cdot \Omega_g$, p is the pair pole number. The stator and rotor fluxes can be expressed as:

$$\phi_s = \begin{pmatrix} \phi_{ds} \\ \phi_{qs} \end{pmatrix} = \begin{pmatrix} L_s\, i_{ds} + M\, i_{dr} \\ L_s\, i_{qs} + M\, i_{qr} \end{pmatrix}, \phi_r = \begin{pmatrix} \phi_{dr} \\ \phi_{qr} \end{pmatrix} = \begin{pmatrix} L_r\, i_{dr} + M\, i_{ds} \\ L_r\, i_{qr} + M\, i_{qs} \end{pmatrix} \tag{2}$$

where L_s, L_r and M are stator, rotor and mutual inductances. The active and reactive powers at the stator are defined as:

$$\begin{cases} P_s = v_{ds}\, i_{ds} + v_{qs}\, i_{qs} \\ Q_s = v_{qs}\, i_{ds} - v_{ds}\, i_{qs} \end{cases} \tag{3}$$

The principle of the conventional VC method consists of orientating the stator flux in such a way that the stator flux vector points into the d-axis direction. This approach is realized by setting the quadrature component of the stator flux to the null value:

$$\phi_s = \phi_{ds} \Rightarrow \phi_{qs} = 0 \tag{4}$$

Using the condition that the per phase stator resistance is neglected, and that the grid system is in steady state that is having a single voltage V_s that leads to stator's constant flux ϕ_s, the voltages can be easily deduced to be as:

$$\begin{cases} v_{ds} = 0 \\ v_{qs} = \omega_s \phi_s = V_s \end{cases} \tag{5}$$

The following equations are obtained when replacing the rotor flux Eq. (2) in Eq. (1) and using the above condition Eq. (5), the rotor voltages become:

$$\begin{cases} v_{dr} = \sigma L_r \dfrac{di_{dr}}{dt} + R_r i_{dr} - \sigma L_r \omega_r i_{qr} + \dfrac{M}{L_s}\dfrac{d\phi_{ds}}{dt} \\ v_{qr} = \sigma L_r \dfrac{di_{qr}}{dt} + R_r i_{qr} + \sigma L_r \omega_r i_{dr} + \omega_r \dfrac{M}{L_s}\phi_s \end{cases} \tag{6}$$

where V_s is the stator voltage magnitude is assumed constant, and $\omega_r = \omega_s - \omega = g\omega_s$ is the slip frequency, and g is the slip range and $\sigma = 1 - \frac{M^2}{L_s L_r}$ is the leakage coefficient. Consequently, with regard to Eq. (4), the fluxes are simplified as indicated below:

$$\begin{cases} \phi_{ds} = L_s i_{ds} + M i_{dr} \\ 0 \quad = L_s i_{qs} + M i_{qr} \end{cases} \tag{7}$$

From Eq. (7), the stator currents can be deduced as:

$$\begin{cases} i_{ds} = \dfrac{\phi_{ds} - M i_{dr}}{L_s} \\ i_{qs} = -\dfrac{M}{L_s} i_{qr} \end{cases} \tag{8}$$

By using Eqs. (3), (5) and (8), the stator active and reactive powers can then be expressed only versus these rotor currents as:

$$\begin{cases} P_s = -V_s \dfrac{M}{L_s} i_{qr} \\ Q_s = -V_s \dfrac{M}{L_s} \left(i_{dr} - \dfrac{\phi_{ds}}{M} \right) \end{cases} \tag{9}$$

2.2. Unbalanced DFIG model

As stated in [10, 11], during unbalanced grid voltage, the DFIG system can be separated into positive, negative and zero sequences. In this chapter, two methods are proposed for separate positive and negative sequences: delay inverse component canceling (DICC) method. And Notch filter method.

In the first method, the components in the three-phase a, b, c system are transformed into two-phase α, β stationary reference frame. Then, the positive and negative components can be determined by the following expression:

$$\begin{pmatrix} v_{\alpha s}^{+} \\ v_{\beta s}^{+} \\ v_{\alpha s}^{-} \\ v_{\beta s}^{-} \end{pmatrix} = \frac{1}{2} \begin{pmatrix} 1 & 0 & 0 & -1 \\ 0 & 1 & 1 & 0 \\ 1 & 0 & 0 & 1 \\ 0 & 1 & -1 & 0 \end{pmatrix} \begin{pmatrix} v_{\alpha s}(t) \\ v_{\beta s}(t) \\ v_{\alpha s}\left(t - \frac{T}{4}\right) \\ v_{\beta s}\left(t - \frac{T}{4}\right) \end{pmatrix} \tag{10}$$

The obtained positive and negative sequences from Eq. (10) in stationary reference frame are transformed into positive and negative sequences in rotating reference frame as follows:

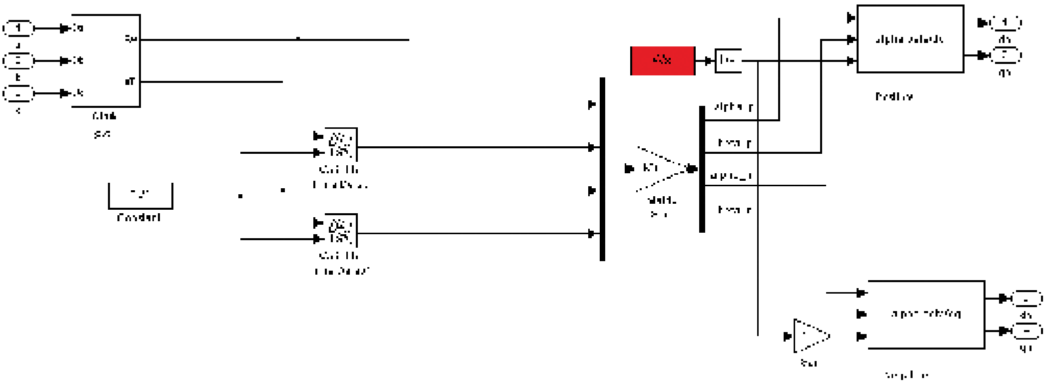

Figure 1. Simulink block for DICC method.

$$\begin{pmatrix} v_{ds}^{+} \\ v_{qs}^{+} \\ v_{ds}^{-} \\ v_{qs}^{-} \end{pmatrix} = \begin{pmatrix} \cos(\theta_s) & \sin(\theta_s) & 0 & 0 \\ -\sin(\theta_s) & \cos(\theta_s) & 0 & 0 \\ 0 & 0 & \cos(-\theta_s) & \sin(-\theta_s) \\ 0 & 0 & -\sin(-\theta_s) & \cos(-\theta_s) \end{pmatrix} \begin{pmatrix} v_{\alpha s}^{+} \\ v_{\beta s}^{+} \\ v_{\alpha s}^{-} \\ v_{\beta s}^{-} \end{pmatrix} \tag{11}$$

The associated Simulink scheme of the separate positive and negative sequences based on DICC method is depicted in **Figure 1**.

In the second method, the component of the negative sequence seems as a second-order harmonic in the positive rotating reference frame d, q^{+} and the component of the positive sequence seems as a second-order harmonic in the negative rotating reference frame d, q^{-}.

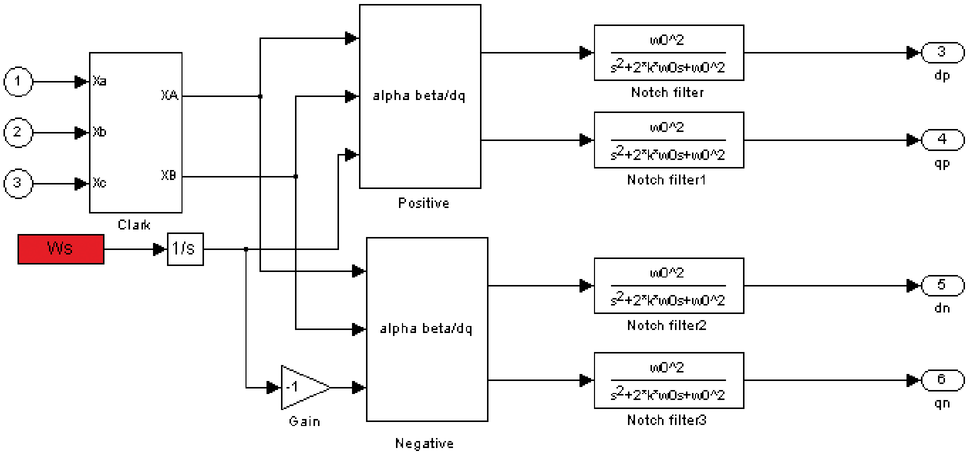

Figure 2. Simulink block for the notch filter method.

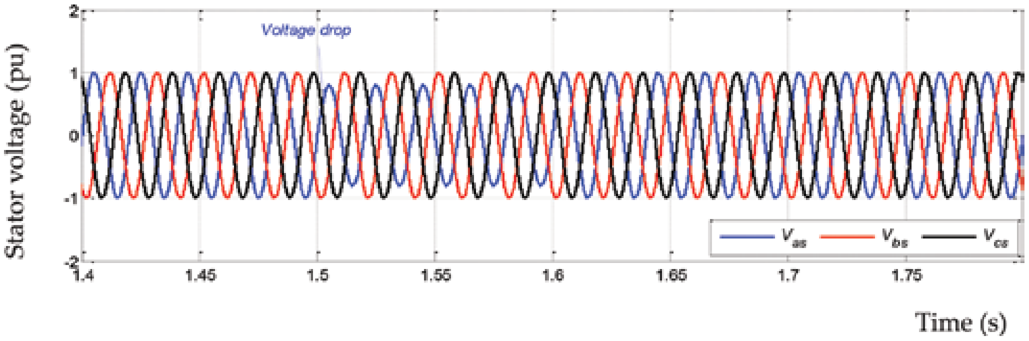

Figure 3. Grid stator voltage.

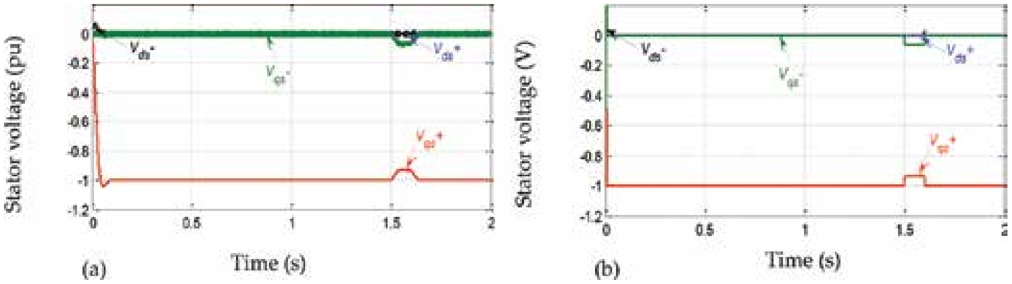

Figure 4. Unbalanced voltages in positive and negative dq rotating reference frame: (a) with DICC method and (b) with notch filter method.

Then, the DC values are bypassed and the high-frequency oscillations are suppressed by the notch filter tuned at $\omega_0 = 2\omega_s$ and $\xi = 0.707$. The associated Simulink scheme of this method is shown in **Figure 2**.

In **Figure 3**, the unsymmetrical voltage dip was applied between 1.5 and 1.6 s. Then, with two separation methods, the positive and negative sequences of the stator voltages in the rotating reference frame d, q are shown in **Figure 4**.

It can be noticed from these figures that the method based on DICC is faster than the method based on the notch filter. Therefore, the DICC method is chosen in this chapter due to its fast and precise characteristics. Assuming that the zero-sequence in the grid is neglected, the unbalanced stator voltages can be written as follows:

$$V_s^+ = \begin{pmatrix} v_{ds}^+ \\ v_{qs}^+ \end{pmatrix} = \begin{pmatrix} R_s\, i_{ds}^+ + \dfrac{d\phi_{ds}^+}{dt} - \omega_s\, \phi_{qs}^+ \\ R_s\, i_{qs}^+ + \dfrac{d\phi_{qs}^+}{dt} + \omega_s\, \phi_{ds}^+ \end{pmatrix}, V_s^- = \begin{pmatrix} v_{ds}^- \\ v_{qs}^- \end{pmatrix} = \begin{pmatrix} R_s\, i_{ds}^- + \dfrac{d\phi_{ds}^-}{dt} + \omega_s\, \phi_{qs}^- \\ R_s\, i_{qs}^- + \dfrac{d\phi_{qs}^-}{dt} - \omega_s\, \phi_{ds}^- \end{pmatrix} \tag{12}$$

The voltages at the rotor side are:

$$V_r^+ = \begin{pmatrix} v_{dr}^+ \\ \\ v_{qr}^+ \end{pmatrix} = \begin{pmatrix} R_r\, i_{dr}^+ + \dfrac{d\phi_{dr}^+}{dt} - (\omega_s - \omega)\,\phi_{qr}^+ \\ \\ R_r\, i_{qr}^+ + \dfrac{d\phi_{qr}^+}{dt} + (\omega_s - \omega)\,\phi_{dr}^+ \end{pmatrix}, V_r^- = \begin{pmatrix} v_{dr}^- \\ \\ v_{qr}^- \end{pmatrix}$$
$$= \begin{pmatrix} R_r\, i_{dr}^- + \dfrac{d\phi_{dr}^-}{dt} - (\omega_s + \omega)\,\phi_{qr}^- \\ \\ R_r\, i_{qr}^- + \dfrac{d\phi_{qr}^-}{dt} + (\omega_s + \omega)\,\phi_{dr}^- \end{pmatrix} \tag{13}$$

The stator and rotor fluxes are:

$$\begin{pmatrix} \phi_{ds}^+ \\ \phi_{qs}^+ \\ \phi_{ds}^- \\ \phi_{qs}^- \end{pmatrix} = \begin{pmatrix} L_s\, i_{ds}^+ + M\, i_{dr}^+ \\ L_s\, i_{qs}^+ + M\, i_{qr}^+ \\ L_s\, i_{ds}^- + M\, i_{dr}^- \\ L_s\, i_{ds}^- + M\, i_{dr}^- \end{pmatrix}, \begin{pmatrix} \phi_{dr}^+ \\ \phi_{qr}^+ \\ \phi_{dr}^- \\ \phi_{qr}^- \end{pmatrix} = \begin{pmatrix} L_r\, i_{dr}^+ + M\, i_{ds}^+ \\ L_r\, i_{qr}^+ + M\, i_{qs}^+ \\ L_r\, i_{dr}^- + M\, i_{ds}^- \\ L_r\, i_{dr}^- + M\, i_{ds}^- \end{pmatrix} \tag{14}$$

Under unbalanced grid, the active and reactive powers expression in Eq. (3) is decomposed into different pulsating components, which can be rewritten as:

$$\begin{pmatrix} P_s \\ Q_s \\ P_{s\sin 2} \\ P_{s\cos 2} \end{pmatrix} = \begin{pmatrix} v_{ds}^+ & v_{qs}^+ & v_{ds}^- & v_{qs}^- \\ v_{qs}^+ & -v_{ds}^+ & v_{qs}^- & -v_{ds}^- \\ v_{qs}^- & -v_{ds}^- & -v_{qs}^+ & v_{ds}^+ \\ v_{ds}^- & v_{qs}^- & v_{ds}^+ & v_{qs}^+ \end{pmatrix} \begin{pmatrix} i_{ds}^+ \\ i_{qs}^+ \\ i_{ds}^- \\ i_{qs}^- \end{pmatrix} \tag{15}$$

In order to obtain a constant stator power, the oscillating terms of the active and reactive powers $P_{s\sin 2}$, $Q_{s\cos 2}$ in (15) are neglected, therefore, only the average terms are controlled. By inverting (15), the stator currents can by calculated as follows:

$$\begin{pmatrix} i_{ds}^+ \\ i_{qs}^+ \\ i_{ds}^- \\ i_{qs}^- \end{pmatrix} = \frac{P_s}{D_1} \begin{pmatrix} v_{ds}^+ \\ v_{qs}^+ \\ -v_{ds}^- \\ -v_{qs}^- \end{pmatrix} + \frac{Q_s}{D_2} \begin{pmatrix} v_{qs}^+ \\ -v_{ds}^+ \\ v_{qs}^- \\ -v_{ds}^- \end{pmatrix} \tag{16}$$

where $D_1 = \left(v_{ds}^{+2} + v_{qs}^{+2}\right) - \left(v_{ds}^{-2} + v_{qs}^{-2}\right)$ and $D_2 = \left(v_{ds}^{+2} + v_{qs}^{+2}\right) + \left(v_{ds}^{-2} + v_{qs}^{-2}\right)$.

Figure 5 shows that the positive stator flux is aligned along with the d^+-axis and rotates at the speed of ω_s, whereas the d^--axis rotates at an angular speed of $-\omega_s$, with the phase angle to the α-axis being $-\theta_s$. Therefore, by using Eq. (12) with stator flux orientation under unbalanced grid, the stator currents are simplified as follows:

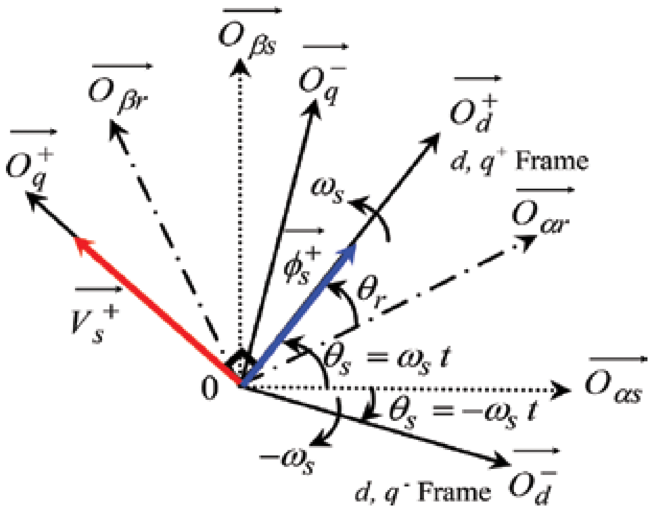

Figure 5. Stator flux orientation under unbalanced grid.

$$\begin{pmatrix} i_{ds}^+ \\ i_{qs}^+ \\ i_{ds}^- \\ i_{qs}^- \end{pmatrix} = \frac{1}{L_s} \begin{pmatrix} \phi_{ds}^+ \\ 0 \\ \phi_{ds}^- \\ 0 \end{pmatrix} - \frac{M}{L_s} \begin{pmatrix} i_{dr}^+ \\ i_{qr}^+ \\ i_{dr}^- \\ i_{qr}^- \end{pmatrix} \tag{17}$$

Combining Eq. (17) with Eq. (16), the rotor currents are written as follows:

$$\begin{pmatrix} i_{dr}^+ \\ i_{qr}^+ \\ i_{dr}^- \\ i_{qr}^- \end{pmatrix} = -\frac{L_s}{M}\frac{P_s}{D_1} \begin{pmatrix} v_{ds}^+ \\ v_{qs}^+ \\ -v_{ds}^- \\ -v_{qs}^- \end{pmatrix} - \frac{L_s}{M}\frac{Q_s}{D_2} \begin{pmatrix} v_{qs}^+ \\ -v_{ds}^+ \\ v_{qs}^- \\ -v_{ds}^- \end{pmatrix} + M \begin{pmatrix} \phi_{ds}^+ \\ 0 \\ \phi_{ds}^- \\ 0 \end{pmatrix} \tag{18}$$

3. Controllers design

The details of the conventional Lyapunov-based robust control have been presented in [16–18], so, this control strategy with unbalanced DFIG model is considered in this chapter.

3.1. Tracking error

In this chapter, J. J. Slotine [16] proposed the used tracking error:

$$S(x) = \left(\frac{\partial}{\partial t} + \lambda_x\right)^{n-1} e(x) \tag{19}$$

where $e(x)$ is the error vector ($e(x) = x^* - x$), λ_x is a positive coefficient, n is the system order. To bring the state variable to the tracking errors, the following two conditions have to be satisfied:

$$S(x) = 0, \quad \frac{d}{dt} S(x) = 0 \tag{20}$$

For n = 1 in Eq. (19), the errors of direct and quadrate rotor currents are chosen as:

$$S(x) = \begin{cases} S_1\left(i_{dr}^{+}\right) = i_{dr}^{+*} - i_{dr}^{+} \\ S_2\left(i_{qr}^{+}\right) = i_{qr}^{+*} - i_{qr}^{+} \\ S_3\left(i_{dr}^{-}\right) = i_{dr}^{-*} - i_{dr}^{-} \\ S_4\left(i_{qr}^{-}\right) = i_{qr}^{-*} - i_{qr}^{-} \end{cases} \tag{21}$$

3.2. Control law

In this chapter, the Lyapunov-based robust control is used to generate voltage references as an input to PWM. The control law satisfies the previous conditions is presented in the following form:

$$V_r == V_{r,eq} + V_{r,n} \tag{22}$$

where V_r is the control vector, $V_{r,eq}$ is the equivalent control vector, $V_{r,n}$ is the switching part of the control law.

The derivative of the tracking error (20) is rewritten as follows:

$$\frac{d}{dt} S(x) = F + D \ V_r \tag{23}$$

From Eq. (20), when the trajectories of rotor currents converge toward their references, the derivative of the tracking error is:

$$\frac{d}{dt} S(x) = F + D \ V_r = 0 \tag{24}$$

The following equation is obtained by replacing the rotor flux Eq. (14) in Eqs. (12) and (13) and combining with Eq. (24):

$$F = \begin{bmatrix} F_1 \\ F_2 \\ F_3 \\ F_4 \end{bmatrix} = \begin{bmatrix} \dot{i}_{dr}^{+*} + \frac{R_r}{\sigma L_r} i_{dr}^{+} - \omega_r i_{qr}^{+} + \frac{M}{\sigma L_r L_s} v_{ds}^{+} \\ \frac{R_r}{\sigma L_r} i_{qr}^{+} + \dot{i}_{qr}^{+*} + \omega_r i_{dr}^{+} + \frac{M}{\sigma L_r L_s} v_{qs}^{+} \\ - \frac{M}{\sigma L_r L_s} \phi_{sd}^{+} (\omega_s - \omega_r) \\ \dot{i}_{dr}^{-*} + \frac{R_r}{\sigma L_r} i_{dr}^{-} - \omega_r i_{qr}^{-} + \frac{M}{\sigma L_r L_s} v_{ds}^{-} \\ \frac{R_r}{\sigma L_r} i_{qr}^{-} + \dot{i}_{qr}^{-*} + \omega_r i_{dr}^{-} + \frac{M}{\sigma L_r L_s} v_{qs}^{-} \\ - \frac{M}{\sigma L_r L_s} \phi_{sd}^{-} (\omega_s + \omega_r) \end{bmatrix} \tag{25}$$

where

$$D = \frac{1}{\sigma\ L_r}\begin{bmatrix} 1 & 0 & 0 & 0 \\ 0 & 1 & 0 & 0 \\ 0 & 0 & 1 & 0 \\ 0 & 0 & 0 & 1 \end{bmatrix} \tag{26}$$

The following control law is obtained:

$$V_r = -D^{-1}\begin{bmatrix} F_1 + K_1 sat(S_1) \\ F_2 + K_2 sat(S_2) \\ F_3 + K_3 sat(S_3) \\ F_4 + K_4 sat(S_4) \end{bmatrix} \tag{27}$$

and

$$sat(S_i) = \begin{cases} 1, & S_i > \lambda_i \\ S_i/\lambda_i & |S_i| \le \lambda_i \\ -1, & S_i < -\lambda_i \end{cases} \tag{28}$$

where λ_i is the width boundary layer and i indicates 1, 2, 3 or 4 and K_1, K_2, K_3 and K_4 are positive control gains of the switching control part.

3.3. Lyapunov stability proof

The stability and robustness of the system are thoroughly investigated and subsequent results are presented in [16–18]. In this chapter, the stability theory of Lyapunov is used to check the convergence of the tracking errors toward the zero by satisfying the following condition:

$$\dot{V} = S^T(x)\,\dot{S}(x) \le 0 \tag{29}$$

Then, the Lyapunov function is obtained as:

$$\dot{V} = S^T(x)\,(F + D\ V_r) \le 0 \tag{30}$$

By using Eq. (27), Lyapunov function Eq. (30) is rewritten as:

$$\dot{V} = S^T(x)\left(F + D\left(-D^{-1}\begin{bmatrix} F_1 + K_1 sat(S_1) \\ F_2 + K_2 sat(S_2) \\ F_3 + K_3 sat(S_3) \\ F_4 + K_4 sat(S_4) \end{bmatrix}\right)\right) \le 0 \tag{31}$$

Or

$$\dot{V} = -S^T(x)\begin{bmatrix} K_1 sat(S_1) \\ K_2 sat(S_2) \\ K_3 sat(S_3) \\ K_4 sat(S_4) \end{bmatrix} \leq 0 \tag{32}$$

From Eq. (32), the Lyapunov function is definitely negative so that the control law becomes stable.

3.4. Lyapunov robustness proof

In practice, the tracking error S will be influenced by the parameter variations and measurement uncertainties. Thus, Eq. (23) is rewritten as:

$$\frac{d}{dt}S(x) = F + D\ \ V_r + H \tag{33}$$

where $H = [H1\ H2\ H3\ H4]^T$ represents system disturbances. Thus, Eq. (35) can be rewritten as:

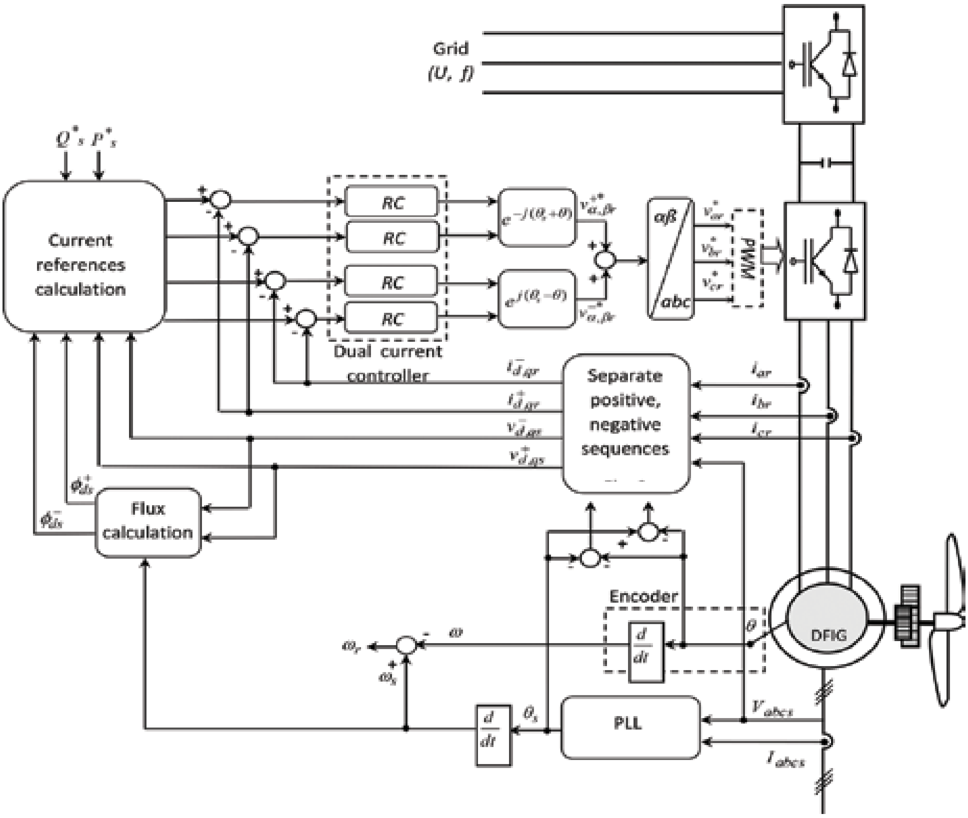

Figure 6. Block diagram of the proposed Lyapunov-based robust control scheme.

$$\dot{V} = S^T(x)\left(\begin{matrix} H_1 \\ H_2 \\ H_3 \\ H_4 \end{matrix} - \begin{bmatrix} K_1 sat(S_1) \\ K_2 sat(S_2) \\ K_3 sat(S_3) \\ K_4 sat(S_4) \end{bmatrix}\right) \leq 0 \tag{34}$$

It is worth mentioning that if the positive control gains satisfy the following condition, specifically, $K1 > |H1|$, $K2 > |H2|$, $K3 > |H3|$ and $K4 > |H4|$ the time derivative of Lyapunov function $\dot{V}$ is still definitely negative. Consequently, the control law features are robust. **Figure 6** shows the block diagram of the VC scheme for DFIG using Lyapunov-based robust control (RC). In this block diagram, the Phase-Locked-Loop (PLL) estimates the frequency, the grid voltage magnitude and the stator angle. The block of separate positive and negative sequences of the current and the voltage shown in **Figure 1** is used in this schema for the dual current controller and the calculation of the current references.

4. Simulation results

The generator is tested under single line to ground fault condition on phase ‘a’; at 1.5 s an unbalanced voltage drop of 20% is created for a time of 0.1 s as shown in **Figure 3**. In this section, all the physical quantities are in per unit values, and the quantities of the rotor are referred to the stator side. **Figure 7** shows the Simulink block diagram of the DFIG wind turbine model. The switching frequency of converter is set to 1 kHz; the nominal DC converter is set to 2000 V. Wind speed varies from 10 to 11 m/s. To examine the validity of the proposed

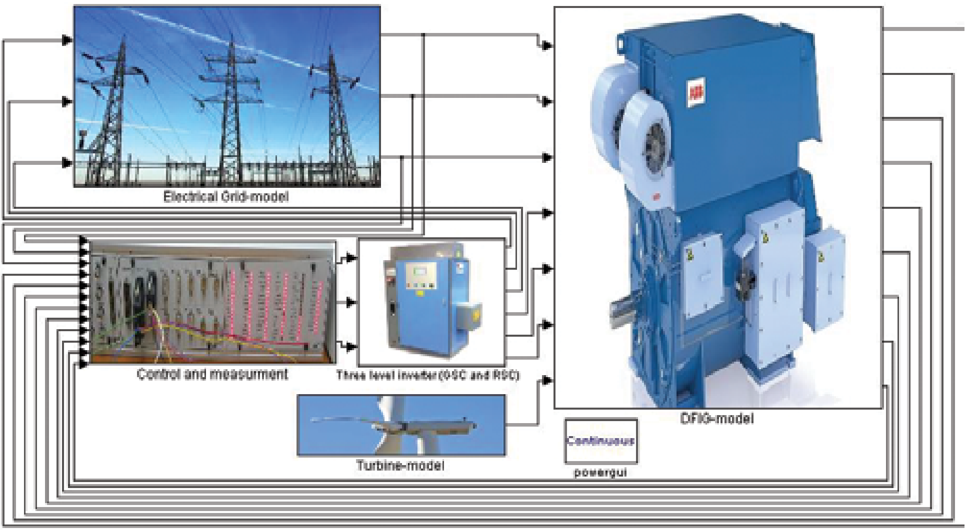

Figure 7. Simulink block diagram of the DFIG wind turbine model.

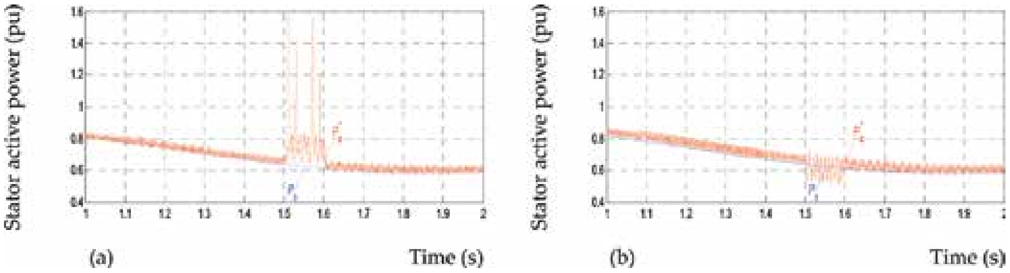

Figure 8. Stator active power (pu): (a) conventional single RCS, (b) proposed dual RCS.

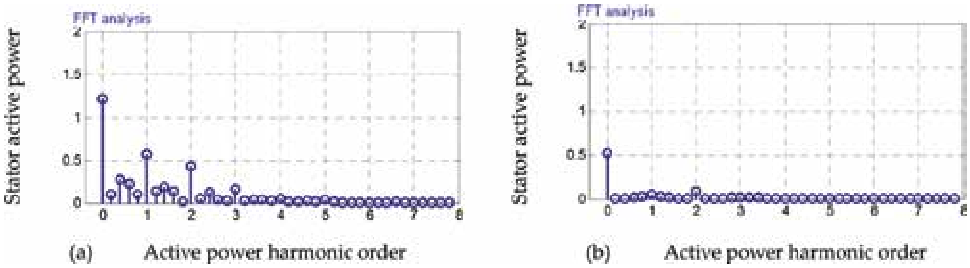

Figure 9. Harmonic spectra of the stator active power (pu): (a) conventional single RCS, (b) proposed dual RCS.

dual Lyapunov based robust control scheme (RCS), these results are compared with the conventional single Lyapunov-based RCS published in [15].

Figures 8(a) and **(b)**, **9(a)** and **(b)**, **10(a)** and **(b)** and **11(a)** and **(b)**, show that, during grid voltage unbalance, if conventional control is applied, the active and reactive powers contain important oscillations due to the nature of the second harmonic at twice the grid frequency (100 Hz) with magnitude of 0.78 pu. The conventional control does not provide adequate control of the negative sequence current during the occurrence or removal of voltage unbalance. Whereas, by using the proposed control method, these oscillations are dramatically reduced because of the negative sequence current compensation, during grid fault, by the dual current control loops which can indirectly control these powers.

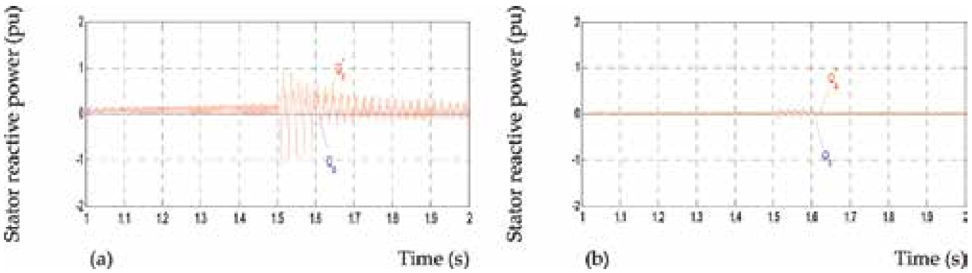

Figure 10. Stator reactive power (pu): (a) conventional single RCS, (b) proposed dual RCS.

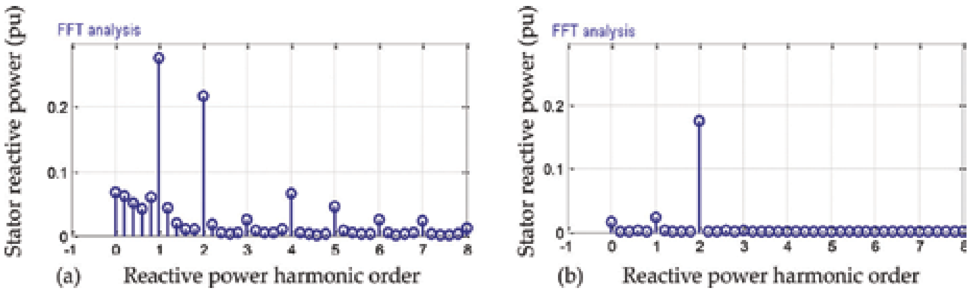

Figure 11. Harmonic spectra of the stator reactive power (pu): (a) conventional single RCS, (b) proposed dual RCS.

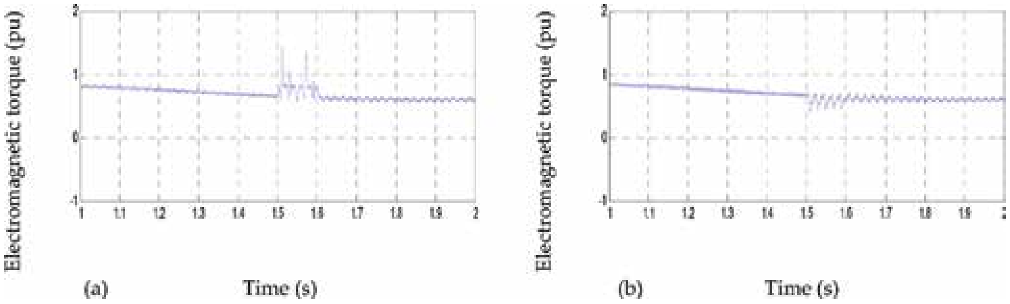

Figure 12. Electromagnetic torque (pu): (a) conventional single RCS, (b) proposed dual RCS.

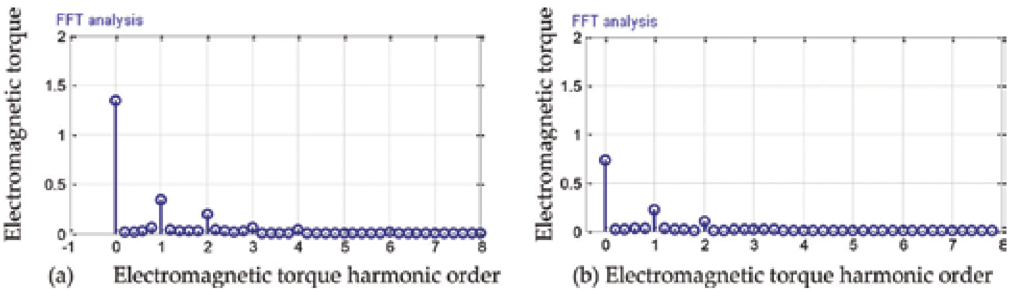

Figure 13. Harmonic spectra of the electromagnetic torque (pu): (a) conventional single RCS, (b) proposed dual RCS.

Figures 12(a) and **(b)** and **13(a)** and **(b)** show that the ripples of the electromagnetic torque are also mitigated with the proposed control. On the contrary, when we use the conventional control method, the electromagnetic torque has oscillations with magnitude of 0.74 pu and frequency of 100 Hz, which might be harmful to the mechanical parts.

Figures 14(a) and **(b)** and **15(a)** and **(b)** show that the stator currents have important harmonics with conventional control, which are injected into grid, but these currents are quite sinusoidal and symmetrical with the proposed control.

Figures 16(a) and **(b)** and **17(a)** and **(b)** show that the currents at the rotor side are also unbalanced with conventional control, but these oscillations are attenuated by using the proposed

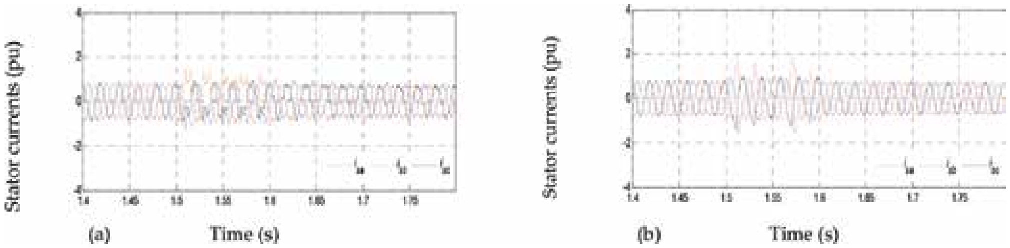

Figure 14. Stator currents (pu): (a) conventional single RCS, (b) proposed dual RCS.

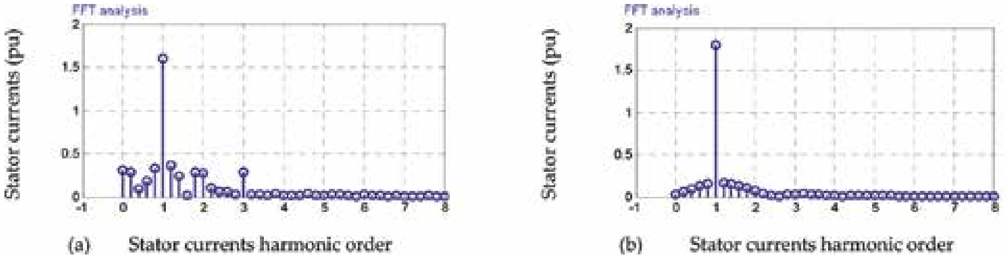

Figure 15. Harmonic spectra of the stator currents (pu): (a) conventional single RCS, (b) proposed dual RCS.

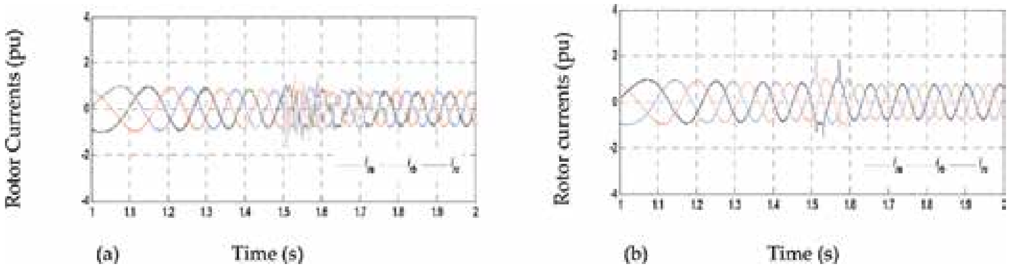

Figure 16. Rotor currents (pu): (a) conventional single RCS, (b) proposed RCS.

control method. This is due to the fact that the conventional control cannot control the negative component introduced by the unbalanced voltage in the stator flux and current vectors to zero. In that situation, interaction of these components in the generator develops motoring and generating behavior resulting in excessive oscillations. The stator flux amplitude is constant at the steady-state and rotates synchronously with the grid voltage. Instantly after the occurrence of the unbalanced voltage dip (see **Figure 3**), two voltages cause a positive and negative flux in the stator. Unlike the case of balanced voltage dip, where two components will be induced in the stator flux: the forced component is rotating with the grid frequency; afterward, the natural flux is static with the stator.

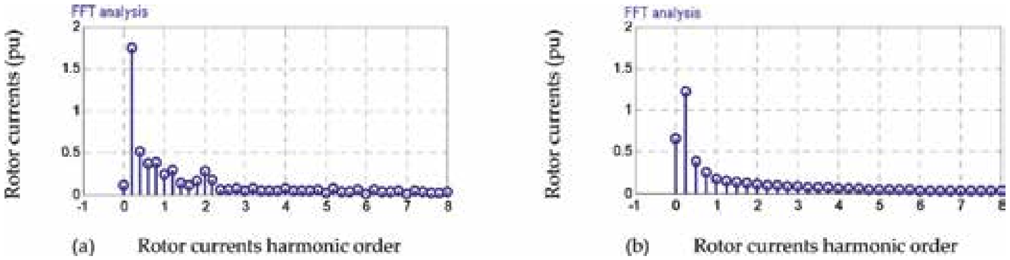

Figure 17. Harmonic spectra of the rotor currents (pu): (a) conventional single RCS, (b) proposed dual RCS.

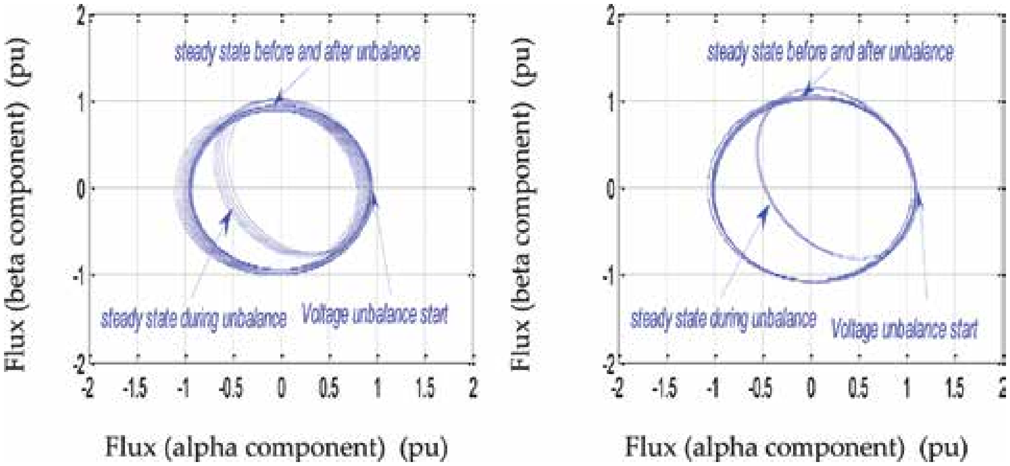

Figure 18. Stator flux (pu): (a) conventional single RCS, (b) proposed dual RCS.

Figure 18(a) and **(b)** shows the trajectory of the stator flux. Before the voltage unbalance, the stator flux traces a circle with radius equal to 1 pu. The flux of the stator with the proposed dual RCS is very well centered compared with that obtained with the conventional single RCS. When the voltage unbalance starts, the ellipse trajectory drawn by the flux is due to the presence of positive and negative flux in the stator rotating in opposite directions, which is a common characteristic in unbalanced voltage sags. Whereas, the natural flux brings the ellipse to be off-center. After the clearance of the voltage unbalance, the natural component of the stator flux is attenuated and the trajectory of the stator flux turns into the center again. However, it is noticed from these figures that compared with the proposed dual RCS, the stator flux trajectory of the conventional single RCS is not well centered with an important transient with a slow decay.

For clear illustrations, **Figures 19** and **20** are included to show the comparative results of ripples pulsating at twice the grid frequency (100 Hz) in the stator active/reactive powers and electromagnetic torque among these different control strategies during network unbalance. As presented, the proposed dual RCS aims at mitigating the torque pulsations and the power

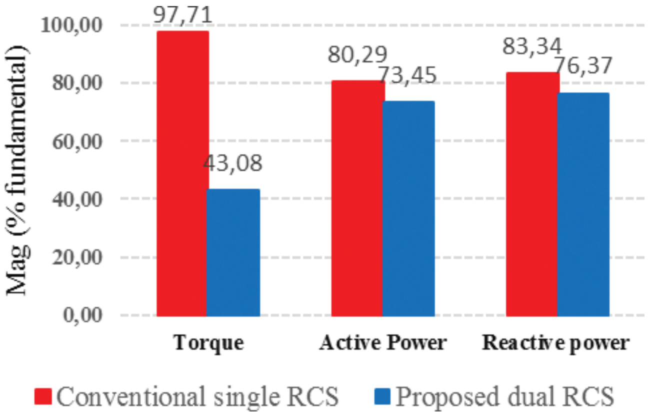

Figure 19. Comparison of ripples in electromagnetic torque, stator active and reactive power between the two control strategies.

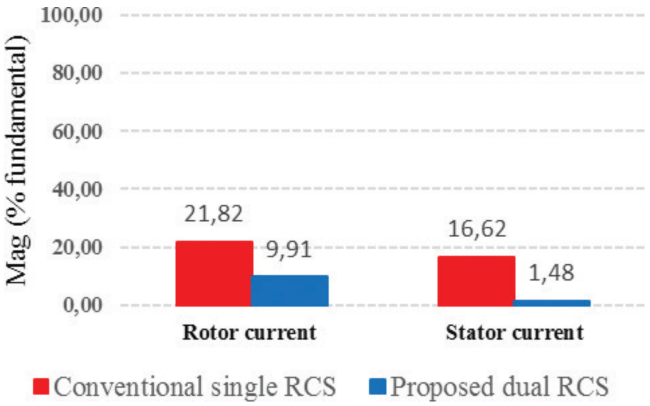

Figure 20. Comparison of harmonics in stator and rotor currents between the two control strategies.

ripples compared with the conventional method. In addition, the proposed dual RCS is able to reduce the harmonics of the rotor and stator currents. It can be concluded from these strategies that the proposed control method can effectively reduce the torque oscillations which incidentally may lead to a decrease of the fatigues on the turbine shaft.

5. Conclusions

In this chapter, an improved control strategy for doubly fed induction generator (DFIG)-based wind turbine under unbalanced grid voltage is presented. The dynamic behavior of DFIG by the proposed control algorithm proved to be suitable by a set of simulation tests using the MATLAB®/Simulink® environment. The results obtained imply that with the conventional single robust control scheme (RCS), the magnitude of the second harmonic oscillations can become high, intolerable and may lead to electrical and mechanical failure in function. After removing the voltage unbalance, in the conventional control method, small oscillations appear in the powers and currents waveforms. On the contrary, when the proposed dual RCS is used, these power oscillations are effectively damped to a reasonable level. Furthermore, the proposed control strategy shows good performances and robustness by eliminating the pulsations in the torque which maybe preferred by wind farm operators since it will mitigate the fatigue of the turbine shaft as well as the gearbox. Moreover, symmetrical and sinusoidal stator and rotor currents are also obtained, in turn minimizing the copper losses in the rotor circuit, when the grid voltage is unbalanced. All computer simulations have been designed with a fixed-step size of 0.5 ms in order to consider digital implementation in future works.

A. Appendix

In this part, simulations are investigated with a 1.5 MW generator connected to a 690 V/50 Hz grid [15].

The generator's parameters are presented below:

Three pole pairs, = 0.012 Ω, = 0.021 Ω, = 0.0135 H, = +2.00372 e−4 H, = +1.7507 e−4 H,

Turbine's parameters: three blades, diameter = 70.5 m, gearbox ratio = 90: inertia (turbine + DFIG) = 1000 kg m^2 and viscous coefficient (turbine + DFIG) = 0.0024 kg m/s.

Author details

Kamel Djamel Eddine Kerrouche[1]*, Lina Wang[1], Alex Van Den Bossche[2], Azzedine Draou[3], Abdelkader Mezouar[4] and Larbi Boumediene[4]

*Address all correspondence to: kerrouche20@yahoo.fr

1 School of Automation Science and Electrical Engineering, Beihang University, Beijing, China

2 Electrical Energy LAB EELAB, Ghent, Belgium

3 Department of Electrical Engineering, Islamic University of Madinah, Madinah,
Saudi Arabia

4 Electro-technical Engineering Lab, Faculty of Technology, Tahar Moulay University, Saida, Algeria

References

[1] Kerrouche K, Mezouar A, Belgacem K. Decoupled control of doubly fed induction generator by vector control for wind energy conversion system. Energy Procedia. 2013;**584**: 239-248

[2] Gayen PK, Chatterjee D, Goswami SK. A low-voltage ride-through capability enhancement scheme of doubly fed induction generator based wind plant considering grid faults. Journal of Renewable and Sustainable Energy. 2016;**8**:025301

[3] Kerrouche KDE, Mezouar A, Boumediene L, Kh B. Modeling and optimum power control based DFIG wind energy conversion system. IREE. 2014;**9**:174

[4] Brekken TKA, Mohan N. Control of a doubly fed induction wind generator under unbalanced grid voltage conditions. IEEE Transactions on Energy Conversion. 2007;**22**:129

[5] Mwasilu F, Justo JJ, Ro K-S, Jung J-W. Improvement of dynamic performance of doubly fed induction generator-based wind turbine power system under an unbalanced grid voltage condition. IET Renewable Power Generation. 2012;**6**:424

[6] Abad G, Rodriguez MA, Iwanski G, Poza J. Direct power control of doubly fed induction generator based wind turbines under unbalanced grid voltage. IEEE Transactions on Power Electronics. 2010;**25**:442

[7] Shehata EG. Active and reactive power control of doubly fed induction generators for wind energy generation under unbalanced grid voltage conditions. Electric Power Components and Systems. 2013;**41**:619

[8] Hu J, Nian H, Hu B, He Y, Zhu ZQ. Direct active and reactive power regulation of DFIG using sliding mode control approach. IEEE Transactions on Energy Conversion. 2010;**25**:1028

[9] Shang L, Hu J. Sliding-mode based direct power control of grid-connected wind-turbine-driven doubly fed induction generators under unbalanced grid voltage conditions. IEEE Transactions on Energy Conversion. 2012;**27**:362

[10] Xu L, Wang Y. Dynamic modeling and control of DFIG-based wind turbines under unbalanced network conditions. IEEE Transactions on Power Systems. 2007;**22**:314

[11] Lee S-B, Lee K-B, Lee D-C, Kim J-M. An improved control method for a DFIG in a wind turbine under an unbalanced grid voltage condition. Journal of Electrical Engineering & Technology. 2010;**5**:614

[12] Norm's IEEE STD 519-1992: IEEE recommended practices and requirements for harmonic control in electrical power systems. April 12, 1993. pp. 15-99

[13] Tedjini H, Meslem Y, Rahli M, Berbaoui B. Shunt active filter in damping harmonics propagation. Advances in Electrical and Computer Engineering. 2010;**10**:108-113

[14] Abdou AF, Abu-Siada A, Pota HR. Improving the low voltage ride through of doubly fed induction generator during intermittent voltage source converter faults. Journal of Renewable and Sustainable Energy. 2013;**5**:043110

[15] Kerrouche KDE, Mezouar A, Boumediene L, Van Den Bossche A. A comprehensive review of LVRT capability and sliding mode control of grid-connected wind-turbine-driven doubly fed induction generator. Automatika—Journal for Control, Measurement, Electronics Computing and Communications. 2016;**60**:922-935

[16] Dash PK, Patnaik RK. Adaptive second order sliding mode control of doubly fed induction generator in wind energy conversion system. Journal of Renewable and Sustainable Energy. 2014;**6**:053143

[17] Kerrouche K, Mezouar A, Boumediene L. A simple and efficient maximized power control of DFIG variable speed wind turbine. In: Proceedings 3rd International Conference on Systems and Control (ICSC) IEEE, Algiers, Algeria. 2013. p. 894

[18] Kerrouche KDE, Mezouar A, Boumediene L, Van Den Bossche A. Modeling and Lyapunov-designed based on adaptive gain sliding mode control for wind turbines. Journal of Power Technologies. 2016;**96**:124

Section 2

Assessment, Reliability and Prospects of Wind Turbines

Chapter 6

Evaluation and Stability Analysis of Onshore Wind Turbine Supporting Structures

Chikako Fujiyama, Yasuhiro Koda and Noriaki Sento

Additional information is available at the end of the chapter

http://dx.doi.org/10.5772/intechopen.75885

Abstract

This chapter shows research of stability of supporting structure of onshore wind turbine foundations based on field measurements, finite element (FE) analysis and laboratory experiment. In order to investigate the relation of action-response of tower-foundation system, long-term field measurements were carried out for two existing onshore wind turbines with/without piles for its foundations. Then, the models were built up for three-dimensional nonlinear FE analyses. The damage processes of reaching failure were examined by FE models, and limit state of foundations was individually defined by fatigue limit state of concrete. Consequently, the stress-number of cycle (S-N) diagram derived from both experiment and analysis was discussed for the assessment of existing structure.

Keywords: concrete, foundation, fatigue, anchor bolt, crack

1. Introduction

Wind power is growing a major industry. At the year of 2006, the total amount of installed wind power capacity reached 74.1 GW in the world [1], while it has reached 486.8 GW in the world at the year of 2016 [2] due to a rapid installation of wind turbine in this decade. In particular, increasing wind energy production has been even more actively touted against the background of the Great East Japan earthquake and the resultant nuclear power plant accident. However, in the past, wind turbines have had troubling experiences of structural collapse as well as failure of blade [3].

In particular, the structures supporting wind turbines, especially the foundation made of concrete, have been paid attentions in recent years. There are the reports that investigate cracks on foundation concrete [4–7]. It is not easy to identify the cause of cracks, while repeated action transferred from the tower is thought to be one of the causes. Therefore, fatigue of supporting structure made of concrete has become a main concern of researchers [7–10]. Even though the cracks are not always the trigger of structural collapse of wind turbine, further investigations are required for safe and steady operation of power plant.

Here, it is important, for practical design, to precisely analyze the responses of structures and to capture the action of wind. The response of existing wind turbine tower was analyzed using wireless system of accelerometers [11]. The development of a health monitoring system for the wind turbine tower-foundation system has been reported [12]. In addition, three-dimensional nonlinear finite element (FE) analyses for wind turbine tower-foundation systems have been conducted using idealized static forces as input [13].

This chapter shows research of stability of supporting structure of onshore wind turbine foundations based on field measurements, laboratory experiment and FE analysis. In order to investigate the relation of action-response of tower-foundation system, long-term field measurements were carried out for an existing onshore wind turbine without piles for its foundations. Then, the model was built up for three-dimensional nonlinear FE analyses. The damage process of reaching failure was examined by FE models. In addition, limit state of foundation was defined by fatigue limit state of concrete. Consequently, the stress-number of cycle (S-N) diagram derived from laboratory experiment and analysis was discussed for the assessment of existing structure.

2. Field measurement

2.1. Overview of target and measurement setup

The responses of structure were investigated using field data, which were measured at a wind turbine equipped in 2003 on the campus of Nihon University and along the Abukuma River in the Fukushima prefecture, Japan. The wind turbine specifications and the positions of the measuring equipment are shown in **Figure 1**. The rated power is 40 kW and rated wind speed is 11 m/s. The cut-in wind speed and cut-out wind speed are 2 and 25 m/s, respectively. This had been continuously operated even during the Great East Japan Earthquake in 2011, which resulted in no visible damage.

The accelerometers were attached at the top and middle of the tower horizontally. There are 60,000 data points for 5 min at a sampling frequency of 200 Hz. The data were recorded every hour when exceeding the acceleration threshold of ±0.7 $\mathrm{m/s^2}$. To investigate the transmission of vibration from the tower to the foundation, strain gauges were attached at the anchor bolts in the east, west, north, and south direction. The sampling conditions were the same as those in the accelerometer. Wind speed and direction were measured using an anemometer attached to the nacelle with a sampling frequency of 1.0 Hz. The measurements have been begun since May 2013.

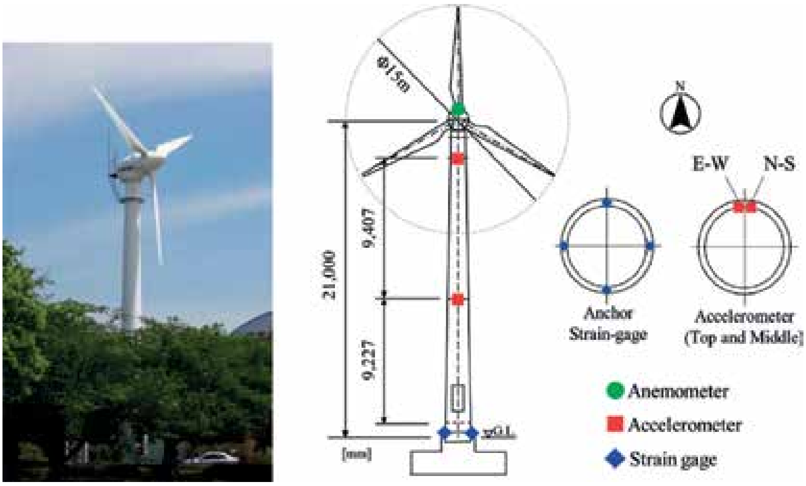

Figure 1. Overview and schematic of the apparatus used in measurements (based on [13]).

2.2. Responses of the tower

Figure 2 shows the maximum wind speed versus the maximum response of acceleration. Despite the scatter of the data, shown as black dots for operating wind speeds of 2–20 m/s, the maximum acceleration increased linearly with wind speed. The red dots represent data recorded while the generator was not operating. The difference between the two datasets suggests that the blade pitch control system dampened the acceleration response.

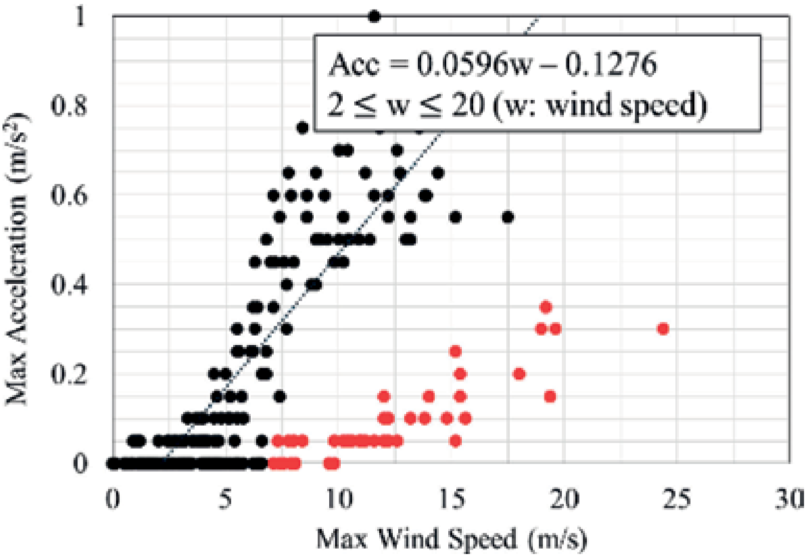

Figure 2. Max acceleration versus max wind speed in October 2013 [13].

The acceleration response of the tower in the time domain and trajectory of the tower displacement, which are derived through double integration of acceleration in the time domain are shown in **Figure 3**. To remove noise, a digital band pass filter with pass band between about 0.1 and 30 Hz was designed. The maximum displacement was about 0.5 cm at the top of the tower in the EW direction. Elliptical trajectories with different main axis were observed for each height in different scales when the wind turbine was operating. In particular, the trajectories of the top and middle of the tower were almost similar. This means that the predominant vibration mode was the primary mode.

2.3. Action to the foundation transmitted from the tower

The strain of nut for anchor bolt clearly depended on the acceleration variations, even though the value of the response was less than 1 μ. This can be explained that the location of strain gauges attached to anchor bolts was not consistent with wind direction which measured max wind speed.

When taking a long-term measurement, time varying character of the wind can be captured in a spectrum. The Fourier spectrum exhibited the waveform shown in **Figure 4**. The natural

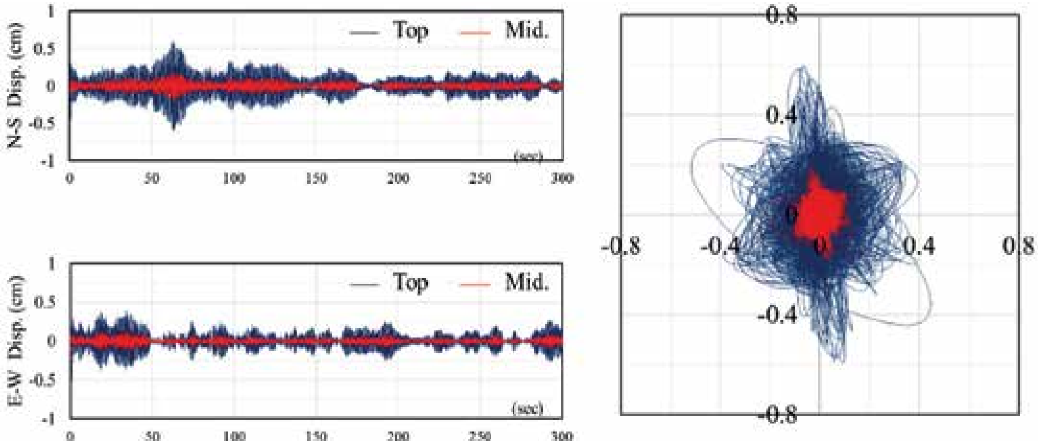

Figure 3. Acceleration response of tower and trajectory of its displacement (based on [13]).

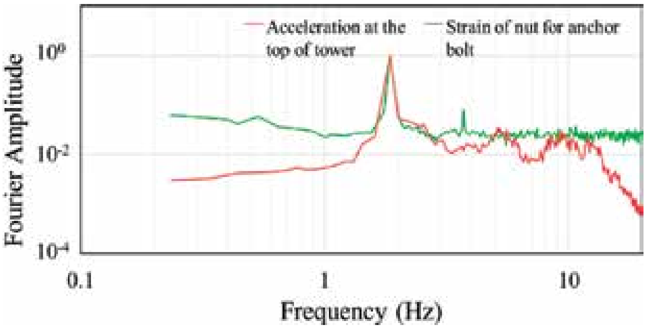

Figure 4. Fourier spectrum of acceleration of tower and strain on anchor bolt (based on [13]).

frequency was 1.8 Hz in the primary mode and 13 Hz in the secondary mode based on the eigenvalue analysis and free vibration tests. The figure suggested the predominant vibration mode transmitted from the tower to the foundation was the primary mode.

3. Finite element analysis

3.1. Modeling

The nonlinear finite element (FE) analysis code COM3D developed by Maekawa et al. [14, 15] are used in this study. The decrease of stiffness and the accumulation of plasticity of concrete subjected cyclic load are carefully formulated for concrete in the code. In particular, employing the logarithmic integral scheme that enabled to calculate fatigue damage of concrete is one of the advantages of this code. The properties for steel are expressed with bi-linear form.

An overview of the FE model is shown in **Figure 5**. The model was modified from the model in the previous study [13] through further material investigation and verifications. Mechanical properties of these constituent materials are summarized in **Table 1**.

In order to simplify structural model, the shape of nacelle and blades was not directly modeled. Alternatively, dead weight of them was applied to certain elements located at the top of with each material density. All the members except anchor bolts and the intermediate restraining reinforcements of the pedestal were modeled by solid element. Exceptions were expressed by line element; in particular, the torque on an anchor bolt was replaced by initial strain of the lines. The boundary condition between steel and concrete was modeled by joint element based on the Mohr–Coulomb theory with 0.6 as friction coefficient. Vertical displacement was restricted at the nodes of the footing bottom surface; however, confinement of surrounding soil was not considered on the side of the footing as same in literature [16].

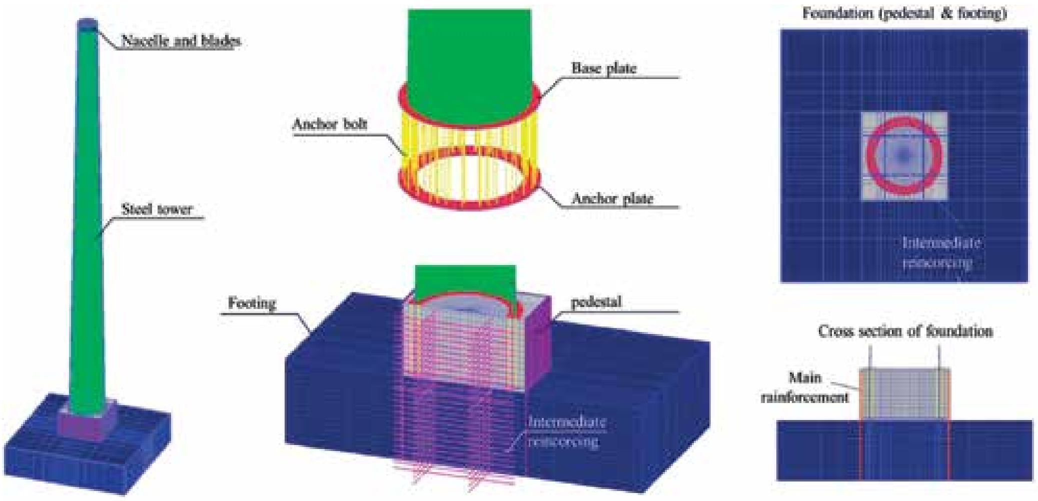

Figure 5. Overview of FE model (based on [10]).

	Young's modulus (GPa)	Compressive strength (MPa)	Yield strength (MPa)	Tensile strength (MPa)	Poisson ratio
Concrete	23.5	21.0	—	8.13	0.2
Anchor bolt	205	—	235	400	0.3
Other steels	205	—	325	490	0.3
Reinforcing bar	205	—	345	517.5	0.3

Table 1. Mechanical properties of each material in FE analysis.

3.2. Verification of the model

The model was verified by the comparison of the analytical result and data obtained during free vibration test. The natural frequency of tower and damping factor calculated by FE analysis were 1.84 Hz and 0.30%. Those obtained from the field test were 1.78 Hz and 0.27% [10].

In addition, the agreement of analytical results and data obtained in field measurement were examined. First, the displacement at the top of tower which was converted using double integration of acceleration in the time domain as mentioned in 2.1.2, was inputted to the model. Then, acceleration of tower, strain of tower body, and strain of anchor bolts calculated by FE analysis were compared with data obtained in the field for six different cases including data during typhoon and earthquakes. Samples of examinations in terms of maximum and minimum values are shown in **Figure 6**. The analysis results tended to show spikes due to the difficulty of convergence of calculation. However, acceptable agreement was seen in all six cases.

3.3. Prediction of failure mode

In order to determine the failure mode of this structure, monotonic horizontal displacement was applied to a node at the top of tower. The bending moment at the bottom of tower versus rotation angle derived from Eq. (1) [10] is shown in **Figure 7**.

$$\phi = arctan\left(\frac{\delta_{zt} - \delta_{zc}}{B}\right) \tag{1}$$

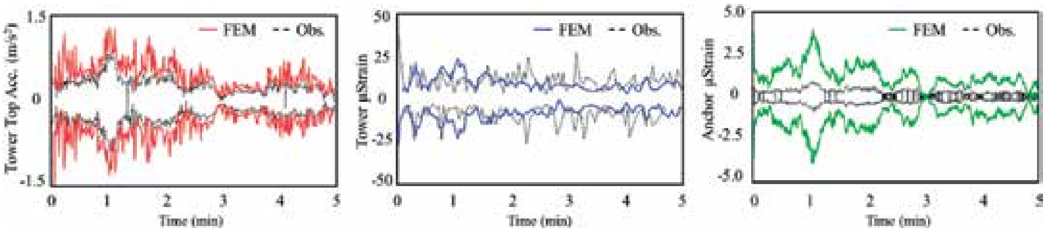

Figure 6. Comparison of FE model and observed data during power generating (left: acceleration at the top of tower; middle: strain of tower body; right: strain of anchor bolt) (based on [10]).

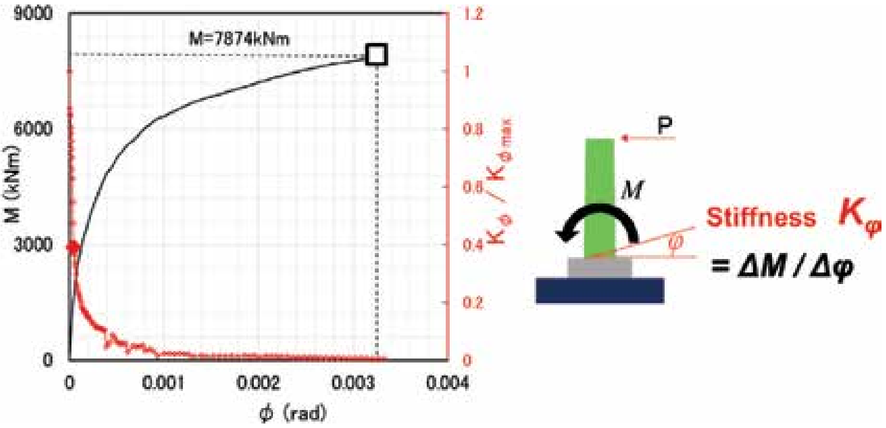

Figure 7. Bending moment at the bottom of tower and rotation angle.

where φ is rotation angle, δzt is vertical displacement of anchor plate in tension side, δzc is vertical displacement of anchor plate in compression side, and B is a diameter of anchor ring.

The moment increased rapidly at the beginning of loading, and it gradually became mild. Then, the moment remained static after when 50% of anchor bolts reached their yielding strength. At the time, the horizontal displacement at the top of tower was 50 cm where the moment and rotation angle reached 7874 kNm and 0.0033 rad. **Figure 7** also shows the normalized stiffness by using the right axis. The stiffness mentioned here means the value that was obtained when moment was divided by the rotation angle. The normalized stiffness means the stiffness normalized by the initial stiffness. According to **Figure 7**, the normalized stiffness significantly dropped in the first 0.0001 rad.

What did cause the significant drop to normalized stiffness? It was the cracking of concrete at the tip of anchor ring inside pedestal (see **Figure 8**). Consequently, the crack developed horizontally and came to the center of the pedestal in the end of analysis (see **Figure 9**). Regarding this FE analysis, the failure mode was a coupling mode of yielding 50% of anchor bolts and development of horizontal crack to more than half of the pedestal's width.

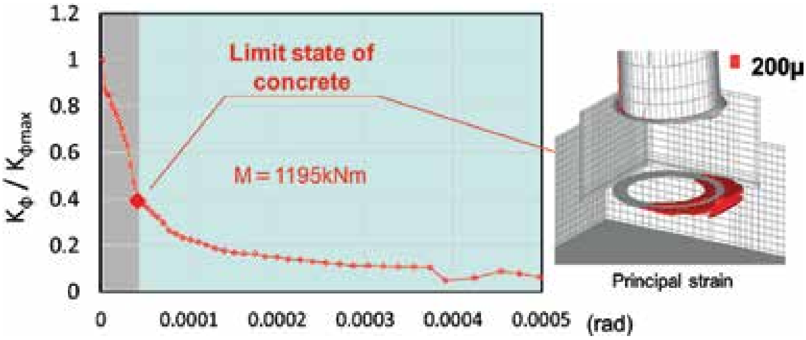

Figure 8. Principal strain distribution at the drop of normalized stiffness.

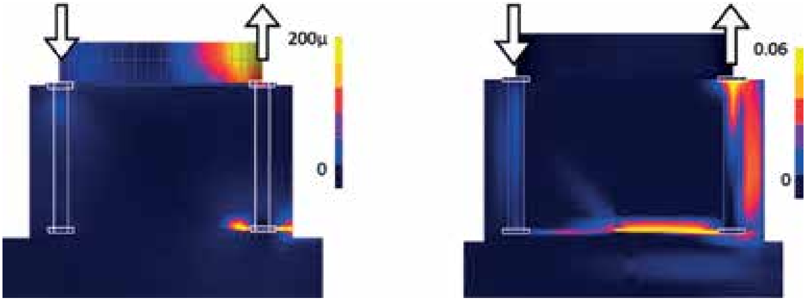

Figure 9. Principal strain distribution of the cross section of joint parts (left: at 1195 kNm of moment; right: at 7874 kNm of moment) (based on [10]).

The ultimate bending moment calculated by the FE analysis was 7874 kNm, it is much higher than the design moment in the case of earthquake in this area; 2430 kNm. This means that the targeted wind turbine has sufficient allowance of safety. However, the cracking moment 1195 kNm is close to the design moment owing to the wind in this area; 855 kNm. Therefore, evaluation of fatigue resistance of concrete foundation is needed.

3.4. Identification of index

Since the cracking inside pedestal was observed as the cause of the decrease of stiffness, evaluation of fatigue resistance of this structure focused on this event. The specific index, space averaged second invariant strain [17] was employed to determine the possibility of cracking. This index is independent of direction of stress or strain that is unsettled at each moment under the vibration of tower, but is a scalar obtained by Eqs. (2) and (3) [17].

$$\sqrt{J_2'} = \sqrt{\frac{2}{3}\left\{\left(\frac{\varepsilon_x-\varepsilon_y}{2}\right)^2+\left(\frac{\varepsilon_y-\varepsilon_z}{2}\right)^2+\left(\frac{\varepsilon_z-\varepsilon_x}{2}\right)^2\right\}+\left(\frac{\gamma_{xy}}{2}\right)^2+\left(\frac{\gamma_{yz}}{2}\right)^2+\left(\frac{\gamma_{zx}}{2}\right)^2} \tag{2}$$

$$\overline{\sqrt{J_2'}} = \frac{\int_V \sqrt{J_2'}\cdot w(x)dV}{\int_V w(x)dV} \quad w(x) = \begin{cases} 1-x/L & x \le L \\ 0 & x > L \end{cases} \tag{3}$$

where, $\sqrt{J_2'}$ is the second invariant of strain, $\overline{\sqrt{J_2'}}$ is the space-averaged second invariant of strain, ε and γ are normal and shear strains respectively, w(x) is a weighting function, x is a distance from the tip of anchor plate in tension side (mm), L is a radius of average volume (mm). For this analysis, L was determined as 200 mm based on [18].

The horizontal displacement of tower versus the space-averaged second invariant of strain is shown in **Figure 10**. The space-averaged second invariant of strain at the occurrence of the horizontal crack determined by **Figure 9** was identified as 0.000032. Thus, threshold value for first limit state of this structure was defined as 0.000032 by the space-averaged second invariant of strain.

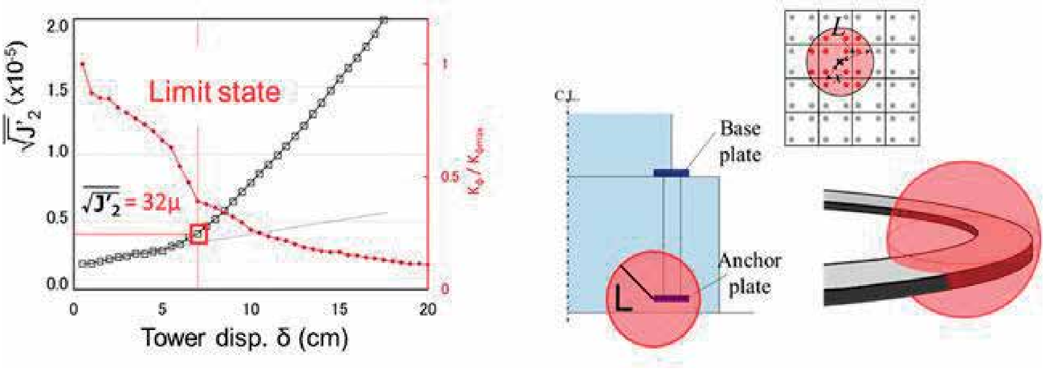

Figure 10. Horizontal displacement of tower versus the space-averaged second invariant of strain.

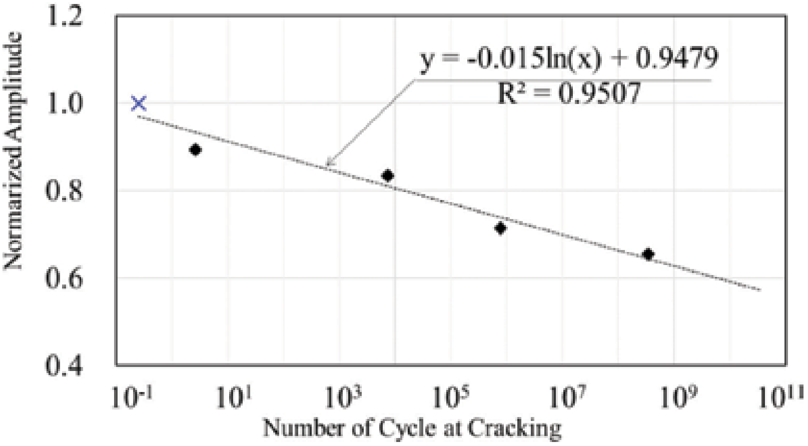

Figure 11. Normalized amplitude of horizontal load—cycles at cracking inside concrete based on FE analysis.

3.5. Evaluation of fatigue resistance of concrete foundation

The fatigue resistance of concrete foundation was examined by FE analysis. Since the horizontal reaction force at the top of tower when the moment was 1195 kNm was about 84kN in FE analysis, input horizontal load at the top of tower was offered as sine wave with different amplitudes. In addition, the number of cycles when the space-averaged second invariant of strain reach threshold value 0.00032 were calculated for each cases. The relationship between the normalized amplitude by 84kN and the number of cycle at threshold value was shown in **Figure 11**.

It should be noted that the design moment owing to the wind in this is 855 kNm that is 71% of the calculated moment 1195 kNm. Thus, according to **Figure 11**, the cracking inside pedestal concrete possibly starts after 763,888 swings of tower due to strong wind. However, the design moment considers safety factor as 3.0.

4. Laboratory experiment

4.1. Equipment, specimen and conditions

Since it is impossible to verify the failure mode and fatigue life of the target structure, laboratory experiment using the 1/12 scale model was prepared. In order to generate high cycle load with reliable stability, a bi-axial shaking table driven by magnetic force was employed for this study (see **Figure 12**). Tri-axial cyclic loading machine controlled hydraulic jack is not suitable for high cycle loading, even though the load generated by hydraulic jack can be higher than inertial force generated by a shaking table.

The overview of specimen is shown in **Figure 13**. This is basically designed as a 1/12 scale model of target structure shown in **Figure 1**. However, the reinforcement ratio in both pedestal and footing is higher than the real structure because it is impossible to simply scale down the diameter of reinforcing bars. The weight of blades and nacelle was 52.5 kgf that reflects the weight of steels set on the top of tower. The tower was made of STK400 steel pipe, and this model was reused for all foundation specimens. The tower model and foundation specimens were tight by eight M8 anchor bolts. The footing was fixed by four bolts at each corner of footing to shaking table.

Accelerometers were set at the top of tower and on top surface of footing to capture horizontal motions in two axes. Laser displacement meters and LVDTs were set for the top of tower and shaking table, respectively to compare the values with obtained from accelerometers. Strains of surfaces of pedestal concrete and surfaces of steel tower were measured by strain gauges. Furthermore, mold-type strain gauges were embedded beside eight anchor bolts to capture the trend of cracking inside concrete.

The conditions of all specimens are shown in **Table 2**. The laboratory experiment consisted of two series. The first series named "N-" was the prototype. The second series named "G-" installed gypsum between tower and foundation to smooth top surface of concrete specimens as well as monitoring strain gauges attached on the nut to control initial torque of anchor

Figure 12. Bi-axial shaking table driven by magnetic power.

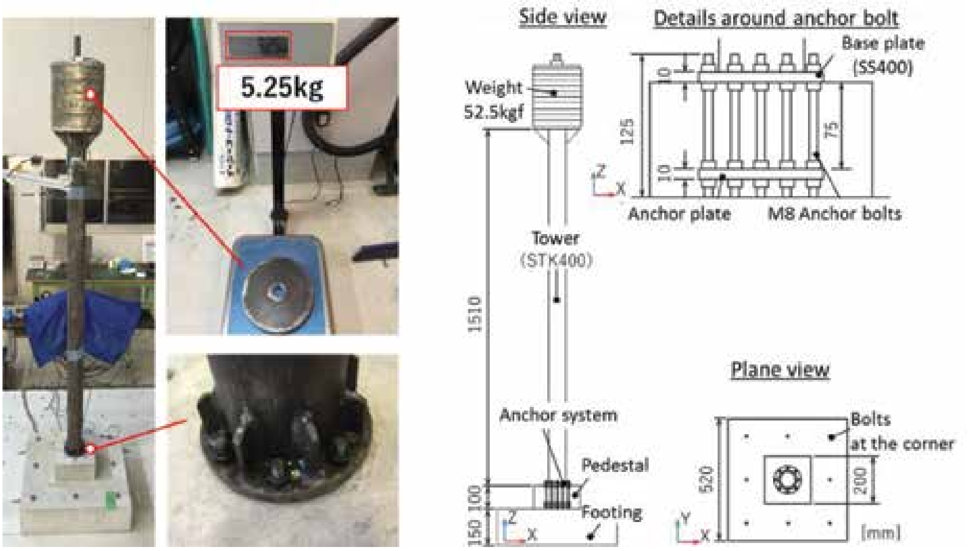

Figure 13. Photos and drawings of specimen.

bolts. All the specimens except G-D-E were examined by 5 Hz sine wave vibrating with different amplitudes. Furthermore, considering the change of main axis of tower vibration in time domain (see **Figure 3**), vibrating of X and Y axis in turn was tried for three cases, that is, N-D-500, N-D-400 and G-D-900. The other hand, G-D-E is the case using X and Y axis actuator simultaneously for reproducing ground acceleration record that was obtained in this area during Great East Japan Earthquake 2011.

4.2. Results

Since it is impossible to observe cracking inside concrete during experiment, the criteria of fatigue failure of these specimens were defined as 20 mm of relative horizontal displacement at the top of tower. It is large enough because 20 mm of the model is almost equivalent to 240 mm for the real structure. Another reason is that the specimens dangerously resonate when the relative displacement exceed 20 mm [19]. Because the natural frequency of specimens which is usually 6.5–7.6 Hz before loading had gradually decreased with increase of number of load cycle due to fatigue damage of concrete.

In the case of N-S-500, sudden fracture of an anchor bolt occurred, then loading was stopped. It failed but the failure mode was different from others. The four surviving cases did not show any changes in measurable data for a long time, then loading was canceled.

The comparison of the development of relative displacement at the top of tower for G-S-900 and G-D-900 was shown in **Figure 14**. It was clear that the G-S-900 under single axis vibration survived longer than G-D-900 under the vibrating of X and Y axis in turn. Interestingly, N-S-500 also survived longer than N-D-500 (see **Figure 15**), even though the failure mode of N-S-500 was different from N-D-500.

Case	Acc. amplitude (gal)	Direction	Cycle	Fail/survive	Gypsum & torque control	Compressive stress of concrete (Mpa)
N-S-700	700	X	1000	Fail	—	27.9
N-S-500	500	X	188,900	Fail*	—	27.9
N-D-500	500	X or Y	X 70,050 Y 64,950	Fail	—	27.9
N-S-400	400	X	102,300	Survive	—	27.9
N-D-400	400	X or Y	X 51,300 Y 51,300	Survive	—	27.9
G-S-900	700–900	X	51,000	Fail	G, T	27.6
G-D-900	700–900	X or Y	X 13,500 Y 13,220	Fail	G, T	27.6
G-S-600	600	X	201,300	Survive	G	27.6
G-S-900C	900	X	79,800	Fail	G, T	27.6
G-D-EQ	Seismic wave	X and Y	5minx10	Survive	G, T	27.6

Table 2. The conditions of all specimens.

The vertical strains inside concrete measured by embedded strain gauges were shown in **Figure 16**. The vibrating direction of G-S-900 is always along X axis. Thus, the amplitude of IS1 and IS5 located in the orthogonal direction was significantly smaller than others. The strains measured in G-D-900 vibrated in both directions demonstrated relatively larger amplitude than G-S-900 in all locations. This suggested that the cracking in wider area possibly accelerated the fatigue damage and led shorter fatigue life.

In order to observe internal cracks, concrete parts were cut in two directions after the loading (see **Figure 17**). The expected cracks from the tip of anchor plate could not be seen clearly for G-S-900 and other specimens under single axis loading, except N-S-700 that failed rapidly in

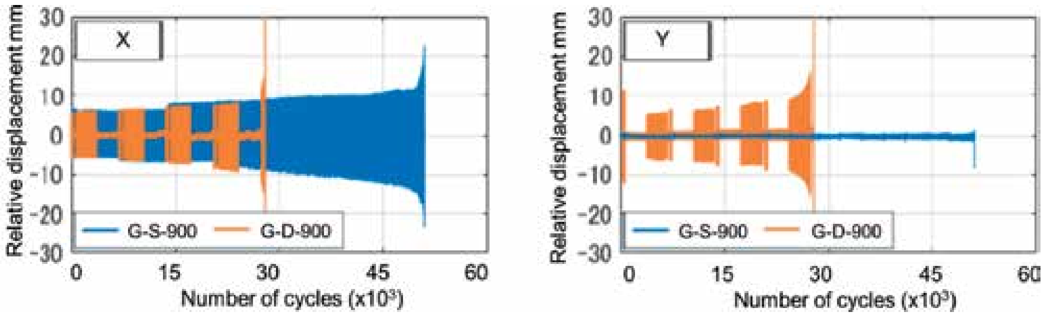

Figure 14. The development of relative displacement at the top of tower (G-S and G-D).

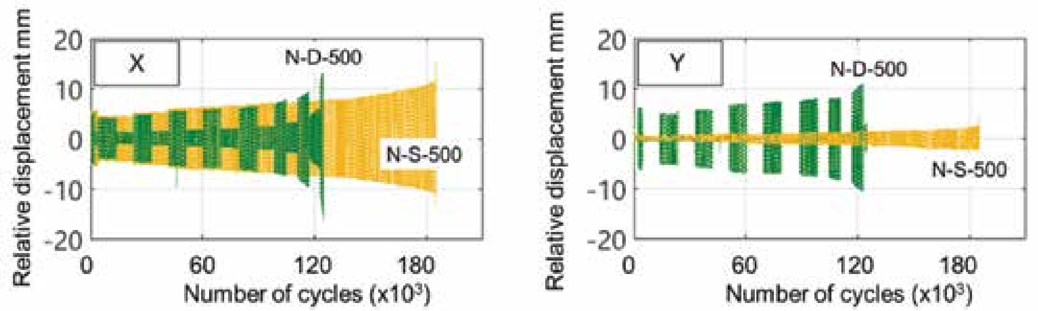

Figure 15. The development of relative displacement at the top of tower (N-S and N-D).

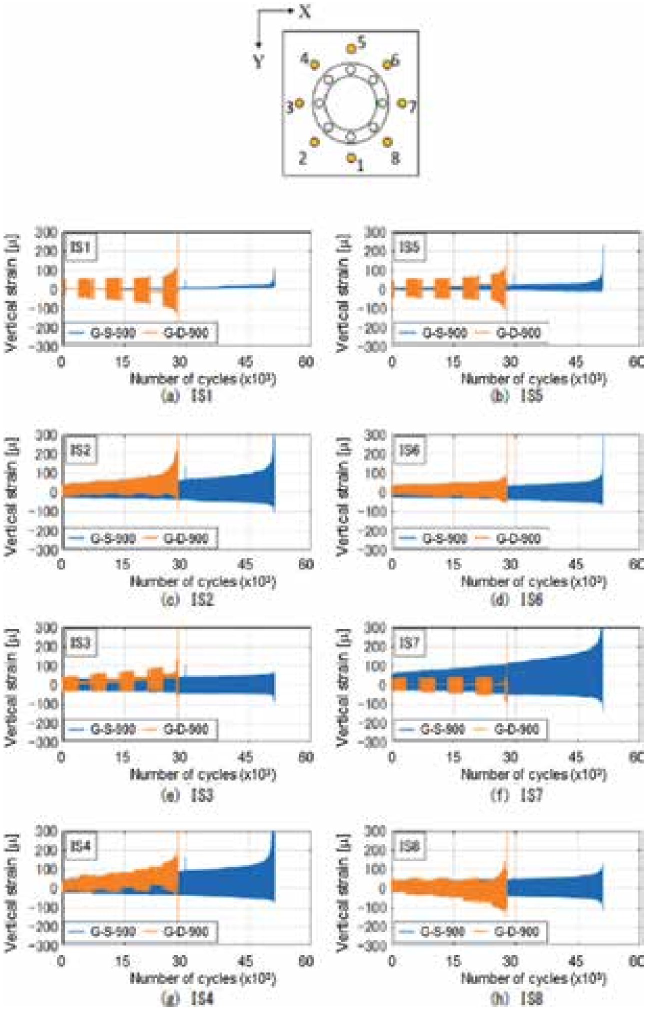

(a) IS1
(b) IS5
(c) IS2
(d) IS6
(e) IS3
(f) IS7
(g) IS4
(h) IS8

Figure 16. Vertical strain inside concrete for G-S-900 and G-D-900.

1000 cycles. Alternatively, unexpected crack at the connection of pedestal and footing was found as pointed by arrows in **Figure 17**. In contrast, obvious cracks were found in both cross sections for G-D-900. On the other hand, the difference was not clear between N-D-500 and N-S-500. These cracks did not always consistent with the internal strains measured by embedded gauge. In other words, it is not easy to capture the occurrence of cracks inside concrete. It should be noted that the strain measured at the bottom of steel tower always remained less than 500 μ, even the model of tower was reused repeatedly.

4.3. Evaluation of fatigue life

The equivalent numbers of cycle were calculated based on Miner's rule [20] shown in Eq. (4) for G-S-900 and G-D-900 because amplitude of input acceleration was increased step by step for these cases.

$$N_{eq} = \sum_{i=1}^{n} \left(\frac{P_i}{P}\right)^{m} \cdot n_i \tag{4}$$

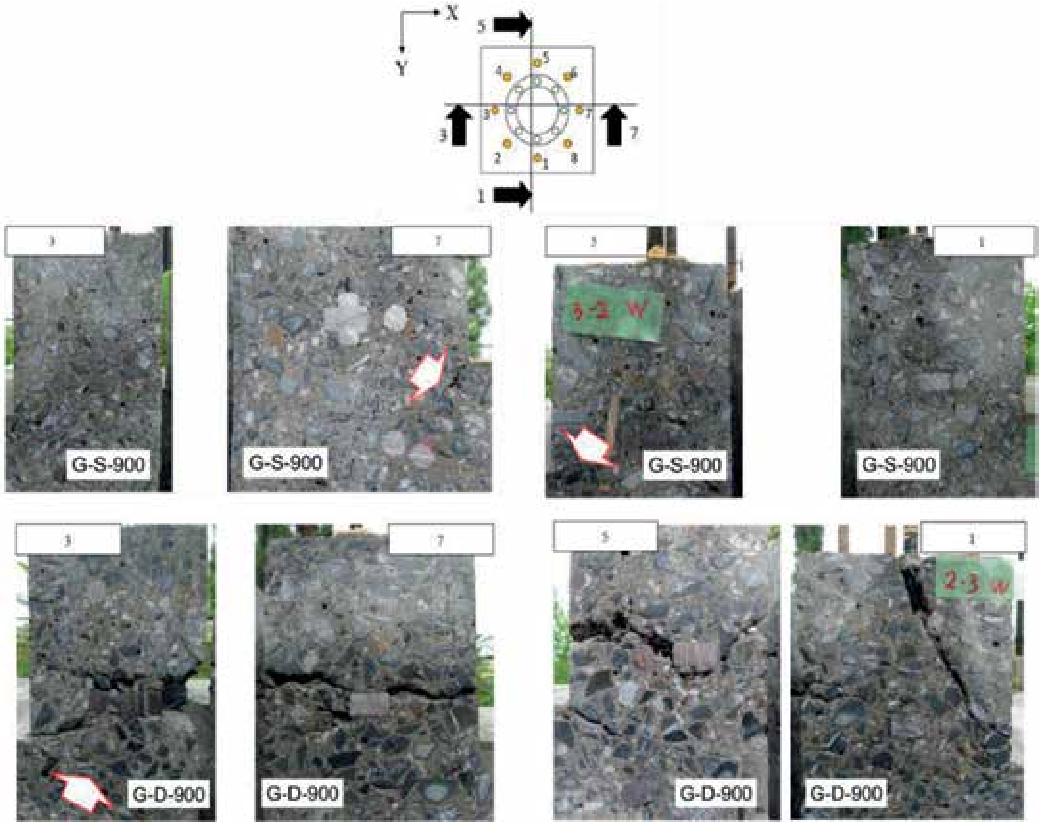

Figure 17. Internal cracks observed after loading for G-S-900 and G-D-900.

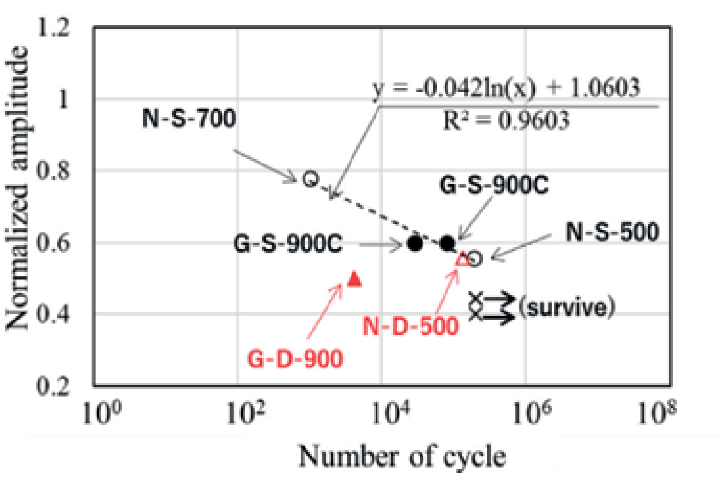

Figure 18. Normalized amplitude of horizontal load—cycles at failure based on experiment.

where N_{eq} is the equivalent number of cycle, P_i is the load, P is the standard load, n_i is the number at P_i, m is the incline of material stress-number of cycle (S-N) curve for fatigue. The m was assumed as 17 based on the S-N curve for fatigue of concrete [20]. If we assume P = 900 gal, the N_{eq} is 28,378 for G-S-900 and the N_{eq} is 4098 for G-D-900.

Furthermore, the difference of experiment conditions between "N-" series and "G-" series should be considered for evaluation. The ultimate load that can make collapse of structure at one cycle should be different in two series. The ultimate acceleration that is proportional to ultimate inertial force at the top of tower was assumed as 800 gal and 1300 gal for "N-"and "G-," respectively.

The number of cycles at each normalized amplitudes in this experiment was summarized in **Figure 18**. The approximate curve for single directional vibration is also shown in the figure. According to this figure, the fatigue life of the specimens vibrated in two directions; N-D-500 and G-D-900 tend to be shorter than lives under single directional vibration.

5. Conclusions

This chapter shows research of stability of supporting structure of onshore wind turbine foundations based on field measurements, finite element (FE) analysis and laboratory experiment. The vibration characteristics of tower were clarified by field measurement. Then, the damage process of reaching failure was examined by FE models. In addition, limit state of foundation was defined by fatigue limit state of concrete. The space-averaged second invariant of strain was proposed as useful index. Consequently, the stress-number of cycle (S-N) diagram derived from laboratory experiment was shown. That suggested that the fatigue life of the specimens vibrated in two directions tends to be shorter than lives under single directional vibration.

Acknowledgements

The authors are grateful to Ueda Y. and Tsuruoka O. for their contributions to the laboratory experiment. The laboratory experiment in this study was financially supported by KAJIMA FOUNDATION from 2016 to 2018. We also wish to thank the Higashi-izu Town government office for sharing its dataset treated in this study.

Author details

Chikako Fujiyama[1]*, Yasuhiro Koda[2] and Noriaki Sento[2]

*Address all correspondence to: fujiyama@hosei.ac.jp

1 Department of Civil and Environmental Engineering, Faculty of Design and Engineering, Hosei University, Tokyo, Japan

2 Nihon University, Koriyama, Fukushima, Japan

References

[1] Global Wind Energy Council. Global Wind 2007 Report, GWEC 2008

[2] Global Wind Energy Council. Global Wind 2016 Report, GWEC 2017

[3] http://www.caithnesswindfarms.co.uk/AccidentStatistics.htm [Accessed: February 09, 2018]

[4] Alonso TR, Dueñas EG. Crack analysis in onshore wind turbine foundations. IABSE Madrid Symposium Report. 2014;**102**:1086-1092

[5] Currie M, Saafi M, Tachtatzis C, Quail F. Structural integrity monitoring of onshore wind turbine concrete foundations. Journal of Renewable Engergy. 2015;**83**:1131-1138

[6] Hassanzadeh M. Cracks in onshore wind power foundations – causes and consequences. Elforsk Rapport. 2012;**11**:56

[7] Chijiwa N, Hong TM, Iwanami M, Saito T, Yamaya A, Motegi H, Shinozaki H. Rapid degradation of concrete anchorage performance by liquid water. Journal of Advanced Concrete Technology. 2015;**13**(10):438-448

[8] Bai X, He M, Ma R, Huang D, Chen J. Modelling fatigue degradation of the compressive zone of concrete in onshore wind turbine foundations. Journal of Construction and Building Materials. 2017;**132**:425-437

[9] Unobe ID, Sorensen AD. Multi-harzard analysis of a wind turbine concrete foundation under wind fatigue and seismic loadings. Jounal of Structural Safely. 2015;**57**:26-34

[10] Yonetsu K, Fujiyama C, Kado M, Maeshima T, Koda Y. Fatigue evaluation for RC foundation of wind turbine based on field measurement and nonlinear FE analysis. Journal of JSCE E2. 2016;**72**(2):68-82 (in Japanese)

[11] Swarzt RA, Lynch JP, Zerbst S, Sweerman B, Rolfes R. Structural monitoring of wind turbines using wireless sensor networks. Smart Structural and System. 2010;**6**(3):183-196 (USA)

[12] Rumsey MA, Paquette JA. Structural Health Monitoring of Wind Turbine Blades. Albuquerque: Sandia National Laboratories; 2007

[13] Fujiyama C, Yonetsu K, Maeshima T, Koda Y. Identifiable stress state of wind turbine tower-foundation system based on field measurement and FE analysis. Procedia Engineering. 2014;**95**:279-289

[14] Maekawa K, Toongoenthong K, Gebreyouhannes E, Kishi T. Direct path integral scheme for fatigue simulation of reinforced concrete in shear. Journal of Advanced Concrete Technology. 2006;**4**(1):159-177

[15] Maekawa K, Gebreyouhannes E, Mishima T, An X. Three-dimensional fatigue simulation of RC slabs under traveling wheel-type loads. Journal of Advanced Concrete Technology. 2006;**4**(3):445-457

[16] Shimodate H, Fujiyama C, Koda Y, Kado M. Analysis of vibration characteristic of wind turbine and prediction of failure mode of footing-tower direct connection system. In: Proceedings of 71st Annual Conference of JSCE; 2016. pp. 13-14 (in Japanese)

[17] Saitoh S, Maki T, Tsuchiya S, Watanabe T. Damage assessment of RC beams by nonlinear FE analyses. Journal of JSCE E2. 2011;**67**(2):166-180 (in Japanese)

[18] Yonetsu K, Fujiyama C, Koda Y, Maeshima T. Strain index for wind turbine tower-foundation joint by using nonlinear FE analysis. In: Proceedings of 70th Annual Conference of JSCE; 2015 (in Japanese)

[19] Ueda Y, Fujiyama C, Sentoh N, Koda Y. Fatigue experiment of wind turbine tower-foundation joint by using shaking table. In: Proceedings of 71st Annual Conference of JSCE; 2016. No. CS3-008 (in Japanese)

[20] Japan Society of Civil Engineers. Standard Specification for Concrete Structures 2007. Design; 2007

Chapter 7

Estimation Method to Achieve a Noise Reduction Effect of Airfoil with a Serrated Trailing Edge for Wind Turbine Rotor

Jaeha Ryi and Jong-Soo Choi

Additional information is available at the end of the chapter

http://dx.doi.org/10.5772/intechopen.73608

Abstract

This chapter describes a wind tunnel experiment that was undertaken to investigate the changes in the aerodynamic performance of a wind turbine due to the inclusion of a 2-Dimension (2D) airfoil with a serrated trailing edge designed to reduce the noise caused by a wind turbine rotor blade. The restrictive condition for the serrated trailing edge equipped with the use of a 2D airfoil was examined through the use of a wind tunnel experiment after studying existing restrictive condition and analyzing prior research on serrated trailing edges. The study was conducted according to Howe's theory, which is a cornerstone of the study of noise reduction effects produced by a serrated trailing edge. For the serrated trailing edge equipped on a 2D airfoil, the wake distribution and the relation to noise were analyzed in order to determine the restrictive condition in accordance with Howe's theory. The results indicated that an empirical formula or a theoretical approach should consider changes in the boundary layer thickness of a 2D airfoil, so an empirical noise prediction formula is suggested for the serrated trailing edge. Also, a comparison and an analysis of the prediction and the experimental results for the noise produced by the NACA0012 or the baseline airfoil equipped with a serrated trailing edge suggested a novel formula for a 2D airfoil. Finally, the 2D airfoil noise data are compared with wind tunnel test data by using an empirical formula estimation method.

Keywords: wind turbine noise, trailing edge serration, wind tunnel test, 2D airfoil noise test, noise reduction effect

IntechOpen

1. Introduction

Studies on serrated trailing edges have been conducted in order to find solutions to noise problems in the wind turbine rotor field. In 1991, Howe [1] suggested a theory to predict noise reduction in a 2D airfoil with a serrated trailing edge. He defined the variables depending on the shapes of the edges and identified differences in noise reduction depending on various aspect ratios of serrated trailing edges. Based on Howe's serrated trailing edge theory, Braun [2] confirmed in 1999 that noise produced by a wind turbine rotor could be reduced by the application of a serrated trailing edge with a diameter of 16 m, and observed that changes in the frequency domains of noises occurred depending on the installation angles of serrated trailing edges.

In 2009, Gruber and Joseph [3] reported the noise reduction effect and the boundary layer thickness of a serrated trailing edge on a 2D airfoil by designing a 2D airfoil based on Howe's theory. Oerlemans et al. [4] applied a serrated trailing edge to a 2.3 MW wind turbine rotor to observe noise changes, and used the beam-forming method to confirm noise changes.

From 2010 to the current, Phillip [5] has been conducting a wind tunnel test on a sawtooth-shaped trailing edge and a slit-shaped trailing edge, and has confirmed the noise reduction effect and predicted noise changes based on Howe's theory. Michel Roger [6] carried out a wind tunnel test on five types of blush-shaped trailing edges. Based on the cross-section of the 2D airfoil of NACA65(12)-1, changes in the frequency components caused by variations in wake and flow were recorded using a hot-wire anemometer. In 2012, Dennis Y.C. Leung [7] applied a trailing edge with a 0° angle of attack to a 2D airfoil, and confirmed noise reduction effects owing to changes in the aspect ratio of serrated trailing edges.

As mentioned above, the theoretical background of the previous studies was based on Howe's theory, but among the experiments involving wind tunnel tests and the actual wind turbine rotor tests, none showed improvements in both aerodynamic performance and noise performance simultaneously. Also, the studies on the noise reduction effect of serrated trailing edges only confirmed the noise reduction effects, while most of the studies on aerodynamic performance also only showed changes in noise performance.

This study aimed to examine changes in both aerodynamic performance and noise reduction by applying serrated trailing edges to 2D airfoils in a wind tunnel experiment. Also, this study proposes a prediction model for noise reduction effects with the use of serrated trailing edges, based on the experimental results obtained from the wind tunnel test.

2. Theoretical background of trailing edge serration

2.1. Noise reduction mechanism of trailing edge serrations

The noise reduction mechanism of trailing edge serrations was introduced by Howe based on an experiment on trailing edge noises in a 2D airfoil [1]. **Figure 1** shows the shape-related variables of

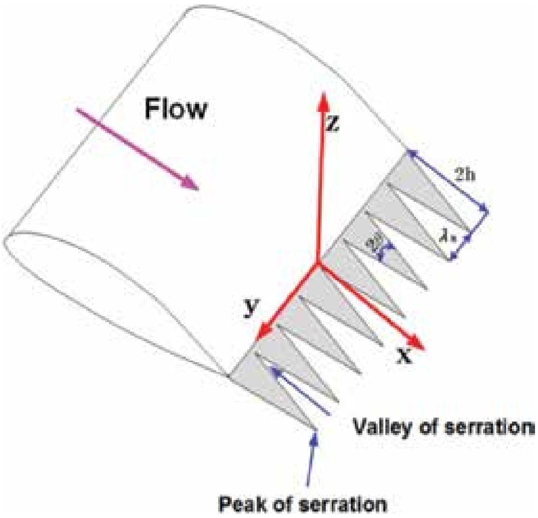

Figure 1. Turbulent flow over a serrated trailing edge [1].

serrated trailing edges applied to 2D airfoils in this study. The noise reduction effects of the serrated trailing edges were defined with the following criteria: span-wise wavelength (λs), amplitude of serrations (h), incline angle (θ), main stream velocity (U), and acoustic frequency (ω).

Howe's theory of the noise reduction effect induced by the use of trailing edge serrations is based on the following preconditions:

1. The airfoil of a serrated trailing edge has a plate shape, and the span of a rotor blade is infinitive.
2. Noises are produced by the turbulent components that pass through the trailing edge with a 0° angle of attack, under the condition that noises are only present in the trailing edge.
3. The Kutta condition is met, and the flow that passes through the plate-shaped airfoil has a low Mach number.
4. Under the same flow conditions, the ratios between the amplitude of serrations and the boundary layer thickness and the wake of 2D airfoils are constant.

Based on the above preconditions, Howe [1] proposed an equation for noise reduction accomplished by serrated trailing edges. Eq. (1) is a function which defines the noise reduction effect (Ψ(ω)) induced by trailing edge serrations with boundary layer thickness (σ), span-wise wavelength (λ), and blade-tip clearance based on the turbulent fluctuation frequency (ω) [1].

$$\Psi(w) = \left(1 + \frac{1}{2}\epsilon\frac{\partial}{\partial\epsilon}\right) f\left(\frac{w\delta}{U_c}, \frac{h}{\lambda}, \frac{h}{\delta}; \epsilon\right) \tag{1}$$

Eq. (2) was created with the root-to-tip distance set at "h ≥ 0", for the case in which a serrated trailing edge is not used.

$$\Psi_0(w) = (w\delta / U_c)^2 / [(w\delta / U_c)^2 + \epsilon^2]^2 \tag{2}$$

The noise reduction effects of serrated trailing edges are produced by changes in the noise components of the turbulent boundary layers of 2D airfoils. At this time, the turbulence-induced frequency is assumed to meet the condition, and the changes in the turbulent boundary layer of serrated trailing edges resulted in the reduction of noises greater than the minimum. Also, under the same boundary layer conditions, the varying noise reduction effects depend on the different aspect ratios of serrated trailing edges [1, 8].

However, when a plate-shaped serrated trailing edge was applied to a 2D airfoil in an actual experiment, it is impossible to meet the preconditions proposed by Howe, which entail an experimental environment with a 0° angle of attack and a constant ratio between the blade-tip clearance and the boundary layer thickness of serrated trailing edges.

In this study, the authors confirmed the preconditions proposed by Howe for the noise reduction effect brought about by the use of serrated trailing edges, and identified the factors restricting the noise reduction effects when a serrated trailing edge is applied to a 2D airfoil in a wind tunnel test. Also, the study proposed a model that predicts airfoil self-noises. In addition, the study utilized the wind tunnel test results to review the validity of the noise prediction empirical model for 2D airfoil self-noises, which was introduced by Brooks.

3. Experimental apparatus and procedures

3.1. 2-Dimension airfoil noise test

This study conducted a wind tunnel test on 2D airfoils in a closed test section with a size of 1.25 × 1.25 m by using the subsonic anechoic wind tunnel test facility at Chungnam National University. The wind tunnel experimental apparatus was set up to measure aerodynamic performance and noise reduction, as seen in **Figure 2**. To assess the aerodynamic performance of 2D airfoils, a three-axis balance was used, whereas a pressure scanner system with 50 pressure holes and 50 channels was installed in order to measure the pressure distribution. Also, a microphone system with a total of seven channels was installed to measure noises, as shown in **Figure 3**. A wind tunnel experiment was measured in the low-speed semi-anechoic wind tunnel at Chungnam National University. The volume of the anechoic chamber was 211.9 m^3 and the tapered anechoic chambers had a cut-off frequency of 150 Hz [9].

Figure 4 shows the 2D cross-section of the experimental models with a downscaled radius 75% as large as the size of an actual rotor. The rotor blade had a chord length of 0.35 m and a span of 1.249 m, and it was made of 60-class aluminum in order to minimize the possible structural vibrations and noises of the experimental models during the wind tunnel test. The model was installed with a structure supporting both ends (by fixing the upper and lower blades) and on a turn table with 360° rotation, and the wind tunnel velocity and airfoil angles of attack could

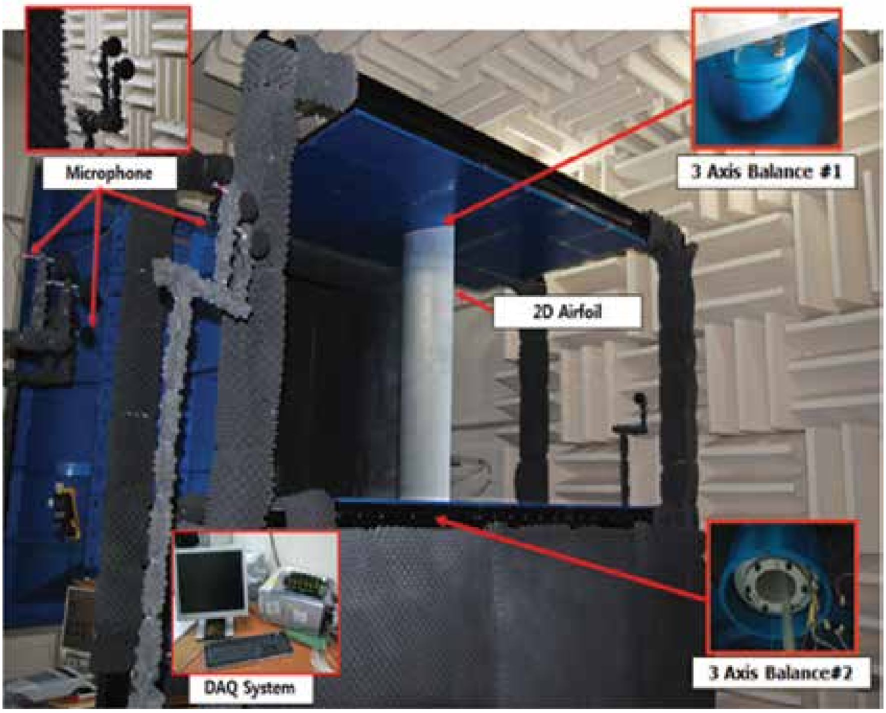

Figure 2. Configuration of wind tunnel test stand for airfoil experiment.

be adjusted depending on the experimental conditions. The aerodynamic performance of the experimental models was measured during the experiment by installing 2EA of three-axis balance. The aerodynamic performance and noise performance were simultaneously measured by installing each three-axis balance in the upper and lower part of the wind tunnel test section and by fixing both tips of the experimental model. The noise performance test was conducted with a wind velocity of about 30 m/s (RE = 700,000) and a Reynolds number in consideration of the downscaling of the rotor radius to 75% of actual size. Noises were measured with a total of seven microphones, which were installed 1750 and 1830 mm away from the trailing edge of the blade. In the 2D airfoil experiment, **Figure 5** shows the total of 7 types of serrated trailing edges were tested together with airfoils; basic information about the shapes of serrated trailing edges is described in **Table 1**. The wind tunnel test on 2D airfoils was conducted in an open experimental section in order to measure the aerodynamic performance and noise performance at the same time. In this case, precise calibration of the open experimental section was necessary to measure aerodynamic performance. Wind tunnel tests in open experimental sections are often subject to a simultaneous occurrence of flow stream line curvature and down-wash deflection phenomena, which rarely happens in free-air conditions. These phenomena resulted in a decrease in the angles of attack and the lift curve slope of the 2D airfoils, and caused drag-changing shapes. The calibration methods suggested by Brooks & Marcolini [11]

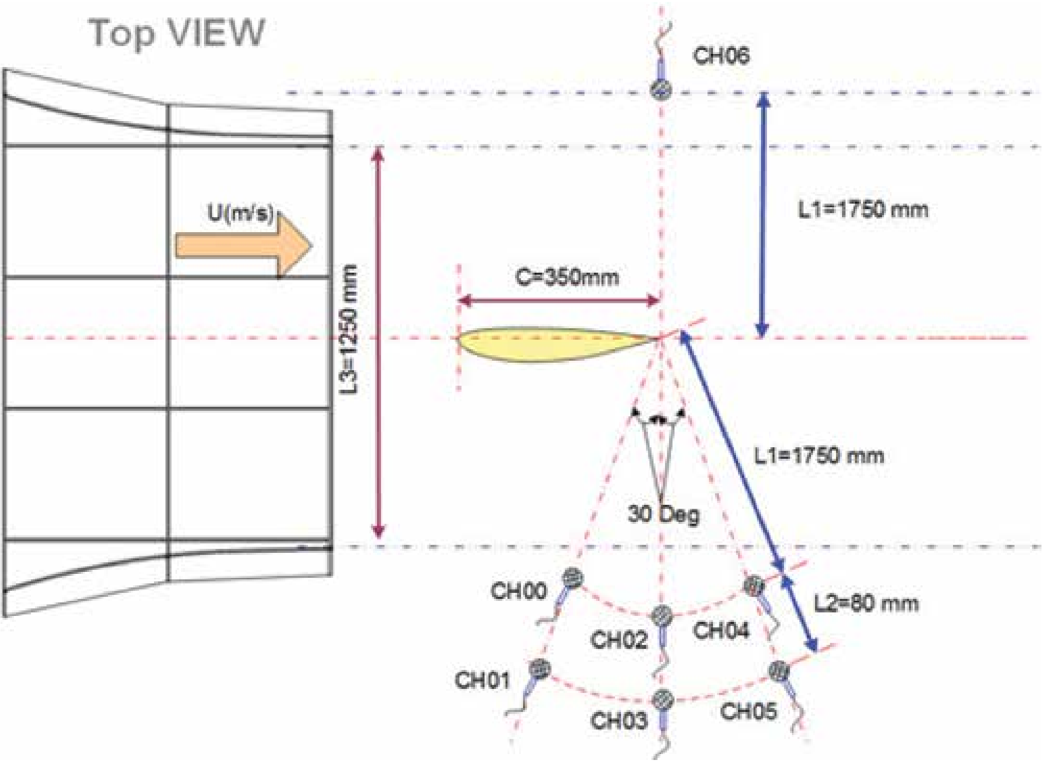

Figure 3. Layout of the microphone array for the 2D airfoil noise test in the open-jet wind tunnel.

and by Garner et al. [12] were applied; tunnel height and chord length were used as major variables in the two calibration methods. The aerodynamics performance experiment results of the 2D airfoil have been introduced by Ryi & Choi [8].

3.2. Noise measurement results of 2D airfoils with trailing edge serrations

Figure 6 shows the differences in noise levels between a 2D airfoil with a rectangular plate-shape trailing edge and a 2D airfoil with serrated trailing edges. A noise value greater than zero indicates the presence of a noise reduction effect. A noise value smaller than zero indicates the absence of a noise reduction effect. It was observed that the noise effect increased with an increase in the angle of attack, and the maximum noise reduction reached about 3 dB.

These experimental results confirmed that the use of serrated trailing edges can improve aerodynamic performance and noise performance. This study intended to confirm the noise reduction effect of serrated trailing edges by applying trailing edge serrations to an existing rotor system.

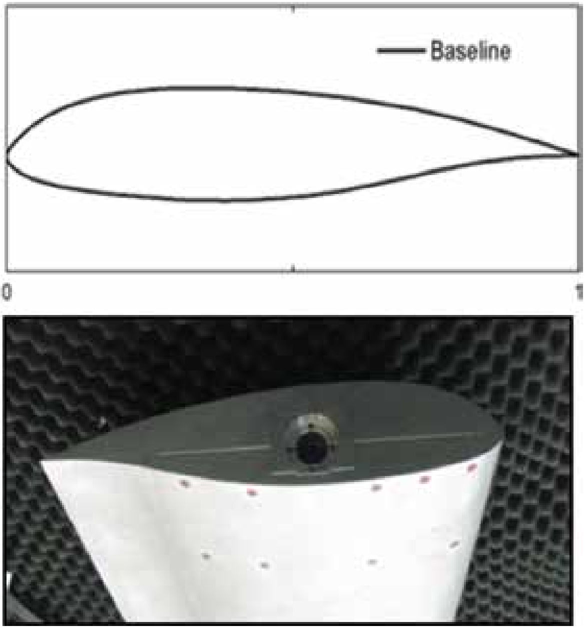

Figure 4. Baseline airfoil test model [10].

$$L_{differance}(dB) = L_{baseline}(dB) - L_{serrated\ T.E.}(dB) \tag{3}$$

As seen in Eq. (3), the study compared differences in noise between the plane-shaped trailing edge and the serrated trailing edge within the same frequency domain. As seen in **Figure 7**, the results confirmed a noise reduction effect in the frequency range of about 500 Hz–20 kHz.

3.3. Experiment on wake characteristics of 2D airfoils with serrated trailing edges

If a serrated trailing edge is attached to a 2D airfoil, a noise reduction effect is produced. However, in such a case, the basic preconditions suggested by Howe's theory are not satisfied, according to the results of previous experiments. This study assumed that the Howe's precondition amplitude of serrations and the boundary layer thickness of 2D airfoils are constant, and this is not satisfied. For this reason, the study set up the experimental apparatus to measure the wake of 2D airfoils, as seen in **Figure 8**, and used a single axis hot-wire anemometer to measure the wake in the y/C direction (span-wise) and in the z/C direction (wake-wise) of serrated trailing edges as well as 8 different types of airfoils.

Figure 9 shows the results of the experiments conducted with eight types of airfoils. Because of the shapes of the serrated trailing edges, measurements were taken at 240 mm. In the case of 2D airfoils with rectangular plate trailing edges, there were no changes in frequency in the span-wise direction depending on the shapes of the serrations, and there were no abnormal phenomena. However, this study assumes distinctive frequency patterns depending on the shapes of serrations and the peak and valley positions. Therefore, the study demonstrated

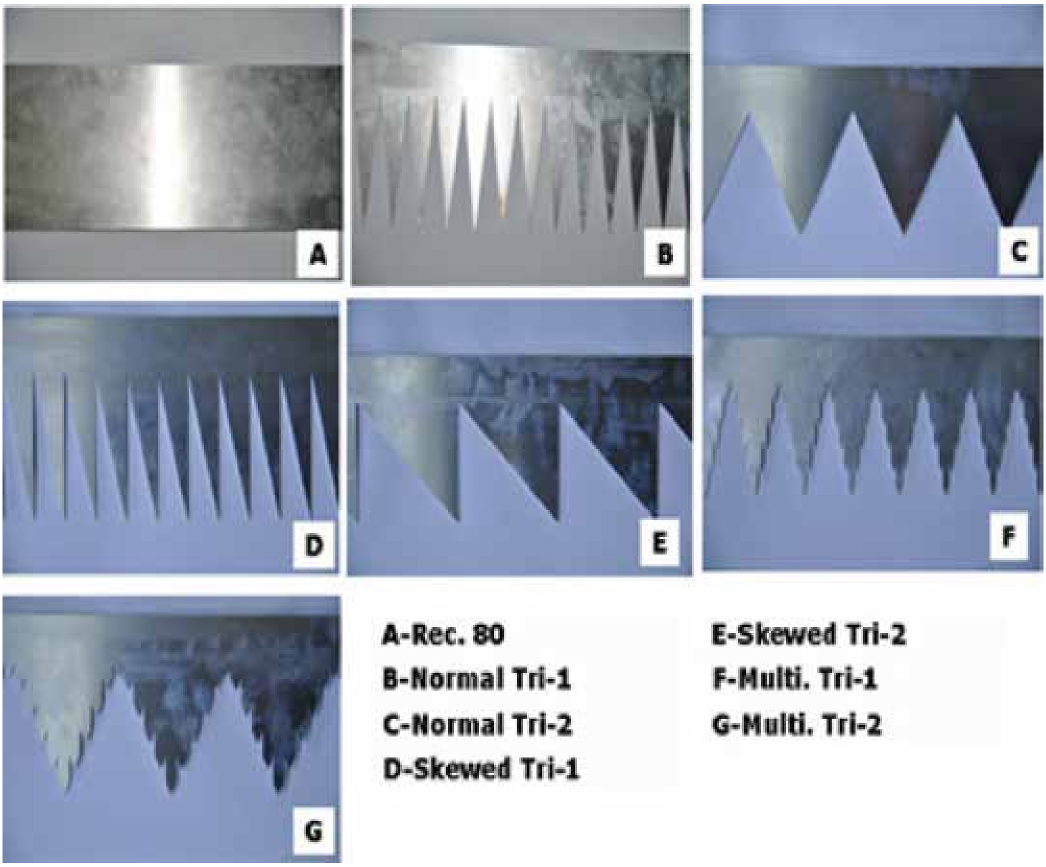

Figure 5. Serration trailing edge test model [10].

Serration type	**λ/h**	**θ (°)**	**λ_s (mm)**	**2h (mm)**
Baseline	N/A	N/A	N/A	N/A
Rec80	N/A	N/A	N/A	N/A
Nor. Tri (narrow)	0.5	7.125	20	80
Nor. Tri (wide)	2	26.565	80	80
Skew. Tri (narrow)	0.5	14.03	20	80
Skew. Tri (wide)	2	22.5	80	80
Multi. Tri (narrow)	1	28.07	40	80
Multi. Tri (wide)	2	26.565	80	80

Table 1. Serrated trailing edge configuration.

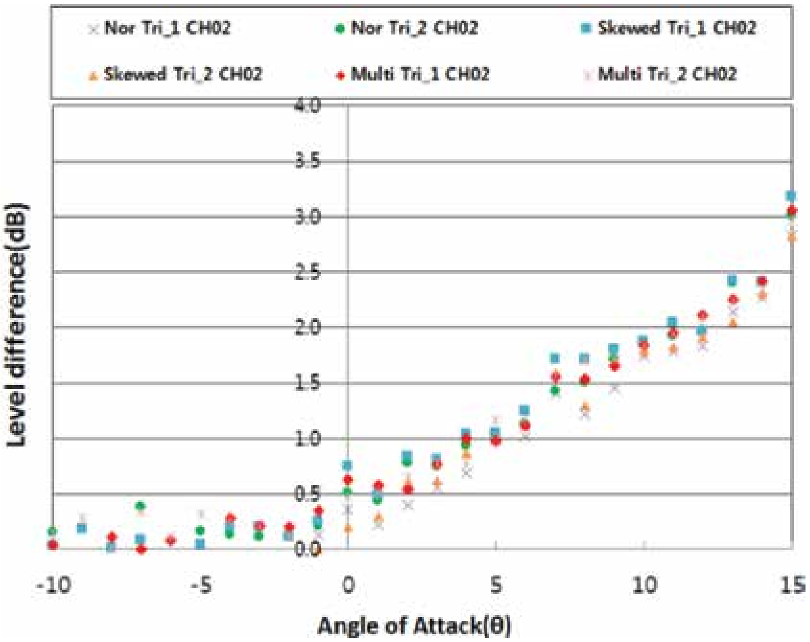

Figure 6. Noise level difference of baseline airfoil with serration trailing edge.

differences in the components of vortex shedding frequency in the wake of the trailing edge when serrated trailing edges were used, under the same operating conditions as for 2D airfoils.

3.4. Measurement of serrated trailing edge wake (*included information*)

The results of the wake measurement of 2D airfoils with serrated trailing edges in the y/C direction revealed that frequency changes occurred depending on the peak and valley positions of the serrated trailing edges. Based on these experimental results, the wake in the z/C direction was measured via the mean flow distribution, depending on the locations of the serrated trailing edges in the span-wise direction. **Figure 10** shows a conceptual diagram of the wake measurement experiment in the z/C direction using the same experimental devices as for the wake measurement experiment in the y/C direction. **Figure 11** gives information about the axial directions of serrated trailing edges and the wake measurement locations. The tip of the serrated trailing edge was defined as the peak, while the inside of the serrated trailing edge was defined as the valley. The wake measurement experiment was conducted by defining the (x, y, z) axes of the tip of the serrated trailing edges as (0, 0, 0).

Figure 12 shows the results of the wake measurements of six types of serrated trailing edges. When serrated trailing edges were attached, varying wake distributions were observed depending on the types of serrated trailing edges. Boundary layer changes of the 2D airfoils and different flow distributions in the peak and valley positions were observed. According to these results, the precondition suggested by Howe to explain the noise reduction effect of serrated trailing edges, that all the boundary layer thicknesses are constant, was not satisfied.

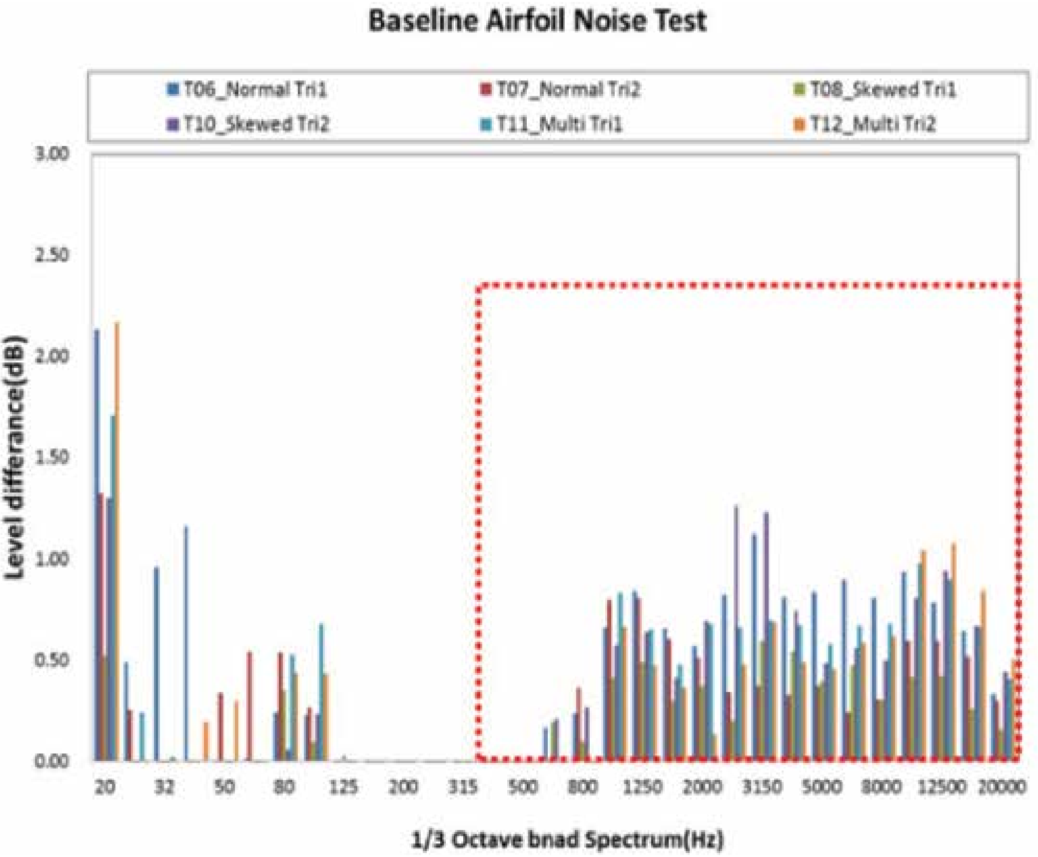

Figure 7. Noise reduced effect for serration trailing edge.

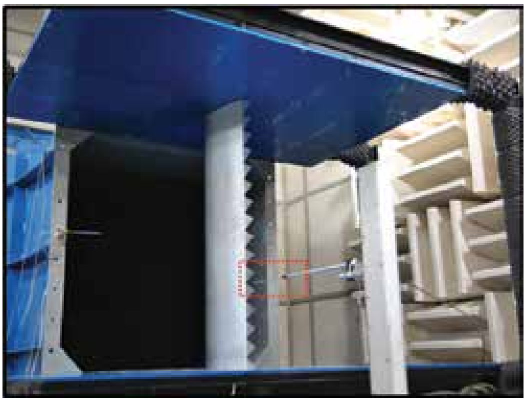

Figure 8. Configuration of wind tunnel test stand for airfoil wake measurement system.

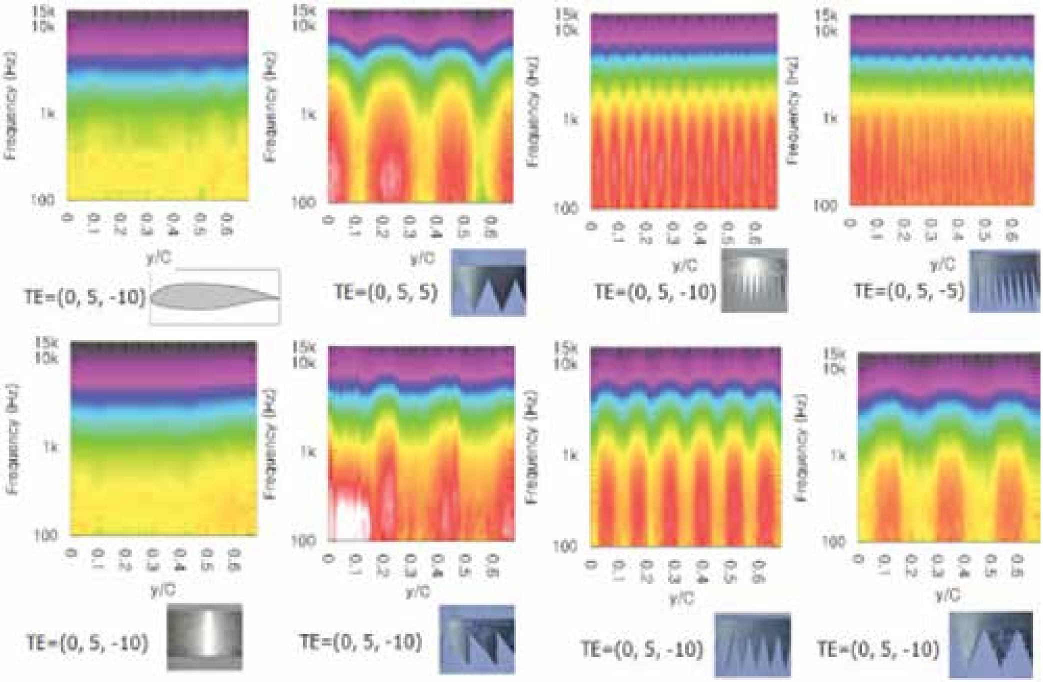

Figure 9. Velocity spectral map for the plate with serrations measured in the span-wise direction: various serration plate.

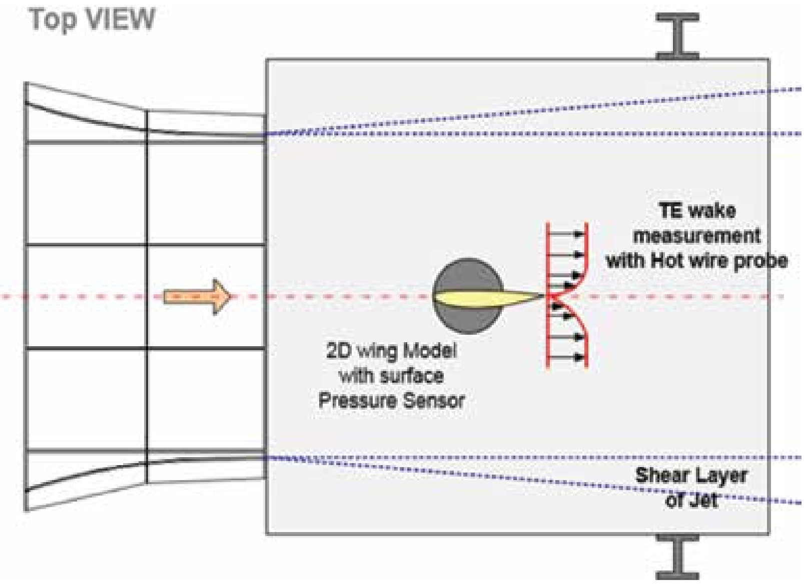

Figure 10. Layout of wake measurement for serration trailing edge in the z-axis direction [8].

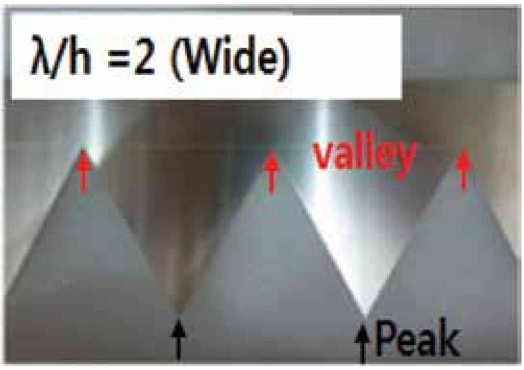

Figure 11. Layout of serration plate [8].

4. Empirical formula for noise reduction prediction in 2D airfoils with serrated trailing edges

In this chapter, we confirmed the noise reduction effect induced by serrated trailing edges and identified changes in aerodynamic performance and noise performance. Thus, this study confirmed changes in the frequency components in the wake and the velocity distribution when a serrated trailing edge was attached to a 2D airfoil.

Noise in a 2D airfoil is caused by the boundary layer between the surfaces of the blades, the vortex in the blades, and blade interference. The noise in the wind turbine blade cross-section is defined as self-noise, and different characteristics of self-noise were observed depending on the cross-sectional shape of the blade, flow conditions, and angles of attack. As 2D airfoil self-noises are usually caused by a combination of multiple factors, it is difficult to identify the exact cause of changes. Brooks et al. [13] suggested an empirical prediction formula based on the results of an aerodynamic noise experiment conducted on an NACA0012 airfoil.

The current study suggests a noise prediction formula for serrated trailing edges using the acoustic model suggested by Brooks, thickness and material for serration strip based on the results of the aerodynamic noise test and the wind tunnel test conducted on serrated trailing edges [14].

$$SPL_{Total} = SPL_{TBLTE} - SPL_{serration\ T.E} \tag{4}$$

The 2D airfoil noises which occur in the wind tunnel test are often heavily influenced by turbulent boundary layers. Based on this fact, Eq. (4) was designed to exclude those noise components which can be altered by serrated trailing edges. **Figure 13** presents information on the noise components of 2D airfoils with serrated trailing edges.

Figure 14 shows the "Bell-Type" function for serration trailing edge about Frequency Domain. As seen in Eqs. (5)–(10), the results confirmed noise reduction effect for various aspect ratios of serrations trailing edge [10] (**Figure 14**).

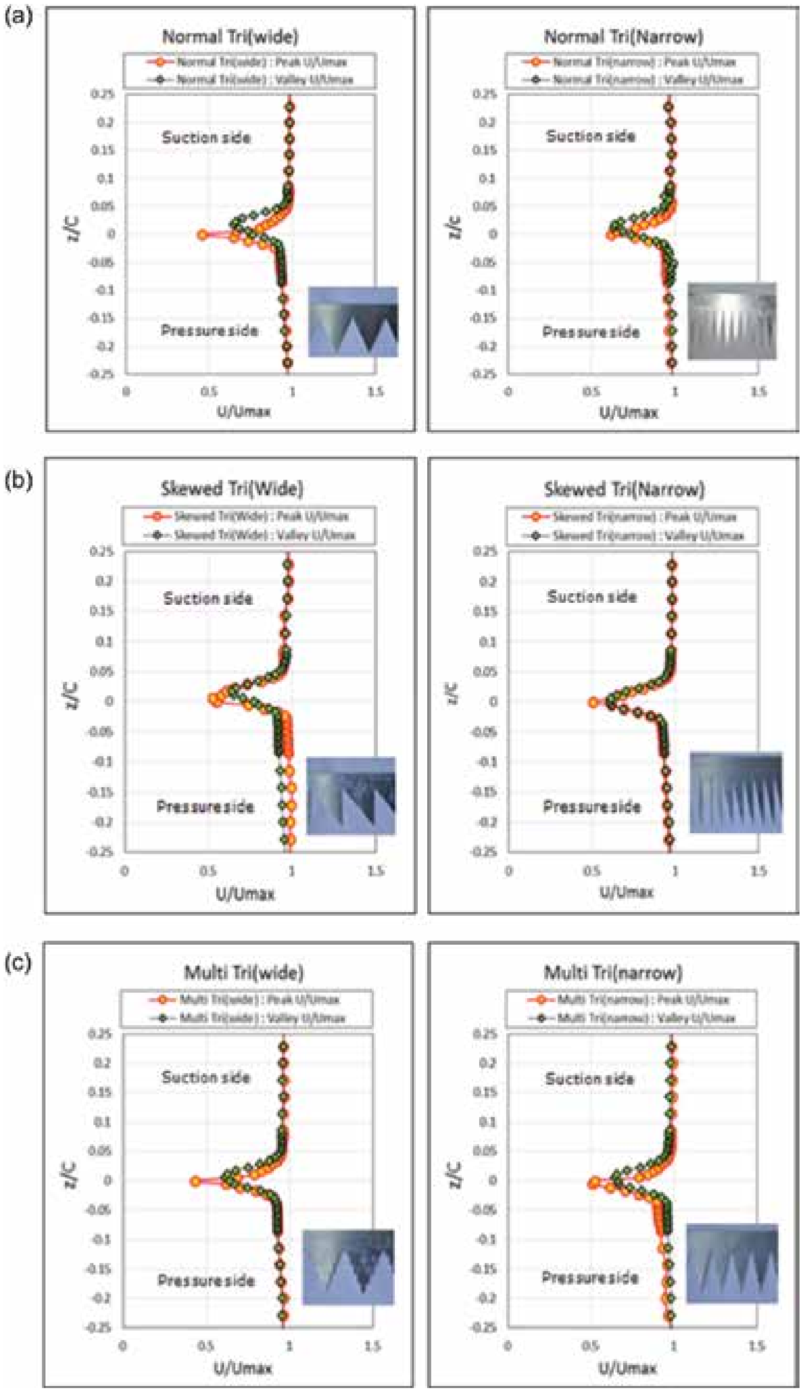

Figure 12. Mean velocity distribution for the plate with different serrations measured in the z axis direction [8]. (a) Nor-mal-type serrations; (b) skewed type serrations; (c) multi-type serrations.

- The predicted sound field spectrum [10]

$$S(f) \approx \frac{1}{8\pi^2 R^2}\left(\frac{U_c L}{c_0}\right) l_y(f)\Phi(f) \tag{5}$$

- Oscillatory function of trailing edge

$$l_y(f) = \frac{U_c}{\varepsilon 2\pi f} \tag{6}$$

- Surface pressure Term: Frequency domain

$$\Phi(f) = \frac{\Phi(St^*) l q^2}{U_{\max}} \tag{7}$$

- Strouhal number function

$$St^* = \frac{f L(x)}{U_{\max}} \tag{8}$$

- Span-wise length scale function

$$L(x) = \left[log\left(\frac{\lambda_s}{h}\right)^{0.015} + 0.12\right]^2 \tag{9}$$

- Estimation function for serration trailing edge noise reduction effect

$$SPL_{serration\,T.E.} = 3.5 - 8\left[\log(St^*) + 0.3\right]^2 - \left[\log\left(\frac{\lambda_s}{h}\right) + 0.4\right]^2 \tag{10}$$

$$\therefore SPL_{serration\,T.E.} \geq 0$$

4.1. Verification of performance of NACA0012 airfoil

The empirical formula for prediction of 2D airfoil self-noises by Brooks was developed based on the results of an experiment conducted on an NACA0012 airfoil. If an airfoil with a camber or a serrated trailing edge is used, it is impossible to directly apply the prediction model suggested by Brooks, because there can be changes not in the blade of a symmetric airfoil but in aerodynamic performance. To predict noise under such conditions, the lift slope was calibrated to the baseline lift coefficient. **Figure 15** gives information about the NACA0012 airfoil with a serrated trailing edge in the wind tunnel test.

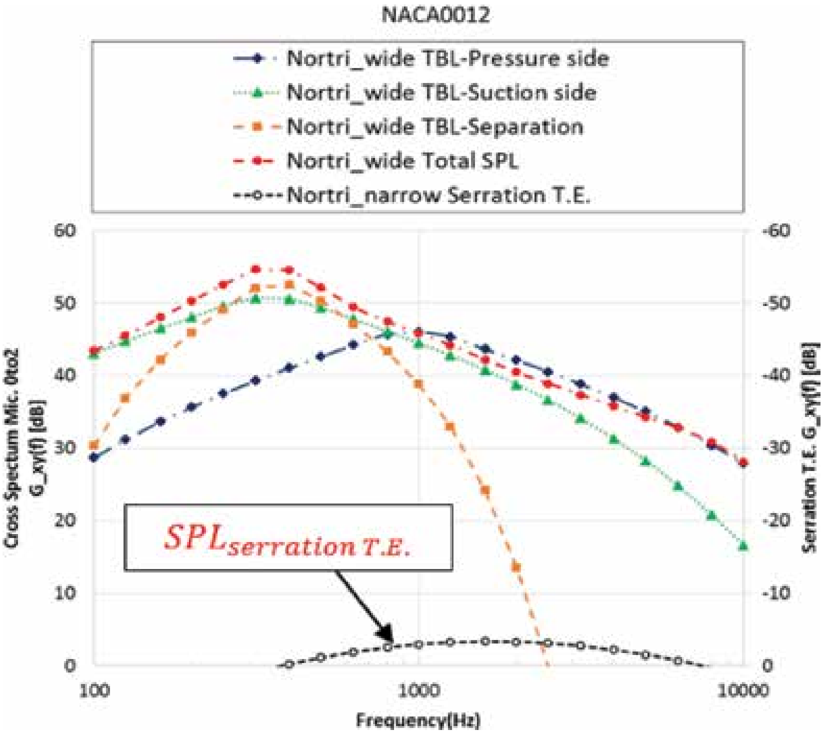

Figure 13. Estimation of serration trailing edge noise.

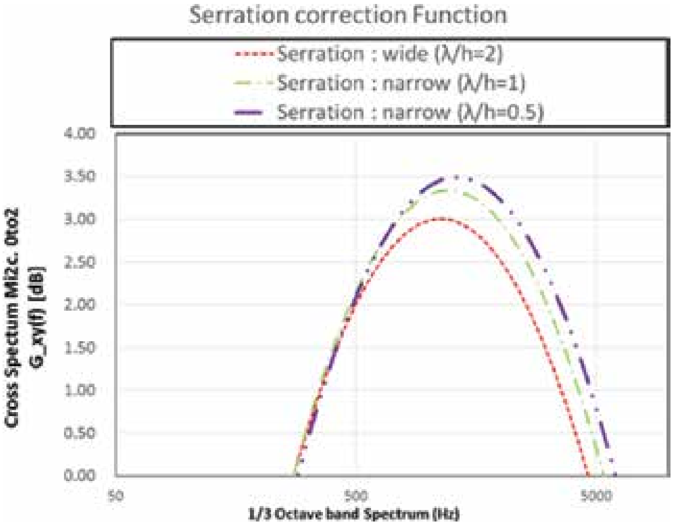

Figure 14. Bell function for serration trailing edge about frequency domain.

To analyze the noise prediction performance of the NACA0012 airfoil, an experiment was conducted under the conditions given in **Table 2**, and the results were used for a comparative analysis. A comparative analysis of the differences between the experimental results and the

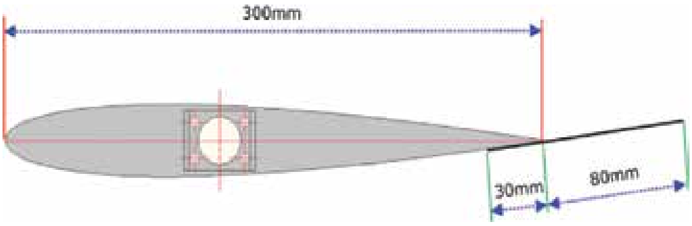

Figure 15. NACA0012 airfoil with serration trailing edge.

Model	Lift coefficient	AOA*	Remark
NACA0012	0.50	5.03	N/A
Serration narrow	0.43	4.43	$\lambda/h = 0.5$
Serration wide	0.42	4.40	$\lambda/h = 2$

Wind speed = 30 m/s.

Table 2. NACA0012 airfoil test condition.

predicted results was carried out under a total of three conditions (one, a 2D airfoil without a serrated trailing edge; and, two and three, the narrow and wide conditions of a normal tri-shaped

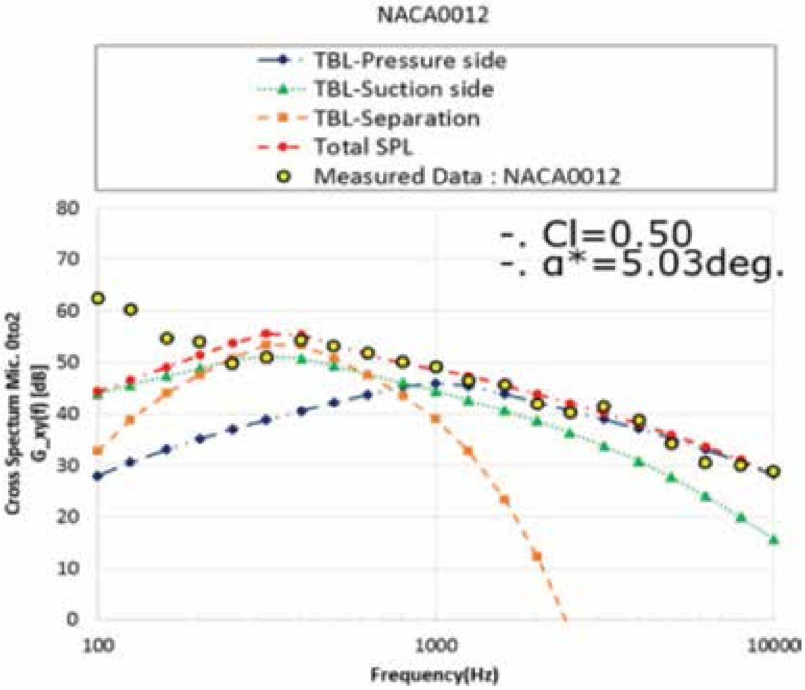

Figure 16. The wind tunnel test and estimation for NACA0012 airfoil condition.

airfoil with a serrated trailing edge). The measurement of noises collected through the microphones was used to calculate the cross spectrum between CH00 and CH02, utilizing a noise prediction program which was developed based on the empirical formula suggested by Brooks et al. [13].

Figure 16 shows the results of comparative analysis of the noise prediction values of the NACA0012 airfoil with the actual measured values. The measured values are consistent with the predicted values. Differences in the low frequency domain (300 Hz or below) can be ascribed to the background noise of the anechoic wind tunnel test facility.

As seen in **Figure 17**, the noise reduction effect produced by a serrated trailing edge was analyzed by applying the contents of the noise prediction formula for the NACA0012 airfoil and the empirical formula suggested by Brooks et al. [13] for prediction of noises in the serrated trailing edge, as seen in Eqs. (5)–(10). After conducting an experiment under the narrow condition, the predicted values were compared with the experimental values. According to the prediction, noises ranging from 500 Hz to 10 kHz should be reduced by the inclusion of a serrated trailing edge. **Figures 17** and **18** shows the results of the experiment conducted under the wide condition, as well as the results of the comparative analysis of the predicted values and the measured values. In accordance with the prediction, it was found that noises ranging from 300 Hz to 8 kHz were reduced (**Figure 18**).

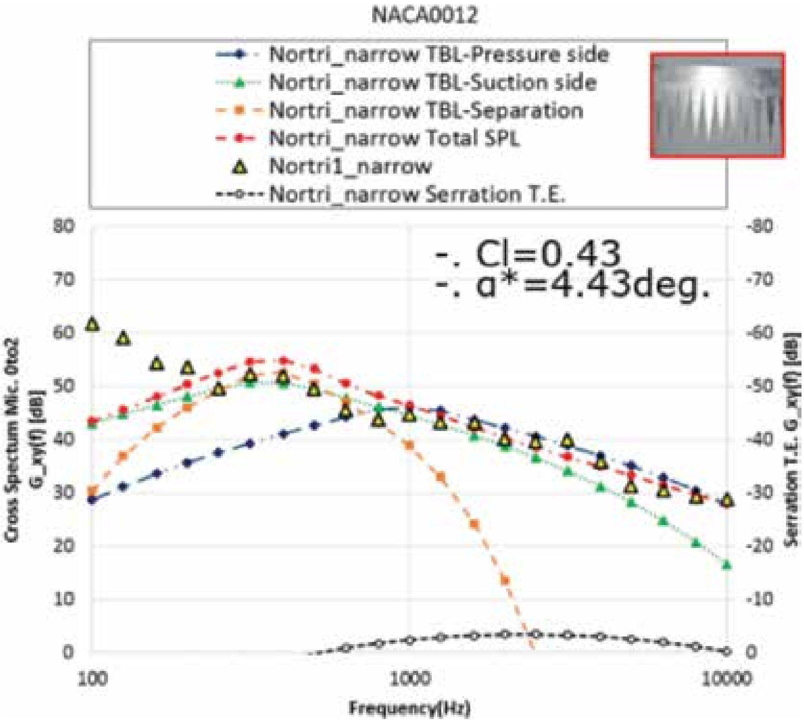

Figure 17. The wind tunnel test and estimation for NACA0012 with narrow serration plate.

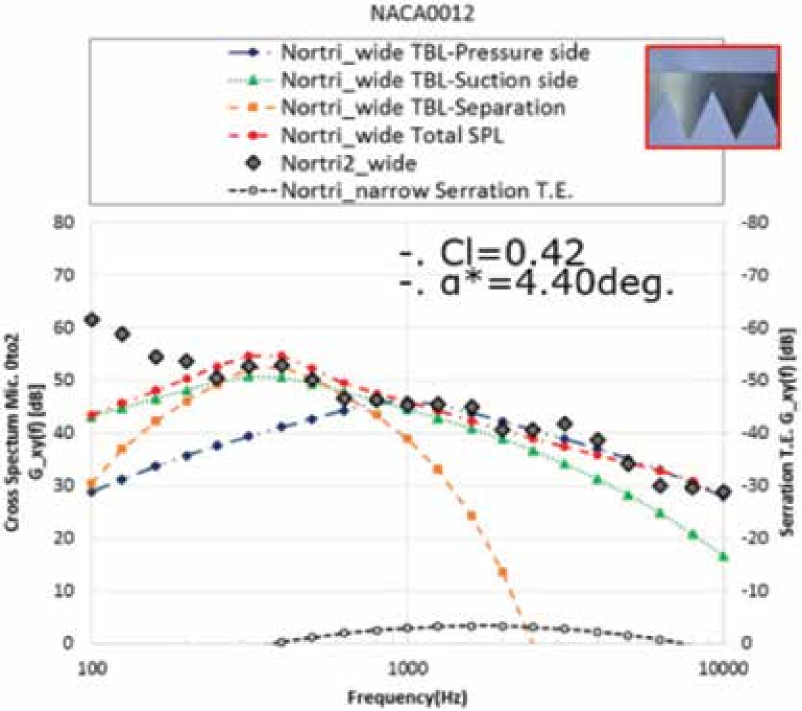

Figure 18. The wind tunnel test and estimation for NACA0012 with wide serration plate.

4.2. Verification of baseline airfoil performance

In this study, using the NACA0012 airfoil, experimentally tested Brooks' noise prediction formula and the noise prediction equation for the serrated tail edge are proposed. The prediction of noise reduction in the baseline airfoil with the shape seen in **Figure 19** was conducted, and the predicted results were compared with the experimentally obtained values. Based on the results of the wind tunnel test, the lift slope was calibrated to the baseline lift coefficient in order to predict airfoil self-noises.

For the analysis of noise prediction of the baseline airfoil, an experiment was conducted under the conditions given in **Table 3**, and the measured results were compared with the predicted results. For a comparative analysis between the predicted values and the experimentally obtained values, the experiment was conducted under a total of three conditions, the single

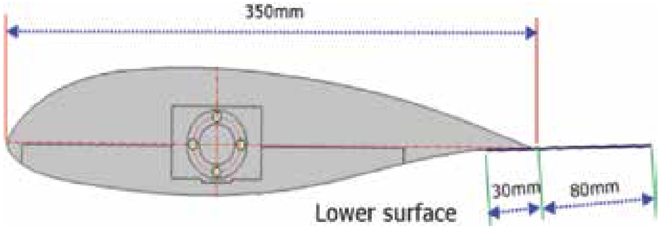

Figure 19. Baseline airfoil with serration trailing edge.

Model	Lift coefficient	AOA*	Remark
Baseline	0.59	4.60	N/A
Serration narrow	0.51	4.48	$\lambda/h = 0.5$
Serration wide	0.55	4.49	$\lambda/h = 2$

Wind speed = 30 m/s.

Table 3. Baseline airfoil test condition.

condition of a 2D airfoil without a serrated trailing edge, and the narrow condition and wide conditions of the normal tri-shaped airfoil with a serrated trailing edge, as was done with the NACA0012 airfoil. The noises collected through the microphones were used to calculate the cross-spectrum between CH0 and CH2, and a noise prediction program which was developed based on the empirical formula suggested by Brooks et al. [13] was utilized to predict 2D airfoil self-noises, as for the NACA0012 airfoil.

Figure 20 shows the results of the comparison between the predicted values of the baseline airfoil and the measured values. It was revealed that the disparities between the measured values of the baseline airfoil and the predicted values were wider than those between the measured and predicted values of the NACA0012 airfoil. **Figures 21** and **22** show the predicted results when a serrated trailing edge was applied to a 2D airfoil. As there were larger

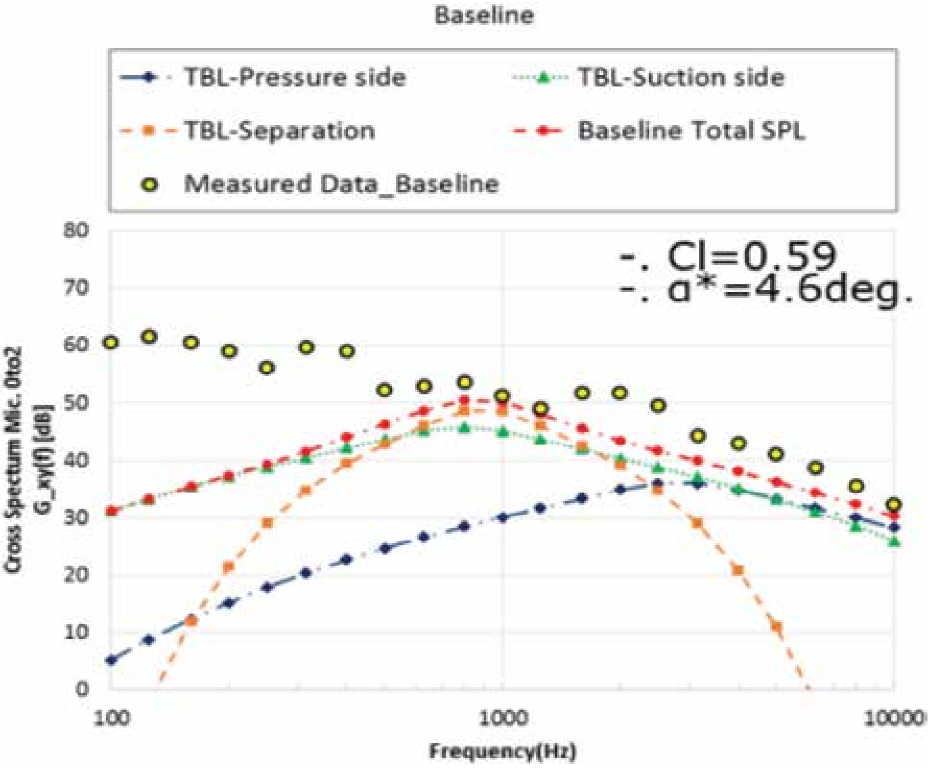

Figure 20. The wind tunnel test and estimation for baseline airfoil condition.

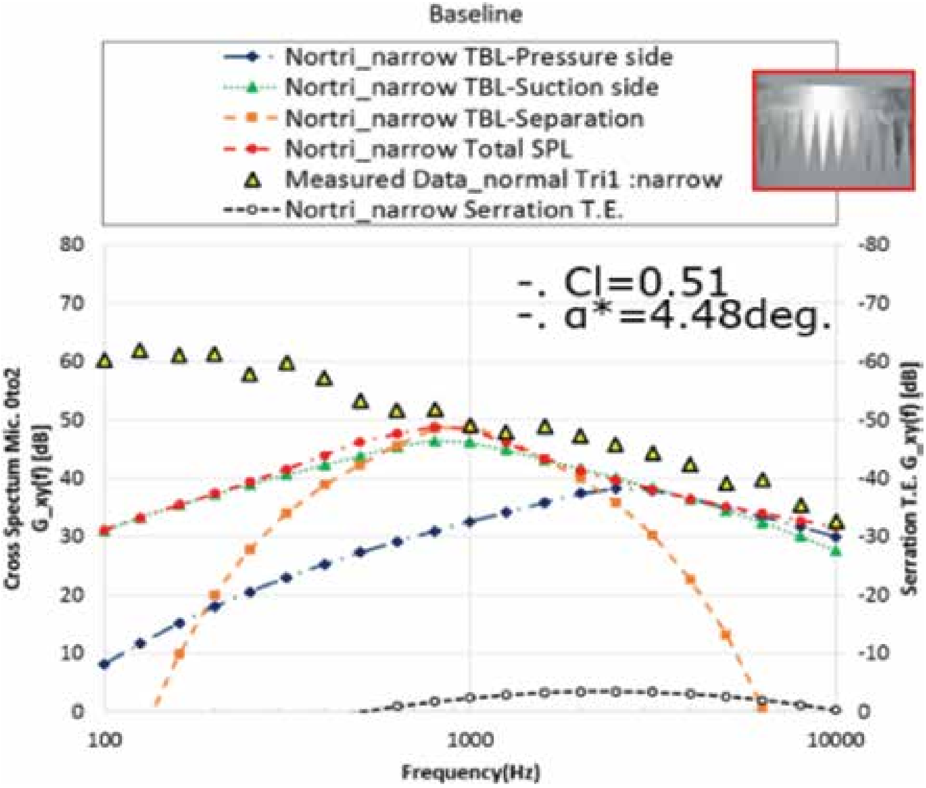

Figure 21. The wind tunnel test and estimation for baseline airfoil with wide serration plate condition.

differences between the predicted values and the measured values in comparison to those of the NACA0012 airfoil, the study showed a similar performance prediction ability under the conditions of interest.

When a serrated trailing edge was applied, noise reduction effects were observed both in the experimental results and the predicted results obtained by the empirical formula, under the same angles of attack. Also, they showed a similar frequency range where noises were reduced. However, it was found that the predicted values were smaller than the experimental values.

4.3. Review of noise reduction effects of 2D airfoils with serrated trailing edges

This study examined the noise reduction effects between the NACA0012 airfoil and the baseline airfoil used by a wind turbine rotor, which is considered a standard airfoil, following the application of serrated trailing edges. In this study, the validity of the noise reduction effect was confirmed under the angle of attack set as a precondition. This study utilized Brooks' empirical formula for noise reduction in 2D airfoils and the 'Bell-type' noise prediction empirical formula in order to examine the noise reduction effect of serrated trailing edges. As mentioned in

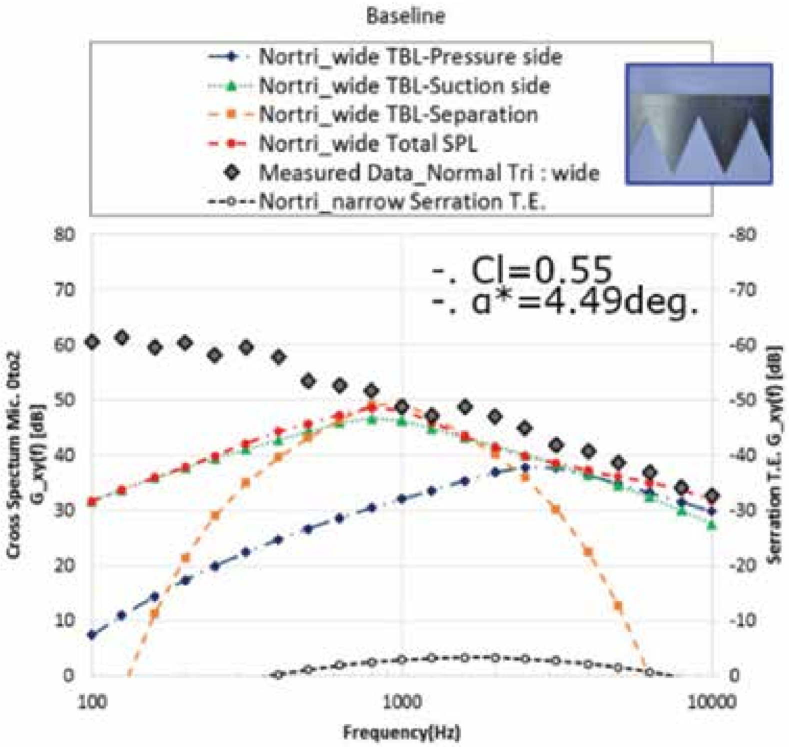

Figure 22. The wind tunnel test and estimation for baseline airfoil with wide serration plate condition.

the beginning of Section 4, however, this study has certain limitations, such as the range of noise experiment results and the limited types of 2D airfoils.

There were differences in the installation angles of serrated trailing edges depending on the shapes of the 2D airfoils, which may have caused variations in the frequency ranges of noise reduction, even when the same serrated trailing edge was used. Such an effect was noted in previous studies conducted from 1997 to 1999 in the JOULE-III program in Europe to measure the noises generated by a wind turbine rotor [12]. If follow-up studies take this effect into account, it may be possible to propose a more accurate noise prediction empirical formula than the one reviewed by this study.

Another limitation is related to the prediction formula defined as “Bell-type” by this study. This study conducted a 2D wind tunnel test on the noise reduction effect induced by serrated trailing edges, based on the baseline 2D airfoil used in actual wind turbine rotors. The contents of **Figure 23** show the noise reduction prediction function of serrated trailing edges ($\mathrm{SPL}_{\text{serration T.E.}}$) and the differences in the noise reduction prediction results between the previously conducted baseline airfoil and the serrated airfoil. The results confirmed that the noise reduction effect appeared as ‘Bell-type’ in various aspect ratios (λ/h) of serrated trailing edges.

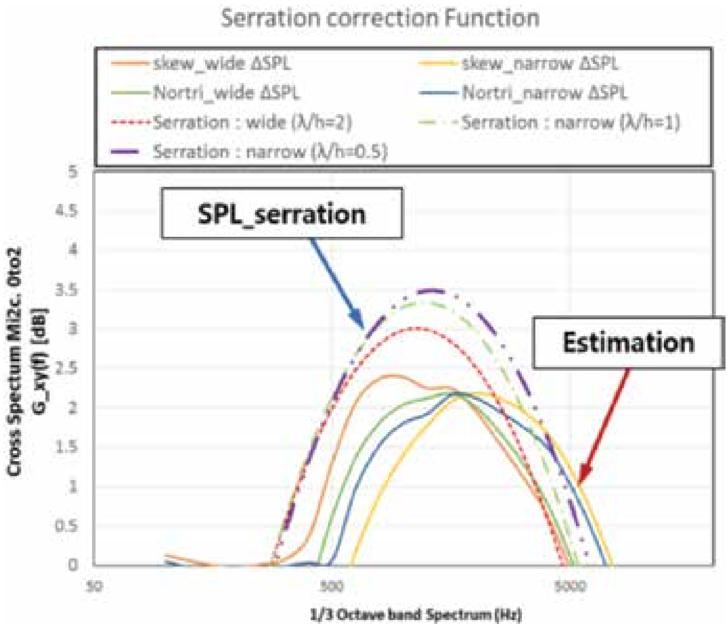

Figure 23. Cross spectrum of baseline airfoil with serration trailing edge.

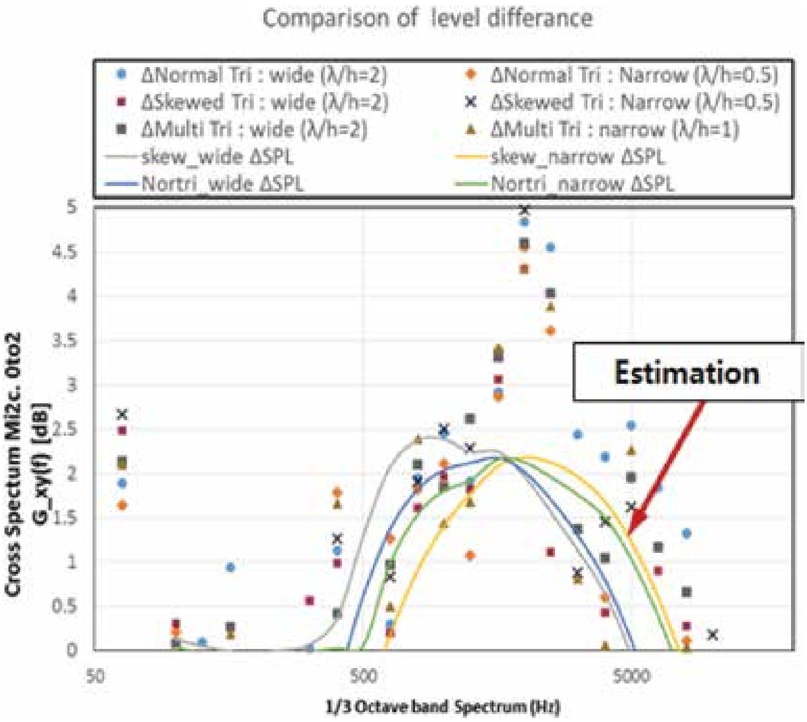

Figure 24. The level difference of baseline airfoil with serration trailing edge.

Figure 24 shows both the predicted results and the experimental results of the noise reduction effect induced by serrated trailing edges. The experimental results showed a 'Bell-type' distribution, but in some conditions, the distribution was more similar to 'Cone-type'. If further experiments are conducted based on the shape of serrated trailing edges, apart from the experimental conditions used in this study, it may be possible to improve the accuracy of the noise prediction formula.

5. Conclusion

A wind tunnel experiment was conducted on 2D airfoils, and the noise reduction effect was examined based on aerodynamic performance. Using the wind tunnel test on 2D airfoils with serrated trailing edges, wake distribution measurements and an analysis of their relationship with acoustic characteristics were conducted in order to examine the restrictive conditions of Howe's theory. These experimental results confirmed that as changes occur in the boundary layer thickness of 2D airfoils, an empirical formula or a theoretical approach which can reflect these changes is necessary. This study suggested an empirical formula for the prediction of noises in serrated trailing edges by utilizing the wind tunnel results on 2D airfoils with serrated trailing edges, based on the acoustic model suggested by Brooks. Also, the wind tunnel test results and noise prediction results of the NACA0012 airfoil with serrated trailing edges were compared with those of the baseline airfoil, and, through this comparative analysis, the study suggested a new noise prediction empirical formula for 2D airfoils. The study confirmed the validity of the proposed noise prediction formula by carrying out aerodynamic performance testing and noise measurements on the NACA0012 airfoil, the baseline airfoil, and the serrated trailing edges. However, as the noise prediction formula for the serrated trailing edges was an empirical formula that was based on limited experimental conditions, errors may have arose because of factors including the installation angles of the serrated trailing edges and the cross-sectional shapes of the 2D blades. To make up for the shortcomings in the test results, additional wind tunnel tests need to be conducted, and in consideration of the test results, further studies need to be conducted on the formation of a more accurate noise prediction formula.

Acknowledgements

This work was supported by research fund of 2014 Chungnam National University of the Korea.

Nomenclature

U	velocity of the free stream (m/s)
λs	span-wise wavelength (mm)
h	amplitude of serrations (mm)

ω	acoustic frequency (Hz)
SPL	sound pressure level, $dB\ re\ 20\mu Pa$

Author details

Jaeha Ryi* and Jong-Soo Choi

*Address all correspondence to: bass83@cnu.ac.kr

Department of Aerospace Engineering, Chungnam National University, Daejeon, Korea

References

[1] Howe MS. Noise produced by a sawtooth trailing edge. Journal of Acoustical Society of America. 1991;**90**(1)

[2] Braun KA. Serrated trailing edge noise (STENO). In: 1999 European Wind Energy Conference, Nice, France; 1-5 March 1999. pp. 180-183

[3] Gruber M, Joseph PF. Experimental investigation of airfoil self noise and turbulent wake reduction by the use of trailing edge serrations. In: P16th AIAA/CEAS Aeroacoustics Conference, AIAA 2010-3803. 2010

[4] Oerlemans S, Fisher M, Maeder T, Kögler K. Reduction of wind turbine noise using optimized airfoils and trailing-edge serrations. National Aerospace Laboratory, NLR-TP-2009-401. 2009

[5] Chong TP, Vathylakis A, Joseph PF, Gruber M. Self-noise produced by an airfoil with nonflat plate trailing-edge serrations. AIAA Journal. 2013;**51**(11):2665-2677

[6] Finez A, Jondeau E, Roger M. Broadband noise reduction with trailing edge brushes. In: 16th AIAA/CEAS Aeroacoustics Conference, AIAA 2010-3980. 2010

[7] Leung DYC, Yang Y. Wind energy development and its environmental impact: A review. Renewable and Sustainable Energy Reviews. 2012;**16**:1031-1039

[8] Ryi J, Choi J-S. Noise reduction effect of airfoil and small-scale rotor using serration trailing edge in a wind tunnel test. Science China Technological Sciences. February 2017; **60**(2):325-332. ISSN: 1674-7321

[9] Ryi J, Choi J-S, Lee S, Lee S. A full scale prediction method for wind turbine rotor noise by using wind tunnel test data. Renewable Energy. May 2014;**65**:257-264. ISSN: 0960-1481

[10] Ryi J. Estimation method to achieve a noise reduction effect and to evaluate the aerodynamic performance of a wind turbine rotor with a serrated trailing edge in a wind tunnel

test [the Degree of Ph.D.]. Department of Aerospace Engineering, Chungnam National University; Feb. 2015

[11] Brooks TF, Marcolini MA. Airfoil trailing edge flow measurements and comparisøn with theory incorporating open wind tunnel corrections. In: AIAA-84-2266, AIAA/NASA 9th Aeroacoustic Conference; 1984

[12] Garner HC, Rogers EWE, Acum WEA, Maskell EC. Subsonic Wind Tunnel Wall Corrections. NATO, AGARD; 1966

[13] Brooks T, Pope D, Marcolini M. Airfoil Self-Noise and Prediction, NASA Reference Publication 1218; 1989

[14] Brooks TF, Marcolini MA. Airfoil tip vortex formation noise. AIAA Journal. Feb. 1986; **24**(2):246-252

Chapter 8

Offshore Wind Feasibility Study in India

Satya Kiran Raju Alluri, Devender Gujjula,
Krishnaveni B, Dhinesh Ganapathi,
S.V.S. Phanikumar, M.V. Ramanamurthy and
M.A. Atmanand

Additional information is available at the end of the chapter

http://dx.doi.org/10.5772/intechopen.74916

Abstract

Offshore wind provides a scalable alternative to conventional energy resources. This chapter provides an insight into various activities of Ministry of Earth Sciences for the realization of offshore wind in India. To understand the hurdles in policy frame work for offshore wind, the evolution of onshore wind policy is analyzed and suitable strategies for offshore wind are proposed. Wind resource assessment results indicated a high offshore potential at Kanyakumari, Rameshwaram, Gulf of Khambhat, and Gulf of Kutch. Commercial viability studies showed levelized cost of electricity (LCOE) of around Rs 10/kWh at identified sites for an internal rate of return (IRR) of 14%. Offshore light detection and ranging (LiDAR)-based data collection platform has been installed at Gulf of Khambhat and Kutch to obtain bankable wind data for the development of offshore wind farms. A preliminary design of substructure by exploring different concepts like monopile, jacket, and gravity-based foundations was carried out based on their suitability for site-specific environmental and soil data. The port facilities along Gujarat and Tamil Nadu coast were assessed, and installation methodology was developed considering marine spread along the Indian coast.

Keywords: offshore wind, India, wind resources, commercial viability, substructure, installation

1. Introduction

The increased environmental awareness, energy security, and depletion of land-based resources are driving the dependence on renewable energy technologies. Wind energy has gained wide acceptance across the globe and presently the focus is toward the development of offshore wind farms. The promising factors for offshore wind development are (1) powerful and consistent winds compared to onshore, (2) low sound pollution and visual intrusion, (3) best benefit to coastal areas due to less transmission cost and losses, and (4) easy transportation of larger capacity turbines.

Europe is leading the offshore wind market since the inception of its first commercial offshore wind project in 1996 with an installed capacity of more than 8 GW connected to grid as of 2014. The installed capacity of wind farms in Europe is 8.045 GW [1], while in China and Japan are 0.67 and 0.05 GW, respectively [2]. Proposals exist to expand the respective capacities to 24 GW (Europe) [3], 10 GW (China) [4], and 1 GW (Japan) [5] by 2020. Actually, more than 90% of the global offshore wind farms were located in European waters, and the contribution from various countries is shown in **Figure 1**. In 2013, the world's largest wind farm "London Array" with a capacity of 630 MW is commissioned in United Kingdom [6]. A project with 0.468 GW capacity is under construction in USA with proposals for expanding the capacity to 10 GW by 2020 [7].

Developing country like India is yet to meet the required energy demands through existing installed capacities of 259 GW [8]. During fiscal year 2013–2014, India has experienced an energy shortage of 4.2% (960 BU against a demand of 1002 BU) with a peak shortage of 4.5% (130 GW against a demand of 136 GW) [9]. The southern region has experienced a severe energy shortage of 6.8% with a peak shortage of 7.6% [9]. Tamil Nadu, Andhra Pradesh, Karnataka, and Kerala belonged to this region and have a coastline of 3100 km [10]. Offshore wind being pollution free would be an ideal solution to meet the increasing demand as these coasts were blessed with significant winds. India initiated the efforts toward the development of offshore wind in the potential locations, and policy guidelines were formulated by the Ministry of New and Renewable Energy (MNRE) to promote offshore wind projects. Prior to finalization of offshore wind policy in India, it was essential to study the key aspects such as identification of potential sites, selection of suitable wind turbines capacity, and arriving at feasible incentives to promote offshore wind, which were performed.

Various technical institutes working with MNRE and the Ministry of Earth Sciences (MoES) along with the global partners carried out offshore wind assessment studies and identified

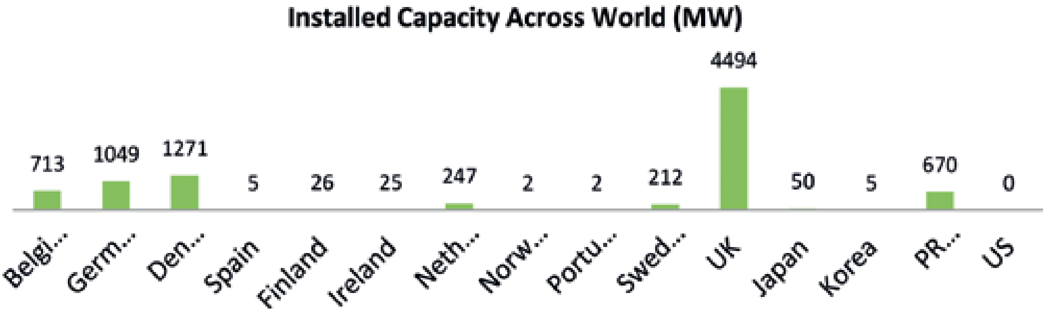

Figure 1. Installed capacity across the world (2014).

the potential sites. The wind resource assessment studies need to be reinforced with suitable data collection in the potential location not only for validation but also for obtaining bankable wind data. National Offshore Wind Energy Policy allows interested government and private agencies to indulge themselves in carrying out met ocean studies in the potential locations. MNRE-National Institute of Wind Energy (NIWE) and M/s Suzlon Energy Limited along with technical expertise from the National Institute of Ocean Technology (NIOT) have installed light detection and ranging (LiDAR)-based Offshore Data Collection Platforms at Gulf of Kambhat and Gulf of Kutch, Gujarat, during fiscal year 2017.

2. Identification of offshore wind potential sites

Wind Atlas gives good indication of the geographical distribution of the wind resource and will be useful for decision making and planning of feasibility studies. However, to meet the bankability requirements, precise measurements are required for a couple of years at the proposed site. Conventionally, Wind Atlas is generated using analytical wind measurements at a number of sites across the country. As long-term historical wind data are not available at all the terrains in India, the National Institute of Wind Energy (NIWE) has used Karlsruhe Atmospheric Mesoscale Model (KAMM)/Wind Atlas Analysis Application (WAsP) developed at Risø DTU National Laboratory and generated numerical Wind Atlas for India [11]. Verification of model results was carried out using measured wind speeds and directions from onshore NIWE metrological masts. The offshore winds till 100-km deep into ocean are also generated using the same model, and results need to be verified using measured offshore winds. The offshore Wind Atlas shows significant potential along the southern Tamil Nadu coast as shown in **Figure 2**.

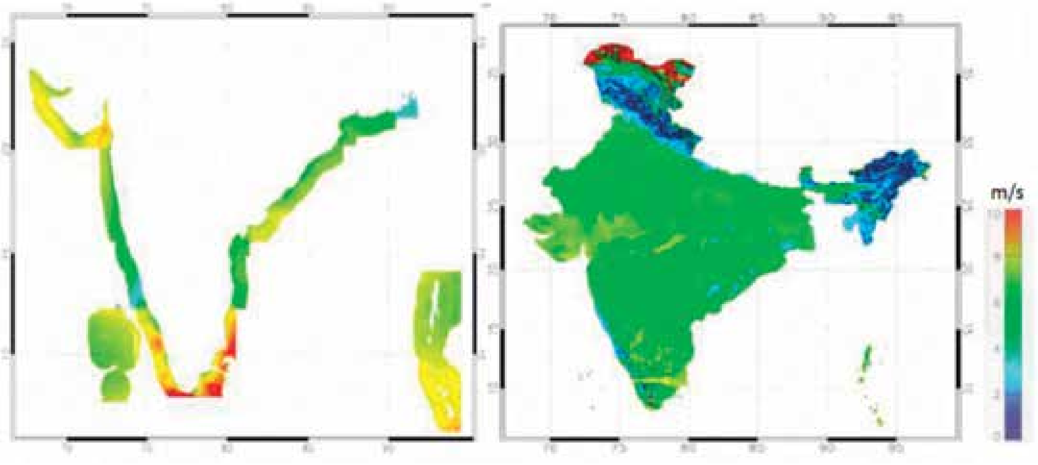

Figure 2. Numerically generated offshore and onshore wind resource maps for India by NIWE (source: Risø DTU, Indian Wind Atlas, Center for Wind Energy Technology [11]).

NIWE has commissioned a 100-m high-guyed offshore mast in the coastal line of Dhanushkodi, Rameshwaram, to understand the wind profile behavior in the region. The measurement is the first of its kind in India being conducted in a narrow strip into the sea at Dhanushkodi, which gives a close representation for offshore wind. The data have been monitored since October 2013, and the 4-year-old measured wind profile at Dhanushkodi looks promising for wind power potential with a mean wind speed of 8.5 m/s.

The European Union (EU) Delegation to India granted the Facilitating Offshore Wind in India (FOWIND) project to the consortium led by the Global Wind Energy Council (GWEC) including DNV-GL, Center for Study of Science, Technology and Policy (CSTEP) with an objective of assessing and promoting the offshore wind power development in India and aiding in facilitating India's transition toward a low carbon energy future. FOWIND reported that a number of agencies and institutions have assessed the offshore wind potential of the Indian coast including the coasts of Gujarat and Tamil Nadu. However, all of these studies are subject to various limitations with a possibility to draw various conclusions. Based on the various studies, FOWIND identified the significant offshore wind potential zones as shown in **Figure 3**. (Source: FOWIND pre-feasibility report at www.fowind.in.)

The Indian National Centre for Ocean Information Services (INCOIS) has developed wind potential maps based on satellite winds from QuickSCAT as shown in **Figure 4** [12]. These satellite-derived winds were validated and calibrated using in situ winds from five moored buoys deployed by the National Institute of Ocean Technology (NIOT) along the Indian coast. The wind potential maps generated by these institutes indicate significant potential along Tamil Nadu and Gujarat coast. It is observed that winds of magnitude 6 m/s or more persist for more than 300 days and 8 m/s or more persists for about 200 days along the southern coasts of Tamil Nadu. The wind potential maps generated by both the institutes indicate Rameshwaram and Kanyakumari along the Tamil Nadu as suitable sites for setting offshore wind farms.

Figure 3. Offshore wind potential zones identified by FOWIND.

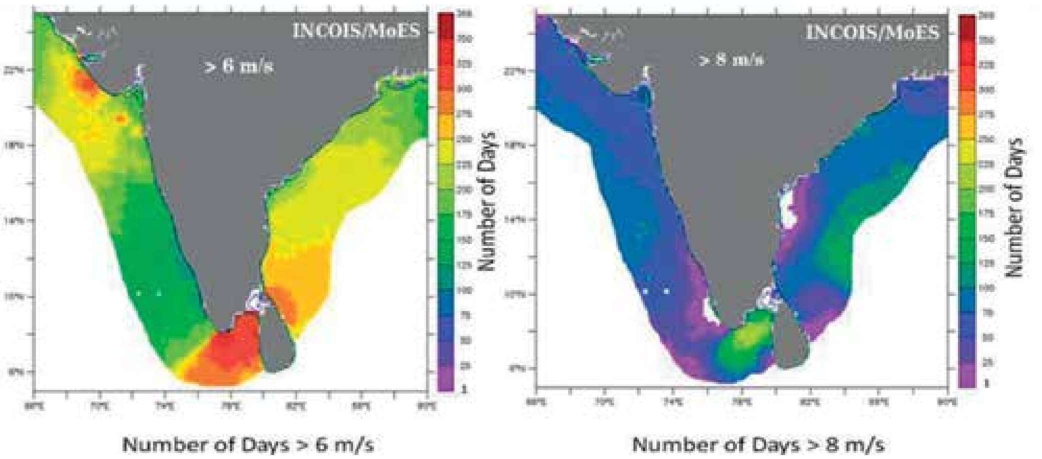

Figure 4. Offshore wind potential maps for Indian coast by Earth System Science Organization (ESSO)-INCOIS.

To study the wind characteristics, the wind speeds along Rameshwaram, Kanyakumari, and Jakhau were obtained from INCOIS at a 10-m elevation and extrapolated to 80 m using power law with a shear coefficient of 0.14 [13]. The mean wind speeds at Rameshwaram, Kanyakumari, and Jakhau for derived winds at an 80-m elevation are 8.5, 9.1, and 7.3 m/s, respectively.

A suitability analysis for these three potential sites along the Indian coast was carried out by Earth System Science Organization (ESSO)-NIOT based on the wind data obtained from ESSO-INCOIS. The properties of various class II wind turbines available in the market, in the range of 2–7 MW, were considered to identify suitable turbine. The uncertainties due to measurement scheme, futuristic wind prediction, and wind shear for measured wind speeds were considered, and the plant load factors at various probabilistic levels like 50 (P50), 75 (P75), and 90% (P90) were arrived at. It is observed that Repower 3.4-MW turbine performs well at both the locations. The power production from wind turbine after accounting for various losses like turbine unavailability (3%), Wake effects losses (8%), and electrical losses (5%) for Repower 3.4 MW turbine is given in **Table 1**.

S. no.	Company	Capacity (MW)	Kanyakumari			Rameshwaram		
			(P90)	(P75)	(P50)	(P90)	(P75)	(P50)
1	Suzlon	2.1	0.43	0.45	0.47	0.37	0.38	0.40
2	Repower	3.2	0.40	0.42	0.44	0.33	0.34	0.36
3	Repower	3.4	0.51	0.53	0.55	0.43	0.45	0.46
4	Repower	5.0	0.39	0.40	0.42	0.33	0.34	0.35
5	Repower	6.2	0.31	0.33	0.34	0.30	0.31	0.32
Plant load factors after incorporating losses in power production								
1	Repower	3.4	0.43	0.45	0.46	0.37	0.38	0.39

Table 1. Performance of wind turbines at potential sites (plant load factor).

Figure 5. Installed LiDAR at Gulf of Khambhat for MNRE-NIWE.

The wind resource assessment is proposed to be validated with LiDAR-based data collection platform. These platforms were designed and successfully installed with the technical support of the National Institute of Ocean Technology (NIOT) at Gulf of Khambhat for M/s NIWE and Gulf of Kutch for M/s Suzlon to obtain wind velocities along with profiles. The platforms at Gulf of Khambhat and Gulf of Kutch have been installed in high tidal currents and poor soil conditions (**Figure 5**). The substructure (monopile) shown in **Figure 5** supports the data collection equipment/wind turbine by absorbing the environmental loads acting on it. The monopile is fabricated using the steel plates and mobilized using barges and installed at the site.

3. Commercial viability studies

Commercial viability studies are important to attract the investors for expensive offshore systems. Offshore development in general and wind projects in particular are complex, capital-intensive engineering endeavors, and a large number of factors influence development. The design, logistics, vessel requirements, and physical infrastructure of each offshore farm are unique but a number of similarities exist between projects. The environmental conditions, the level of competition, and government support are regional and country-specific and they play a key role in offshore wind viability studies.

The capital cost of offshore wind turbine systems is significantly higher than land-based systems because of the higher cost in foundations, installation, operation and maintenance, and complex logistics. The offshore environment is significantly more uncertain and difficult than onshore and thus more costly and risky. The offshore environment involves personnel traveling to and from offshore turbines, and this increases equipment and time costs as well as insurance costs due to increased risks. Offshore work involves increased risks of strong winds which affect the amount of time available for maintenance and installation which in turn influence capital and operation costs. Offshore environments are corrosive to electrical and structural equipment and require turbines to be marinized with cathodic and humidity protection. Capital expenditures for offshore wind projects depend on marine vessel day rates which are uncertain, and offshore foundations require more steel for jackets and pilings than onshore foundations. The components that affect the capital cost of wind turbine are (1) wind turbine and its installation, (2) substructure and its installation, and (3) electrical systems and its installation (inner array cables, export cables, and substation).

The capital cost is modeled with hypothetical 170-MW wind farm composed of 50, 3.4-MW turbines. The turbine data available in open source are considered (Repower) for this study. The farm considered in shallow water of 10–15-m water depth with a 5-m diameter monopile with 100-mm thick and 30-m penetration into seabed. The cost of various components, operation and maintenance cost, is considered as per existing wind farms and modified to Indian conditions, which is explained in detail in subsequent sections.

The primary capital cost for onshore wind projects is the turbine; installation costs make up about 14% of the total capital costs. For offshore wind projects, the cost of installation is higher, approximately 20% of the total costs, and the costs of building the foundations account for another 20% of capital costs. For offshore wind, operation and maintenance costs make up a larger proportion of the overall components of the COE. This is likely due to the costs of accessing offshore wind farms and maintaining turbines in operating condition. The components considered are substructure, transition piece, wind turbine, installation of the above three components, inner array and export cables laying, and offshore substation installation [1, 14–19].

3.1. Substructure and transition piece

One of the most significant challenges facing offshore wind engineers is the effective and cost-efficient fixing of the turbine tower to the seabed. To date, this has typically been achieved via a monopile foundation which constitutes approximately 20–25% of the total capital expenditure in offshore wind farm construction. In this study, monopile- and gravity-based foundations are considered for capital cost estimation. For substructure and transition piece fabrication, Rs. 200/− per kg is considered based on the market studies for monopile and Rs. 25,000/− per cubic meter for gravity foundation (including concrete reinforcement and handling).

3.2. Wind turbine

The wind turbine itself is the most important cost component of an offshore wind project constituting from 30 to 40% of the total capex. Here, the turbine cost is considered based on interaction with the Original Equipment Manufacturers (OEMs). A range of interacting drivers will affect costs into the future, like increasing competition, competing markets, innovation, scale effects, and standardization before drawing conclusions about the overall scale and trajectory of change to turbine costs.

3.3. Installation

Foundation, turbine, substation, and cable installation together comprise approximately 20% of overall capex. At present, no offshore wind projects have been developed or are under construction in India, and since there is no direct Indian experience to draw upon, a comparative statistical assessment is used in the analysis. In this study, the installation methodology used in European offshore projects is reviewed; the costing of marine spread is accounted for considering the availability in India and nearby countries like Singapore, Middle East, and Korea.

3.3.1. Foundation installation

Monopile foundations consist of a large cylindrical steel pile and a steel structure (transition piece) placed over and grouted onto the monopile. Monopiles may be transported to the site by the installation vessel (considered in this study); they may be barged to the site, they may be transported by a feeder vessel, or they may be capped and wet-towed. The pile is upended by a crane and/or a specialized pile-gripping device, and a hydraulic hammer drives the pile into the seabed to a predetermined depth. The time to drive the piles depends on the soil type, diameter and thickness of the piles, burial depth, and the weight of the hammer. A rocky subsurface may prevent driving operations, in which case a drill will be inserted into the pile to drill through the substrate. After the monopile is secured, a transition piece is grouted onto the pile. The transition piece is typically installed immediately after piling by the same vessel that drove the pile, but if two vessels are employed in installation, a separate vessel may follow behind the foundation installation. The area around the monopile may need to be protected with rocks to guard against erosion (scour protection).

All these activities need to be performed in a highly dynamic offshore environment, and hence expensive vessels are required for safe installation. Presently, such barges are available in countries like Europe, Chain, Japan, and Korea only. Based on the ease of transportation, Korean vessels are considered for cost estimation with day rates as per market rates. The cost of bringing the vessels from Korea (4000 nm), the travel time of 60 days (for both ways) at a speed of 6 knots, the installation rate of 3.1 days per unit [14], and hiring rates of 140,000 USD/day all inclusive are considered along with the tug.

3.3.2. Turbine

There are a large number of options for turbine installation. The method used to install turbines is determined by available vessels, the turbine model, and the desire to minimize the number of offshore lifts. If the number of lifts is minimum, it is noted that crane capacity will increase accordingly.

As mentioned in Section 3.3.1, these vessels also should be obtained from the same countries. Based on the ease of transportation, Korean vessels are considered for cost estimation with day rates as per literature and market. The cost of bringing the vessel from the Korea (4000 nm), the travel time of 36 days (for both ways) at a speed of 10 knots, the installation rate of 4.0 days per unit, and the hiring rates of 200,000 USD/day are all inclusive.

3.3.3. Electrical infrastructure

The electrical infrastructure at an offshore wind farm includes inner-array cables which connect turbines together in series, export cable which transmits electricity to shore, and, potentially, one or more electrical substations to increase voltage prior to export. Offshore wind power cable is usually buried in the seafloor. There are several methods for installation, but in most cases, cable is simultaneously laid and buried by either an underwater plow or a remotely operated vehicle (ROV). Presently, such barges are available in countries like Singapore and Malaysia nearer to India. Hence, the cost of bringing the vessel from Singapore or Malaysia (1600 nm), the travel time of 10 days (for both ways) at a speed of 15 knots, the installation rate of 0.7 km/day, and the hiring rates of 125,000 USD/day for export cable and 50,000 USD for in-array cables are all inclusive.

The grid infrastructure is a concern for renewable energy in India and will be facing challenges for offshore wind developments due to large-scale variable generation technology. These challenges include grid strengthening, grid/code balance at national scale, and so on. Technical Standard for Grid Connectivity such as Grid Code (IEGC 2010) and GEGC-2004 can be updated.

The capital cost is estimated for three cases comprising different scenarios, and the summary is provided in **Table 2**.

Case 1: Considering the present scenario in India, with most of the marine spread from nearby countries and using average installation rates per unit-based existing wind farms [14].

Case 2: Assuming the required marine spread to be available in India and using optimistic installation rates per unit based on existing wind farms [14].

Case 3: Considering innovative gravity-based foundation for Rameshwaram based on site-specific soil stratum in addition to Case 2.

A study was conducted to check the commercial viability of offshore wind farms along Tamil Nadu coast. The general cash flow for a wind turbine is shown in **Figure 6**. The capital cost for setting up a wind turbine is raised by an investor with certain equity and the rest as debited from bank at an interest rate during loan tenure. In India, Indian Renewable Energy Development Agency Limited (IREDA) provides soft loans for 70% of capital cost with an interest rate of 11.90–12.50% based on grade for a tenure of 10–15 years. However, if the tenure is more than 12 years, an additional interest rate will be charged. In this study, an interest

S. no.	Component	Cost in Indian rupees (crores)		
		Case 1	Case 2	Case 3
1	Foundation (material and fabrication)	9.81	9.81	1.5
2	Transition piece (material and fabrication)	3.67	3.67	3.67
3	Installation of substructure and transition piece	4.25	1.48	0.07
4	Turbine	23.8	23.8	23.8
5	Installation of wind turbine	6.40	1.90	1.90
6	Electrical infrastructure (material and installation)	10.68	8.84	8.84
7	Port-handling charges and project development	2.17	1.89	3.25
	Total	60.78	51.40	43.05

Table 2. Capital cost summary for hypothetical 170-MW wind farm consisting of 50 numbers of 3.4 MW turbines.

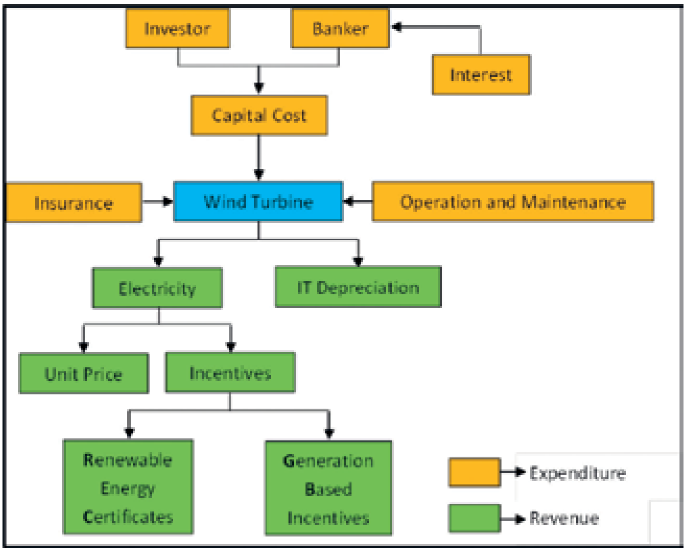

Figure 6. Cash flow for wind turbine project.

rate of 12.5% for a tenure of 12 years is considered. After commissioning of wind farm, the components that contribute for cash-out flow are insurance (0.1% of initial cost) and operation and maintenance charges. The returns include unit price paid for electricity produced, fiscal incentives, and income tax depreciation. The main incentives provided by the Indian government for wind energy are generation-based intensive (GBI) and renewable energy certificates (RECs). GBI of Rs. 0.50/kWh will be provided with a cap of Rs. 1 crore/MW for a period of 10 years through IREDA. The Central Electricity Regulatory Commission (CERC) has notified that the floor and ceiling prices will range from Rs. 1.5 to 3.9 per unit (for non-solar RECs) [17]. In this study, RECs of Rs. 1.5/kWh is considered. The accelerated depreciation of 80% in the first year is reinitiated in 2014. All these incentives are considered in this study.

Developers should structure the repayments which will give the lenders a comfortable zone and aim for higher debt-service coverage ratios. For banks to finance a wind farm, an average DSCR of 1.3 is required. The unit prices of electricity for three different scenarios are listed in **Table 3** for a DSCR of 1.3 at P50 PLF level.

	Kanyakumari		**Rameshwaram**	
	LCOE with no incentives (Rs.)	**Unit price with existing incentives (Rs.)**	**LCOE with no incentives (Rs.)**	**Unit price with existing incentives (Rs.)**
Case 1	8.23	4.71	9.38	5.52
Case 2	7.24	3.98	8.21	4.66
Case 3	—	—	7.17	3.89

Table 3. Unit pricing with and without incentives.

4. Development of substructures for offshore wind

The support platform costs about 24% [20] of the total system cost and needs to be optimized to increase the commercial viability of offshore wind projects. The substructure concepts used to support offshore wind turbine include monopiles, gravity-based structures, jackets, tripods, tripiles, and floating platforms [21]. The choice of foundation depends on water depth, environmental, and geotechnical conditions. Monopiles and gravity-based foundations are generally adopted for shallow water depth below 30 m. As the water depths increase, these foundations yield larger lateral deflection and rotations at a nacelle level. Therefore, a braced frame structure like jacket and tripod is used at a transition water depth of 30–50 m. In ultra-deep water (>50 m), floating compliant structures are adopted [22].

The preliminary analysis of site and environmental conditions indicate the suitability of monopile along Gulfs of Gujarat due to shallow water depths, gravity-based foundations at Rameshwaram due to shallow water depths and moderated soil conditions, and jackets at Kanyakumari due to moderate depths and soil conditions. Therefore, the preliminary design of three substructure concepts, monopile, gravity, and jacket, based on static and earthquake loadings was taken up. The typical configurations of three substructure configurations considered are shown in **Figure 7**.

4.1. Methodology

The optimum substructure configuration for offshore wind turbine can be arrived only by considering the in-place behavior of structure along with suitable installation methodology.

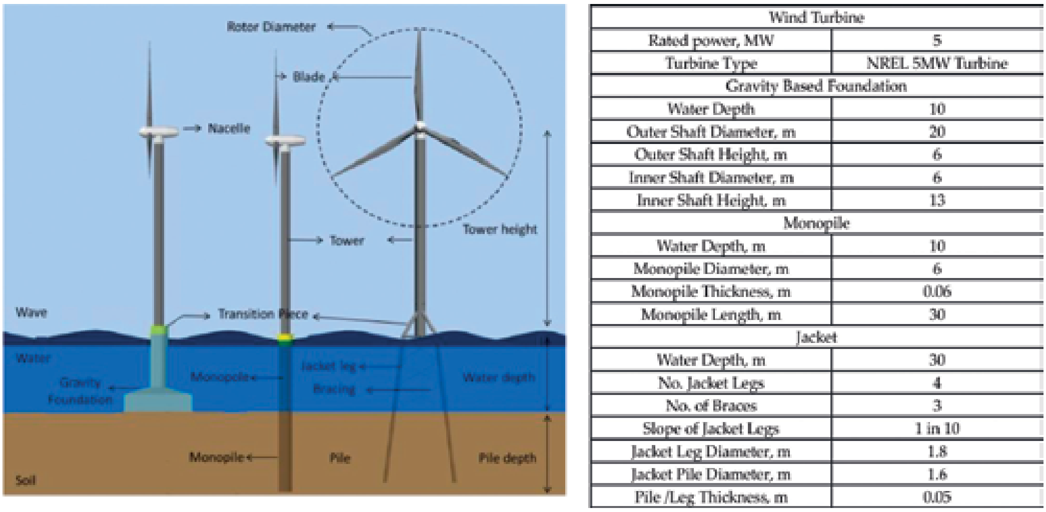

Wind Turbine	
Rated power, MW	5
Turbine Type	NREL 5MW Turbine
Gravity Based Foundation	
Water Depth	10
Outer Shaft Diameter, m	20
Outer Shaft Height, m	6
Inner Shaft Diameter, m	6
Inner Shaft Height, m	13
Monopile	
Water Depth, m	10
Monopile Diameter, m	6
Monopile Thickness, m	0.06
Monopile Length, m	30
Jacket	
Water Depth, m	30
No. Jacket Legs	4
No. of Braces	3
Slope of Jacket Legs	1 in 10
Jacket Leg Diameter, m	1.8
Jacket Pile Diameter, m	1.6
Pile /Leg Thickness, m	0.05

Figure 7. Gravity, monopile and jacket substructure configurations.

The structure has to be analyzed for combined aerodynamic and hydrodynamic forces to understand the in-place behavior. Then, the structure should be designed for safely transferring the forces into the soil by satisfying serviceability and strength aspects. The detailed design methodology is given in **Figure 8**.

The aerodynamic loads are estimated using open-source tool "FAST" based on Blade element momentum theory. The wave kinematics is obtained using a suitable wave theory, and the hydrodynamic forces are estimated using Morison's equation. The soil interaction is modeled as springs with a suitable stiffness. The structural behavior of the entire system is analyzed using finite element method and members are designed. The gravity-based foundation is checked against stability due to sliding, overturning, and bearing. It is proposed to transport the gravity foundation through flotation and ballast at the proposed location. The draft of foundation is estimated using static stability conditions, and the response amplitude operators are estimated for dynamic stability.

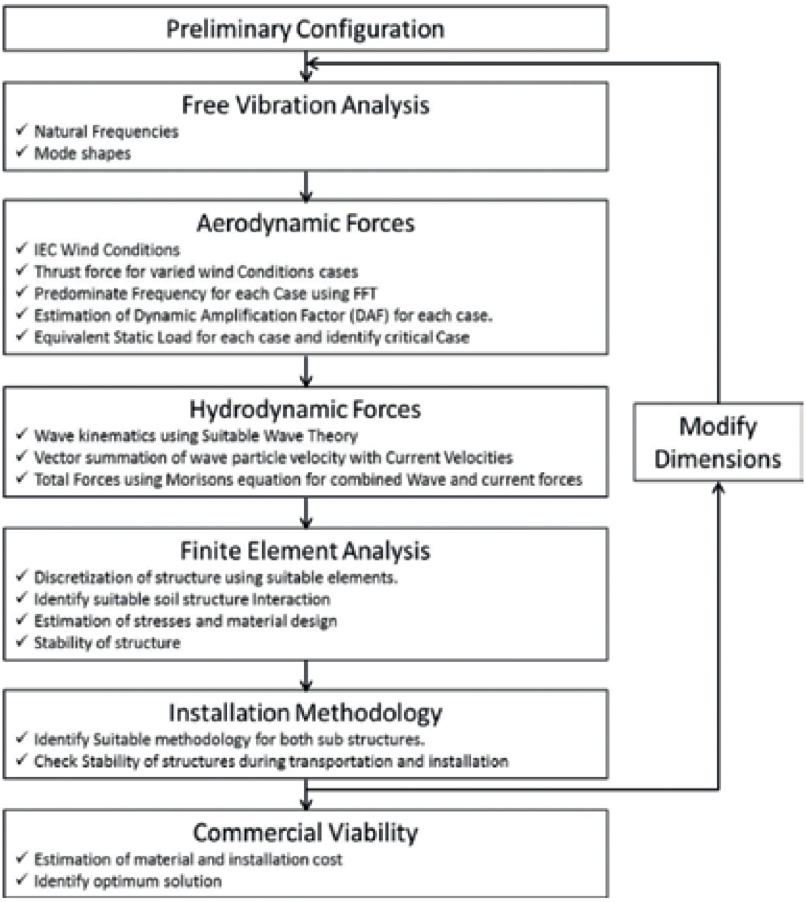

Figure 8. Methodology for substructure development.

4.2. Structural analysis and design of substructure

4.2.1. Aerodynamic loads on turbine

The behavior of NREL 5-MW turbine has to be studied under various design conditions like power production, power production plus occurrence of fault, start up, normal shut down, emergency shutdown, parked, parked with fault conditions, transport, assembly, maintenance, and repair. The International Electrotechnical Commission [24, 25] has provided models for the wind conditions during these design conditions, and these models have to be established for various wind speeds as per IEC code. The obtained wind time history from these models can be converted to thrust force on turbine using open-source tool FAST. This tool works under beam element momentum theory, which is a combination of Blade element theory and momentum theory. The Blade element theory assumes the rotor blade sections as infinitesimally small thickness like a two-dimensional aerofoil. Aerodynamic forces for each segment are estimated considering local flow conditions, and the overall forces are obtained by integrating all the sections. The momentum theory assumes the loss of momentum due to work done by airflow through the rotor plane on the blade elements. The induced velocities are calculated from the momentum lost in the flow in the axial and tangential directions. These induced velocities from momentum theory are used by Blade element theory for the calculation of thrust forces on turbine.

The thrust force time history obtained from FAST is converted to equivalent static load for all the load conditions. The equivalent static load can be obtained by multiplying the maximum dynamic load in time history with the dynamic amplification factor. The dynamic amplification factor depends on the spacing of the natural frequency of structure and the dominant frequency of force time history and estimated using the DAF Eq. (1). The natural frequency of the structure is obtained using eigen value analysis, and the dominant frequency of force is obtained using Fast Fourier Transform. The damping in the structure is considered as 2%. It is observed that the maximum aerodynamic load of 1.6 MN was obtained for extreme operating gust case, and this is used for the design of sub-structure

$$\mathrm{DAF} = \frac{1}{\sqrt{(1-\mathrm{r}^2)^2 + (2\zeta \mathrm{r})^2}} \tag{1}$$

where r is the ratio of forcing frequency to the natural frequency of structure and ζ is the damping ratio.

4.2.2. Hydrodynamic loads on substructure

The substructure has to be designed for a designed wave height of 4 m and a period of 12 s. The hydrodynamic forces for this wave conditions are estimated using Morison's equation, which is applicable for members with a diameter smaller than 0.2 times of wavelength [26]. Considering the general dimensions of substructure for fixed offshore wind turbines, Morison's expression is commonly used. It is a semi-empirical formula which assumes the total force as a sum of inertia component due to the fluid acceleration and a drag component due to fluid velocity. The wave kinematics such as velocity and acceleration required by Morison's equation can be obtained from various wave theories like linear/airy wave theory, Stokes wave theory (up to fifth-order approximations), stream function wave theory (up to 22nd-order approximations), and cnoidal wave theory. The choice of wave theory depends on wave height (H), wave period (T), and water depth (d). A chart based on experimental results is available to guide the use of wave theory based on two non-dimensional parameters (H/gT2) and (d/gT2). Based on this chart, Stokes second-order [27] wave theory is used.

The currents mostly exist in the same direction of wave, and it will be the critical case for design. A surface current of 1.5 m/s with one-seventh power profile [28] variation is considered for the design of substructure. The current velocity exerts drag force on the structure and cannot be algebraically added to wave forces because of nonlinear term in the Morison's drag equation. Therefore, the total drag force due to wave and current is obtained by considering the vector sum of current velocity and water particle velocity. The combined drag and inertia force (including wave and current) vary with time and will be maximum only at one occasion. In order to find the maximum force, phase angle is varied from 0 to 360° with an increment of 10° and the base shear for each case is estimated. It is observed that the maximum base shear is at 300° phase angle, and this case is used for the design of substructure.

4.2.3. Earthquake loads

Wind turbines are slender structures with a large mass at the top. The slender and relative long first natural periods may reduce the seismic forces but the high top mass may induce increased inertia force [29]. The structure is discretized into beam elements of 1 m and the masses at each nodal level are lumped accordingly (the turbine mass is lumped at the top of the tower). The free vibration analysis is carried out, and the natural frequencies are given in **Table 4**.

Response spectral method is used for the estimation of earthquake forces for both the substructure concepts. In this method, earthquake acceleration is obtained by combining the acceleration coefficients of different mode shapes. For each mode, the acceleration coefficient is obtained from the design spectrum of IS 1893:2002 [30] and combined using complete quadratic combination (CQC) modal [31]. The parameters considered for obtaining seismic coefficient are zone factor—0.16, reduction factor—2, importance factor—1.5, and soil type—medium soil. The damping ratio of 2.0% is considered as the material is steel [32]. This seismic coefficient is multiplied with seismic mass and acceleration due to gravity (g) to obtain

Mode no.	Natural periods (s)		
	Gravity foundation	Monopile	Jacket
1 & 2	3.065	3.244	2.03
3 & 4	0.382	0.419	0.42

Table 4. Natural periods of various substructures.

earthquake forces. The earthquake loads are then combined with operational environmental conditions with a wave height of 2 m and a period of 8 s along with 0.7 m/s surface currents.

4.2.4. Structural analysis of monopile

The monopile, monopole, and tower are modeled using beam elements. The mesh of pile is refined with a 1-m length, and at the end of each element, three nonlinear springs (two horizontal and one vertical spring) are modeled to simulate the behavior of the soil for a 1-m layer. Two horizontal springs represent the lateral stiffness and the vertical springs represent the axial stiffness. The nonlinear properties for horizontal springs are governed by p-y curve (lateral load vs. deflection of the pile), vertical springs for all layers except bottom-most layer by t-z curves (skin frictional resistance vs. deflection along pile), and vertical spring for bottom-most layer by Q-z curve (tip resistance vs. pile tip deflection). These curves are generated using API RP 2A–WSD, and the soil profiles considered are given in **Table 5**.

Monopile and jacket substructures with soil characteristics shown in **Table 5** were analyzed for extreme environment loads as described in Sections 4.2.2 and 4.2.3. The deflected profiles are shown in **Figure 9**. The observed deflections are well below the allowable limit (i.e., 1.25 times the tower height [33]).

4.2.5. Structural analysis of gravity-based foundation

The monopole and tower are modeled using the beam elements and analyzed for extreme conditions. The gravity-based foundation is modeled using a three-noded plate as shown in **Figure 10**, and rigid links are used to transfer the loads at the base of the monopole to the inner shaft of the gravity-based foundation. The gravity foundation mainly consists of five components: base plate, outer shaft, inner shaft, inclined shaft, and stiffeners (**Figure 10**). The base plate of the foundation is 20-m diameter, with two concentric shafts. The inner shaft has a radius of 3 m and 13-m height, which holds the monopole. The outer shaft has a radius of 10 m and its height being 6 m. An inclined slab connects the top of the inner and the outer shaft. There are six stiffeners to connect the inner and outer shafts and to increase the stiffness. The modeled structure is designed for bending moments in orthogonal directions, and the reinforcement is proved as per IS 456. The grades of concrete and steel for design are M40 and Fe415, respectively. The configuration of foundation is also checked for stability against sliding and overturning and bearing with a factor of safety of 22, 31 and 3, respectively.

S. no.	Depth (m)	Description	SPT value
1	3	Gray fine sand	12
2	10	Gray silty fine sand	34
3	12	Crushed pieces of rock	50 (for 6-cm penetration)
4	18	Fine silty sand	71
5	21	Silty fine sand	34

Table 5. Soil parameters considered for design.

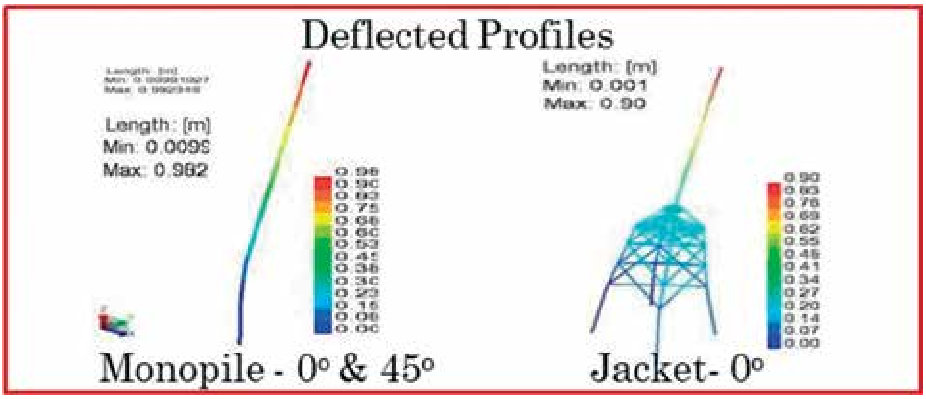

Figure 9. Deflected profiles for monopile and jacket structures.

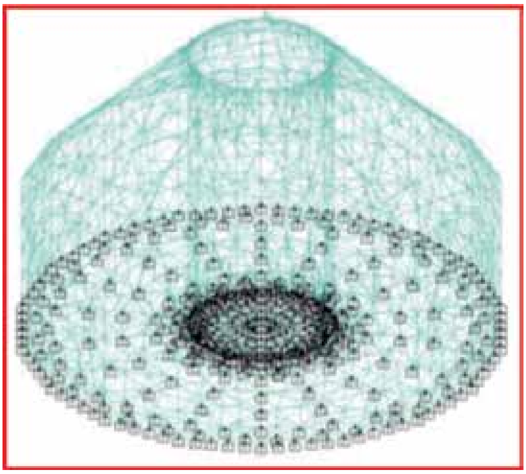

Figure 10. FEM models gravity-based foundation.

5. Installation methodology

5.1. Monopile

The length of monopile is 30 m with diameters of 6 m and requires huge hydraulic hammers for driving the pile. These hammers are usually equipped on a floating barge or jack-up platforms. Jack-up platforms are generally used under severe sea-state conditions and floating barges for relatively calm sea conditions. The jack-up platforms are associated with high rentals and less deck space than floating barges. In case of floating barges, the large deck space on the barge can reduce the time and costs needed for the transportation of monopiles and transition pieces by using the barge as a floating storage. Considering the low-wave climate along potential sites of Tamil Nadu, floating barge would be an ideal solution. However, these vessels (floating barges/specialized jack-up platforms) are not available in India and have to be hired from Europe or to be developed in India. Hence, the cost of mobilization and demobilization will be high during the installation phase of offshore wind project.

The installation methodology for a monopile using specialized vessel is shown in **Figure 11**. The ship is loaded with four to five monopiles in the port and sailed to the wind farm. The monopile will be lowered through a guide with the help of a deck crane and driven using a hydraulic hammer. Once the monopile is driven to the required depth, the transition piece is installed over it. The gap between the monopile and the transition piece is grouted for appropriate transfer of loads and to adjust the alignment of platform. The main advantage of the monopile is easy and quick installation. On the other hand, its disadvantages include high cost due to unavailability in India and additional charges for mobilization and demobilization.

5.2. Gravity-based foundation

The installation methodology for gravity-based foundation is shown in **Figure 12**. The gravity-based foundation is constructed on a steel platform nearby the fishing harbor. The monopole is then installed through the inner ring of the foundation. In the second stage, the landside edge of the platform is raised by hydraulic jacks. The gravity-based foundation is slid into the water. Due to buoyancy effects, the structure will float. The gravity-based foundation is then towed to the required position using a tug. Before lowering the foundation, the seabed has to be leveled using a gravel bed. The foundation is then positioned using tugs and then lowered by ballasting water into it. The hollow chambers inside the foundation are filled with plain cement concrete to increase the stability of the foundation.

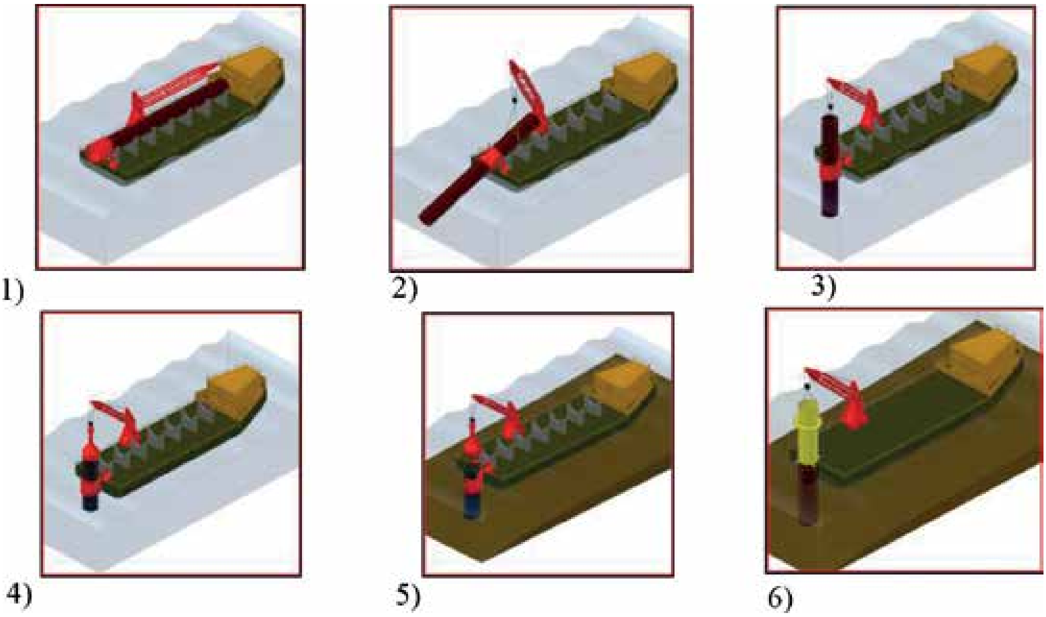

Figure 11. Installation methodology of monopile.

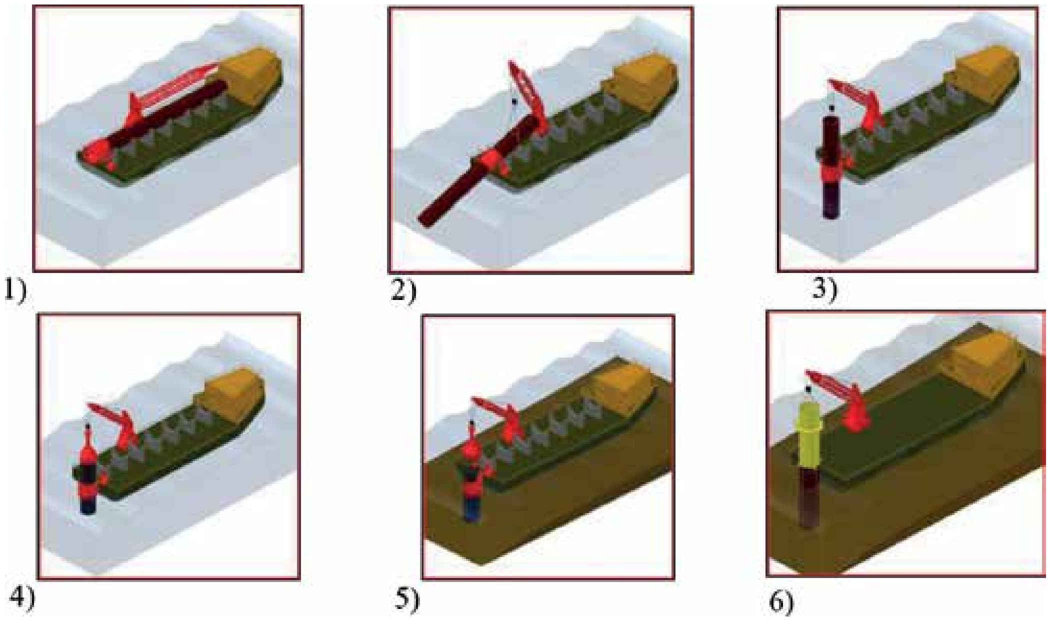

Figure 12. Installation methodology of gravity foundation.

The static stability of the foundation is carried out, and the draft is estimated to be 4 m from the bottom. As the foundation needs to be towed for a long distance, it is essential to identify the natural frequencies and response amplitude operations (RAO). Natural frequencies and RAOs are computed for three translation modes and three rotation modes. It is observed that the natural frequency is far away from the encounter frequency of waves (5–10 s).

6. Summary and conclusions

Offshore wind being pollution-free would be an ideal solution to meet the increasing demand as Indian coast is blessed with significant winds. The Ministry of New and Renewable Energy (MNRE) has published the offshore wind policy for offshore wind development in India [23]. Offshore wind would be commercially viable, if potential sites are identified and economical substructure concepts along with installation methodology are developed considering local conditions. Hence, studies were taken up to identify potential sites, perform commercial viability studies, and design the optimum substructure configuration along with installation methodology.

Wind assessment studies based on secondary wind data like offshore satellite winds and onshore mast data by various organizations helped in identifying potential sites along the coast of Gujarat and Tamil Nadu. Commercial viability studies based on these data were carried out and indicated the need for suitable incentives by the Government of India to attract huge investments for offshore wind industry. NIWE has attempted to capture the offshore wind parameters by installing an onshore mast in a narrow strip extending into the sea. LiDAR-based offshore wind data collection platforms are successfully commissioned in Gulf of Khambhat for MNRE-NIWE and Gulf of Kutch for M/S Suzlon with technical support from NIOT for recording the continuous wind data and validation.

Considering the bathymetry and geotechnical conditions along potential sites, three substructure concepts, monopile, gravity-based foundation, and jacket, were analyzed. A preliminary design based on aerodynamic loads on turbine, hydrodynamic loads on the structures, pile-soil interaction, and floatation analysis for gravity-based structures is carried out to arrive at suitable substructure concepts for Gujarat and Tamil Nadu. Installation methodologies were developed for identified substructure concepts for Indian scenario and the infrastructure needs assessed. These studies will also assist in arriving at the cost for implementation of the offshore wind farm projects.

Acknowledgements

The authors wish to express their sincere thanks to Dr. Satheesh C. Shenoi, Director, NIOT, for his keen interest and encouragement. They also express their gratitude to the National Institute of Wind Energy and M/s Suzlon for their support in LiDAR project. The authors thankfully acknowledge the support extended by MoES in funding the project.

Author details

Satya Kiran Raju Alluri*, Devender Gujjula, Krishnaveni B, Dhinesh Ganapathi,
S.V.S. Phanikumar, M.V. Ramanamurthy and M.A. Atmanand

*Address all correspondence to: raju@niot.res.in

National Institute of Ocean Technology, Chennai, Tamil Nadu, India

References

[1] European Wind Energy Association. The European Offshore Wind Industry-Key Trends and Statistics 2014; 2015

[2] Global Wind Energy Council. Global Wind Statistics 2014. Brussels, Belgium; 2014

[3] European Wind Energy Association. Wind Energy Scenarios for 2020. July 2014

[4] FOWIND. Offshore Wind Policy and Market Assessment. December 2014

[5] Energy Next. March 2013. [Online]. http://www.energynext.in/japan-to-increase-its-offshore-wind-capacity-to-40-times-by-2020/

[6] London Array. 2013. [Online]. http://www.londonarray.com/wp-content/uploads/London-Array-Brochure.pdf

[7] A National Offshore Wind Strategy: Creating an Offshore Wind Energy Industry in the United States. U.S. Department of Energy's (DOE); February, 2011

[8] Central Electricity Authority. Installed Capacity January 2015. [Online]. Available: http://www.cea.nic.in/reports/monthly/inst_capacity/jan15.pdf. [Accessed: 01 February 2015]

[9] Central Electricity Authority. Load Generation Balance Report 14-15 [Online]. Available: http://www.cea.nic.in/reports/yearly/lgbr_report.pdf. [Accessed 01 July 2014]

[10] Indian Agricultural Statistics Research Institute. Agriculture Research Data Book—2002 [Online]. Available: http://www.iasri.res.in/agridata/02data%5Cchapter%204%5Cdb2002tb4_5.htm [Accessed: 01 July 2014]

[11] CWET, Riso DTU. The Indian Wind Atlas. Chennai: Center for Wind Energy Technology; 2010

[12] Harikumar R, Sabique L, Balakrishnan Nair TM, Shenoi SSC. Report on the assessment of wind energy potential along the Indian coast for offshore wind farm advisories. INCOIS Tech. Rep. INCOIS-MOG&ISG-TR-2011-07; 2011

[13] International Electrotechnical Commission. Wind turbines—Part 3: Design requirements for offshore wind turbines. No. IEC61400-3; 2009

[14] Kaiser MJ, Snyder B. Offshore Wind Energy Installation and Decommissioning Cost Estimation in the US Outer Continental Shelf. Louisiana: Energy Research Group LLC; 2010

[15] Kaiser MJ, Snyder BF. Modeling offshore wind installation costs on the US outer continental shelf. Renewable Energy. 2013;**50**:676-691

[16] Uraz E. Offshore Wind Turbine Transportation & Installation Analyses Planning Optimal Marine Operations for Offshore Wind Projects; 2011

[17] Fingersh LJ, Hand MM, Laxson AS. Wind Turbine Design Cost and Scaling Model; 2006

[18] Greenacre P, Gross R, Heptonstall P. Great Expectations: The Cost of Offshore Wind in UK Waters. UK Energy Research; 2010

[19] Snyder B, Kaiser MJ. Ecological and economic cost-benefit analysis of offshore wind energy. Renewable Energy. 2009;**34**(6):1567-1578

[20] Zhang J et al. Response surface based cost model for onshore wind farms using extended radial basis functions. Proceedings of the ASME 2010 International Design Engineering Technical Conferences & Computers and Information in Engineering Conference, IDETC/CIE 2010-29121; 2010

[21] The European Wind Energy Association. The European Offshore Wind Industry—Key Trends and Statistics 2015; 2016

[22] Wen Chen I et al. Design and analysis of jacket substructures for offshore wind turbines. Energies—Open Access Energy Research, Engineering and Policy Journal; 2016

[23] Wind Energy Division, Ministry of New and Renewable Energy. National Offshore Wind Energy Policy, No. 51/58(Cab.)/2011-WE; 2015

[24] Jonkman J et al. Definition of a 5 MW wind turbine for offshore system development. In: Technical Report of National Renewable Energy Laboratory, TP-500-38060; 2009

[25] International Electrotechnical Commission. Wind turbines: Design requirements for offshore wind turbines. IEC. 2009;**61400**(Part 3)

[26] Techet AH. Morrison's Equation. Massachusetts Institute of Technology; 2004

[27] Schaffer HA, Second–order wavemaker theory for irregular waves. Ocean Engineering. 1996;**23**(1):47-48

[28] Bryden IG, Couch SJ, Owen A, Melville G. Tidal current resource assessment. Proceedings of the Institution of Mechanical Engineers, Part A: Journal of Power and Energy;**221**(2): 125-135

[29] Daxton O. Analysing the effect of earth quake on wing turbine [MS thesis]. Civil Engineering, REYKJAVIK University; 2014

[30] Indian Standards. Criteria for earthquake resistant design of structures, general provisions and buildings. IS 1893 (Part 1); 2002

[31] Der Kiureghian A, Nakamura Y. CQC modal combination rule for high frequency modes. Earthquake Engineering and Structural Dynamics. 1993;**22**:943-956

[32] Papageorgiou AV, Gantes CJ. Equivalent Uniform Damping Ratio for Irregular in Height Concrete/Steel Structural Systems. Eurosteel 2009; Austria; 2008

[33] Nicholson JC. Design of wind turbine tower and foundation systems: Optimization approach [Master's thesis]. University of Iowa; 2011

Chapter 9

Reliability Analysis of Wind Turbines

Caichao Zhu and Yao Li

Additional information is available at the end of the chapter

http://dx.doi.org/10.5772/intechopen.74859

Abstract

With the rapid development of wind power industry, the reliability of wind turbines has become a hotspot in wind power research. The failure modes and research progress of wind turbine reliability both at home and abroad are analyzed. The failure modes, failure causes and detection methods of some key components in the wind turbines are summarized. Also, the frequently used methods of reliability analysis and research status of wind turbine reliability are analyzed. Following this, research focuses, methods and measures to improve wind turbine reliability are presented. We also shed light on the condition monitoring and assessment process with condition monitoring system and supervisory control and data acquisition. It is of great significance to reduce the cost of operation and maintenance and to improve the safety of wind turbines.

Keywords: wind turbines, failure modes, reliability analysis, condition monitoring, assessment

1. Introduction

Fossil fuels are nonrenewable and their associated prices are fluctuating sharply. Meanwhile, the increasing environmental and climatic concerns of the current times have moved the research focus from conventional electricity resources to renewable resources [1, 2]. Renewable energy resources, such as wind, solar and geothermal power, are clean alternatives to fossil fuels. Among them, wind energy is one of the most promising renewable energy resources in the world today. The main attractions of wind energy are a large resource and low environmental impact. In this condition, wind energy is developing rapidly. For example, over 51.2 GW of capacity was installed in 2014 [3].

In recent years, wind power industry has been flourishing all over the world, and in some countries, the focus has been gradually shifted from land-based to offshore wind farms [4]. On a global basis, the size of the annual market grew 42% year-over-year in 2014 compared to a 20% fall in 2013 [3]. By the end of 2014, the cumulative installed capacity climbed to 372 GW [5, 6], which is shown in **Figure 1**. Policy-driven accelerations play a very important role in market growth, especially in China, Germany and the United States. In these three countries, China is the world's largest wind power market with 23.2 GW of new wind power installed in 2014. The development of wind power in China is shown in **Figure 2**. **Figure 3** shows the top 10 countries of newly installed capacity from January to December in 2014 [6]. The total installed capacity is up to 51,473 MW, and the share of China is 45.1%. With more

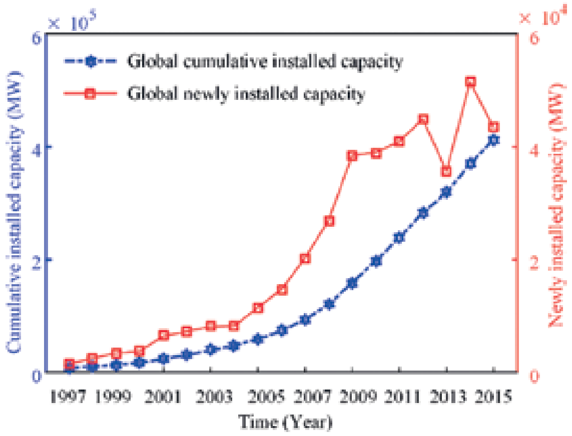

Figure 1. The global wind power capacity.

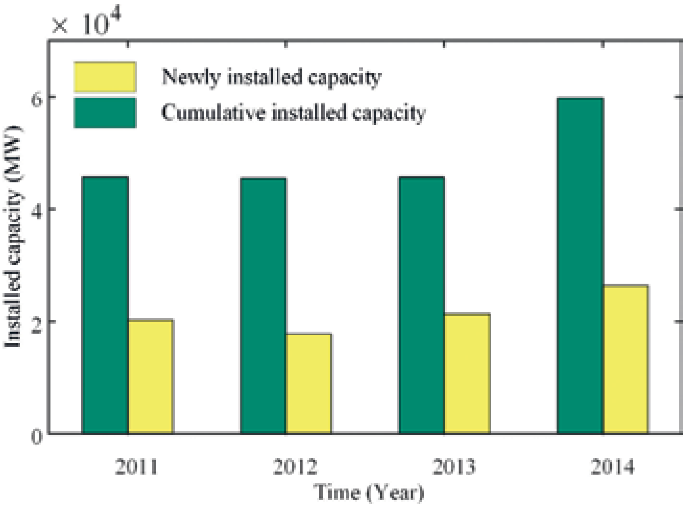

Figure 2. Development of wind power in China.

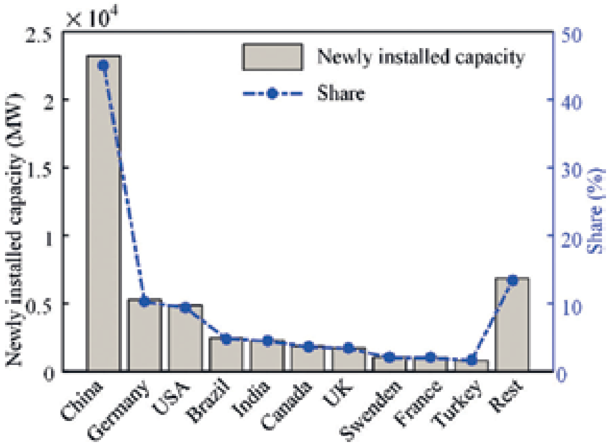

Figure 3. Top 10 newly installed capacity Jan.–Dec. 2014.

and more wind turbines being installed, lots of potential problems still need to be solved, such as fatigue, failures, condition monitoring, operation and maintenance, which are especially true in the current circumstances where the tower height, rotor diameter and overall turbine weights have almost quadrupled in size and capacity [7]. Hence, the reliability of wind turbines is becoming more important now than ever before.

2. Developments and challenges

In the late 1970s, in response to the oil price increasing around that time, a number of government programs were initiated with the objective of developing suitable wind turbines. To reduce the dependence on conventional electricity sources, the related countries carried out many programs and focused on the development of wind turbines, rating up to 4 MW and diameters up to 100 m. Some examples are included in **Table 1**. Furthermore, wind energy has witnessed rapid development in few decades, making it one of the fastest growing sources of electricity in the world today. But it is thought that wind energy is still immature these days. Due to technological advancements, policy initiatives and economic drivers, wind energy is now able to make a cost-competitive contribution to our growing energy needs. For example, over 240,000 commercial-sized wind turbines were operating in the world by 2014, producing 4% of the world's electricity [8, 9]. Wind power showed the potential for replacing natural gas in electricity generation on the cost basis. Technological innovations continue to drive new developments in the application of wind power. Until now, the cumulative installed capacity has been more than 400 GW.

With the growing number of the wind turbines, the industry still needs to face numerous challenges. A number of wind turbine components are prone to failure, and it is difficult and expensive to repair or replace them. For example, bearings, inverters and gearboxes raise the maintenance issues. Still, wind energy challenges still exist due to: (1) poor performance and

Location	Name	Rating (MW)	Diameter (m)	Blades	Date	Features
Canada	Eole	3.6	64	2	1987	Vertical axis, direct drive
Denmark	Tjaereborg	2	61	3	1988	
Germany	Growian	3	100	2	1981	
Germany	Monopteros	0.64	50	1	1989	
Italy	Gamma 60	1.5	60	2	1991	Variable speed, Power control by yaw
Netherlands	Newecs 45	1	45	2	1985	
Spain	AWEC-60	1.2	60	3	1989	Variable speed
Sweden	WTS-3	3	78	2	1982	
UK	LS1	3	60	2	1987	Partial span pitch control
USA	WTS-4	4	78	2	1982	Similar to WTS3 (Sweden)
USA	MOD-5B	3.2	99	2	1987	Variable speed

Table 1. Some of the early prototype machines, mostly funded by governments.

reliability and (2) rising costs driven by transportation, maintenance, and so on. To achieve a longer life of wind turbines and to reduce the cost of maintenance, the development of technologies for improving the reliability of wind turbines is an important consideration for future development, especially for offshore wind turbines. Hence, measures must be taken to improve the reliability of wind turbines.

3. Wind turbine failure modes

Nowadays, the development of wind turbines tends toward larger and heavier structures, which increases the failure frequency. In reality, the failure rates are also very different between onshore and offshore wind turbine systems for the same type. **Figure 4** shows failure rates of wind turbine systems and components [10]. The results in **Figure 4** show that some key components have higher failure rates than that of other components, and the same components working offshore have much higher failure rates than those working onshore.

For a wind turbine transmission system, key components like the generator, gearbox and blades have the highest failure rates. The gearbox failures are mainly caused by gears and bearings; the generator failures are mainly caused by bearings. **Table 2** shows the failure modes, failure causes and detection methods of wind turbine key components and subassemblies.

3.1. Gearbox failure modes

Any key components fail in the gearbox, it may result in high cost of maintenance and high production loss and may take longer time to repair, especially for offshore wind turbines. The

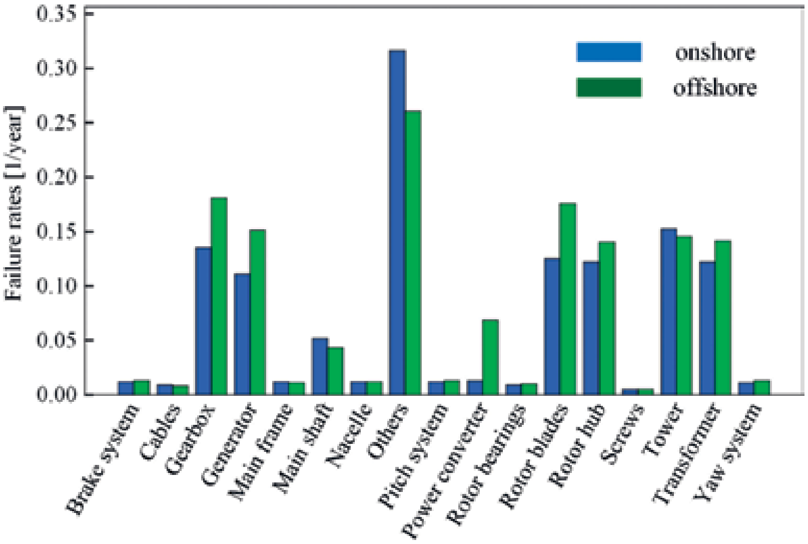

Figure 4. Failure rates for wind turbine subassemblies working onshore and offshore.

regular failure modes of gearbox are bearing failures, gear fatigue, wear, fracture, insufficient lubrication, and so on. **Figure 5** shows three common failure modes of gearbox, in which fatigue failures are the most common. The bolts connecting the front box, ring and middle box sometimes fail because of the strong and unbalanced axial forces acting on the bolts. The bolt failure is shown in **Figure 6**. The result in **Figure 5** shows that the section is smooth, so the failure is caused by fatigue fracture. However, the experiments show that a relief notch, a proper taper of thread and a thread root radius can increase its carrying capacity and reliability.

3.2. Generator failure modes

The generator is one of the most key components with high failure rates since it connects to the high-speed shaft of the wind turbine gearbox with time-varying mechanical torques. Four failure root causes are: design issues, operations issues, maintenance practices and environmental conditions. The failure rates of wind turbine generators have a close relationship with their power rating, working environment, and so on. **Figure 7** shows failure rates of subassemblies of onshore and offshore wind turbine systems. Different failure causes may lead to different generator failure modes, including design issues, operation issues, maintenance and external environment, which is shown in **Table 3**. **Figure 8** shows three common failure modes of the generator where the bearing failure is the most common.

3.3. Rotor blade failure modes

The rotor blades of wind turbine are driven by the wind energy and transform wind energy to mechanical energy. Because blades often suffer alternating stress and complex environments, they have high failure rates, with the main failure modes being fatigue, fracture, crack, wear, freezing and sensor failure. **Figure 9** shows failure modes of the blades. Due to

Objects	**Function**	**Failure mode**	**Cause**	**Detection method**
Blades	Capture wind	Fracture, edge crack, stuck, motor failure, pitch bearing failure	Fatigue loads higher than anticipated, extreme loads, environment influences, imbalance	Excessive vibration sensed by rotor bearing accelerometer in hub; high stresses recorded by operating instrumentation
Main shaft	Transmit large torque	Fracture	Fatigue loads underestimated; operation of WTG at off-design conditions; material properties below specs	Low-speed sensor; bearing vibration sensor
Yaw system	Enable the nacelle to rotate on the tower	Increased bearing friction	Cracked roller; galled surface; lack of lubrication	Yaw error signal
High-speed shaft	Stop and hold the shaft during shutdown and operation	Low or higher brake torque	Environment effect	Tachometer
Gearbox	Transmit torque with speed increase	Internal gear tooth failure	Fatigue loads underestimated; exceeding design load; improper material; loss of lubricating oil	Vibration sensor
Hub assembly	Transmit torque from blades	Structure failure; bolt failure	Excessing design loads; excessive preload; stress corrosion	Rotor bearing accelerometer; periodic inspection for loose or missing bolts
Oil seals	Retain oil in main bearing housing; exclude foreign matter	Cut or wear in lip	Installation damage; wear	Low oil switch
Filters	To extract and hold all particulate contaminants from hydraulic fluid	Case leakage	Damage to case or seals	Low oil; level switch
Generator	Generate electric power	Overheat; fault; jammed bearing; bearing seizure; overspeed;	Overload; no excitation; environmental effects; misalignment; fatigue; mechanical failure; loss of drivetrain control	Protective relays; overspeed detection; testing
Lubrication	Lubricate gearbox and rotor bearing	Loss of oil; overheating; oil under temperature	Pump failure; leakage; diverting valve failure; ambient temperature above or below design conditions; excessive friction losses; diverting valve failure	Oil flow switch; oil temperature sensor; air temperature

Table 2. Summary of failure modes of components.

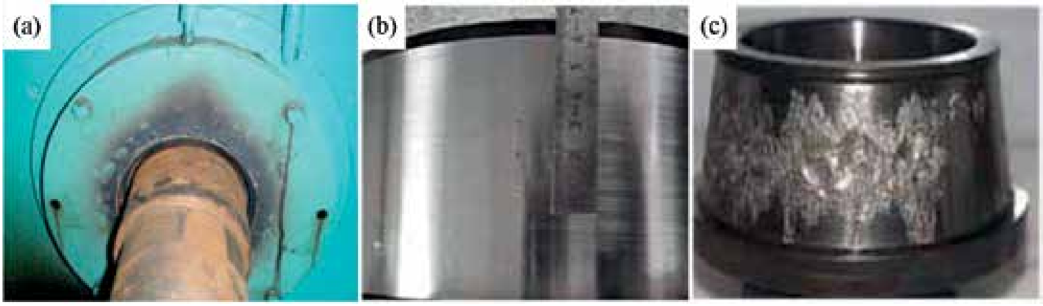

Figure 5. Bearings failure: (a) bearing in gearbox; (b) and (c) failure appearance of bearing.

Figure 6. Bolt faults of wind turbine gearbox.

the high location of rotor blades, they are difficult to repair and maintain which leads to high cost. Hence, in order to produce high-reliability blades, it is important and meaningful to study the relationship among failure modes, reliability and internal/external loads.

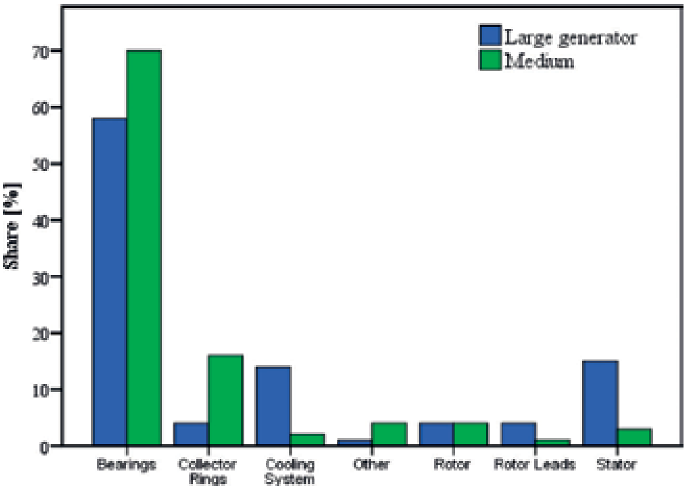

Figure 7. Failure rates of subassemblies of onshore and offshore.

Items	Failure modes
Design issues	(1) Electrical insulation inadequate; (2) loose components (wedges, banding); (3) crimped lead connections; (4) transient shaft voltages; (5) rotor lead failures and (6) complex structure
Operations issues	(1) Improper installation; (2) voltage irregularities; (3) improper grounding; (4) overspeed conditions and (5) transient damage
Maintenance practices	(1) ignoring alignment; (2) cooling system failures leading to heat related failure; (3) bearing failure and (4) rotor lead failures
Environmental condition	(1) Wind leading; (2) thermal cycling; (3) moisture/arid; (4) contamination and (5) electrical storms

Table 3. Failure modes of the generator.

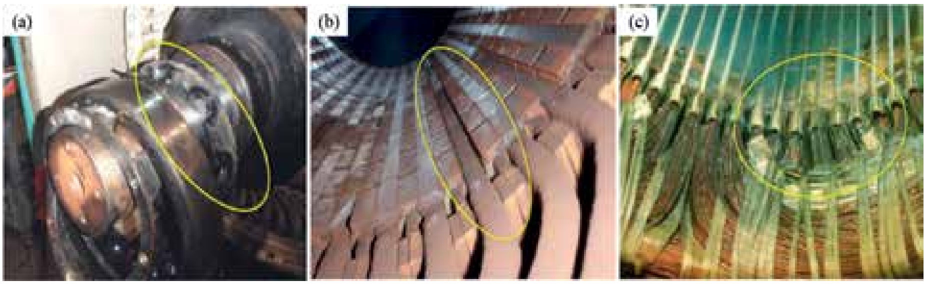

Figure 8. Generator failure: (a) bearing, (b) magnetic wedge loss and (c) contamination.

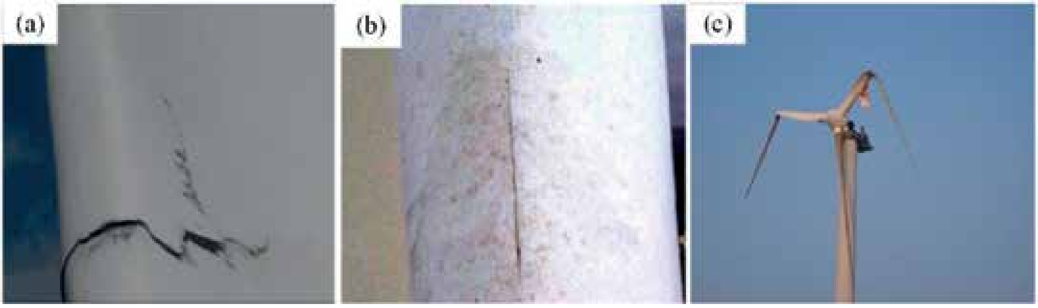

Figure 9. Failure modes of the blades. (a) Trailing edge crack; (b) leading edge failure and (c) blade fracture.

4. Wind turbine reliability analysis

The reliability definition is the probability that subassembly will meet its required function under a stated condition for a specified period of time. For an unrepairable system, the rating scale is reliability; for a repairable system, the rating scale is availability. Wind turbines consist of both unrepairable systems and repairable systems like gears, bearings, bolts and electronic components. So both reliability and availability should be considered to assess the wind turbines. **Figure 10** shows the failure rates of different subassemblies and its downtime after failure. The results in **Figure 10** show that the lower the subassembly's reliability, the longer is the downtime of the corresponding subassembly.

The reliability of wind turbine system is becoming more and more important with the continued growth and expansion of markets for wind turbine technology. In addition, wind turbines with reduced repair and maintenance (R&M) requirements and higher reliability are needed emergently. However, wind turbines produced by different companies have different reliability. There is no unified evaluation criterion. The current reliability analysis methods mainly focus on gear transmission systems of wind turbines and ignore the influences of other systems. The effects of the reliability model are limited if the system is simplified and seen as a series or parallel connection. Due to high costs of repair and maintenance, it is essential to study the health management systems of wind turbines and develop maintenance strategies in order to improve reliability and reduce unexpected repair and maintenance. The high-reliability systems can be achieved from three aspects, as shown in **Figure 11**.

4.1. Reliability analysis methods

There are two kinds of reliability analysis methods: statistical method based on database and stress-strength interference theory based on loads.

4.1.1. Statistical method based on database

The failure rates of wind turbines are time-varying during its lifetime, but the failure rates of repairable systems follow a bathtub curve. With a service life of around 20 years, wind turbine failure rates are assumed to follow the famous bathtub curve, as shown in **Figure 12**. Weibull

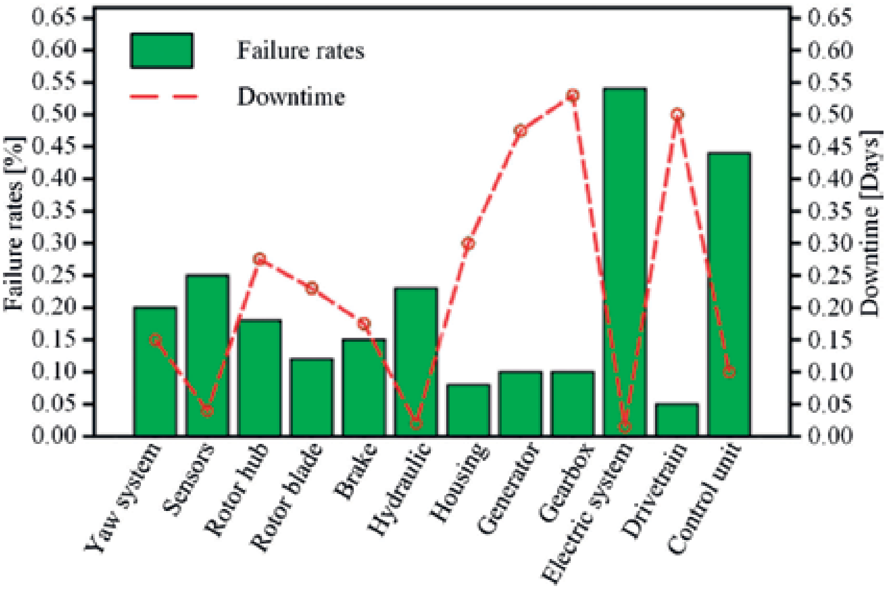

Figure 10. Failure rates and downtime for different subassemblies (DFIG).

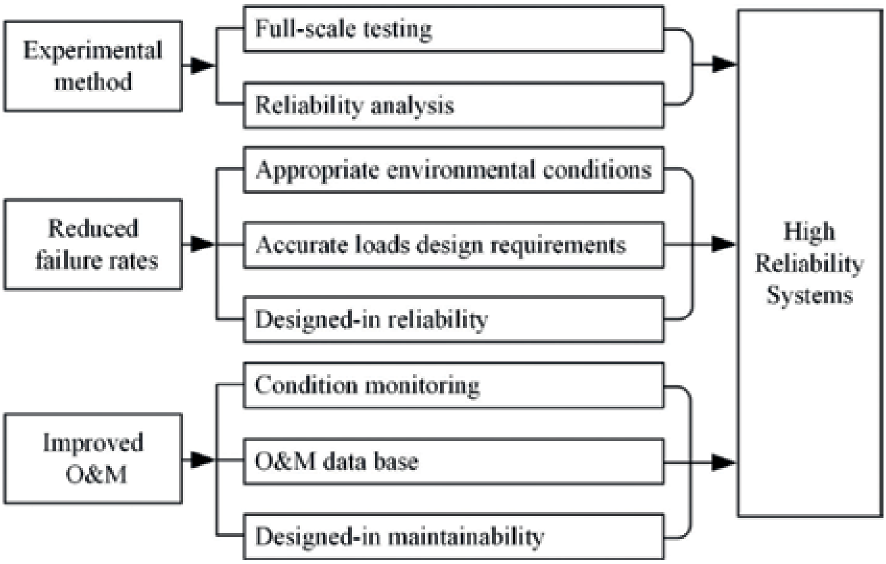

Figure 11. The requirements for developing the high-reliability systems.

distribution, gamma distribution and lognormal distribution are three commonly used methods in wind turbine reliability analysis. A method with mixtures of Weibull distribution with increasing hazard rates is written as follows [11]:

$$F(t) = \lambda\left[1 - \exp\left(-\left(\frac{t - t_0}{\eta_1}\right)^{\beta_1}\right)\right] + (1 - \lambda)\left[1 - \exp\left(-\left(\frac{t - t_0}{\eta_2}\right)^{\beta_2}\right)\right] \tag{1}$$

where t is time, $t > 0, \beta_1 \cdot \beta_2 > 1$, $\beta_1 \cdot \beta_2$ are shape parameters, β_1, β_2 are scale parameters and λ is the mixing parameter, $t_0 = 0, \eta_1 = 10, \eta_2 = 100, \beta_1 = 5, \beta_2 = 5$.

Figure 13 shows the fault probability density function. The results in **Figure 13** show that there are two peaks which represent early failures and wear out failures, respectively, and the failure

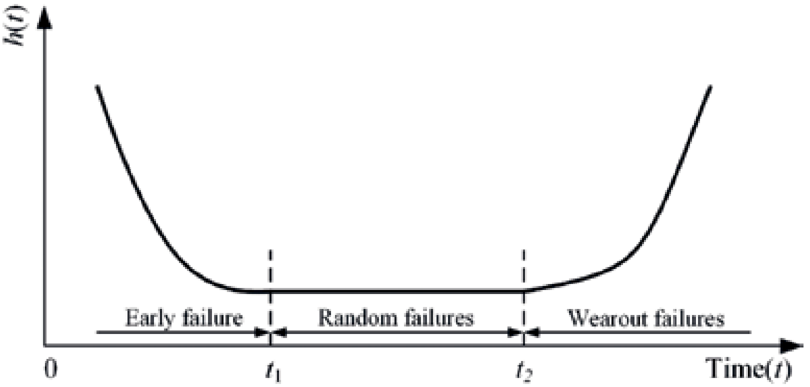

Figure 12. Bathtub curve of failure rates for repairable system.

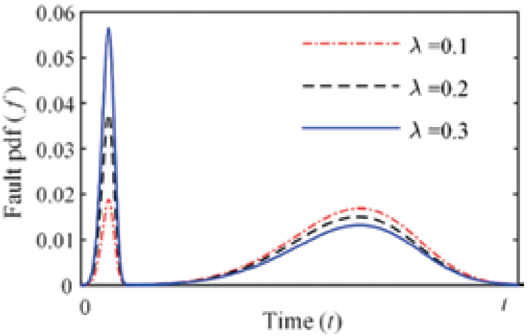

Figure 13. Fault probability density function.

rates are obvious higher at these two peaks. When the weighting factor equals 0.1, 0.2 and 0.3, the differences just happen at the peaks. Therefore, a proper weighting factor should be selected to meet the failure rate changes of wind turbines in different working environments. **Figure 14** shows the change of failure rates over time. The results in **Figure 14** show that a wind turbine is at running-in stage where its wear is large, and the failure rates are fluctuating and then stable. The failure rates of wind turbines will become higher and higher at the wear-out stage. Failure rate function curves with different weighting factors just show a difference at peak values, which has something to do with capacity and conditions. **Figure 15** shows the reliability function diagram which has three phases. The reliability in Phase I decreases sharply because newly installed wind turbines need to adapt to the environment. The reliability in Phase II is stable. There is a sharp decline in Phase III, which represents that the wind turbine has entered into wear-out failures, and its failure rates are high. Above all, it can be found that the bathtub curve can simulate the failure rate change among its service life as well.

4.1.2. Stress-strength interference theory based on loads

Random loads and fatigue strength of wind turbine subassemblies follow a normal distribution. The probability density function of stress and strength is expressed by the following equations:

$$f(S) = \frac{1}{\sqrt{2\pi}\,\sigma_s} \exp\left(-\frac{1}{2}\left(\frac{S - u_s}{\sigma_s}\right)^2\right) \tag{2}$$

$$g(\delta) = \frac{1}{\sqrt{2\pi}\,\sigma_\delta} \exp\left(-\frac{1}{2}\left(\frac{\delta - u_\delta}{\sigma_\delta}\right)^2\right) \tag{3}$$

where S, δ are stress and strength random variables, respectively; σ_s, σ_δ are the standard deviation of stress random variable and strength random variable, respectively; and u_s, u_δ are the expectation of stress random variable and strength random variable, respectively.

Figure 16 is a common practice to represent stress-strength interference. The figure shows the probability density function of stress and strength and their interference (overlap) over time.

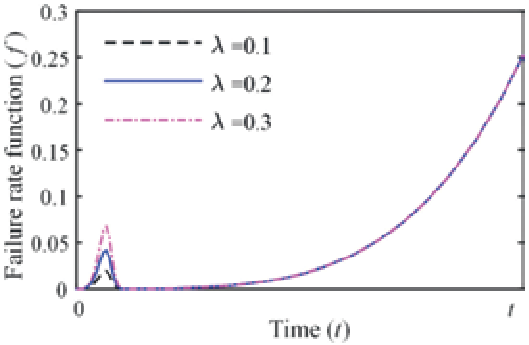

Figure 14. Failure rate function.

The interference is failure probability. The larger the area of the interference, the higher is the failure probability. Moreover, the interference area will become larger and larger over time in service life. The reliability of the system is:

$$\text{Reliability} = 1 - \text{Interference} \tag{4}$$

A new random variable z can be introduced, which is defined by

$$z = \delta - S \tag{5}$$

Then, the random variable z also follows normal distribution, so the reliability of stress-strength interference theory model is:

$$R = \int_0^{\infty} \frac{1}{\sqrt{2\pi}\,\sigma_z} \exp\left(-\frac{(z-u_z)^2}{2\sigma_z^2}\right) dz \tag{6}$$

where σ_z is the standard deviation of z and u_z is the expectation of z.

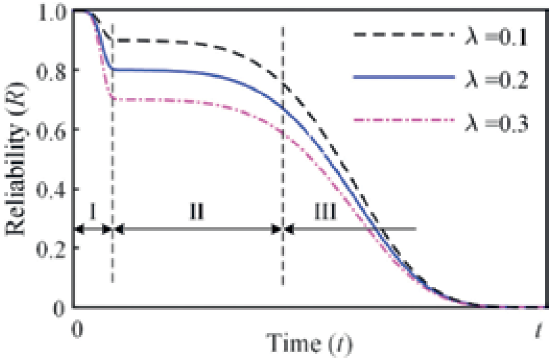

Figure 15. Reliability function.

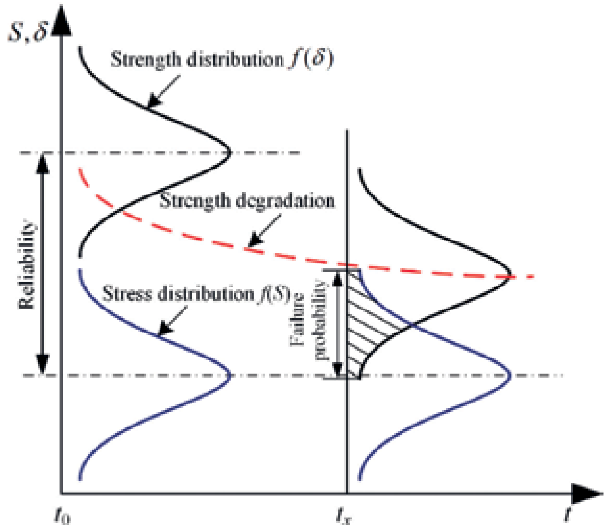

Figure 16. Graphical representation of stress-strength interference.

The dynamic reliability of gears can be calculated by the reliability calculation equation with the mean and standard deviation of gear fatigue stress and fatigue strength. **Figure 17** shows the reliability of high-speed stage gear. The figure shows that the reliability declines heavily before 20,000 h.

4.2. Current gearbox reliability analysis

High-performance gearboxes with large transmission ratios are available, which have been used in many areas. However, wind turbine gearboxes have more challenging and a greater

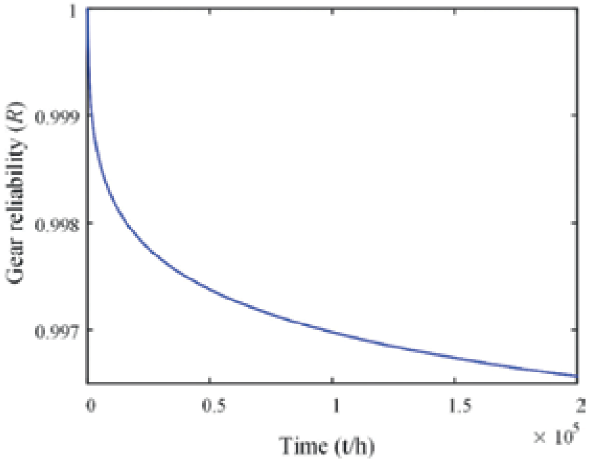

Figure 17. Reliability of high-speed stage gear.

number of technical requirements, like high reliability, safety and up to 25 years of operating life. Due to its complex structure and variable conditions, gearboxes have been and still are a source of failure and so have been paid more attention in the industry. Nowadays, the capacity of the multistage planetary wind turbines that are installed is up to the megawatt power classes. Hence, it is important to point out that the reliability of wind turbine gearboxes has great influences on wind turbines.

The current reliability research methods of the wind turbine gearbox include finite element method (FEM), lumped mass method (LMM), statistical methods based on database, experiment method (EM), simulation with software, and so on. Statistical methods based on database are most commonly used.

The researchers in national renewable energy laboratory (NREL) have done much milestone work. Generator and gearbox models have been produced in Matrix Laboratory (MATLAB) and NREL's Fatigue, Aerodynamics, Structures and Turbulence (FAST) [12]. NREL proposed that it is essential to bring all the parties involved in the gearbox-design process together to achieve the common goal of improving the reliability and lifetime of gearboxes [13]. The effects of different constant rotor torque and moment conditions and intentional generator misalignment on gearbox motion and high-speed shaft loads are examined [14].

The condition monitoring and fault diagnosis based on condition monitoring system (CMS) and supervisory control and data acquisition (SCADA) are also popular in wind turbine industry. The whole condition monitoring and assessment process within the system boundary include hard platform, condition monitoring and administrators of wind farms. Hard platform for wind farms includes the wind turbines, meteorological stations and monitoring data

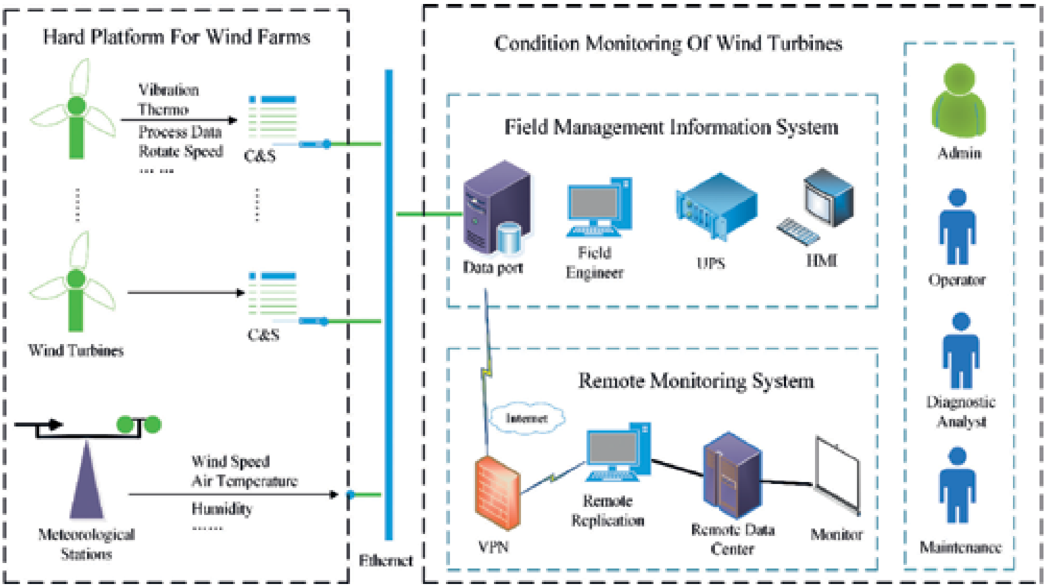

Figure 18. Flowchart of the condition monitoring and assessment process.

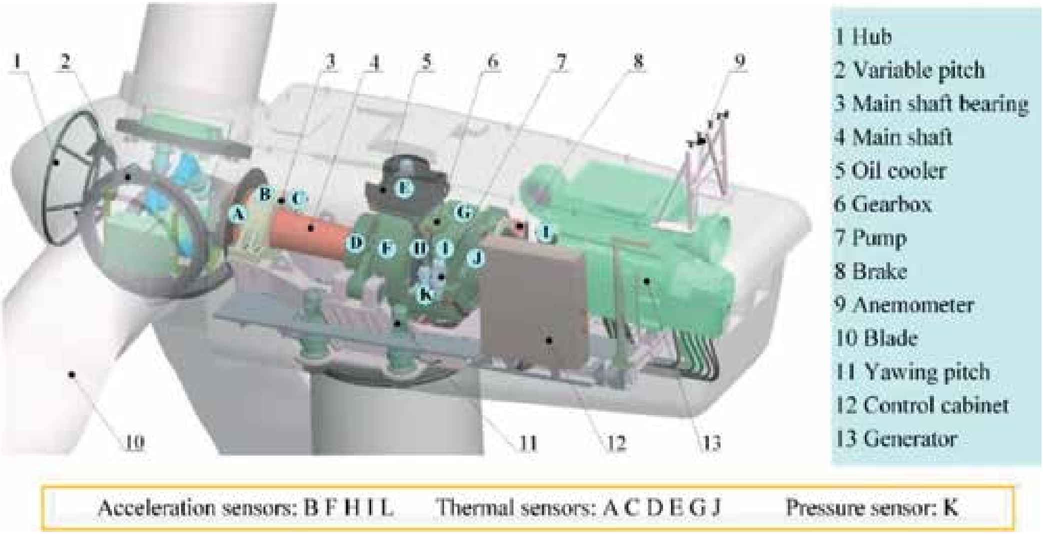

Figure 19. The distributions of the sensors.

via CMS and SCADA. Condition monitoring can be divided into remote monitoring system (RMS) and field management information system (FMIS); where, the FMIS includes data port, field engineer, uninterruptible power system (UPS) and human-machine interaction (HMI), and the RMS includes remote replication and a data center. The boundaries of the condition monitoring and assessment process for the wind turbine gearboxes are shown in **Figure 18**.

The condition monitoring systems of the CMS and SCADA can reflect the real-time running status of the wind turbine gearbox. The framework of the indices and project layers for the assessment of the wind turbine gearbox are established based on the CMS and SCADA. The goal layer can be classified into five project layers, and simultaneously, each project layer consists of the monitoring indices. For example, the goal layer can be divided into main shaft bearing (MSB), planetary stage (PS), low-speed stage (LSS), intermediate-speed stage (IMS), high-speed stage (HSS) and external factors (EF). The monitoring objects mainly consist of the nacelle, main shaft, bearing, cooling system, lubrication system and other related variables. **Figure 19** shows the location distribution of the sensors.

5. Conclusions

In order to solve reliability problems in wind power industry, scholars all over the world proposed many methods. But these reliability analysis methods mainly focus on gear transmission systems of wind turbines and ignore the influences of other systems. The effects of the reliability analysis are limited if the system is simplified and seen as a series or parallel connection. Based on the abovementioned analysis and field research, some key conclusions are proposed:

(1) The reliability research based on the fatigue life.

The fatigue failure is the common failure modes of wind turbines. It needs to study the whole wind turbine fatigue life and reliability. With design parameters and the dynamic model, the failure correlation of key components is calculated. Following this, matrixes of loads and contact stresses can be calculated considering the operation environment of wind turbines. Finally, it is possible to produce the fatigue cumulative damage of key components.

(2) The gradual change mechanism and physical representation of component health status.

Combining loads and fault statistical data, the gradual change mechanism of health status needs to be studied with the function of key components and mechanism characteristics, and to seek the physical representation that is related to the component health status. This is helpful to develop the trend model and thresholds of the physical representation of fault status. Following the abovementioned method, it is possible to assess and pre-estimate the reliability of components and subassemblies.

(3) Reliability research based on the whole wind turbine's dynamics.

Considering the influences of the random wind speed and waves, the dynamic model is established including components from blades to the foundation, by which the dynamic reliability of the wind turbine structure and drivetrain is studied. Following this, it is possible to evaluate the dynamic reliability of the whole wind turbine. However, the current reliability research ignored the influences of waves on the foundation and the tower, which would bring big errors to the reliability research. Therefore, it is essential and urgent to develop a set of the reliability engineering model and test method of wind turbines considering the influences of waves and the sea wind.

(4) Remote real-time assessment system of the wind turbine reliability based on the fusion data.

It is clear that most wind turbines have been installed both SCADA and CMS, but they are independent and cannot achieve the mutual support of test results. Therefore, it is meaningful to mix two sets of the test data based on SCADA and CMS. Following this, the feature data can be extracted and transferred to the data center by the Internet. When the feature data reach the data center, they can be used to calculate and assess the dynamic reliability of wind turbines through engineering models and hardware and software equipment immediately, which will cut the operation and maintenance cost and improve the operating efficiency of wind turbines sharply.

Acknowledgements

The authors wish to acknowledge the financial support from the Innovation Project of the City of Chongqing (cstc2015zdcy-ztzx70012, cstc2015zdcy-ztzx70010) and Chongqing Graduate Research and Innovation Project (CYB16024).

Author details

Caichao Zhu* and Yao Li

*Address all correspondence to: cczhu@cqu.edu.cn

The State Key Laboratory of Mechanical Transmissions, Chongqing University, Chongqing, China

References

[1] Hansen A, Iov F, Blaabjerg F, Hansen L. Review of contemporary wind turbine concepts and their market penetration. Wind Engineering. 2004;**28**:247-263

[2] Clive PJM. Windpower 2.0: Technology rises to the challenge. Environmental Research Web. 2008

[3] Jesse Broehl EA. Executive summary: World wind energy market update 2015. In: A BTM Navigant Wind Report; 2015

[4] Wu J, Wang Z-X, Xu L, Wang G-Q. Key technologies of VSC-HVDC and its application on offshore wind farm in China. Renewable and Sustainable Energy Reviews. 2014; **36**:247-255

[5] G.W.E. Council. Global Wind Energy Outlook 2014. GWEC Global Wind Energy Council. Vol. October; 2014

[6] G.W.E. Council. Global Wind Report; Annual Market Update 2014. Global Wind Energy Council; 2014

[7] Pérez JMP, Márquez FPG, Tobias A, Papaelias M. Wind turbine reliability analysis. Renewable and Sustainable Energy Reviews. 2013;**23**:463-472

[8] Wind in numbers. Global Wind Energy Council; 2014

[9] IEC61400-1. Wind Turbines-Part 1: Design Requirement. WWEA; 2014. p. 8

[10] Dinmohammadi F, Shafiee M. A fuzzy-FMEA risk assessment approach for offshore wind turbines. IJPHM Special Issue on Wind Turbine PHM (Color); 2013:59

[11] Klutke G-A, Kiessler PC, Wortman M. A critical look at the bathtub curve. IEEE Transactions on Reliability. 2003;**52**:125-129

[12] Singh M, Muljadi E, Jonkman J, Gevorgian V, Girsang I, Dhupia J. Simulation for Wind Turbine Generators—With FAST and MATLAB-Simulink Modules. Golden, CO: National Renewable Energy Laboratory (NREL); 2014

[13] Oyague F, Butterfield C, Sheng S. Gearbox reliability collaborative analysis round robin. In: Report No. NREL/CP-500-45325. Golden, CO: National Renewable Energy Laboratory; 2009

[14] Keller J, Guo Y, Sethuraman L. Gearbox reliability collaborative investigation of gearbox motion and high-speed-shaft loads. Contract; 2016

Edited by Kenneth Eloghene Okedu

This book is intended for academics and engineers working in universities, research institutes, and industry sectors wishing to acquire new information and enhance their knowledge of the current trends in wind turbine technology. Readers will gain new ideas and special experience with in-depth information about modeling, stability control, assessment, reliability, and future prospects of wind turbines. This book contains a number of problems and solutions that can be integrated into larger research findings and projects. The book enhances studies concerning the state of the art of wind turbines, modeling and intelligent control of wind turbines, power quality of wind turbines, robust controllers for wind turbines in cold weather, etc. The book also looks at recent developments in wind turbine supporting structures, noise reduction estimation methods, reliability and prospects of wind turbines, etc. As I enjoyed preparing this book, I am sure that it will be valuable for a large sector of readers.

Published in London, UK

IntechOpen

ISBN 978-1-83881-662-9